Electronic Supplementary Material (ESI) for Physical Chemistry Chemical Physics.

Electronic Supplementary Information (ESI) to accompany:

Separating Mixtures by Exploiting Molecular Packing Effects in Microporous Materials

Rajamani Krishna*

Van ‘t Hoff Institute for Molecular Sciences, University of Amsterdam, Science Park 904,

1098 XH Amsterdam, The Netherlands

*email: r.krishna@contact.uva.nl

ABSTRACT

We examine mixture separations with microporous adsorbents such as zeolites, metal-organic frameworks (MOFs) and zeolitic imidazolate frameworks (ZIFs), operating under conditions close to pore saturation. Pore saturation is realized, for example, when separating bulk liquid phase mixtures of polar compounds such as water, alcohols and ketones. For the operating conditions used in industrial practice, pore saturation is also attained in separations of hydrocarbon mixtures such as xylene isomers, and hexane isomers. Separations under pore saturation conditions are strongly influenced by differences in saturation capacities of the constituent species; the adsorption is often in favor of the component with the higher saturation capacity. Effective separations are achieved by exploiting differences the efficiency with which molecules pack within the ordered crystalline porous materials. For mixtures of chain alcohols, the shorter alcohol can be preferentially adsorbed because of its higher saturation capacity. With hydrophilic adsorbents, water can be selectively adsorbed from water/alcohol mixtures. For separations of o-xylene/m-xylene/p-xylene mixtures, the pore dimensions of MOFs can be tailored in such a manner as to allow optimal packing of the isomer that needs to be adsorbed preferentially. Subtle configurational differences between linear and branched alkane isomers result in significantly different packing efficiencies within the pore topology of MFI, AFI, ATS, and CFI zeolites.

A common characteristic feature of most separations that are reliant on molecular packing effects is that adsorption and intra-crystalline diffusion are synergistic; this enhances the separation efficiencies in fixed bed adsorbers.

Keywords: polar compounds; saturation capacity; molecular packing; entropy effects; xylene isomers; alkane isomers;

Table of Contents

1. Preamble

This ESI accompanying our review article *Separating Mixtures by Exploiting Molecular Packing Effects in Microporous Materials* provides (a) simulation methodology for transient breakthroughs, (b) data on pure component isotherms used to analyze the variety of separations, (c) IAST calculations of mixture adsorption equilibria, (d) simulations of transient breakthroughs of mixtures in fixed bed adsorbers, (e) additional background information of the importance of MOFs in aromatics separations. The detailed analysis of each separation in this ESI follows the same sequence as that of the discussions in the manuscript.

For ease of reading, this ESI is written as a stand-alone document; as a consequence, there is some overlap of material with the main manuscript.

2. Introduction

Microporous materials such as zeolites, metal-organic frameworks (MOFs), and zeolitic imidazolate frameworks (ZIFs) offer considerable potential as energy-efficient alternatives to conventional separation processes such as distillation, absorption, and extraction.

The majority of current research on MOFs and ZIFs appears to be focused on separations of mixtures of light gaseous compounds. A common feature of separations of gaseous mixtures is that even for operations at pressures ranging to 1 MPa, pore saturation conditions are often not reached; these separations are largely reliant on differences in adsorption strengths, and binding energies. For example, the selective adsorption of CO_2 from mixtures containing N_2, H_2, CO, and CH_4 can be realized by selective binding of CO_2 with either the metal atoms (M) of CuBTC,[1] Cu-TDPAT,[2] M-MOF-74[3, 4] or the extra-framework cations of NaX zeolite.[5] The quadrupole moment of N_2 is about four times that of O_2; as a consequence, for zeolites LiX, LTA-4A, and LTA-5A, the adsorption selectivity is in favor of N_2.[6, 7] The differences in the polarizabilities of noble gases such as Kr, and Xe can be exploited to recover each of these components in adsorbers packed with say NiMOF-74,[8, 9] or CuBTC.[8, 10]

For mixture adsorption, let us define the fractional occupancy within the pores, θ_t

$$\theta_t = \sum_{i=1}^{n} \frac{q_i}{q_{i,sat}} \tag{1}$$

where q_i is the molar loading of species i in the mixture, and $q_{i,sat}$ is its saturation capacity.

Figure 1a shows the variation of θ_t with total gas pressure, p_t, for adsorption of 20/80 CO_2/H_2 mixtures in Cu-TDPAT, 50/50 CO_2/CH_4 mixtures in NiMOF-74, and 15/85 CO_2/N_2 mixtures in MgMOF-74. For all these separations, under the range of operating conditions used in practice (indicated by the shaded areas), the fractional pore occupancy θ_t is commonly below 0.6. The separation characteristics for such mixtures are dictated by differences in one or more of the following characteristics (a) van der Waals interactions and polarizability, (b) electrostatic interactions, and (c) π-electron transfers.

Figures 1b, and 1c present the data on θ_t vs p_t for O_2/N_2, Kr/Xe, and C_2H_4/C_2H_6 separations with different materials; in these cases too we note that the fractional occupancy is lower than 0.6 for typical operating conditions.

Figure 1d shows the variation of θ_t for adsorption of equimolar water/ethanol, and methanol/ethanol/1-propanol/1-butanol mixtures in ZIF-8. We note that for pressures higher than 100 kPa, the pores are saturated. Typically, separations of dilute solutions of bioalcohols involve liquid phase mixtures at near ambient conditions;[11] this ensures pore saturation.

For separation of mixtures of hexane isomers, industrial processes often operate under conditions in which pore saturation prevails, i.e. $\theta_t \approx 1$; see calculations in Figure 1e for separations with $Fe_2(BDP)_3$ and MFI zeolite.[12]

Industrial separations of o-xylene/m-xylene/p-xylene/ethylbenzene mixtures with BaX zeolite are currently carried out in simulated moving bed (SMB) adsorbers in which the bulk phase is in the liquid state, typically with molar densities of 7 – 10 mol L^{-1}.[13, 14] From the adsorption equilibrium data in Figure 1f, we see that pore saturation conditions prevail in industrial separations.

In contrast to separations under conditions for which $\theta_t < 0.6$, the separations at conditions close to pore saturation (i.e. $\theta_t \approx 1$), are significantly influenced by differences in saturation capacities, that reflect differences in the efficiencies by which the molecules pack, or stack, themselves within the microporous channels. The elucidation, and elaboration, of such molecular packing, or entropy, effects that favor adsorption of smaller molecules is the primary objective of this article. By a careful, detailed, analysis of a wide variety of separations we shall highlight a variety of separation strategies that can be employed in practice in order to increase the efficacies of separations. Often, such strategies are not intuitively obvious. The separations that are examined in this article include: (a) mixtures of alcohols, (b) water/alcohol mixtures, (c) water/hydrocarbons, (d) butane isomers, (e) hexane isomers, (f) xylene isomers, (g) chlorofluorocarbons mixtures, and (h) ethylbenzene/styrene. We shall demonstrate that molecular packing effects often overshadow the influences of adsorption strengths and binding energies, of paramount importance in separations at low occupancies, θ_t.

The secondary objective of this Perspective is to demonstrate the possibility of tailoring the pore geometries in order to enhance the separation selectivity in favor of one of the components. Use of bespoke-tailored MOFs for selective adsorption of p-xylene from a mixture of xylene isomers may result in significant improvements to current technologies that use BaX zeolite.

3. Structural information on zeolites, MOFs, and ZIFs

The crystallographic data for all-silica zeolites are available on the zeolite atlas website of the International Zeolite Association (IZA).[15] Table 1 gives salient information on the variety of all-silica zeolite structures discussed in this Perspective article. The unit cell dimensions, and pore volumes are summarized in Table 2.

The Si/Al ratios of cation-exchanged zeolites are as follows.

NaX (106 Si, 86 Al, 86 Na^+, Si/Al=1.23),

NaY (144 Si, 48 Al, 48 Na^+, Si/Al=3),

LTA-5A (96 Si, 96 Al, 32 Na^+, 32 Ca^{++}, Si/Al=1)

LTA-4A (96 Si, 96 Al, 96 Na^+, Si/Al=1)

The structural details, including pore volume data, are given in Table 5 and Table 6.

The surface area of various structures were determined using the method described by Düren et al.[16]. The information is summarized in Table 7.

Table 3 gives information on the cage volumes.for cage-type structures. Table 4 provides data on the window dimensions. The window dimensions are determined using the van der Waals diameter of Si and O atoms of the framework to be 2.7 Å; this is in line with the data provided in the IZA atlas.[15]

The structural information for the metal organic frameworks (MOFs) and ZIFs (zeolitic imidazolate frameworks) have been taken from various publications.

For IRMOF-1 (= MOF 5 = $Zn_4O(BDC)_3$ with BDC^{2-} = 1-4 benzenedicarboxylate), we used the structural data published by Dubbeldam et al. [17, 18]

The structural information for CuBTC ($Cu_3(BTC)_2$ with BTC = 1,3,5-benzenetricarboxylate, also known as HKUST-1) have been taken from Chui et al. [19] and Yang and Zhong [20]. The crystal structure of Chui et al. [19] includes axial oxygen atoms weakly bonded to the Cu atoms, which correspond to water ligands. Our simulations have been performed on the dry CuBTC with these oxygen atoms removed.

The structural information for Zn(bdc)dabco is from Bárcia et al.[21] and Lee et al. [22]

MIL-47 structural data was taken from Alaerts et al. [23], Finsy et al. [24], and Barthelet et al. [25]

The structural data for MIL-53 (Cr) = $Cr(OH)(O_2C\text{-}C_6H_4\text{-}CO_2)$ was taken from Coombes et al [26] (the simulations were carried out with the large-pore (-lp) structure).

The structural information on MgMOF-74 (= $Mg_2(dobdc)$ = Mg\(dobdc) with dobdc = ($dobdc^{4-}$ = 1,4-dioxido-2,5-benzenedicarboxylate)), ZnMOF-74 (= $Zn_2(dobdc)$ = Zn\(dobdc)), CoMOF-74 = ($Co_2(dobdc)$ = Co\(dobdc)), NiMOF-74 = ($Ni_2(dobdc)$ = Ni\(dobdc)), were obtained from a variety of references.[8, 9, 27-32]

The structural information on FeMOF-74 (= $Fe_2(dobdc)$ = Fe\(dobdc) with dobdc = ($dobdc^{4-}$ = 1,4-dioxido-2,5-benzenedicarboxylate)) is from Bloch et al.[33]

The structural information on $Fe_2(BDP)_3$ is from Herm et al.[34]

The structural information for Co(BDP) with (BDP^{2-} = 1,4-benzenedipyrazolate) is from Choi et al.[35] and Salles et al.[36].

The information on Cu-TDPAT is from Wu et al.[2]

The salient information on MOF and ZIF structures are summarized in Table 8.

The ZIF-8 = Zn(methylimidazole)$_2$ structure was constructed on the basis of the structural data from Banerjee et al.[37]. The original structural data files (cif file) contain solvent molecules; these were removed and the solvent-free structures were considered.

Table 9 gives information on the unit cell dimensions, and pore volumes for MOFs and ZIFs.

The surface area of various structures were determined using the method described by Düren et al.[16]. See the ESI accompanying the review of Krishna[38] for further details. The information is summarized in Table 10.

It should also be noted here that for many MOFs detailed structural data are also not available.

4. CBMC simulation methodology

We present below a brief summary of the CBMC simulation methodology.

We first consider CBMC simulations for alkanes that are used to examine separations of alkane isomers. The linear and branched alkanes are described with a united-atom model, in which CH_3, CH_2, and CH groups are considered as single interaction centres. When these pseudo-atoms belong to different molecules or to the same molecule but separated by more than three bonds, the interaction is given by a Lennard-Jones potential. The Lennard-Jones parameters are chosen to reproduce the vapour-liquid curve of the phase diagram as shown in Siepmann et al.[39]. For simulations with linear and branched alkanes with two or more C atoms, the beads in the chain are connected by harmonic bonding potentials. A harmonic cosine bending potential models the bond bending between three neighboring beads, a Ryckaert-Bellemans potential controls the torsion angle. Details for the alkane model can be found in Dubbeldam et al.[40, 41]

Following Kiselev and co-workers[42], we consider the lattice structures to be rigid and we assume that interactions of an alkane with the zeolite are dominated by the dispersive forces between alkane pseudo atoms and the oxygen atoms of the zeolite. This is a very common approximation because the large oxygen atoms account for most of the potential energy and essentially shield the much smaller silicon atoms. The oxygen-adsorbate potential is an effective potential which implicitly includes the Si-contribution. These interactions are described by a Lennard Jones potential, which parameters are given by Dubbeldam et al. [40, 41] The Lennard-Jones potentials are shifted and cut at 12 Å.

The methodology and force fields for simulations with water and alcohols are from Krishna and van Baten.[43-46]

The methodology and details of the simulations for xylenes are from Torres-Knoop et al.[47]

In all cases, the size of the simulation box was large enough to yield reliable data on adsorption isotherms. Periodic boundary conditions were employed.

Adsorption isotherms are conveniently computed using Monte Carlo simulations in the grand-canonical ensemble. In this ensemble the temperature and chemical potentials are imposed. The average number of adsorbed molecules per unit cell of the zeolite follows from the simulations. The characteristics of these type of simulations is that during the calculations attempts are made to change the total number of particles by making attempts to insert molecule into or remove molecules from the zeolite. To make these types of moves possible for the long chain alkanes, we use the Configurational-Bias Monte Carlo (CBMC) technique.[48, 49]Instead of inserting a molecule at a random position, in a CBMC simulation, a molecule is grown atom by atom in such a way that the "empty spots" in the zeolite are found. This growing scheme gives a bias that is removed exactly by adjusting the acceptance rules.[48, 49]

These simulations were performed in cycles and in each cycle, an attempt to perform one of the following moves was made:

(1) displacement of a randomly selected chain. The maximum displacement was adjusted to an overall acceptance of 50%.

(2) rotation of a chain around its center of mass. The chain is chosen at random and the maximum rotation angle is selected to accept 50% of the moves.

(3) partly regrowing of a chain; a chain is selected at random and part of the molecule is regrown using the CBMC scheme. It is decided at random which part of the chain is regrown and with which segment the regrowing is started. For branched alkanes, the approach in Vlugt et al.[48]

(4) exchange with a reservoir; it is decided at random whether to add or to remove a molecule from the zeolite following the acceptance rules derived in Vlugt et al.[48]

(5) change of identity (only in the case of mixtures); one of the components is selected at random and an attempt is made to change its identity.[48] The acceptance rules for these trial moves can be found in Frenkel and Smit.[49]

Typically the number of MC cycles performed is 10^7. Of these, 15% are displacements, 15% rotations, 15% partial re-growths, 50% exchanges with the reservoir and the remaining 5% of the moves were attempts to change the identity of a molecule.

The MD simulation strategies used are described in the Supporting Information accompanying our previous works.[38, 50]

5. Simulation methodology for transient breakthrough in fixed bed adsorbers

Fixed bed, packed with crystals of microporous materials, are commonly used for separation of mixtures (see schematic in Figure **2**); such adsorbers are commonly operated in a transient mode, and the compositions of the gas phase, and component loadings within the crystals, vary with position and time. During the initial stages of the transience, the pores are loaded up gradually, and only towards the end of the adsorption cycle are conditions corresponding to pore saturation achieved. Put another way, separations in fixed bed adsorbers are influenced by both the Henry regime of adsorption as well as the conditions corresponding to pore saturation. Experimental data on the transient breakthrough of mixtures across fixed beds are commonly used to evaluate and compare the separation performance of zeolites and MOFs.[12, 34, 51-53] For a given separation task, transient breakthroughs provide more a realistic evaluation of the efficacy of a material, as they reflect the combined influence of adsorption selectivity, adsorption capacity, and intra-crystalline diffusion limitations.[12, 54]

We describe below the simulation methodology used to perform transient breakthrough calculations that are presented in this work. This simulation methodology is the same as that used in our previous published work.[12]

Assuming plug flow of an *n*-component gas mixture through a fixed bed maintained under isothermal conditions, the partial pressures in the gas phase at any position and instant of time are obtained by solving the following set of partial differential equations for each of the species *i* in the gas mixture.[55]

$$\frac{1}{RT}\frac{\partial p_i(t,z)}{\partial t} = -\frac{1}{RT}\frac{\partial\left(v(t,z)p_i(t,z)\right)}{\partial z} - \frac{(1-\varepsilon)}{\varepsilon}\rho\frac{\partial \overline{q}_i(t,z)}{\partial t}; \quad i = 1,2,...n \tag{2}$$

In equation (2), t is the time, z is the distance along the adsorber, ρ is the framework density, ε is the bed voidage, v is the interstitial gas velocity, and $\overline{q}_i(t,z)$ is the *spatially averaged* molar loading within the crystallites of radius r_c, monitored at position z, and at time t.

At any time t, during the transient approach to thermodynamic equilibrium, the spatially averaged molar loading within the crystallite r_c is obtained by integration of the radial loading profile

$$\overline{q}_i(t) = \frac{3}{r_c^3}\int_0^{r_c} q_i(r,t)r^2 dr \tag{3}$$

For transient unary uptake within a crystal at any position and time with the fixed bed, the radial distribution of molar loadings, q_i, within a spherical crystallite, of radius r_c, is obtained from a solution of a set of differential equations describing the uptake

$$\frac{\partial q_i(r,t)}{\partial t} = -\frac{1}{\rho}\frac{1}{r^2}\frac{\partial}{\partial r}\left(r^2 N_i\right) \tag{4}$$

The molar flux N_i of component i is described by the simplified version of the Maxwell-Stefan equations in which both correlation effects and thermodynamic coupling effects are considered to be of negligible importance[12]

$$N_i = -\rho Đ_i \frac{\partial q_i}{\partial r} \tag{5}$$

Summing equation (**3**) over all n species in the mixture allows calculation of the *total average* molar loading of the mixture within the crystallite

$$\overline{q}_t(t,z) = \sum_{i=1}^{n} \overline{q}_i(t,z) \tag{6}$$

The *interstitial* gas velocity is related to the *superficial* gas velocity by

$$v = \frac{u}{\varepsilon} \tag{7}$$

In industrial practice, the most common operation is with to use a step-wise input of mixtures to be separation into an adsorber bed that is initially free of adsorbates, i.e. we have the initial condition

$$t = 0; \quad q_i(0,z) = 0 \tag{8}$$

At time, $t = 0$, the inlet to the adsorber, $z = 0$, is subjected to a step input of the n-component gas mixture and this step input is maintained till the end of the adsorption cycle when steady-state conditions are reached.

$$t \geq 0; \quad p_i(0,t) = p_{i0}; \quad u(0,t) = u \tag{9}$$

where u is the superficial gas velocity at the inlet to the adsorber.

Besides, the breakthrough simulations with a step-input (9), we also carried out simulations for a packed bed adsorber with injection of a short duration pulse of the mixture to be separated. This type of simulation is particularly useful to demonstrate the fractionating capability of adsorbents. For simulation of pulse chromatographic separations, we use the corresponding set of inlet conditions

$$0 \leq t \leq t_0; \quad p_i(0,t) = p_{i0}; \quad u(0,t) = u \tag{10}$$

where the time for duration of the pulse is t_0. The pulse duration is generally very short, and therefore pore saturation conditions are never approached at any position at any time t. Therefore, pulse chromatographic simulations, and the corresponding experiments, do not reflect molecular packing effects. We shall elaborate on later.

If the value of $\frac{Ð_i}{r_c^2}$ is large enough to ensure that intra-crystalline gradients are absent and the entire crystallite particle can be considered to be in thermodynamic equilibrium with the surrounding bulk gas phase at that time t, and position z of the adsorber

$$\overline{q}_i(t,z) = q_i(t,z) \tag{11}$$

The molar loadings at the *outer surface* of the crystallites, i.e. at $r = r_c$, are calculated on the basis of adsorption equilibrium with the bulk gas phase partial pressures p_i at that position z and time t. The adsorption equilibrium can be calculated on the basis of the Ideal Adsorbed Solution Theory (IAST) of Myers and Prausnitz.[56] In all the simulation results we present in this article, the IAST calculations use pure component isotherms fitted with the dual-Langmuir-Freundlich model

$$q_i = q_{i,A,sat}\frac{b_{i,A}p_i^{\nu_{i,A}}}{1+b_{i,A}p_i^{\nu_{i,A}}} + q_{i,B,sat}\frac{b_{i,B}p_i^{\nu_{i,B}}}{1+b_{i,B}p_i^{\nu_{i,B}}} \tag{12}$$

with the fits parameters as specified in the accompanying Tables of this document.for every separation that has been examined.

For presenting the breakthrough simulation results, we use the dimensionless time, $\tau = \frac{tu}{L\varepsilon}$, obtained by dividing the actual time, t, by the characteristic time, $\frac{L\varepsilon}{u}$, where L is the length of adsorber, u is the superficial fluid velocity, ε is the bed voidage.[54] For all the simulations reported in this article we choose L = 0.3 m; u = 0.04 m s^{-1}; ε = 0.4. For pulse chromatographic simulations, we choose the duration of the pulse is t_0 = 10 s.

6. Separation of mixtures of 1-alcohols using CHA and SAPO-34

Let us examine the data on the pure component isotherms for a series of 1-alcohols in CHA, which is a cage type zeolite that consists of 316 Å^3 sized cages separated by 3.8 Å × 4.2 Å sized windows. CBMC simulations of pure component 1-alcohols with C atoms in the 1 – 6 range in CHA at 300 K, as reported in the work of Krishna and van Baten,[57] are shown in Figure **3**a. The continuous solid lines in Figure **3**a are fits using the dual-Langmuir-Freundlich model with parameters as specified in Table 11. The saturation capacities, $\Theta_{i,sat}$, decreases from 5.4 molecules per cage for methanol to 1 molecule per cage for 1-hexanol; see data in Figure **3**b. Figure **3**c presents snapshots of the location, and conformations, of the 1-alcohols within the cages of CHA at saturation conditions. Except for methanol, the saturation cage capacity has an integer value because 1-alcohol molecules cannot locate at the window regions.

The CBMC simulations for ethanol - 1-propanol mixtures are shown in Figure 4a. For total fluid phase fugacities, $f_t < 300$ kPa, the adsorption selectivity is strongly in favor of the longer 1-propanol molecule. However, when the total fluid phase fugacity f_t exceeds 600 kPa, we find a reversal of selectivity. This selectivity reversal is entropy-based and is ascribable to the significantly higher saturation capacity of ethanol (4 molecules per cage) in comparison to that of 1-propanol (2 molecules per cage). The shaded region in Figure 4a indicates that the bulk fluid phase is in the liquid phase for the range of fugacities, f_i. This region has been estimated using the Peng-Robinson equation of state. The CBMC data for mixture adsorption indicates that selectivity reversal is ensured when adsorption is from the *liquid* phase mixture and under these conditions the adsorption favors the alcohol with the *shorter* chain length.

The CBMC simulations for ethanol - 1-hexanol mixtures are shown in Figure 4b. For total fluid phase fugacities, $f_t < 100$ kPa, the adsorption selectivity is strongly in favor of the longer 1-hexanol molecule. However, when the total fluid phase fugacities, f_t exceed 200 kPa, we find a reversal of selectivity. This selectivity is entropy-based and is ascribable to the significantly higher saturation capacity of ethanol (4 molecules per cage) in comparison to that of 1-hexanol (1 molecule per cage). The shaded region in Figure 4b indicates that the bulk fluid phase is in the liquid phase for the range of fugacities, f_i.

The continuous solid lines in Figures 4a,b are the predictions of the Ideal Adsorbed Solution Theory (IAST) of Myers and Prausnitz [56] using pure component isotherm fits. The IAST calculations have been presented here to demonstrate that selectivity reversal is not an unexpected phenomenon, but is a natural result that is obtained for a mixture of two species having (1) lower adsorption strength, but higher saturation capacity, and (2) higher adsorption strength, but lower saturation capacity. When saturation conditions are approached the component with the higher saturation capacity is invariably preferred. This is due to the fact that vacant "sites" are more easily filled by the smaller molecule at near-saturation conditions. Though the predictions of the IAST are in general qualitative agreement with CBMC simulations, the agreement is not quantitatively perfect in Figure 4b.

Remy et al.[58] report experimental data on transient breakthroughs of (a) ethanol/1-propanol and (b) ethanol-1-hexanol mixtures in a fixed bed adsorber packed with SAPO-34, that has the same structural topology as CHA; see Figure 5. The experiments carried out in the liquid phase are quite remarkable because the component that is eluted first from the adsorber is the alcohol with the longer chain length. The rationalization of these experimental data can be traced to the entropy effects that favor the shorter alcohols under conditions such that the bulk fluid phase is in the liquid state; cf. Figure 4. When operating under conditions such that the bulk fluid phase is a liquid mixture, both adsorption and diffusion favor the uptake of the shorter alcohol, and the longer alcohol is rejected in a fixed bed adsorber. Both adsorption and intra-crystalline diffusion act synergistically in such separations; further explanations are provided in earlier works.[12, 59]

7. Separation of mixtures of 1-alcohols and water using ZIF-8

ZIF-8 has the sodalite (SOD) topology and consists of 1168 Å^3 sized cages separated by 3.3 Å sized windows. In view of the larger cage capacity of ZIF-8 compared to CHA, we should expect the saturation loadings to be significantly higher in ZIF-8. Figure 6a shows the experimental data of Zhang et al.[60] of pure component adsorption isotherms for 1-alcohols in ZIF-8 at 308 K. The saturation capacities are: methanol ≈ 16 molecules/cage; ethanol ≈ 9 molecules/cage; 1-propanol ≈ 7 molecules/cage; 1-butanol ≈ 6 molecules/cage. Due to the larger cage volume of ZIF-8, the saturation capacities are significantly higher than for CHA. Figure 6b compares the saturation capacities of CHA zeolite and ZIF-8 for various 1-alcohols. Furthermore we note that the differences in the cage capacities of 1-alcohols in ZIF-8 are larger than the corresponding ones in CHA. This would imply that the separations at pore saturation conditions are more effective with ZIF-8 as compared to CHA.

IAST calculations of the component loading in ZIF-8 in equilibrium with bulk fluid phase containing an equimolar methanol/1-ethanol/1-propanol/1-butanol mixture are shown in Figure 7. At total pressures below 10 kPa, the hierarchy of component loadings is "normal", i.e. decreases with decreasing chain length: 1-butanol > 1- propanol > ethanol > methanol. At pressures above 300 kPa, the hierarchy of component loadings is reversed, and increases with decreasing chain length: 1-butanol < 1- propanol < ethanol < methanol. The shaded region in Figure 7 indicates that the bulk fluid phase is in the liquid phase. The IAST calculations show that for separations of liquid mixtures, the adsorption selectivity is in favor of the component with the shorter chain length, precisely analogous to the results for CHA zeolite presented in Figure 4.

Transient breakthroughs for an equimolar methanol/1-ethanol/1-propanol/1-butanol mixture at 308 K at a total pressure of 10 kPa are shown in Figure 8a. We note that the hierarchy of breakthroughs is methanol, ethanol, 1- propanol, 1-butanol, i.e. the 1-alcohol with the longer chain length elutes at a later time. A completely different picture emerges for an equimolar methanol/1-ethanol/1-propanol mixture at 308 K at a total pressure of 300 kPa; see Figure 8b. In this case, the hierarchy of breakthroughs is 1-propanol, ethanol, methanol, i.e. alcohols with a longer chain length are eluted earlier; these results are precisely analogous to the experimental data of Remy et al.[58] for 1-alcohols separation with SAPO-34, presented in Figure 5. It is particularly noteworthy, that for the simulations at a total pressure of 300 kPa, adsorption and diffusion serve to complement each other. The shorter alcohol has the higher value of intra-crystalline diffusivity, and also the higher adsorption strength; as a consequence, the separation is synergistic.[12, 59]

Due to hydrophobicity of ZIF-8, the adsorption loading of water is significantly lower than that of 1-alcohols; see Figure 6a. Consequently, ZIF-8 has significant potential for use in recovery of alcohols from biofuel products that, typically, are *dilute* alcohol-in-water solutions. In such recovery processes, it is essentially to use materials that selectively adsorb the alcohols and *reject* water. Figure 9 shows transient breakthrough simulations for 1-alcohols/water mixture using ZIF-8. The inlet consists of 90% water, containing 2.5% each of methanol, 1-ethanol, 1-propanol, and 1-butanol at a total pressure of 10^5 Pa. As desired, water is the first component to be rejected. Subsequently, the sequence of breakthroughs is methanol, ethanol, 1-propanol, and 1-butanol that corresponds to the adsorption strengths in the Henry regime; this sequence is similar to that obtained earlier in Figure 8a, corresponding to low pressure operation. The experimental breakthroughs of alcohols and water reported by Saint-Remi et al.[11] are in qualitative agreement to that obtained in Figure 8a. It must be emphasized that the separation of dilute alcohol/water mixtures is based on adsorption selectivities in the Henry regime and not by molecular packing effects. Molecular packing effects are in play near pore saturation conditions.

The separation performance of ZIF-8 for water/alcohols separations is expected to be significantly superior to that of CHA or SAPO-34 because for its significantly larger cage volume. Consequently, the saturation loadings are higher in magnitude; this leads to longer breakthrough times in fixed bed adsorption devices.[12]

Sun et al.[61] claim that their MOF Dysprosium oxalate is suitable for recovery of bio-alcohols; these authors have reported experimental data on pure component isotherms for water, methanol, and ethanol. The isotherms indicate that this MOF is selective for adsorption of water from aqueous alcohol mixtures. Their experimental pulse chromatographic experiments show that water elutes last. Such characteristics are undesirable for recovery of bio-alcohols from dilute solutions.

8. Separation of mixtures of 1-alcohols using ZIF-68

Van der Perre et al.[62] have investigated separations with ZIF-68 whose structure consists of ZnN_4 tetrahedra that are connected by both polar 2-nitroimidazole (nIM) ligands and nonpolar benzimidazole (bIM) ligands. It has the same topology as GME zeolite, with 1D channels of two different sizes; see Figure 10 for pore landscape. Figure 10 shows the experimental data of Van der Perre et al.[62] for pure component adsorption isotherms of 1-alcohols in ZIF-68 at 323 K. With increasing chain length, the saturation capacities are significantly lowered.

Figure 11a shows IAST calculations of the component loadings for equimolar 6-component methanol/ethanol/1-propanol/1-butanol/1-pentanol/1-hexanol mixture. At pressures below about 1 MPa, the adsorption loadings increases with increasing chain length. However, for pressures above about 2 MPa the component loading decreases with increasing chain length; this is because of entropy effects that favor shorter 1-alcohols. At 323 K, the bulk fluid phase is in the liquid state for $p_t > 1$ MPa; this implies that for adsorption of liquid phase mixtures, entropy effects will favor the shorter alcohol.

As an example, let us consider transient uptake in ZIF-68 crystal of a binary equimolar ethanol/1-butanol mixture at 323 K. The IAST calculations in Figure 11b show that for $p_t = 400$ kPa, the adsorption is in favor of 1-butanol, whereas for $p_t = 4$ MPa, the adsorption is in favor of ethanol. Figures 12a, and 12b show simulations of transient uptake within ZIF-68 crystal exposed to a bulk gas phase pressure of (a) 400 kPa, and (b) 4 MPa. The values of the intra-crystalline diffusivities used in the simulations are based on the experimental data of Van der Perre et al;[62] the diffusivity of ethanol is 25 times higher than that of 1-butanol. For bulk fluid pressure $p_t = 400$ kPa, the uptake of 1-butanol at equilibrium is about twice that of ethanol, in line with the IAST calculations in Figure 11b. However, for fluid pressure $p_t = 4$ MPa, the uptake of 1-butanol at equilibrium is 60% that of ethanol; Figure 12b. Van der Perre et al.[62] have experimentally measured the uptake of ethanol/1-butanol liquid phase mixtures in ZIF-68 and found results that are in qualitative agreement with those presented in Figure 12b. A further important aspect of the data in Figure 12b is that both adsorption and diffusion favor the shorter 1-alcohol, i.e. there is synergy between these two phenomena.

The experimental uptake data of Van der Perre et al.[62] offer convincing evidence of the entropy effects that influence separations of mixtures of 1-alcohols in ZIF-68.

A further important aspect is that both adsorption and diffusion favor the shorter 1-alcohol, i.e. there is synergy between adsorption and diffusion. This synergy arise because of the combination of two reasons: (1) the adsorption of shorter alcohol is preferred because of molecular packing effects, and (2) the diffusivity of the shorter alcohol is higher based on the diffusivities reported by Van der Perre et al.[62] It must however be remarked that the diffusivity data of Van der Perre et al.[62] were measured at low occupancies, and these data would be relevant at pore saturation provided slowing-down effects are not significant.[12] Generally speaking, slowing-down effects will mitigate against the synergistic aspects.

9. Separation of water/benzene mixtures using CuBTC

The structure of CuBTC (=$Cu_3(BTC)_2$, also known as HKUST-1) consists of two types of "cages" and two types of "windows" separating these cages. Large cages are inter-connected by 9 Å windows of square cross-section. The large cages are also connected to tetrahedral-shaped pockets of ca. 6 Å size through triangular-shaped windows of ca. 4.6 Å size. The tetrahedral pockets can accommodate small molecules such as water but larger molecules can be excluded in these pockets; they must locate only in larger cages.[63]

Figure 13 shows the experimental data of Zhao et al.[64] for pure isotherms of water and benzene measured at temperatures of 288 K, 298 K, 308 K, and 318 K. These isotherm data are for adsorption from vapor phase mixtures.

Let us consider the separation of equimolar water(1)/benzene(2) vapor phase mixtures using CuBTC. Figure 14a presents IAST calculations of the adsorption selectivities as a function of the total bulk pressure, p_t. For operations at $T > 308$ K and pressures $p_t < 10$ kPa, the selectivity is in favor of benzene that has the higher adsorption strength, resulting from π electron exchanges between the benzene rings of the guest molecules and the unsaturated Cu atoms of CuBTC. High temperatures and low pressures imply low pore occupancies. The situation is dramatically different when we operate at pressures $p_t > 10$ kPa, the selectivity is in favor of water, that has the higher saturation capacity.

In Figure 14b the adsorption selectivity is plotted as a function of the total mixture loading, $q_t = q_1 + q_2$. We note from the data in Figure 14b that at mixture loadings $q_t > 18$ mol kg^{-1}, the influence of temperature is practically negligible. Furthermore, the data shows that for $q_t > 18$ mol kg^{-1}, the selectivity is in favor of water by about two orders of magnitude. The selectivities are in favor water because of entropy effects, that are influenced by saturation capacities.

Figures 15a, and 15b shows transient breakthrough simulations for (a) 13/87 water/benzene, and (b) 34/66 water/benzene mixtures in a fixed bed adsorber packed with CuBTC at 308 K. These simulations show that water can be selectively adsorbed from these two mixtures. Experimental verification of such water-selective adsorption is to be found in Figure 10 of the paper of Zhao et al.[64]

Figure 15c shows pulse chromatographic simulations for pulse input of 34/66 water/benzene mixture at 8.15 kPa. The sequence of pulses demonstrates that benzene is the more strongly adsorbed component. The reason for this is that pulse chromatographic experiments and simulations reflect the adsorption hierarchy as dictated by the Henry regime; they do not reflect molecular packing effects.

Though no experimental data are reported as yet, we should expect CuBTC to be also effective for separation of water/alcohol mixtures. An important advantage of CuBTC in such separations is its larger pore volume (0.86 cm^3/g), that is higher than that of ZIF-8 (0.5 cm^3/g), ZIF-68 (0.439 cm^3/g), and ZIF-71 (0.736 cm^3/g). Larger pore volume results in higher saturation capacities, and better separations in fixed bed adsorbers because the breakthrough times will be longer.

10. Separation of water/methanol, and water/ethanol mixtures using FAU, DDR, MFI, and FER zeolites

We now consider the separation of water/methanol, and water/ethanol mixtures by adsorption in all-silica FAU zeolite that consists of 786 Å^3 cages, that are separated by 7.3 Å size windows. Figure 16 shows CBMC simulations of Krishna and van Baten[43] for pure component adsorption isotherms for water, methanol, and ethanol in all-silica FAU zeolite at 300 K. Above fluid phase fugacities of 10^4 Pa, pore saturation is reached and the hierarchy of saturation capacities water >> methanol > ethanol is a reflection of the size of the molecules.

Figures 17a, and 17b present CBMC simulations for adsorption of equimolar ($f_1=f_2$) (a) water/methanol, and (b) water/ethanol in FAU zeolite at 300 K. In the Henry regime of adsorption, the water loading is significantly below that of the alcohol. However, we note that at total bulk fluid phase fugacities, $f_t = f_1+f_2 > 2\times10^4$ Pa, the adsorption is in favor of water, a consequence of entropy effects. IAST calculations are able to provide a reasonably good description of mixture adsorption equilibrium for both water/methanol and water/ethanol mixtures.

IAST calculations are able to quantitatively reproduce the reversal of selectivity, in favor of water, that occurs at $f_t = f_1 + f_2 > 2\times10^4$ Pa; see Figures 17c, and 17d.

For $f_t > 10^6$ Pa, we determine that the bulk fluid phase for water/methanol and water/ethanol will be in the liquid state. This implies that for separation of water/methanol and water/ethanol mixtures from the liquid state, the selectivity will be in favor of water.

Figure 18 present the results of MD simulations of Krishna and van Baten[43] for self-diffusivities of (a) water, and methanol in water/methanol mixtures, (b) water and ethanol in water/ethanol mixtures in FAU zeolite at 300 K. We note that the water diffusivity is higher, by a factor of two, than the partner alcohol molecules.

The data in Figures 17, and 18 imply that for separation of water/methanol and water/ethanol mixtures from liquid phase mixtures, both adsorption and diffusion will favor selective uptake of water. This synergistic effect will enhance the separation potential.[12, 59]

Consider the separation of water/methanol, and water/ethanol mixtures by adsorption in all-silica DDR zeolite that consists of 278 $Å^3$ cages, that are separated by 3.65 Å × 4.37 Å size windows. Figure 19 shows CBMC simulations of Krishna and van Baten[43] for pure component adsorption isotherms for water, methanol, and ethanol in DDR at 300 K. Above fluid phase fugacities of 10^5 Pa, pore saturation is reached and the hierarchy of saturation capacities water >> methanol > ethanol is a reflection of the size of the molecules.

Figures 20a, and 20b present CBMC simulations for adsorption of equimolar (f_1=f_2) (a) water/methanol, and (b) water/ethanol mixtures in DDR zeolite. In the Henry regime of adsorption, the water loading is significantly below that of the alcohol. However, we note that at total bulk fluid phase fugacities, $f_t = f_1 + f_2 > 10^5$ Pa, the adsorption is in favor of water. This is due to entropy effects. IAST calculations are able to provide a qualitatively reasonable description of mixture adsorption equilibrium for both water/methanol and water/ethanol mixtures.

IAST calculations are able to qualitatively reflect the reversal of selectivity, in favor of water, that occurs at $f_t = f_1 + f_2 > 10^5$ Pa; see Figures 20c, and20d.

For $f_t > 10^6$ Pa, we determine using the Peng-Robinson equation of state that the bulk fluid phase for water/methanol and water/ethanol will be in the liquid state. This implies that for separation of water/methanol and water/ethanol mixtures from the liquid state, the selectivitity will be in favor of water.

Figure 21 presents the results of MD simulations of Krishna and van Baten[43] for self-diffusivities of water, and methanol in water/methanol mixtures in DDR. We note that the water diffusivity is higher, by about one order of magnitude, than the partner methanol molecules.

The data in Figures 20, and 21 imply that for separation of water/methanol and water/ethanol mixtures from liquid phase mixtures, both adsorption and diffusion will favor water. This synergistic effect will enhance the separation potential of DDR.

Consider the separation of water/methanol, and water/ethanol mixtures by adsorption in all-silica MFI zeolite that consists of intersecting channels of 5.5 Å. Figure 22 shows CBMC simulations of Krishna and van Baten[43] for pure component adsorption isotherms for water, methanol, and ethanol in MFI at 300 K. Above fluid phase fugacities of 10^5 Pa, pore saturation is reached and the hierarchy of saturation capacities water >> methanol > ethanol is a reflection of the size of the molecules.

Figures 23a, and 23b present CBMC simulations for adsorption of equimolar (f_1=f_2) (a) water/methanol, and (b) water/ethanol mixtures in MFI zeolite. In the Henry regime of adsorption, the water loading is significantly below that of the alcohol. However, we note that at total bulk fluid phase fugacities, $f_t = f_1+f_2 > 10^5$ Pa, the adsorption is in favor of water. This is due to entropy effects. IAST calculations are able to provide a qualitatively reasonable description of mixture adsorption equilibrium for both water/methanol and water/ethanol mixtures.

IAST calculations are able to qualitatively reflect the reversal of selectivity, in favor of water, that occurs at $f_t = f_1+f_2 > 10^5$ Pa; see Figures 23a, and 23b.

For $f_t > 10^6$ Pa, we determine using the Peng-Robinson equation of state that the bulk fluid phase for water/methanol and water/ethanol will be in the liquid state. This implies that for separation of water/methanol and water/ethanol mixtures from the liquid state, the selectivitity will be in favor of water.

Figure 24 present the results of MD simulations of Krishna and van Baten[43] for self-diffusivities of water, and methanol in water/methanol mixtures in DDR. We note that the water diffusivity is higher, by about a factor two, than the partner methanol molecules.

The data in Figures 20, and 21 imply that for separation of water/methanol and water/ethanol mixtures from liquid phase mixtures, both adsorption and diffusion will favor water. This synergistic effect will enhance the separation potential of MFI.

Consider the separation of water/methanol, and water/ethanol mixtures by adsorption in all-silica FER zeolite. Figure 25 shows CBMC simulations for pure component adsorption isotherms for water, methanol, and ethanol in FER at 300 K. Above fluid phase fugacities of 10^5 Pa, pore saturation is reached and the hierarchy of saturation capacities water >> methanol > ethanol is a reflection of the size of the molecules.

Figures 26a, and 26b present IAST calculations for adsorption of equimolar (f_1=f_2) (a) water/methanol, and (b) water/ethanol in FER zeolite. In the Henry regime of adsorption, the water loading is significantly below that of the alcohol. However, we note that at total bulk fluid phase fugacities, $f_t = f_1+f_2 > 100$ kPa, the adsorption is in favor of water.

IAST calculations demonstrate the reversal of selectivity, in favor of water, that occurs at $f_t = f_1+f_2 >$ 100 kPa; see Figure 26c.

For $f_t > 10^6$ Pa, we determine using the Peng-Robinson equation of state that the bulk fluid phase for water/methanol and water/ethanol will be in the liquid state. This implies that for separation of water/methanol and water/ethanol mixtures from the liquid state, the selectivitity will be in favor of water.

Figure 27 present the results of MD simulations for self-diffusivities of water, and ethanol in as function of the composition of water/ethanol mixtures in FER. Except in the regions of high ethanol concentrations, the diffusivity of water is significantly higher than that of ethanol. Further insights into the diffusivities in FER are provided by Kärger et al.[65]

The data in Figures 26, and 27 imply that for separation of water/methanol and water/ethanol mixtures from liquid phase mixtures, both adsorption and diffusion will favor water. This synergistic effect will enhance the separation potential of FER.

11. Separation of mixtures containing water, methanol, and ethanol using ZIF-71

ZIF-71 possess a three-dimensional pore network formed by large cages interconnected via small windows;[66] see pore landscapes in Figure 28. The CBMC simulations of Nalaparaju et al.[66] for water/methanol and water/ethanol mixtures in ZIF-71 provide convincing evidence of the entropy effects that manifest at pore saturation conditions. CBMC simulations of the pure component isotherms of water, methanol and ethanol in ZIF-71 at 298 K are shown in Figure 28a. The significantly higher saturation capacity of water compared to that of methanol and ethanol is evident. Figures 28b, and 28c shows CBMC simulations of the component loadings for equimolar (b) water/methanol, (c) water/ethanol mixtures in ZIF-71. For total pressures below 20 kPa, the adsorption is in favor of the alcohol. However, as the total pressure increase above 20 kPa, entropy effects cause the water loadings to exceed that the partner alcohol molecules. At 100 kPa, the water/methanol and water/ethanol adsorption selectivities approach values of about 5; see Figure 28d. These results imply that for adsorption from liquid phase mixtures, water can be selectively adsorbed from water/alcohol mixtures.

12. Separations of water/alcohol mixtures using LTA zeolite

Let us consider the LTA zeolite for which the all-silica form (i.e. without cations, also called ZK-4) consists of 743 Å^3 cages that are separated by windows of approximately 4.1 Å × 4.7 Å. Figure 29 presents snapshots showing the location of cations in the industrially important LTA-4A (96 Si, 96 Al, 96 Na$^+$, Si/Al=1), and LTA-5A (96 Si, 96 Al, 32 Na$^+$, 32 Ca^{++}, Si/Al=1) zeolites. In LTA-4A, some of the Na$^+$ cations partially block the window regions,[67-71] thereby effectively reducing the aperture size that is available for inter-cage hopping of molecules. The Na^+ and Ca^{++} cations in LTA-5A, on the other hand, do not locate near the window regions and there is no blocking. This implies that diffusional influences are much stronger in LTA-4A than in LTA-5A zeolite. The presence of bulkier K^+ cations in LTA-3A (96 Si, 96 Al, 96 K^+, Si/Al=1) causes the window blocking effect to be significantly enhanced, when compared to LTA-4A. For this reason, LTA-3A zeolite is used for selective removal of water from gaseous streams (dehumidification) and water/alcohol mixtures (dehydration) mixtures.[72] It has to be mentioned that it is common to find information in the published literature that suggest that 3A, 4A, and 5A zeolites have window apertures, respectively, of 3 Å, 4 Å, and 5; this is not precisely correct. The degree of blocking (by the cations Na^+ or K^+) of the window apertures of the pristine framework with 4.1 Å × 4.7 Å decreases in the order as we progress from 3A, and 4A, to 5A.

Let us examine the experimental data on the pure component isotherms for water and ethanol in LTA-4A published by Pera-Titus et al; [73] see Figure 30. We note that the saturation capacity of water is considerable higher than that of ethanol. The experimental data for adsorbed phase component loadings from vapor phase water/ethanol mixtures at 2.1 kPa are shown in Figure 31a. The component loadings are reasonably well predicted by IAST calculations (indicated by the continuous solid line). The validation of IAST calculations is important for the analysis of other mixture separations that are analyzed in this article. The water/ethanol adsorption selectivities range from 10 – 300, increasing with increasing water mole fraction in the bulk vapor phase; see Figure 31b. From the data of Pera-Titus et al., [73] the ratio of the diffusivities of water in LTA-4A to that of ethanol is in the range 10- 100. Therefore, we should expect permeation selectivities to be about two to three orders of magnitude large; this is confirmed by the experimental data.

An important application of LTA-4A is separation of water/ethanol mixtures by pervaporation. Conventional distillation of ethanol/water mixtures can produce ethanol with a purity close to 95 wt% owing to azeotrope formation. For obtaining say 99.5% pure ethanol, we need to feed the obtained 95 wt% ethanol product to an azeotropic distillation column with an entrainer such as benzene, or cyclohexane. A better alternative, avoiding the use of entrainers, is to adopt a hybrid scheme (see Figure

32) in which the 95 wt% ethanol top product is fed to a hydrophilic LTA-4A zeolite membrane pervaporation unit. The desired 99.5% pure ethanol product is recovered as retentate. Water has a significantly higher diffusivity than ethanol due to the narrow window aperture; both adsorption and diffusion in LTA-4A favors permeation of water across the membrane.

Diffusion –selective separation of water/methanol mixtures is the underlying mechanism with Ln-MOF with pyrazine-2,5-dicarboxylate ligands as linkers.[74]

Uchida and Mizuno[75] report uptake data for water, methanol, and ethanol in zeotype polyoxometalate-macro-cation ionic crystal, whose channels are not large enough to allow methanol and ethanol to enter.

13. Separation of methanol/ethanol mixtures using UCY-5, and Ce(BTB)

Efthymiou et al.[76] report experimental data on the uptake of methanol/ethanol mixtures in the liquid phase using a flexible Lanthanide MOF, UCY-5, with Ce^{3+} as the metal ions. Transient uptake experiments of the component uptakes from binary 1:1 and 1:2 methanol/ethanol *liquid* phase mixtures are plotted in Figures 33a, and 33b. At long times, i.e. as equilibrium is approached, we note that the component loadings of methanol are significantly higher than that of ethanol, even in the case of 1:2 bulk liquid phase mixtures. This provides conclusive proof that the adsorption is strongly in favor of methanol that has the shorter chain length. We believe that their experiments are a clear confirmation of the molecular packing effects that favor methanol over ethanol. Furthermore, we note that the uptake of ethanol is significantly slower than that of methanol, by about an order of magnitude. This implies that both adsorption and diffusion are synergistically in favor of methanol. This synergistic effect is, in principle, analogous to that observed for mixtures of 1-alcohols in SAPO-34.

Unfortunately, the pure component isotherms for methanol and ethanol in UCY-5 were not reported by Efthymiou et al. [76] Therefore, it is not possible to model their transient uptake of methanol/ethanol mixtures. To demonstrate molecular packing effects in the separation of methanol/ethanol mixtures, we analyze the published isotherm data for methanol and ethanol in Ce(BTB).

Lin et al.[77] present experimental isotherm data for methanol, ethanol, 1-propanol, 2-propanol, and 1-butanol in a homochiral ultramicroporous lanthanide–organic framework, Ce(BTB) (H_3BTB =1,3,5-benzenetrisbenzoic acid). Their data show the following hierarchy of saturation capacities methanol >> ethanol > 1-propanol > 1-butanol >> 2-propanol. This hierarchy of saturation capacities implies that it is possible to separate mixtures of 1-alcohols based on the chain length.

Let us analyse the separation of methanol/ethanol mixtures. On the basis of the fits of the pure component isotherms (cf. Figure 34a), we performed IAST calculations for equimolar bulk fluid mixture adsorption in Ce(BTB); see Figure 34b. For total pressures larger than 20 kPa, the selectivity is favor of methanol. Figure 34c presents simulation results for transient uptake of methanol/ethanol within crystals of Ce(BTB) exposed to 1:1 fluid mixture at a total pressure of 100 kPa. The transient simulations are performed assuming that the intra-crystalline diffusivity of methanol is an order of magnitude higher than that of ethanol; the simulation methodology is provided in our earlier work.[12] The uptake characteristics have qualitative similarities to that reported for UCY-5 by Efthymiou et al.[76] (cf. Figures 33). Both adsorption and diffusion act synergistically in the selective adsorption of methanol from methanol/ethanol mixtures.

14. Separation of mixtures containing water, methanol, and ethanol using CID-1

Horike et al.[78] report experimental data for pure component isotherms of water, methanol and ethanol in a porous interdigitated coordination polymer CID-1; see Figure 35a. The saturation capacities of water, methanol, and ethanol are in the ratios 6:2:1. Figures 35b, 35c, and 35d present IAST calculations for the component loadings for equimolar (b) water/methanol, (c) water/ethanol, and (d) methanol/ethanol mixtures. For adsorption of water/methanol, and water/ethanol mixtures at ambient pressure, the adsorption selectivity is overwhelming in favor of water; alcohol molecules are practically excluded from CID-1 due to entropy effects that favor water because of its higher saturation capacity. Near pore saturation conditions, the selective adsorption of water from water/methanol and water/ethanol mixtures has been observed earlier for FAU (Figure 17), DDR (Figure 20), FER (Figure 26), and ZIF-71 (Figure 28).

Entropy effects are less strong for separation of methanol/ethanol mixtures because of smaller differences in the saturation capacities. In this case, exclusion of ethanol from the pores occurs at 1000 kPa pressure, corresponding to bulk *liquid* phase. This implies that separation of mixtures of alcohols from bulk liquid phase mixtures will be strongly selective to the shorter chain alcohol; this result is analogous to that obtained earlier for SAPO-34 (cf. Figure 5), and ZIF-8 (cf. Figure 8). For operations at a total pressures larger than 10 kPa, an important consequence of molecular packing effects is that the adsorption selectivity is strongly in favor of the smaller molecule; see Figure 35b. The IAST calculations in Figure 35 imply also that clean separations of water/methanol, water/ethanol, and methanol/ethanol mixtures are to be expected using CID-1 at p_t = 100 kPa. To confirm this expectation, Figure 36 presents transient breakthrough simulations for (a) 20/80 water/methanol, and (b) 11/89 water/ethanol, and (c) 50/50 methanol/ethanol mixtures in a fixed bed adsorber packed with CID-1 at 298 K. In all three cases, the component with the higher saturation capacity elutes at a later time; this is a direct consequence of molecular packing effects. Of particular interest is the separation of the 11/89 water/ethanol mixtures, that corresponds to the azeotropic composition. We note that ethanol is scarcely adsorbed and is rejected almost immediately after feed mixture injection.

15. Separation of water/methanol mixtures with Cu-GLA

Chen et al.[79] report experimental data on pure component isotherms for water and methanol in Cu-GLA (= Cu(GLA)(4,4′-Bipy)$_{0.5}$; GLA = glutarate, 4,4′-Bipy = 4,4′-bipyridine) at 298 K; see Figure 37a. IAST calculations of the component loadings for water/methanol mixtures show that adsorption from liquid phase mixtures, the adsorption is overwhelmingly in favor of water. Methanol can be excluded from the pores. It must be stressed that this exclusions is not as a consequence of diffusion but because of entropy effects that favor water molecules with the higher packing efficiency. The separation principle has been observed earlier for FAU (Figure 17), DDR (Figure 20), FER (Figure 26), ZIF-71 (Figure 28), CID-1 (Figure 35), and JUC-110 (Figure 42).

16. Separation of mixtures of water and alcohols with Co(pbdc)

Figure 38a presents the pure component isotherms for water, methanol, ethanol, 1-propanol, and 2-propanol at 298 K reported by Zheng et al.[80] in Co(pbdc) with a 2-fold interpenetrating net. For pressures greater than 10 kPa, the hierarchy of component loadings is water > methanol > ethanol > 1-propanol > 2-propanol. Figure 38b presents IAST calculations of water/alcohol selectivities for four different mixtures. In all four cases, we note that at total pressures below about 20 kPa, the selectivity is in favor of the alcohols. However, entropy effects cause a reversal in selectivities as the pores become increasingly occupied; as the pressures are increased above 100 kPa the adsorption favors the water molecules. The IAST calculations suggest that Co(pbdc) has the potential to selectively adsorb water from mixtures with any of the alcohols; this separation principle has been observed earlier for FAU (Figure 17), DDR (Figure 20), FER (Figure 26), ZIF-71 (Figure 28), and CID-1 (Figure 35). For mixtures of alcohols, the adsorption is in favor of the "smaller" or "shorter" alcohol. Interestingly, this MOF can selectively adsorb 1-propanol from 1-propanol/2-propanol mixtures.

Figure 39a shows the transient breakthrough simulations for water/ethanol mixture with the azeotropic composition of 11 mol % water. The breakthrough simulations indicate that the azeotropic mixture can be separated in a fixed bed adsorber packed with Co(pbdc).

The transient breakthrough simulations in Figure 39b, and 39c demonstrate that water/1-propanol and water/2-propanol mixtures of azeotropic compositions can be separated in a fixed bed adsorber packed with Co(pbdc).

17. Separation of water and alcohols with Zn(II)-MOF

Figure 40a presents the pure component isotherms for water, methanol, ethanol, 1-propanol, and 2-propanol at 298 K reported by Zheng et al.[81] in a microporous Zn(II)-MOF = $[\mathrm{Zn(HPyImDC)(DMA)}]_n$ (DMA = N,N′-dimethylacetamide), possessing exposed Zn(II) cation sites following activation. IAST calculations of component loadings for 5-component mixtures in Zn(II)-MOF are shown in Figure 40b. At bulk pressures greater than say 100 kPa, we have pore saturation and molecular packing effects lead to the following hierarchy of component loadings water > methanol > ethanol > 1-propanol > 2-

propanol. The IAST calculations suggest that Zn(II)-MOF has the potential to separate selective water from mixtures with any of the alcohols; this separation principle has been observed earlier for FAU (Figure 17), DDR (Figure 20), FER (Figure 26), ZIF-71 (Figure 28), CID-1 (Figure 35), Cu-GLA (Figure 37), and Co(pbdc) (Figure 38). For mixtures of 1-alcohols, Zn(II)-MOF has the ability to selectively adsorb the shorter alcohol. Interestingly, this MOF can selectively adsorb 1-propanol from 1-propanol/2-propanol mixtures.

Figure 41a shows the transient breakthrough simulations for water/ethanol mixture with the azeotropic composition of 11 mol % water. The breakthrough simulations indicate that the azeotropic mixture can be separated in a fixed bed adsorber packed with Zn (II) MOF.

The transient breakthrough simulations in Figures 41b, and 41c demonstrate that water/1-propanol and water/2-propanol mixtures of azeotropic compositions can be separated in a fixed bed adsorber packed with Zn (II) MOF.

Gu et al.[82] have reported the selective uptake of water from various organic compounds (ethanol, acetone, tetrahydrofuran, benzene, toluene, xylene) using Zn (II) and a rigid planar ligand IDC3-(imidazole-4,5-dicarboxylate); this MOF consists of a 3D porous metal-organic framework (MOF) with 1D open channels. The selective adsorption of water reported with this Zn(II) MOF is most likely due to entropy effects, but the authors themselves do not offer this explanation.

18. Separation of mixtures containing water, methanol, and ethanol using JUC-110

The experimental isotherm data of Borjigin et al.[83] for pure component isotherms of water, methanol and ethanol in JUC-110 indicate the hierarchy of adsorption strengths water > methanol > ethanol over the entire range of pressures; see Figure 42a. These pure component isotherms indicate that the pore dimensions of JUC-110 are such as to effectively exclude ethanol. In other words, the separations of mixtures containing water, methanol, and ethanol are primarily dictated by size exclusion. The IAST calculations presented in Figure 42b, 42c, and 42d show that the larger sized molecules in the mixture can be virtually excluded. Unlike the other examples discussed in the foregoing sections, this exclusion is not based on entropy principles.

The IAST calculations in Figure 42 imply also that clean separations of water/methanol, water/ethanol, and methanol/ethanol mixtures are to be expected using JUC-110. To confirm this expectation, Figure 43 presents transient breakthrough simulations for (a) 20/80 water/methanol, and (b) 11/89 water/ethanol, and (c) 50/50 methanol/ethanol mixtures in a fixed bed adsorber packed with JUC-110 at 298 K. In all three cases, the component with the smaller molecular size elutes at a later time; this is a direct consequence of size exclusion effects. Of particular interest is the separation of the 11/89 water/ethanol mixtures, that corresponds to the azeotropic composition. We note that ethanol is scarcely adsorbed and is rejected almost immediately after feed mixture injection. Borjigin et al.[83] also present pulse chromatographic experiments with water/ethanol mixtures to show that ethanol is eluted almost immediately after feed injection.

19. Separations of Aromatics: Process background and potential for improvements

Aromatic hydrocarbons, that are valuable feedstocks in the petrochemical industries, are most commonly obtained from catalytic reforming of naphtha. The xylene isomers, o-xylene, m-xylene and in particular p-xylene, are important chemical intermediates. Ortho-xylene is oxidized to make phthalic anhydride which is used to make phthalate plasticizers among other things. Meta-xylene is oxidized to produce isophthalic acid, which is used in unsaturated polyester resin. However, p-xylene has the largest market of the three isomers; the demand for p-xylene is several times that of m-xylene and o-xylene. The largest use of p-xylene is in its oxidation to make terephthalic acid, that is used in turn to make polymers such as polyethylene terephthalate (PET) and polybutylene terephthalate (PBT). PET is one of the largest volume polymers in the world, and is used to produce fibers, resins, films, and blown beverage bottles.

In a commonly used separation scheme (cf. Figure 44), the xylenes rich stream from the bottom of the reformer splitter is routed to a xylenes splitter. Here, the heavier aromatics (C9+) are removed from the bottom of the column. The overhead stream from the xylenes splitter containing o-xylene, m-xylene, p-xylene, and ethylbenzene need to be separated for recovery of p-xylene. Due to the very small differences in boiling points, p-xylene recovery form o-xylene/m-xylene/p-xylene/ethylbenzene mixtures is not possible by use of distillation technology. There are, however, significant differences in the freezing points (see Figure 45) that allow fractional crystallization to be used for separations. The differences in the freezing points arise because of differences in the stacking efficiencies of molecules. Para-xylene has the highest freezing point because these molecules stack most efficiently; pure p-xylene crystals are the first to emerge from the solution upon cooling. However, the energy requirements for fractional crystallization are high because of the need to cool to temperatures of about 220 K. Selective adsorption of xylene isomers within the pores of ordered crystalline micro-porous materials is an energy-efficient alternative to fractional crystallization. In currently used technology the separation is carried out using cation-exchanged Faujasite (FAU) zeolite in a Simulated Moving Bed (SMB) adsorption separation unit.

An SMB unit consists of a set of interconnected columns in series; countercurrent flow of the solid and liquid phases is simulated by the periodic shifting of the inlets and outlets in the direction of the liquid flow. Commonly used SMB technologies are UOP's Parex, Axens' Eluxyl, and Toray's Aromax.[13, 84] In Figure 46 the SMB process for separation of a feed mixture containing o-xylene/m-xylene/p-xylene/ethylbenzene is depicted in its (mathematically) equivalent form of true moving bed with counter-current contacting between the down-flowing adsorbent material and up-flowing desorbent (eluent) liquid.

The typical composition of a mixed xylenes feed to a simulated moving bed (SMB) adsorber is 19% ethylbenzene, 44% m-xylene, 20% o-xylene, and 17% p-xylene. Since the adsorbent particles are in contact with a mixture in the *liquid* phase, the pores of the adsorbent material are practically saturated with guest molecules. The hierarchy of adsorption strengths is dictated by molecular packing, or entropy, effects. Binding energies of guest molecules with the framework walls or non-framework cations do not solely determine the separation performance. As pointed out by Peralta et al.[85], adsorbents selective to p-xylene are desirable for high productivities; they need to adsorb only ~20% of the feed, whereas an adsorbent that rejects p-xylene would have to adsorb 80% of the feed. In current industrial practice the adsorbent used is BaX zeolite, that selectively adsorbs p-xylene. Typically, BaX zeolite also contains other cations such as K^+. The separation of xylenes at pore saturation is influenced also factors other than molecular packing effects. For illustration, Figure 47a shows the pure component isotherms for hydrocarbons in BaX zeolite at 453 K, plotted using the Langmuir parameters reported by Minceva and Rodrigues.[13, 14] Industrial operations are for molar concentrations exceeding about 7 mol L^{-1}, corresponding to liquid phase operations.

Let us calculate the fractional occupancy within the pores, θ_t, using Equation (1) for adsorption of 4-component o-xylene/m-xylene/p-xylene/ethylbenzene mixtures at two different temperatures 393 K, and 453 K as a function of the total molar concentration in the liquid phase, c_t; see Figure 47b. The IAST calculations for mixture adsorption equilibrium in BaX show that the fractional occupancies within the pores are in excess of 0.9; see Figure 47b at both 393 K and 453 K, when $c_t > 7$ mol L^{-1}. This provides evidence that the pores are saturated. The IAST calculations of adsorption equilibrium also show that the selectivity of BaX becomes increasingly in favor of p-xylene as pore saturation conditions are approached; see Figures 47c, and 47d.

The desorbent used in the UOP Parex unit is p-diethylbenzene (pDEB).[86] pDEB has been found to have approximately the same affinity for BaX zeolite as does p-xylene, balancing the amount of desorbent required for p-xylene desorption while not excluding the p-xylene from adsorbing in the adsorption zone. pDEB boils at 450 K while the highest - boiling xylene, o-xylene, boils at 417.6 K so there is substantial relative volatility to perform the distillative separations economically.[86]

In the configuration depicted in Figure 46, the feed mixture containing o-xylene, m-xylene, p-xylene, and ethylbenzene is introduced at a port near the middle of the SMB unit.[13, 84] The eluent is introduced at the bottom. For a clearer appreciation of the SMB operations, Figure 48 presents typical liquid phase concentrations of o-xylene, m-xylene, p-xylene, ethylbenzene along the adsorber height. The extract phase, containing the more strongly adsorbed p-xylene, is recovered at the bottom section of the column, below the feed injection port. The raffinate phase, containing the more weakly adsorbed o-xylene, m-xylene, and ethylbenzene is tapped off at a location in the upper section above the feed injection port. Four different operation zones can be distinguished.

Zone 1: Regeneration of adsorbent,

Zone 2: Desorption of the less strongly adsorbed components o-xylene, m-xylene, and ethylbenzene,

Zone 3: Adsorption of the more strongly adsorbed p-xylene,

Zone 4: Regeneration of the eluent.

The components o-xylene, m-xylene, and ethylbenzene, contained in the rafffinate phase of the SMB unit, are sent to a xylenes isomerization unit. In the isomerization unit the xylenes mixture is re-equilibrated, and the main products are benzene, toluene, and p-xylene.

On examination of the boiling points of the C8 aromatics, we note that o-xylene has the highest boiling point; see Figure 45. A xylenes splitter, which ordinarily would separate the C9+ aromatics from the xylenes (cf. Figure 44), can be redesigned to remove o-xylene as well; this alternative configuration is depicted in Figure 49. In this configuration, the fractionation split in the xylenes splitter is between m-xylene and o-xylene with a temperature difference of only 5 K; consequently we need a super-fractionating tower containing about 135 fractionating trays. The overhead product from the xylenes splitter, rich in ethylbenzene, p-xylene, and m-xylene is fed to a recovery unit for p-xylene. The bottoms product from the super-fractionator is routed to a further distillation column in which o-xylene is separated from C9+ aromatics and recovered as overhead product. In the configuration shown in Figure 49, both the xylenes splitter and o-xylene recovery columns are super-fractionators that have high energy demands.

There is considerable potential for use of metal-organic frameworks (MOFs) adsorbents for use in one or more of the following separation tasks.

(1) For realizing improvements in the SMB adsorber we need to discover adsorbents that have both higher uptake capacity and selectivity of p-xylene when compared to BaX zeolite, whose

performance has been benchmarked in Figure 47. Better MOF adsorbents will result in lower recirculation flows of eluent, and solids and this will result in significant economic advantages.

(2) Both the distillation columns in the processing scheme shown in Figure 49 could be replaced by an adsorption unit, perhaps operating using SMB technology, with a MOF adsorbent that is selective to o-xylene.

(3) MOFs could be used for separation of a mixture of benzene, toluene, and non-aromatics as replacement for extractive distillation depicted in Figure 44. A hybrid combination of distillation and adsorption is also another option.

(4) MOFs could be used for separation of ethylbenzene/styrene mixtures either as total, or partial, replacement of the vacuum distillation tower currently used; see Figure 44.

A common feature of all the aromatics separation is that the operation conditions are such that the pores are nearly saturated with guest molecules. Therefore, molecular packing effects are of primary importance in the separations. Components that pack most efficiently are the ones that are selectively adsorbed. For any adsorbent material, the packing efficiencies of any aromatic molecule are dictated by a combination of two factors: (a) molecular dimensions, and (b) departures from planarity.

20. Separation of o-xylene/m-xylene/p-xylene/ethylbenzene

The height and width of the C8 aromatics are: o-xylene: 8 Å × 7.4 Å; m-xylene: 8.9 Å × 7.4 Å; p-xylene: 9.3 Å × 6.7 Å; ethylbenzene: 9.5 Å × 6.7 Å; styrene: 9.3 Å × 6.7 Å; see dimensions provided in Figure 50. A further point to note is that xylene isomers are flat; these isomers can align themselves parallel to the channel walls, affording better van der Waals interactions with the framework atoms. By contrast, ethylbenzene is not a flat molecule; the ethyl branch is not in the same plane as the benzene ring; see Figure 51.

Due to the differences in the molecular dimensions of the xylene isomers, the efficiencies with which the xylene isomers stack within the channels of different dimensions are different. We can deliberately choose a material with a specified channel dimension in order to allow the optimum stacking of one or other of the xylene isomers. Stacking xylenes within 1D channels of MOFs is analogous to stacking books within bookshelves.[12, 47] Consider the stacking of o-xylene and p-xylene within one-dimensional (1D) channels that are 8.5 Å wide; see Figures 52a, and 52b. Within 8.5 Å channels, the stacking efficiency of o-xylene is higher than that of p-xylene, i.e. more o-xylene molecules can be packed within a channel of a given length. The channel size is not wide-enough to allow p-xylene to stack vertically, and fewer molecules of p-xylene can be packed within the same channel length.

Experimental data[24, 87, 88] for MIL-47 and MIL-53 with 1D rhombohedric channels of 8.5 Å confirm that these MOFs are selective to adsorption of o-xylene when operating at conditions close to pore saturation. The snapshots in Figure 53, obtained from CBMC simulations,[47] clearly show the optimal stacking of o-xylene within 8.5 Å channels of MIL-47. The pure component isotherm data[47] show that the saturation capacity of o-xylene is the higher than that of other xylenes; see Figure 53.

Experimental data of Niekiel et al.[89] for adsorption isotherms for xylene isomers in CAU-13 show strong selectivity towards o-xylene that has optimal stacking within the 8.46 Å channels. Fang et al.[90] report pulse breakthrough simulations for 4-component o-xylene/m-xylene/p-xylene/ethylbenzene in MOF-CJ3 that indicate adsorption selectivity towards o-xylene. MOF-CJ3 has that has square channels of approximately 8 Å size that is perhaps sufficient for commensurate stacking of o-xylene.

The MOFs MIL-47, MIL-53, CAU-13, and MOF-CJ3 are potentially usable as partial replacement of the distillation columns in Figure 49. Within the channels of these MOFs, the o-xylene molecules stack themselves *parallel* to the surrounding walls, along the 1D channel axis.

The work of Chiang et al.[91] indicates that the aluminophosphate molecular sieve $AlPO_4$-5 (with AFI zeolite topology) has the capability of separating xylene isomers; Figure 54 shows their experimental data for pure component isotherms for xylenes in $AlPO_4$-5 at 303 K. The hierarchy of saturation capacities is o-xylene >> p-xylene ≈ m-xylene. On the basis of molecular dimensions of the isomers, Chiang et al.[91] have argued that the differences in the saturation capacities reflect differences in packing arrangements within the 1D channels of $AlPO_4$-5. For m-xylene, and p-xylene, either the “height” or “width” is too large to allow vertical alignment; the orientation of these isomers occurs at an inclination. The “height” and “width” of o-xylene are both small enough for this isomer to be stacked vertically, face-to-face. The orientations of orhto, meta, and para isomers of xylene are pictured in Figure 4 of the paper by Chiang et al;[91] see discussions on these cartoons shown in their paper. An important consequence of the differences in the orientation of isomers is that the "footprints" of o-xylene molecules is significantly shorter than the footprints of m-xylene, and p-xylene molecules. Shorter footprints result in higher saturation capacities, as evidenced in the data in Figure 54.

Figure 55 shows the values of the isosteric heats of adsorption, Q_{st}, of xylene isomers in AFI zeolite. o-xylene molecules can fit snugly within the 8.4 Å grooves of AFI and for this reason the value of Q_{st} is significantly higher than that of m-xylene and p-xylene; see discussions in Chiang et al.[91] regarding Figure 4 of their publication.

IAST calculations for adsorption equilibrium for 3-component o-xylene(1)/m-xylene(2)/p-xylene(3) mixtures at 303 K are shown in Figures 56a,c. Figures 56b,d compares the o-xylene/p-xylene and o-xylene/m-xylene selectivities. We note that $AlPO_4$-5 is p-xylene selective in the Henry regime, but becomes strongly o-xylene selective as pore saturation is approached. It is noteworthy that at $p_t > 10$ Pa, i.e. $\theta_t > 0.6$, the adsorption is strongly in favor of o-xylene. This would imply that selectivity reversal occurs.

Transient breakthroughs at a total xylenes pressure $p_t = 30$ kPa are shown in Figure 57a; the separation is in favor of o-xylene. Hu et al.[92, 93] report transient breakthrough experiments to demonstrate that the breakthrough of o-xylene occurs significantly later than that of either m-xylene or p-xylene, in qualitative agrement with the results presented in Figure 57. It is also noteworthy that $AlPO_4$-5 zeolite has been patented by Exxon Research & Engineering for o-xylene selective separation of aromatic mixtures.[94]

Figure 57b presents pulse chromatographic simulations for injection of an equimolar mixture at 30 kPa in a bed of $AlPO_4$-5. We note that the elution sequence is now m-xylene, o-xylene, and p-xylene. This sequence is dictated by the adsorption strengths in the Henry regime. The point we wish to stress here is that pulse chromatographic experiments, and simulations, do not reflect molecular packing effect that manifest at pore saturation. It is therefore surprising to note that some journal papers[23] that have examined the separation of xylene isomers with MOFs have presented pulse chromatographic experiments to demonstrate separability at pore saturation.

Torres-Knoop et al.[47] have adopted a conceptual approach, using CBMC simulations for selecting MOFs that have the desired selectivity to p-xylene. Within the one-dimensional 10 Å channels of MAF-X8, we have commensurate stacking of p-xylene; see snapshots in Figure 58a. Co(BDP), that has 10 Å square-shaped 1D channels of Co(BDP), also allows p-xylene to stack vertically (cf. Figure 58b), resulting in selectivity in favor of p-xylene.[47] Commensurate stacking within 1D channels of MAF-X8, results in strong selectivity in the favor of the p-xylene as saturation conditions are approached; this is verified by CBMC simulations for a 4-component mixture shown in Figure 59. In the study of Torres-Knoop et al., [47] MAF-X8 emerged as the best MOF for separation of 4-component o-xylene/ m-xylene/ p-xylene/ethylbenzene mixtures.

In a recent paper, Mukherjee et al.[95] have presented pure component adsorption isotherm data at 298 K for o-xylene, m-xylene, p-xylene, and ethylbenzene in a Zn(II)-based dynamic coordination framework, $[Zn_4O(L)_3]$ where the ligand L = 4, 4'- ((4-(tert-butyl) - 1,2-phenylene)bis(oxy))dibenzoate). The MOF structure gets transformed in such a manner as to allow optimal packing of p-xylene within the cavities. The pure component isotherm data show that the saturation capacity of p-xylene is 3 mol/kg which is comparable to that reported for MAF-X8 by Torres-Knoop et al.[47] Remarkably, $Zn_4O(L)_3$ appears to adsorb less than about 0.5 mol/kg of o-xylene, m-xylene, and ethylbenzene. Unfortunately, Mukherjee et al.[95] do not report IAST calculations of selectivities for $Zn_4O(L)_3$, but our estimates indicate separation selectivities in favor of p-xylene in excess of 100, significantly higher than that for BaX and MAF-X8. In view of this further experimental work on breakthroughs, and stability tests are required in order to demonstrate the efficacy of $Zn_4O(L)_3$ for replacement of BaX in the process scheme shown in Figure **44**.

21. Separation of ethylbenzene/styrene mixtures

Maes et al.[96] and Remy et al.[97] have demonstrated that MIL-47 (V) and MIL-53 (Al) also have the potential for separation of mixtures of styrene and ethylbenzene. Styrene is a flat molecule; by contrast, ethylbenzene is not a flat molecule; the ethyl branch is not in the same plane as the benzene ring; see Figure 51. Due to differences in the flatness, styrene has stronger interactions with the metal framework. Being flat styrene molecules stack more efficiently within the 1D channels of MIL-47 (V) and MIL-53 (Al). The pure component isotherm data of Maes et al.[96], measured for bulk liquid phases show that the adsorption loadings of styrene are higher than that of ethylbenzene. Figures 60a, and 60b present the experimental data of Maes et al.[96] for transient breakthroughs of ethylbenzene/styrene mixtures in MIL-47(V) and MIL-53(Al). These data demonstrate that styrene is selectively adsorbed. There is a need to find MOFs that offer significantly better separations than those afforded by MIL-47 (V) and MIL-53 (Al).

22. Separating hexane isomers with AFI, CFI, and ATS zeolites

Consider the adsorption of a mixture of hexane isomers nC6/3MP/22DMB within the 1D channels of AFI zeolite; the CBMC mixture simulation results are presented in Figure 61a. Near pore saturation conditions, the hierarchy of adsorption strengths is nC6 < 3MP << 22DMB.[98] The hierarchy of component loadings is primarily dictated by the molecular footprints (see Figure 61b). The linear nC6 has a longer "footprint" and occupies a larger segment of the channel. 22DMB is the most compact molecules and has the smallest footprint; consequently, a greater number of di-branched isomers can be located within a given length of the channels when compared to nC6. 3MP has a footprint has footprints with an intermediate character. The di-branched isomers are selectively adsorbed with AFI zeolite from the nC6/3MP/22DMB mixture.[98]

ATS and CFI zeolites, patented by Chevron for application in the alkane isomerization process [99, 100] have 1D channels similar to that of AFI zeolite.[12, 34] Figures 62a, and 62b present CBMC simulations for adsorption equilibrium in nC6/2MP/3MP/22DMB/23DMB mixtures in (a) ATS, and (b) CFI zeolites. The linear nC6 has the lowest loading because it has the longest footprint in the 1D channels of ATS and CFI.[34]

Molecular length entropy effects dictates the sorption hierarchy in CFI, and ATS; a similar situation holds for MOR that has 6.5 Å × 7 Å sized 1D channels.[12, 98, 101, 102]

From a practical point of view it is not desirable to separate hexane isomers using AFI, ATS, and CFI; the reasons for this are explained in detail in previous works. [12, 34]

23. Separating hexane isomers using MFI zeolite

The MFI pore topology consists of a set of intersecting straight and zig-zag channels of approximately 5.5 Å size; see Figure 63. Separations of hexane isomers with MFI are based on the exploitation of the differences in molecular configurations. Linear molecules such as n-hexane (nC6) can locate anywhere along the channels, as illustrated in the computational snapshots in Figure 63. The length of nC6 is commensurate with the distance between adjoining intersections;[48] consequently, nC6 can be packed very efficiently within the channel network with a saturation loading $\Theta_{i,sat} = 8$ molecules per unit cell. Branched molecules such as iso-butane (iC4), 2-methylpentane (2MP), 3-methylpentane (3MP), 2,2 dimethylbutane (22DMB), and 2,3 dimethylbutane (23DMB) are bulkier; these locate preferentially at the intersections that afford extra "leg room". The availability of intersection sites is limited to a total of 4 per unit cell of MFI. Indeed, the saturation capacities of 22DMB and 23DMB correspond to $\Theta_{i,sat} = 4$ molecules per unit cell, significantly lower than that of the linear isomer nC6. Figure 64 compares CBMC simulations of pure component isotherms for 2MP with the experimental data; the strong inflection in the 2MP isotherm is a direct evidence of configurational differences. Loadings in excess of 4/uc of 2MP can only be achieved with an "extra push", i.e. with vastly increased pressures.

The differences in the packing efficiencies of linear and branched isomers, often referred to as configuration entropy effects,[48, 103, 104] can be usefully exploited for separation of the hexane isomers to obtain different products with different degrees of branching.[12, 34, 41, 104]

To illustrate this separation principle, let us consider CBMC simulations of loadings in the adsorbed phase in equilibrium with equimolar binary gas phase containing a mixture of nC6 and 2MP with equal partial pressures $p_1 = p_2$ in the bulk gas phase; see Figure 65a. Up to total hydrocarbons pressures $p_t = p_1 + p_2 = 2$ Pa, the component loadings Θ_i of each component increases in an expected manner; increasing p_t leads to a corresponding increase in the component loading Θ_i. At 2 Pa pressure the total loading $\Theta_t = 4$/uc, signifying that all the intersection sites are fully occupied. To further adsorb 2MP we need to provide an extra "push". Energetically, it is more efficient to obtain higher mixture loadings by "replacing" the 2MP with nC6; this *configurational entropy* effect is the reason behind the curious maxima in the 2MP loading in the mixture. The experimentally determined loadings from IRM[59] are also plotted in Figure 65a. There is good agreement of the IRM data and the CBMC mixture simulations. The IRM experiments offer direct experimental verification of the configurational entropy effects in mixture adsorption for nC6/2MP that was first observed on the basis of CBMC mixture simulations.[48, 103]

Figure 65a also shows the IAST calculations (continuous solid lines) with CBMC simulations of component loadings of binary nC6/2MP mixtures. The IAST estimations of the component loadings are of good accuracy. The influence of configurational entropy effects on separations is best quantified by the *adsorption selectivity* S_{ads}, defined by

$$S_{ads} = \frac{\Theta_1/\Theta_2}{p_1/p_2} = \frac{\Theta_1/\Theta_2}{f_1/f_2} \tag{13}$$

For equimolar binary gas phase mixtures, Equation (13) simplifies to yield

$$S_{ads} = \frac{\Theta_1}{\Theta_2} \quad \text{(for equimolar gas mixture with } p_1 = p_2\text{)} \tag{14}$$

The calculations of S_{ads} are shown in Figure 65b. We note that for total loadings $\Theta_t < 4$/uc, $S_{ads} \approx 1$, suggesting that adsorptive separations of nC6/2MP are not feasible for pressures below $p_1 + p_2 < 2$ Pa. However, when the total loadings of the adsorbed phase Θ_t exceeds 4/uc, the values of S_{ads} increase significantly to values by 10 - 100. This implies that sharp separations of the linear and branched hexanes are possible provided the operating conditions correspond to total mixture loadings $\Theta_t > 4$/uc.

The transient uptake of nC6(1)/2MP(2) mixtures within MFI crystals were monitored using IRM in a set of four runs reported by Titze et al.[59] In all four runs, the bulk gas mixture (with $p_1 = p_2$) was maintained at a constant temperature of 298 K. The total pressure p_t was increased in a step-wise manner, Run 1: p_t = 0 to 2.6 Pa; Run 2: p_t = 2.6 to 4 Pa; Run 3: p_t = 4 to 12.2 Pa; Run 4: p_t = 12.2

to 102 Pa. Each run was allowed sufficient time to equilibrate, before application of the subsequent pressure step; the IRM transient uptake data are summarized in Figure 66. We note that the transient uptake of nC6 has a fundamentally different character than that of its partner 2MP. The transient uptake of 2MP uptake is observed to be significantly influenced by the entropy effects that govern mixture adsorption. After the initial increase in the uptake in Run 1, the 2MP uptake in subsequent Runs 2, 3, and 4 decreases because the total mixture loadings $\Theta_t > 4$, and entropy effects are in play, causing a reduction in its equilibrium loading with increase in p_t. Entropy effects also cause the nC6 uptake to become progressively "sharper" as witnessed by the progressively faster equilibration in Runs 2, 3, and 4.

The continuous solid lines in Figure 66 represent simulations of the uptake in which the Maxwell-Stefan diffusivities $Đ_1$ and $Đ_2$ are fitted for each of the four runs. The uptake simulations capture, nearly quantitatively, the essential features of the transient IRM uptake data for all four runs, including the nC6 overshoot observed in Run 1. The overshoot of nC6, observed in Run 1 is traceable to thermodynamic coupling effects, as explained in detail in the publication of Titze et al.[59] and Krishna.[12] Analogous overshoots in the transient uptake of the more mobile partner species have been reported for N_2/CH_4 mixtures in LTA-4A,[105] benzene/p-xylene in ZSM-5,[106, 107] benzene/ethylbenzene in ZSM-5,[106, 107] n-heptane/benzene in NaX, [108] ethanol/1-propanol in SAPO-34,[109] and methanol/1-propanol in SAPO-34,[109] methanol/ethanol in SAPO-34.[109] Overshoots in the flux of the more mobile partner have also been reported for transient permeation of CH_4/nC_4H_{10},[110] nC4/iC4,[111] nC6/2MP,[112] nC6/22DMB,[112] m-xylene/p-xylene,[113] and p-xylene/m-xylene/o-xylene[113] mixtures across MFI membranes.

Figure 67 summarizes the fitted values of M-S diffusivities; the data is presented as $Đ_1/r_c^2$, and $Đ_2/r_c^2$ where r_c is the effective crystal radius. Each of the diffusivities is strongly dependent on the loading of 2MP, increasing by a factor of 10 as we progress from Run 1 to Run 4; the ratio $Đ_1/Đ_2$ has a constant value of 100. Also indicated at the top of Figure 67 are the values of the total mixture loadings Θ_t for each of the four Runs. We note that as we proceed from Run 1 the total mixture loading increases from $\Theta_t = 4.5$/uc in Run 1, to $\Theta_t = 7.54$/uc in Run 4, the 2MP loading decreases from 1.84/uc to 0.14/uc, emphasizing the configurational-entropy effects. Concomitantly, we note that the diffusivities of both species, nC6 and 2MP, increase by about an order of magnitude with increased total mixture loading, Θ_t. While there are many practical examples of increased adsorption leading to a lowering of diffusivities [114, 115], nC6/2MP uptake data in MFI reported by Titze et al.[59] are unique because the diffusivity trends in Figure 67 imply that configurational entropy effects results in a synergy between mixture adsorption and mixture diffusion. Entropy effects cause 2MP to be excluded from the adsorbed phase for operations at $\Theta_t > 4$; concomitant with this exclusion is an increase, by about an order of magnitude, in the diffusivities of both species.

Configurational entropy effects, first elucidated using CBMC simulations,[12, 48, 103, 104] can be used to fractionate a 5-component nC6/2MP/3MP/22DMB/23DMB mixture with MFI zeolite. Figure 68a shows that for mixture loading $\Theta_t > 4$ molecules/uc, the hierarchy of component loadings is nC6 > 2MP > 3MP > 23DMB > 22DMB. The mono-branched and di-branched isomers locate preferentially at the channel intersections that offer more "leg-room" for these bulkier, more-compact, branched isomers (see snapshots in Figure 68b). But the number of intersections are limited to 4 per unit cell; this limits the saturation capacities. The configurational-entropy principle to separate hexane isomers using MFI zeolite The di-branched isomers have significantly lower diffusivities, and the separations in fixed bed adsorbers benefit from the synergy between adsorption and diffusion.[12] The transient breakthrough of hexane isomers in a fixed bed adsorber packed with MFI zeolite shows the sequence 22DMB, 23DMB, 3MP, 2MP, and nC6; see Figure 68c. The desired high RON products 22DMB and 23DMB can be recovered in the early stages of the breakthrough; this satisfies the process requirements.

The synergistic effects between adsorption and diffusion in MFI is the primary reason that MFI has superior separation performance as compared to other zeolites and MOFs, including $Fe_2(BDP)_3$.[12, 34]

24. Separation of mixtures of C4 hydrocarbons

The separation of unsaturated olefins and dienes from C4 hydrocarbon mixtures is important in petrochemical processing. The C4 hydrocarbons possess similar sizes and boiling points; see Table 33. Due to the closeness of the boiling points (iso-butane = 261.45 K; iso-butene = 266.25 K; 1-butene = 266.85 K; 1,3 butadiene = 268.75 K; normal butane = 272.65 K; trans-2-butene = 273.45 K; cis-2-butene = 276.85 K), the separation of C4 streams to recover the valuable 1,3-butadiene, 1-butene, and iso-butene by distillation is difficult and energy intensive. 1,3-butadiene, an important raw material for preparation of synthetic rubber, i.e. copolymers of styrene and butadiene, is usually recovered from the C4 stream by extractive distillation using an entrainer such as dimethyl formamide (DMF). Under mild acid catalytic conditions, iso-butene can be selectively reacted to form methyl tert-butyl ether (MTBE). 1-butene, has high commercial value as a co-monomer for polyethylene (LLDPE), but its recovery from a C4 fraction, devoid of 1,3 butadiene and iso-butene, requires a set of two distillation columns as shown schematically in Figure 69. The differences in the boiling point of key components in the two distillation columns are, respectively, 5 K and 6K. Due to these small differences in boiling points (indicated in Figure 69), we need two tall columns with as many as 200 theoretical trays.

There are considerable economic advantages in replacing the energy-demanding distillation separation scheme in Figure 69 with selective adsorption. Figure 70 shows a processing scheme for separation of C4 hydrocarbons based on selective adsorption. Each of the adsorbers demands "discovery" of the best MOF adsorbent.

We summarize below some of the published research on the appropriate adsorbents.

In a US patent awarded to UOP, Preignitz[116] claims the selective adsorption of 1,3-butadiene from mixtures containing another unsaturated C4 hydrocarbons using 13 X zeolite. The selective adsorption of 1,3 butadiene from 1-butene using Ag-Y zeolite is suggested by Takahashi et al.[117]

Granato et al.[118] present isotherm data for iso-butane and 1-butene in 13X zeolite. Their isotherm data indicate 1-butene/iso-butane adsorption selectivities in the range of 10 – 16.

In the work of Jin et al.[119], a mesoporous adsorbent containing ferrous/cuprous ionic species (Fe–Cu/MCM- 41) has been developed for selective separation of 1-butene/n-butane due to π-complexation of the metal-ions with the olefin.

Hartmann et al.[120] have presented experimental data on pure component isotherms and mixture breakthroughs to demonstrate the separation of iso-butane/iso-butene mixtures using $Cu_3(BTC)_2$; see Figure 71. The adsorptive separation step exploits the strong interactions between double bond of isobutene with Cu^{2+}; the unsaturated molecules bond preferentially with the co-ordinatively unsaturated Cu atoms.

Wang et al.[121] investigated the separation of 1-butene and n-butane using MFI zeolite with different Si/Al ratios. With increasing number of extra-framework Na^+, the adsorption selectivity increases in favor of 1-butene.

In a computational study, Kim and Jung[122] have examined the feasibility of separating 1-butene from other butane isomers by use of FeMOF-74. 1-butene, that has a terminal double bond, has the smallest steric interactions with the framework and therefore can approach the metal binding sites more closely for stronger π-complexation. It remains to be experimentally determined whether selective adsorption of 1-butene is feasible.

The above mentioned separations rely on differences in adsorption strengths; in the following paragraphs, we highlight two separation strategies that rely on molecular packing effects for separation of C4 hydrocarbons.

Consider the separation of n-butane (nC4) from iso-butane (iC4) using MFI zeolite. The linear n-butane can locate anywhere along the channels (see Figure 72a). The more compact iso-butane is severely constrained within the 5.5 Å channels and prefers to locate at the intersections between the channels because such locations offer more “leg room” (see Figure 72b). The number of intersection sites is restricted to a 4 per unit cell of MFI. To achieve loadings of iso-butane > 4 molecules per unit cell, an “extra push” is required. Energetically, it is much more efficient to adsorb the linear n-butane to obtain higher loadings. CBMC simulations for mixture adsorption (cf. Figures 72c,d) show that for total mixture loadings Θ_t > 4 molecules per unit cell, the selectivity is strongly in favor of the linear isomer.[59, 123, 124] We also note that the IRM experimental data of Titze et al. [59] are in excellent agreement with the CBMC mixture simulation data, and provide convincing proof of molecular packing effects that favor nC4.

Experimentally, the MFI membrane permeation selectivity is found to be strongly in favor of the linear isomer.[113, 125] A further point to stress is that nC4/iC4 separations using MFI in both fixed bed adsorbers and membrane devices benefits from the synergy between adsorption and diffusion; both of these act in favor of the linear isomer. This has been established in the MAS PFG NMR experiments of Fernandez et al.[126] and the transient uptake data of Chmelik et al.[127]

Tijsebaert et al.[128] have demonstrated the potential of RUB-41 all-silica zeolite, that has the RRO structural topology, for separation of cis-2-butene and trans-2-butene from 1-butene; this separation is of industrial importance because 1-butene is needed in the production of e.g. linear low density polyethylene (LLDPE). RUB-41 comprises a 2-dimensional intersecting channel system consisting of an 8-membered ring channel (0.27 × 0.5 nm) along [001], and a 10-membered ring channel (0.4 × 0.65 nm) along [100]. The measured data on adsorption indicates that the adsorption equilibrium, and saturation capacities follow the hierarchy cis-2-butene > trans-2-butene >> 1-butene; see Figure 73a. This hieararchy is most likely a reflection of molecular packing effects. Breakthrough experiments, carried out in the liquid phase, indicate that 1-butene breaks through earlier than either cis-2-butene, or trans-2-butene; see Figures 73a, and 73b.

25. Separation of chlorofluorocarbons with MFI zeolite

Peng et al.[129] discuss the need for separation of CFC-115 (1-chloro-1,1,2,2,2-pentafluoroethane) and HFC-125 (1,1,1,2,2-pentafluoroethane). The boiling points of CFC-115 (234.1 K) and HFC-125 (224.7 K) are very close, and their mixtures can form azeotropes. Therefore, cryogenic extractive distillation has been the dominant technology utilized to separate these mixtures. Adsorptive separations offer energy-efficient alternatives to distillation. Towards this end, Peng et al.[129] have reported the pure component isotherm data for CFC-115 and HFC-125 in MFI zeolite; see Figure 74a. Due to the presence of the bulky chloro-group at the 1-position, CFC-115 locates preferentially at the intersections of MFI, that provides the required leg-room. Consequently, the pure component isotherm of CFC-115 shows a pronounced inflection at a loading of 4 molecules per unit cell. HFC-125 can locate can locate comfortably within the channels, and the pure component isotherms do not show any pronounced inflection characteristics.

Figure 74b shows IAST calculations of the component loadings for equimolar CFC-115/HFC-125 mixtures in MFI zeolite. For total pressures $p_t < 3$ kPa, the adsorption selectivity is in favour of CFC-115. However, due to configurational entropy effects, the adsorption selectivity is in favour of HFC-125 at total pressures $p_t > 5$ kPa. The principle of separation is entirely analogous to that of the separation of hexane isomers discussed in detail in the earlier section.

Figure 75 present transient breakthrough simulations for equimolar CFC-115/HFC-125 mixture with MFI zeolite at (a) $p_t = 1$ kPa, and (b) $p_t = 100$ kPa. If the chosen operating conditions are such that $p_t = 1$ kPa, then HFC-125 can be recovered in pure form during the adsorption cycle; see Figure 75a. We note from the breakthroughs at $p_t = 100$ kPa that the HFC-125 is more strongly adsorbed in MFI; consequently it can only be recovered in the desorption (blowdown) cycle; see Figure 75b.

The entropy effects that cause HFC-125 to be preferentially adsorbed at high loadings are specific to MFI zeolite. In order to demonstrate this, let us consider the separations of CFC-115/HFC-125 mixtures using Varuf Activated Carbon. Figure 76a present data on pure component isotherms; no inflection characteristics are exhibited by either CFC-115 or HFC-125. The IAST calculations show that CFC-115 is more strongly adsorbed over the entire range of pressures. There is no selectivity reversal as witnessed for MFI zeolite. Molecular packing effects are specific to guest/host combinations; they are not the exclusive property of either guest species or host material.

26. Separation of aromatics using MFI zeolite

Let us examine the separation of aromatics using MFI zeolite. Figure 77 shows the experimental data of Lee and Chiang [130] for pure isotherm data for benzene, toluene, p-xylene, and ethylbenzene in MFI zeolite at 283 K. The pure component isotherms display inflection characteristics at a loading of 0.7 mol kg^{-1}, which corresponds to 4 molecules per unit cell of MFI zeolite. The reason for this inflection is that the intersections are preferred locations of aromatic molecules; there are 4 intersection sites per unit cell of MFI zeolite; see snapshots in Figure 77. The inflection is particularly strong for ethylbenzene, that is difficult to locate within the channels; the saturation capacity of ethylbenzene 6 molecules/uc, compared to 8/uc for the other guest aromatics.

Let us investigate the separation of mixtures of benzene and ethylbenzene, important in the process for alkylation of benzene.[131, 132] Figure 78a presents IAST calculations of the component loadings for adsorption of equimolar mixtures benzene, and ethylbenzene in MFI zeolite at 283 K. We note that there is a reversal of selectivity at total pressure p_t = 1 kPa. For p_t < 1 kPa, ethylbenzene is more strongly adsorbed, but for p_t > 1 kPa, molecular packing effects cause benzene to be the more strongly adsorbed component.

In Figure 78b, the IAST calculations for the component loadings are plotted against the fractional occupancy, θ_t. in order to emphasize that selectivity reversal occurs at pore saturation, $\theta_t \approx 1$.

Figures 78c, and 78d show transient breakthrough simulations for equimolar feed mxture of benzene, and ethylbenzene in MFI zeolite at 283 K at total pressures of (b) 4 kPa, and (c) 20 kPa, respectively. We note that for p_t = 4 kPa, ethylbenzene is the more strongly adsorbed component, whereas for p_t =20 kPa, benzene is the more strongly adsorbed component. At first sight the transient breakthroughs in Figure 78b appears to be incompatible with the IAST calculations in Figure 78a. The explanation for this discrepancy is as follows. In the transient breakthroughs, the MFI crystals get progressively loaded with the guest molecules, and molecular packing effects come into play only towards the end of the cycle when pore saturation is approached. This implies that the breakthrough characteristics are influenced by the entire range of pressures 0 - p_t , and not just by the conditions corresponding to p_t = 4 kPa. The breakthrough characteristics of Figure 78b are dominated by the initial phases during which ethylbenzene is the more strongly adsorbed component. This re-emphasizes the need for performing transient breakthroughs as being truly representative of industrial separations.

27. Separation of benzene/cyclohexane mixtures

Cyclohexane, and important industrial chemical, is produced by catalytic hydrogenation of benzene. The unreacted benzene is present in the effluent from the reactor must be removed from the desired product. The separation of benzene and cyclohexane is difficult because the differences in the boiling points is only 0.6 K (cf. Figure 79). Currently technologies use extractive distillation with entrainers such as sulpholane, dimethylsulfoxide, N-methylpyrrolidone, and N-formylmorpholine; such processes are energy intensive. Adsorptive separations offer the energy-efficient alternatives to extractive distillation, especially for mixtures containing small percentage of benzene, as is commonly encountered.

Takahashi and Yang[133] have presented pure component isotherm data for benzene and cyclohexane to show that cation-exchange Faujasites Na-Y, Pd-Y, and Ag-Y zeolites have high selectivity for adsorption of benzene, due to π-complexation; cyclohexane does not form π-complexes.

An alternative to cation-exchange Faujasites, as suggested by Ren et al.[134] is to use a porous aromatic framework, PAF-2. The pure component isotherm data for PAF-2 shown in Figure 2b of Ren et al.[134] indicate that the saturation capacity of benzene is much higher than that of cyclohexane; this is perhaps due to molecular packing effects. Figure 79 shows the molecular structures of benzene and cyclohexane; it appears that stacking of flat benzene molecules is easier than stacking cyclohexanes in either the boat or chair configurations. In addition to molecular packing effects, the higher π–π interaction between the benzene molecule and the aromatic framework of PAF-2 also contributes to good separations.

Lin et al.[135] present the pure component isotherm data for benzene and cyclohexane for Mn triazolate MOF that also indicates a sign indicate that the saturation capacity of benzene is much higher than that of cyclohexane. Both the above mentioned MOFs appear to have potential for selective adsorption of benzene.

28. Conclusions

The following major conclusions emerge from our detailed analysis of separations of mixtures operating close to pore saturation conditions.

(1) In contrast to separations under conditions for which $\theta_t < 0.6$, the separations at conditions close to pore saturation, i.e. $\theta_t \approx 1$, are significantly influenced by differences in saturation capacities. The saturation capacities are a direct reflection of the efficiencies by which molecules pack, or stack, themselves within the microporous channels. For operations in which the bulk mixture to be separated is in the liquid phase, pore saturation is assured.

(2) For mixtures of 1-alcohols, molecular packing effects can be exploited to selectively adsorb the shorter alcohol. The entropy effects are quantitatively predicted by the IAST calculations. Such separations have been experimentally demonstrated for separations with SAPO-34, ZIF-68, UCY-5, and Ce(BTB). An important feature of such separations is that intra-crystalline diffusion and mixture adsorption proceed hand-in-hand, i.e. they are synergistic.

(3) For selective adsorption of alcohols from dilute aqueous solutions, we need to use hydrophobic adsorbents in order to ensure rejection of water from the pores. This possibility has been demonstrated for ZIF-8 (cf. Figure 9).

(4) The separation of water/benzene vapor mixtures with CuBTC is a good illustration of the relative importance of adsorption strengths and saturation capacities. For operations at lower temperatures and higher pressures, the separation is selective to water that has the higher saturation capacity. In contrast, operations at higher temperatures, and lower pressures are selective to benzene that has the higher adsorption strength.

(5) Selective adsorption of water from water/alcohol mixtures can be achieved with hydrophilic adsorbents such as LTA-4A, CID-1, Cu-GLA, Co(pbdc), JUC-110, and Zn(II)-MOF by choosing conditions close to pore saturation. Large differences in saturation capacities, results in better separations. In particular, CID-1 appears to have good separation potential. Another important factor is that intra-crystalline diffusion effects act in a manner that is synergistic with adsorption.

Currently, LTA-4A and LTA-5A are used for selective water pervaporation in membrane processes. There is considerable scope for development of hydrophilic MOFs for water-selective separations from mixtures.

(6) The separation of o-xylene/m-xylene/p-xylene/ethylbenzene mixtures is crucially dependent on the geometry and size of the microporous channels. Ortho-xylene molecules are able to stack optimally, parallel to the 8.5 Å rhombohedric channel walls of MIL-47 and MIL-53; this results in strong selectivity to o-xylene. $AlPO_4$-5 is also selective to o-xylene, because it has the shortest footprint within the 1D channels. MAF-X8 that has larger 10 Å channels allows efficient, commensurate, stacking of p-xylene molecules, resulting in higher saturation capacities. The MOF $Zn_4O(L)_3$ is reported by Mukherjee et al.[95] to dynamically transform its crystal structure to allow optimal packing of p-xylene; it allows practically none of the other C8 aromatics to adsorb. This dynamic MOF needs further experimental investigation.

(7) Pulse chromatographic experiments and simulations of the kind shown in Figure 57b do not reflect molecular packing effects. Rather, these are dictated by adsorption strengths in the Henry regime.

(8) Separations of hexane isomers with AFI, ATS, and CFI zeolites are reliant on the differences in the footprints of linear, branched, and di-branched isomers. More compact di-branched molecules are selectively adsorbed because they have significantly shorter footprints and, consequently, higher saturation capacities. Separation based on differences in molecular footprints could be effectively utilized for separation of mixtures of butenes.[128]

(9) The separation of hexane isomers using MFI zeolites rely on subtle differences in molecular configurations. The linear isomers can locate comfortable along both the straight and zig-zag channels. By contrast, the mono-branched and di-branched isomers experience steric constraints and locate preferentially at the channel intersections that offer more leg-room. Since the number of intersection sites is restricted to 4 per unit cell, the saturation capacities of di-branched isomers

are constrained to 4 molecules per unit cell. The differences in the packing efficiencies results in sharp separations when operating at conditions close to saturation.

(10) Mixtures of chlorofluorcarbons CFC-115 and HFC-125 can be separated using MFI zeolite by relying on the configurational differences that result from the bulky chloride at the 1-position of CFC-115. From leg-room considerations, CFC-115 prefers location at the channel intersections. Consequently, separations at high loadings become selective to HFC-115.

(11) A characteristic feature of many, if not most, separations that are reliant on molecular packing effects is that adsorption and intra-crystalline diffusion are synergistic; this enhances the separation efficiencies in fixed bed adsorbers.

Finally, we must remark that our analysis of separations in this Perspective has been conceptual. In practical applications, other aspects such as stability, regenerability, and costs will come into play in choosing the right adsorbent.

29. Notation

b_A	dual-Langmuir-Freundlich constant for species *i* at adsorption site A, $\mathrm{Pa}^{-\nu_i}$
b_B	dual-Langmuir-Freundlich constant for species *i* at adsorption site B, $\mathrm{Pa}^{-\nu_i}$
c_i	molar concentration of species *i* in gas mixture, mol m^{-3}
c_{i0}	molar concentration of species *i* in gas mixture at inlet to adsorber, mol m^{-3}
$Đ_i$	Maxwell-Stefan diffusivity, m^2 s^{-1}
f_i	partial fugacity of species *i*, Pa
f_t	total fugacity of bulk fluid mixture, Pa
L	length of packed bed adsorber, m
n	number of species in the mixture, dimensionless
N_i	molar flux of species *i*, mol m^{-2} s^{-1}
p_i	partial pressure of species *i* in mixture, Pa
p_t	total system pressure, Pa
q_i	component molar loading of species *i*, mol kg^{-1}
q_t	total molar loading for mixture adsorption, mol kg^{-1}
$q_{i,sat}$	molar loading of species *i* at saturation, mol kg^{-1}
r_c	radius of crystallite, m
R	gas constant, 8.314 J mol^{-1} K^{-1}
S_{ads}	adsorption selectivity, dimensionless
t	time, s
T	absolute temperature, K
u	superficial gas velocity in packed bed, m s^{-1}
v	interstitial gas velocity in packed bed, m s^{-1}

Greek letters

ε	voidage of packed bed, dimensionless
Γ_i	thermodynamic correction factor, dimensionless
θ_t	fractional occupancy for mixture adsorption, dimensionless

Θ_i	loading of species *i*, molecules per unit cage, or per unit cell
Θ_t	total mixture loading, molecules per unit cage, or per unit cell
ν	exponent in dual-Langmuir-Freundlich isotherm, dimensionless
τ	time, dimensionless

Subscripts

i	referring to component *i*
t	referring to total mixture

Table 1. Salient information on zeolite structures.

Zeolite	**Channel or window size/ Å**
AFI	12-ring 1D channels of 7.3 Å size
BEA	Intersecting channels of two sizes: 12-ring of 7.1 Å - 7.3 Å and 10-ring of 5.6 – 5.6 Å
CHA	316.4 $Å^3$ size cages separated by 3.77 Å × 4.23 Å size windows.
DDR	277.8 $Å^3$ size cages separated by 3.65 Å × 4.37 Å size windows
FAU	785.7 $Å^3$ size cages separated by 7.4 Å size windows. The sodalite cages are blocked in simulations and are not accessible to guest molecules; these are excluded for pore volume determination. Cage size is calculated on the basis of the equivalent sphere volume.
FER	10-ring 1D main channels of 4.2 Å -5.4 Å size, connected with 8-ring side pockets of 3.5 Å -4.8 Å size
LTA-Si	743.05 $Å^3$ size cages separated by 4.11 Å × 4.47 Å size windows. The sodalite cages are blocked in simulations and are not accessible to guest molecules.
LTL	12-ring 1D channels of 7.1 Å size
MOR	12-ring 1D main channels of 6.5 Å -7 Å size, connected with 8-ring side pockets of 2.6 Å -5.7 Å size
MFI	10-ring intersecting channels of 5.1 Å – 5.5 Å and 5.3 Å – 5.6 Å size

Table 2. Unit cell dimensions, unit cell volumes, pore volumes of various all-silica zeolites. Also indicated are the framework density, ρ, (expressed as kg per m^3 framework).

Structure	*a* / Å	*b* / Å	*c* / Å	Unit cell volume/ $Å^3$	Fractional pore volume	Pore volume/ cm^3/g	Framework density/ kg/m^3
AFI	23.77	13.73	8.48	2768.52	0.274	0.159	1729.88
BEA	12.66	12.66	26.41	4232.91	0.408	0.271	1508.56
BOG	20.24	23.80	12.80	6163.21	0.374	0.241	1995.52
CHA	15.08	23.91	13.80	4974.57	0.382	0.264	1444.10
DDR	24.01	13.86	40.89	13605.72	0.245	0.139	1759.99
FAU	24.28	24.28	24.28	14313.51	0.439	0.328	1338.37
FER	19.16	14.13	7.49	2026.65	0.283	0.160	1772.33
LTA-Si	24.61	24.61	24.61	14905.10	0.399	0.310	1285.25
MFI	20.02	19.90	13.38	5332.03	0.297	0.165	1796.39
MOR	18.09	20.52	7.52	2793.03	0.285	0.166	1714.69
SOD-Si	8.89	8.89	8.89	702.59	0.241	0.142	1704.10
CFI	13.695	5.021	25.497		0.261	0.1432	1821.03
ATS	13.1483	21.5771	5.1639		0.297	0.1817	1635.37

Table 3. Cage volume for cage-type structures. The cage sizes were calculated after determining the pore volume from molecular simulations; these values are not available in the IZA atlas. Also indicated is the diameter of a equivalent sphere with the same cage volume.

Structure	Pore volume per unit cell/ Å^3	Volume per cage/ Å^3	Cage diameter/ Å
FAU-Si	6285.6	785.7	11.45
LTA-Si	5944.38	743.05	11.23
LTA-4A	5552.0	694	11
LTA-5A	5620.4	702.56	11.03
CHA	1898.40	316.4	8.45
DDR	3333.53	277.8	8.09
TSC = 4 “LTA-cages” and 4 “TSC-supercages”	13182.60	2552.6	16.96
ZIF-8	2336.97	1168.48	13.07

Table 4. Window sizes of cage-type structures. The Foster diameters were obtained using the Delaunay triangulation method described in Fosterr et al.[136].

Structure	d_{min}/ Å	d_{min}/ Å	Foster diameter, d_{Foster} Å
LTA-Si	4.11	4.47	4.11
LTA-4A	4	4.58	4
LTA-5A	4	4.58	4
CHA	3.77	4.23	3.77
DDR	3.65	4.37	3.65
ZIF-8			3.26 (flexible windows)

Table 5. Data on zeolite structures with cations (data on all-silica structures also included for comparison purposes). The number of atoms per unit cell of these structures are specified.

Zeolite	**Si**	**Al**	**Si/Al**	**Na+**	**Ca++**
LTA-5A	96	96	1	32	32
LTA-4A	96	96	1	96	0
NaX	106	86	1.23	86	0
NaY	144	48	3	48	0

Table 6. Unit cell dimensions, unit cell volumes, pore volumes of cation-exchanged zeolites. Also indicated are the framework density, ρ, (expressed as kg per m^3 of (framework +cations)).

Structure	a / Å	b / Å	c / Å	Unit cell volume/ Å^3	Fractional pore volume	Pore volume/ cm^3/g	Framework density/ kg/m^3
NaY (48 Na+)	25.03	25.03	25.03	15677.56	0.41	0.303	1333.2
NaY (54 Na+)	25.03	25.03	25.03	15677.56	0.41	0.303	1347.1
NaX	25.03	25.03	25.03	15677.56	0.40	0.280	1421.28
LTA-5A	24.56	24.56	24.56	14805.39	0.38	0.25	1508.38
LTA-4A	24.56	24.56	24.56	14805.39	0.38	0.25	1529.55

Table 7. Molecular simulations of pore volumes and surface areas for zeolites.

Structure	**Pore volume** / $cm^3\ g^{-1}$	**Surface area** / $m^2\ g^{-1}$	**Delaunay diameter**/ Å
MFI	0.165	487.2	5.16
BEA	0.271	922.7	5.87
MOR	0.166	416.7	7.47
FER	0.160	402.5	6.44
FAU-Si	0.328	1086	4.65
LTA-Si	0.310	896	7.37
CHA	0.264	757.5	3.98
DDR	0.139	350	4.02
CFI	0.1432		
ATS	0.1817		

Table 8. Salient structural information on MOFs and ZIFs.

MOF	**Channel dimensions**
CuBTC	The CuBTC structure consists of two types of "cages" and two types of "windows" separating these cages. Large cages are inter-connected by 9 Å windows of square cross-section. The large cages are also connected to tetrahedral-shaped pockets of ca. 6 Å size through triangular-shaped windows of ca. 4.6 Å size
IRMOF-1	Two alternating, inter-connected, cavities of 10.9 Å and 14.3 Å with window size of 8 Å.
MOF-177	Tetrahedral $[Zn_4O]^{6+}$ units are linked by large, triangular tricarboxylate ligands. Six diamond-shaped channels (upper) with diameter of 10.8 Å surround a pore containing eclipsed BTB^{3-} moieties.
MIL-47	One-dimensional diamond-shaped channels with free internal diameter of ca 8.5 Å
MIL-53 (Cr)-lp	One-dimensional lozenge-shaped channels with free internal diameter of ca 8.5 Å
Zn(bdc)dabco	There exist two types of intersecting channels of about 7.5 Å × 7.5 Å along the *x*-axis and channels of 3.8 Å × 4.7 Å along *y* and *z* axes.
ZIF-8	SOD topology consisting of cages separated by narrow windows of about 0.34 nm size. The volume of each cage is 1168 $Å^3$.
MgMOF-74	One-dimensional hexagonal-shaped channels with free internal diameter of ca. 11 Å
ZnMOF-74	One-dimensional hexagonal-shaped channels with free internal diameter of ca. 11 Å
NiMOF-74	One-dimensional hexagonal-shaped channels with free internal diameter of ca. 11 Å
CoMOF-74	One-dimensional hexagonal-shaped channels with free internal diameter of ca. 11 Å
$Fe_2(BDP)_3$	One-dimensional triangular-shaped channels with free internal diameter of ca. 4.9 Å

Table 9. Unit cell dimensions, unit cell volumes, pore volumes of various MOFs and ZIFs. Also indicated are the framework density, ρ, (expressed as kg per m^3 of framework).

Structure	*a* / Å	*b* / Å	*c* / Å	Unit cell volume/ $Å^3$	Fractional pore volume	Pore volume/ cm^3/g	Framework density/ kg/m^3
CuBTC	26.34	26.34	26.34	18280.82	0.759	0.863	878.83
IRMOF1	25.83	25.83	25.83	17237.49	0.812	1.369	593.21
MOF-177	37.072	37.072	30.033	35745.50	0.840	1.968	426.60
MIL-47	6.81	16.12	13.92	1527.32	0.608	0.606	1004.48
MIL-53 (Cr)-lp	16.73	13.04	6.81	1486.14	0.539	0.518	1041.53
Zn(bdc)dabco	10.93	10.93	9.61	1147.61	0.662	0.801	826.20
ZnMOF-74	25.93	25.93	6.84	3981.47	0.709	0.582	1219.30
MgMOF-74	25.86	25.86	6.91	4005.02	0.708	0.782	905.37
NiMOF-74	25.79	25.79	6.77	3898.34	0.695	0.582	1193.81
CoMOF-74	25.89	25.89	6.80	3949.17	0.707	0.599	1180.26
FeMOF-74	26.16	26.16	6.84	4055.94	0.705	0.626	1126.43
Co(BDP)	13.2529	13.253	13.995	2458.09	0.669	0.927	721.55
$Fe_2(BDP)_3$	7.104	26.49	45.35	8535.33			1145
ZIF-8	16.99	16.99	16.99	4905.20	0.476	0.515	924.25
ZIF-68	26.64	26.64	18.49	11363.62	0.453	0.439	1032.84
ZIF-71	28.55	28.55	28.55	23280.71	0.638	0.736	1154.70

Table 10. Molecular simulations of pore volumes and surface areas for the MOFs, and ZIFs

Structure	**Pore volume** / $cm^3\ g^{-1}$	**Surface area** / $m^2\ g^{-1}$	**Delaunay diameter**/ Å
IRMOF1	1.369	3522.2	7.38
CuBTC	0.848	2097.0	6.23
MIL47	0.606	1472.8	8.03
MIL53(Cr)-lp	0.518	1280.5	7.40
Zn(BDC)dabco	0.801	2022.5	8.32
ZnMOF-74	0.582	1176.0	9.49
MgMOF-74	0.782	1640.0	10.66
NiMOF-74	0.582	1239.0	9.80
CoMOF-74	0.599	1274.0	9.52
FeMOF-74	0.626	1277.3	11.1
Co(BDP)	0.927	2148.8	10
ZIF-8	0.515	1164.7	3.26
ZIF-68	0.439		
ZIF-71	0.736		

Table 11. Dual-site Langmuir-Freundlich parameters for pure component water, and 1-alcohols in CHA at 300 K. The fit parameters are based on the CBMC simulations of pure component isotherms presented in earlier work.[57] Note that the saturation capacities are specified in molecules per cage; multiply these by 1.387 to obtain the values in mol per kg framework.

$$\Theta_i = \Theta_{i,A,sat} \frac{b_{i,A} f_i^{\nu_{i,A}}}{1 + b_{i,A} f_i^{\nu_{i,A}}} + \Theta_{i,B,sat} \frac{b_{i,B} f_i^{\nu_{i,B}}}{1 + b_{i,B} f_i^{\nu_{i,B}}}$$

	Site A			Site B		
	$\Theta_{i,A,sat}$ Molecules cage^{-1}	$b_{i,A}$ $\mathrm{Pa}^{-\nu_i}$	$\nu_{i,A}$ dimensionless	$\Theta_{i,B,sat}$ molecules cage^{-1}	$b_{i,B}$ $\mathrm{Pa}^{-\nu_i}$	$\nu_{i,B}$ dimensionless
methanol	12	7.86×10^{-59}	17	9	8.32×10^{-6}	1
methanol	2.7	6.77×10^{-11}	3.3	2.7	4.45×10^{-4}	1
ethanol	2	7.93×10^{-5}	0.87	2	3.6×10^{-3}	1.14
1-propanol	1	1.28×10^{-2}	1.8	1	9.11×10^{-2}	1
1-butanol	1	0.231	1.46	1	0.5066	1
1-pentanol	0.5	19.26	1.72	0.5	6.91	1
1-hexanol	0.5	2561	2.4	0.5	24.8	1

Table 12. Dual-site Langmuir-Freundlich parameters for adsorption of water, methanol, ethanol, 1-propanol, and 1-butanol at 308 K in ZIF-8. The experimental data are from Zhang et al.[60] These fits are for the "adsorption" branch of the isotherms.

Adsorbate	Site A			Site B		
	$q_{A,sat}$ mol kg^{-1}	b_{A0} $\mathrm{Pa}^{-\nu_A}$	ν_A dimensionless	$q_{B,sat}$ mol kg^{-1}	b_{B0} $\mathrm{Pa}^{-\nu_B}$	ν_B dimensionless
water	3	1.45×10^{-19}	4.8	2	4.3×10^{-4}	0.62
methanol	7	3.58×10^{-39}	10.6	4.7	5.08×10^{-8}	1.8
ethanol	4.5	1.11×10^{-35}	11.6	2	2.92×10^{-6}	1.6
1-propanol	3.1	2.55×10^{-34}	14	1.7	9.9×10^{-9}	3
1-butanol	3	5.49×10^{-31}	17	1.34	1.06×10^{-3}	1.4

Table 13. Dual-site Langmuir-Freundlich parameters for adsorption of 1-alcohols at 323 K in ZIF-68. These fits are based on the experimental isotherm data of van der Perre et al.[62].

Adsorbate	Site A			Site B		
	$q_{A,sat}$ mol kg^{-1}	b_{A0} $\mathrm{Pa}^{-\nu_A}$	ν_A dimensionless	$q_{B,sat}$ mol kg^{-1}	b_{B0} $\mathrm{Pa}^{-\nu_B}$	ν_B dimensionless
methanol	5	1.48×10^{-33}	9	5.5	7.38×10^{-4}	0.75
ethanol	1.8	2.43×10^{-40}	12	4.5	1.58×10^{-3}	0.9
1-propanol	1.2	4.76×10^{-21}	8.5	3.3	7.22×10^{-3}	1
1-butanol	1.1	1.14×10^{-2}	1	2.5	0.384	1
1-pentanol	1	0.129	1	1.9	1.645	1
1-hexanol	2.4	1.5	1	0.08	300000	1

Table 14. Dual-Langmuir-Freundlich fits of the isotherms of water and benzene in CuBTC. These fits are based on the experimental data from Zhao et al.[64], obtained at 288 K, 298 K, 308 K, and 318 K. Note that the fit parameters provided in Table 2 of their paper are incorrect. We have re-fitted the scanned experimental isotherm data of Zhao et al.[64]

	Site A				Site B			
	$q_{A,sat}$ mol kg^{-1}	b_{A0} $\mathrm{Pa}^{-\nu_i}$	E_A kJ mol^{-1}	ν_A dimensionless	$q_{B,sat}$ mol kg^{-1}	b_{B0} $\mathrm{Pa}^{-\nu_i}$	E_B kJ mol^{-1}	ν_B dimensionless
water	20	3.18×10^{-22}	99.6	1.6	60	4.16×10^{-60}	236	5
benzene	2.7	1.7×10^{-8}	35	0.7	7.6	4.93×10^{-8}	5	3

Table 15. Dual-site Langmuir-Freundlich parameters for adsorption of water, methanol, and ethanol at 300 K in all-silica FAU zeolite. The fit parameters are based on the CBMC simulations of pure component isotherms presented in earlier work.[43]

Adsorbate	Site A			Site B		
	$q_{A,sat}$ mol kg^{-1}	b_{A0} $\mathrm{Pa}^{-\nu_A}$	ν_A dimensionless	$q_{B,sat}$ mol kg^{-1}	b_{B0} $\mathrm{Pa}^{-\nu_B}$	ν_B dimensionless
water	16	1.54×10^{-121}	33	4.6	624×10^{-5}	1
methanol	3.4	6.36×10^{-16}	4.6	5.8	1.68×10^{-4}	1
ethanol	2.5	3.19×10^{-13}	4.9	2.9	1×10^{-3}	1.05

Table 16. Dual-site Langmuir-Freundlich parameters for pure component water, methanol, and ethanol at 300 K in all-silica DDR zeolite. The fit parameters are based on the CBMC simulations of pure component isotherms presented in earlier work.[43] Note that the saturation capacities are specified in molecules per cage; multiply these by 0.832157 to obtain the values in mol per kg framework.

	Site A			Site B		
	$\Theta_{i,A,sat}$ Molecules cage^{-1}	$b_{i,A}$ $\mathrm{Pa}^{-\nu_i}$	$\nu_{i,A}$ dimensionless	$\Theta_{i,B,sat}$ molecules cage^{-1}	$b_{i,B}$ $\mathrm{Pa}^{-\nu_i}$	$\nu_{i,B}$ dimensionless
water	8.083	3.85×10^{-16}	4	2.667	1.73×10^{-5}	1
methanol	2.1667	1.49×10^{-4}	1.25	1.9167	6×10^{-4}	0.77
ethanol	1.8167	7.66×10^{-3}	1	0.775	8.59×10^{-6}	1

Table 17. Dual-site Langmuir-Freundlich parameters for adsorption of water, methanol, and ethanol at 300 K in all-silica MFI zeolite. The fit parameters are based on CBMC simulations of Krishna and van Baten.[43]

Adsorbate	Site A			Site B		
	$q_{\mathrm{A,sat}}$ mol kg^{-1}	b_{A0} $\mathrm{Pa}^{-\nu_A}$	ν_{A} dimensionless	$q_{\mathrm{B,sat}}$ mol kg^{-1}	b_{B0} $\mathrm{Pa}^{-\nu_B}$	ν_{B} dimensionless
water	6.7	6.37×10^{-24}	6.2	3.6	1.09×10^{-5}	1.04
methanol	2.4	1×10^{-4}	1.64	1.4	1.92×10^{-3}	0.7
ethanol	1.1	2.82×10^{-4}	2.7	1.7	1.91×10^{-2}	0.9

Table 18. Dual-site Langmuir-Freundlich parameters for adsorption of water, methanol, and ethanol at 300 K in all-silica FER zeolite. The fit parameters are based on unpublished CBMC simulations of pure component isotherms.

Adsorbate	Site A			Site B		
	$q_{\mathrm{A,sat}}$ mol kg^{-1}	b_{A0} $\mathrm{Pa}^{-\nu_A}$	ν_{A} dimensionless	$q_{\mathrm{B,sat}}$ mol kg^{-1}	b_{B0} $\mathrm{Pa}^{-\nu_B}$	ν_{B} dimensionless
water	10	4.44×10^{-47}	10.4	4	9.36×10^{-7}	1
methanol	3.2	8.44×10^{-6}	1.4	1.2	9.24×10^{-4}	0.53
ethanol	1.9	5.86×10^{-4}	1.4	0.9	4.62×10^{-2}	0.26

Table 19. The dual-site Langmuir-Freundlich parameters for unary isotherm for water and ethanol in LTA-4A zeolite. The fit parameters are obtained from the experimental data of Pera-Titus et al.[73], at 305 K, 333 K, 363 K, 393 K, and 423 K.

The *b* parameters are *T*-dependent, $b_A = b_{A0} \exp\left(\frac{E_A}{RT}\right); \quad b_B = b_{B0} \exp\left(\frac{E_B}{RT}\right)$

	Site A				Site B			
	$q_{\mathrm{A,sat}}$ mol kg^{-1}	b_{A0} $\mathrm{Pa}^{-\nu_i}$	E_{A} kJ mol^{-1}	ν_{A} dimensionless	$q_{\mathrm{B,sat}}$ mol kg^{-1}	b_{B0} $\mathrm{Pa}^{-\nu_i}$	E_{B} kJ mol^{-1}	ν_{B} dimensionless
water	2.1	2.1×10^{-60}	269	7.26	9.7	5.81×10^{-8}	33	0.83
ethanol	1.85	5.24×10^{-13}	43.3	1.9	1.4	2.65×10^{-10}	40	1.7

Table 20. Dual-site Langmuir-Freundlich parameters for adsorption of water, and methanol at 298 K in Ce(BTB). These fits are for the "adsorption" branch of the isotherms.[77]

Adsorbate	Site A			Site B		
	$q_{A,sat}$ mol kg^{-1}	b_{A0} $\mathrm{Pa}^{-\nu_A}$	ν_A dimensionless	$q_{B,sat}$ mol kg^{-1}	b_{B0} $\mathrm{Pa}^{-\nu_B}$	ν_B dimensionless
methanol	4	1.49×10^{-51}	13.4	8	1.02×10^{-4}	1
ethanol	1.8	6.67×10^{-20}	5.65	7	1.5×10^{-4}	1

Table 21. Dual-site Langmuir-Freundlich parameters for adsorption of water, methanol, and ethanol at 298 K in CID-1. These fits are for the "adsorption" branch of the isotherms.[78]

Adsorbate	Site A			Site B		
	$q_{A,sat}$ mol kg^{-1}	b_{A0} $\mathrm{Pa}^{-\nu_A}$	ν_A dimensionless	$q_{B,sat}$ mol kg^{-1}	b_{B0} $\mathrm{Pa}^{-\nu_B}$	ν_B dimensionless
water	6.8	2.32×10^{-77}	23.2	0.9	1.18×10^{-4}	1
methanol	1.06	1.37×10^{-51}	16.4	1.45	8.43×10^{-6}	1.8
ethanol	1.3	2.39×10^{-3}	1.43			

Table 22. Dual-site Langmuir-Freundlich parameters for adsorption of water, and methanol at 298 K in Cu-GLA. These fits are for the “adsorption” branch of the isotherms.[79]

Adsorbate	Site A			Site B		
	$q_{A,sat}$ mol kg^{-1}	b_{A0} $\mathrm{Pa}^{-\nu_A}$	ν_A dimensionless	$q_{B,sat}$ mol kg^{-1}	b_{B0} $\mathrm{Pa}^{-\nu_B}$	ν_B dimensionless
water	4.6	3.76×10^{-57}	17.6	0.6	1.18×10^{-4}	1
methanol	1.15	1.26×10^{-34}	16.9	1	7.02×10^{-6}	1.5

Table 23. Dual-site Langmuir-Freundlich parameters for adsorption of water, methanol, ethanol, 1-propanol, and 2-propanol at 298 K in Co(pbdc). These fits are for the “adsorption” branch of the isotherms.[80]

Adsorbate	Site A			Site B		
	$q_{\mathrm{A,sat}}$ mol kg^{-1}	b_{A0} $\mathrm{Pa}^{-\nu_A}$	ν_{A} dimensionless	$q_{\mathrm{B,sat}}$ mol kg^{-1}	b_{B0} $\mathrm{Pa}^{-\nu_B}$	ν_{B} dimensionless
water	3.2	9×10^{-20}	5	3.6	2×10^{-5}	1
methanol	2	1.9×10^{-5}	1.6	2	1.51×10^{-5}	1
ethanol	0.9	9.66×10^{-19}	8.4	1.2	3.71×10^{-5}	1
1-propanol	1.1	7×10^{-4}	1			
2-propanol	0.72	1×10^{-3}	1			

Table 24. Dual-site Langmuir-Freundlich parameters for adsorption of water, methanol, ethanol, 1-propanol, and 2-propanol at 298 K in Zn(II)-MOF.

Adsorbate	Site A			Site B		
	$q_{\mathrm{A,sat}}$ mol kg^{-1}	b_{A0} $\mathrm{Pa}^{-\nu_A}$	ν_{A} dimensionless	$q_{\mathrm{B,sat}}$ mol kg^{-1}	b_{B0} $\mathrm{Pa}^{-\nu_B}$	ν_{B} dimensionless
water	2	6.5×10^{-3}	0.6	10	2.66×10^{-6}	1
methanol	1	1.28×10^{-36}	1	3.5	5.08×10^{-3}	1
ethanol	0.4	2.65×10^{-6}	2.2	1.1	1.25×10^{-6}	1.2
1-propanol	0.3	1.04×10^{-8}	2.7	2.4	1.98×10^{-6}	1
2-propanol	1.2	1×10^{-6}	1			

Table 25. Dual-site Langmuir-Freundlich parameters for adsorption of water, methanol, and ethanol at 298 K in JUC-110. These fits are for the “adsorption” branch of the isotherms. [83]

Adsorbate	Site A			Site B		
	$q_{A,sat}$ mol kg^{-1}	b_{A0} $\mathrm{Pa}^{-\nu_A}$	ν_A dimensionless	$q_{B,sat}$ mol kg^{-1}	b_{B0} $\mathrm{Pa}^{-\nu_B}$	ν_B dimensionless
water	2	3.32×10^{-3}	1.2	4.1	1.18×10^{-4}	1.75
methanol	1.15	5.66×10^{-3}	1	0.85	8.5×10^{-3}	1
ethanol	0.84	1.5×10^{-5}	1			

Table 26. Dual-Langmuir-Freundlich fits of the isotherms of o-xylene, m-xylene, and p-xylene in AFI zeolite. These fits are based on the experimental data from Chiang et al.[91], obtained at temperatures of 303 K, 318 K, and 333 K. These fits are for the "adsorption" branch of the isotherms.[81] The T-dependent parameters b_A, and b_B are $b_A = b_{A0} \exp\left(\frac{E_A}{RT}\right); \quad b_B = b_{B0} \exp\left(\frac{E_B}{RT}\right)$

	Site A				Site B			
	$q_{A,sat}$ mol kg^{-1}	b_{A0} $\mathrm{Pa}^{-\nu_i}$	E_A kJ mol^{-1}	ν_A dimensionless	$q_{B,sat}$ mol kg^{-1}	b_{B0} $\mathrm{Pa}^{-\nu_i}$	E_B kJ mol^{-1}	ν_B dimensionless
o-xylene	0.36	7.4×10^{-21}	113	1.3	0.51	2.2×10^{-3}	6	0.62
m-xylene	0.46	7×10^{-18}	93	1.83	0.47	4.72×10^{-12}	58	0.8
p-xylene	0.6	5.35×10^{-12}	63.5	1.1	0.66	9.77×10^{-11}	48	0.65

Table 27. Dual-site Langmuir-Freundlich parameters C8 hydrocarbons at 433 K in MIL-47(V). The saturation capacities are expressed in molecules per unit cell; these numbers need to be multiplied by the conversion factor of 1.082.

	Site A			Site B		
	$q_{\mathrm{i,A,sat}}$ molecules uc^{-1}	$b_{\mathrm{i,A}}$ $\mathrm{Pa}^{-\nu_{iA}}$	$\nu_{\mathrm{i,A}}$ dimensionless	$q_{\mathrm{i,B,sat}}$ molecules uc^{-1}	$b_{\mathrm{i,B}}$ $\mathrm{Pa}^{-\nu_{iA}}$	$\nu_{\mathrm{i,B}}$ dimensionless
o-xylene	2.8	5.03×10^{-3}	1.08	0.8	3.78×10^{-4}	0.8
m-xylene	2.6	2.48×10^{-3}	1.1	0.8	3.86×10^{-5}	0.9
p-xylene	2.8	3.22×10^{-3}	1.07	0.8	3.23×10^{-5}	0.9
ethylbenzene	0.9	3.94×10^{-4}	0.62	2.2	4.73×10^{-3}	1.05

Table 28. Dual-site Langmuir-Freundlich parameters for C8 hydrocarbons at 433 K in MIL-53(Al). The saturation capacities are expressed in molecules per unit cell; these numbers need to be multiplied by the conversion factor of 1.0724.

	Site A			Site B		
	$q_{\mathrm{i,A,sat}}$ molecules uc^{-1}	$b_{\mathrm{i,A}}$ $\mathrm{Pa}^{-\nu_{iA}}$	$\nu_{\mathrm{i,A}}$ dimensionless	$q_{\mathrm{i,B,sat}}$ molecules uc^{-1}	$b_{\mathrm{i,B}}$ $\mathrm{Pa}^{-\nu_{iA}}$	$\nu_{\mathrm{i,B}}$ dimensionless
o-xylene	2.2	7.22×10^{-3}	1.05	0.74	2.21×10^{-4}	0.74
m-xylene	1.9	5.01×10^{-3}	1	0.9	7.44×10^{-5}	0.74
p-xylene	2	5.34×10^{-3}	1.06	0.81	1.47×10^{-4}	0.8
ethylbenzene	0.65	6.02×10^{-5}	0.79	2	6.97×10^{-3}	1

Table 29. Dual-site Langmuir-Freundlich parameters for C8 hydrocarbons at 433 K in MAF-X8.

	Site A			Site B		
	$q_{\mathrm{i,A,sat}}$ mol kg^{-1}	$b_{\mathrm{i,A}}$ $\mathrm{Pa}^{-\nu_{iA}}$	$\nu_{\mathrm{i,A}}$ dimensionless	$q_{\mathrm{i,B,sat}}$ mol kg^{-1}	$b_{\mathrm{i,B}}$ $\mathrm{Pa}^{-\nu_{iA}}$	$\nu_{\mathrm{i,B}}$ dimensionless
o-xylene	1.55	1.33	0.42	1.75	5.72×10^{6}	1.1
m-xylene	1.4	1.24×10	0.6	1.85	2.24×10^{6}	1.06
p-xylene	1.55	1.33×10	0.54	1.75	5.12×10^{7}	1.2
ethylbenzene	1.4	11	0.74	1.3	3.76×10^{4}	1

Table 30. Dual-site Langmuir-Freundlich parameters for pure component hexane isomers at 433 K in ATS.

	Site A			Site B		
	$q_{\mathrm{i,A,sat}}$ mol kg^{-1}	$b_{\mathrm{i,A}}$ $\mathrm{Pa}^{-\nu_{iA}}$	$\nu_{\mathrm{i,A}}$ dimensionless	$q_{\mathrm{i,B,sat}}$ mol kg^{-1}	$b_{\mathrm{i,B}}$ $\mathrm{Pa}^{-\nu_{iA}}$	$\nu_{\mathrm{i,B}}$ dimensionless
nC6	0.82	2.21×10^{-4}	1	0.54	9.78×10^{-7}	1
2MP	0.95	3.82×10^{-4}	1	0.37	6.41×10^{-7}	1
3MP	0.98	3.17×10^{-4}	1	0.285	4.34×10^{-7}	1
22DMB	1.03	2.57×10^{-4}	1	0.18	1.1×10^{-7}	1
23DMB	1.03	5.91×10^{-4}	1	0.2	3.11×10^{-7}	1

Table 31. Dual-site Langmuir-Freundlich parameters for pure component hexane isomers at 433 K in CFI.

	Site A			Site B		
	$q_{\mathrm{i,A,sat}}$ mol kg^{-1}	$b_{\mathrm{i,A}}$ $\mathrm{Pa}^{-\nu_{iA}}$	$\nu_{\mathrm{i,A}}$ dimensionless	$q_{\mathrm{i,B,sat}}$ mol kg^{-1}	$b_{\mathrm{i,B}}$ $\mathrm{Pa}^{-\nu_{iA}}$	$\nu_{\mathrm{i,B}}$ dimensionless
nC6	0.25	2.92×10^{-8}	1	0.59	3.41×10^{-4}	1
2MP	0.22	5.07×10^{-7}	1	0.61	7.71×10^{-4}	1
3MP	0.18	7.59×10^{-6}	1	0.65	8.03×10^{-4}	1
22DMB	0.11	2.65×10^{-5}	1	0.73	1.02×10^{-3}	1
23DMB	0.83	1.96×10^{-3}	1			

Table 32. Dual-site Langmuir-Freundlich parameters for pure component isotherms for nC6 and 2MP in MFI at 298 K.

	Site A			Site B		
	$\Theta_{i,A,sat}$ molecules uc^{-1}	$b_{i,A}$ $Pa^{-\nu_i}$	$\nu_{i,A}$ dimensionless	$\Theta_{i,B,sat}$ molecules uc^{-1}	$b_{i,B}$ $Pa^{-\nu_i}$	$\nu_{i,B}$ dimensionless
nC6	6.6	0.708	0.83	1.4	16.6	1.5
2MP	4	4.51	1.05	4	7.92×10^{-6}	1.13

Table 33. Molar masses and boiling points of C4 hydrocarbons.

	Molar mass mol g^{-1}	Boiling point K
iso-butane (2-methylpropane)	58.124	261.45
iso-butene (= 2-methylpropene)	56.108	266.25
1-butene	56.108	266.85
1,3 butadiene	54.092	268.75
normal butane	58.124	272.65
trans-2-butene	56.108	273.45
cis-2-butene	56.108	276.85

Table 34. Dual-site Langmuir-Freundlich parameters for isotherms of CFC-115, and HFC-125 in MFI zeolite and in Vruf Activated Carbon. Fits of the experimental isotherm data in the paper of Peng et al.[129], measured at temperatures of 273 K, 298 K, 323 K, and 348 K. The *b*-parameters are *T*-dependent,

$$b_A = b_{A0} \exp\left(\frac{E_A}{RT}\right); \quad b_B = b_{B0} \exp\left(\frac{E_B}{RT}\right)$$

	Site A				Site B			
	$q_{\mathrm{A,sat}}$ mol kg^{-1}	b_{A0} $\mathrm{Pa}^{-\nu_i}$	E_{A} kJ mol^{-1}	ν_{A} dimensionless	$q_{\mathrm{B,sat}}$ mol kg^{-1}	b_{B0} $\mathrm{Pa}^{-\nu_i}$	E_{B} kJ mol^{-1}	ν_{B} dimensionless
CFC-115/ MFI	1	1.86×10^{-15}	57	1.1	0.69346	1.2×10^{-10}	45	1
HFC-125/ MFI	0.2	5.85×10^{-38}	173	1.88	1.8	7.56×10^{-11}	40	1
CFC-115/ Vruf AC	5.2	9.5×10^{-8}	22	0.7	0.4	1.61×10^{-9}	39	0.82
HFC-125/ Vruf AC	6.4	3×10^{-8}	21.4	0.75	0.4	7.73×10^{-10}	39	0.8

Table 35. Dual-Langmuir-Freundlich fits of the isotherms of benzene, toluene, p-xylene, and ethylbenzene in MFI zeolite. These fits are based on the experimental data from Lee et al.[130] The *b*-parameters are *T*-dependent, $b_A = b_{A0} \exp\left(\frac{E_A}{RT}\right)$; $b_B = b_{B0} \exp\left(\frac{E_B}{RT}\right)$

	Site A				Site B			
	$q_{\mathrm{A,sat}}$ mol kg^{-1}	b_{A0} $\mathrm{Pa}^{-\nu_i}$	E_{A} kJ mol^{-1}	ν_{A} dimensionless	$q_{\mathrm{B,sat}}$ mol kg^{-1}	b_{B0} $\mathrm{Pa}^{-\nu_i}$	E_{B} kJ mol^{-1}	ν_{B} dimensionless
benzene	0.69346	2×10^{-43}	187	3.4	0.69346	3.12×10^{-14}	69	1.5
toluene	0.69346	9.1×10^{-20}	95	2.8	0.6	6.32×10^{-21}	91	1.7
p-xylene	0.69346	2.18×10^{-16}	94	1.7	0.69346	5.42×10^{-63}	330	5
Ethyl benzene	0.26	1.99×10^{-38}	178	2.7	0.79	7.79×10^{-17}	84	1.6

30. References

(1) Hamon, L.; Jolimaître, E.; Pirngruber, G. D. CO_2 and CH_4 Separation by Adsorption Using Cu-BTC Metal-Organic Framework, *Ind. Eng. Chem. Res.* **2010**, *49*, 7497–7503.

(2) Wu, H.; Yao, K.; Zhu, Y.; Li, B.; Shi, Z.; Krishna, R.; Li, J. Cu-TDPAT, an *rht*-type Dual-Functional Metal–Organic Framework Offering Significant Potential for Use in H_2 and Natural Gas Purification Processes Operating at High Pressures, *J. Phys. Chem. C* **2012**, *116*, 16609-16618.

(3) Mason, J. A.; Sumida, K.; Herm, Z. R.; Krishna, R.; Long, J. R. Evaluating Metal-Organic Frameworks for Post-Combustion Carbon Dioxide Capture via Temperature Swing Adsorption, *Energy Environ. Sci.* **2011**, *4*, 3030-3040.

(4) Herm, Z. R.; Swisher, J. A.; Smit, B.; Krishna, R.; Long, J. R. Metal-Organic Frameworks as Adsorbents for Hydrogen Purification and Pre-Combustion Carbon Dioxide Capture *J. Am. Chem. Soc.* **2011**, *133*, 5664-5667.

(5) Belmabkhout, Y.; Pirngruber, G.; Jolimaitre, E.; Methivier, A. A complete experimental approach for synthesis gas separation studies using static gravimetric and column breakthrough experiments, *Adsorption* **2007**, *13*, 341-349.

(6) Krishna, R. A Smörgåsbord of Separation Strategies using Microporous Crystalline Materials, *Indian Chem. Eng.* **2014**, *56*, 147-174.

(7) Rege, S. U.; Yang, R. T. Limits for Air Separation by Adsorption with LiX Zeolite, *Ind. Eng. Chem. Res.* **1997**, *36*, 5358-5365.

(8) Liu, J.; Thallapally, P. K.; Strachan, D. Metal−Organic Frameworks for Removal of Xe and Kr from Nuclear Fuel Reprocessing Plants, *Langmuir* **2012**, *28*, 11584-11589.

(9) Liu, J.; Strachan, D. M.; Thallapally, P. K. Enhanced noble gas adsorption in Ag@MOF-74Ni, *Chem. Commun.* **2014**, *50*, 466-468.

(10) Gurdal, Y.; Keskin, S. Atomically Detailed Modeling of Metal Organic Frameworks for Adsorption, Diffusion, and Separation of Noble Gas Mixtures, *Ind. Eng. Chem. Res.* **2012**, *51*, 7373-8382.

(11) Saint-Remi, J. C.; Rémy, T.; van Huskeren, V.; van de Perre, S.; Duerinck, T.; Maes, M.; De Vos, D. E.; Gobechiya, E.; Kirschhock, C. E. A.; Baron, G. V.; Denayer, J. F. M. Biobutanol Separation with the Metal–Organic Framework ZIF-8, *ChemSusChem* **2011**, *4*, 1074-1077.

(12) Krishna, R. The Maxwell-Stefan Description of Mixture Diffusion in Nanoporous Crystalline Materials, *Microporous Mesoporous Mater.* **2014**, *185*, 30-50.

(13) Minceva, M.; Rodrigues, A. E. Understanding and Revamping of Industrial Scale SMB Units for p-Xylene Separation, *A.I.Ch.E.J.* **2007**, *53*, 138-149.

(14) Minceva, M.; Rodrigues, A. E. Adsorption of xylenes on Faujasite-type zeolite. Equilibrium and Kinetics in Batch Adsorber, *Chem. Eng. Res. Des.* **2004**, *82*, 667-681.

(15) Baerlocher, C.; McCusker, L. B. Database of Zeolite Structures, http://www.iza-structure.org/databases/, International Zeolite Association, 10 January 2002.

(16) Düren, T.; Millange, F.; Férey, G.; Walton, K. S.; Snurr, R. Q. Calculating Geometric Surface Areas as a Characterization Tool for Metal-Organic Frameworks, *J. Phys. Chem. C* **2007**, *111*, 15350-15356.

(17) Dubbeldam, D.; Walton, K. S.; Ellis, D. E.; Snurr, R. Q. Exceptional Negative Thermal Expansion in Isoreticular Metal–Organic Frameworks, *Angew. Chem. Int. Ed.* **2007**, *46*, 4496-4499.

(18) Dubbeldam, D.; Frost, H.; Walton, K. S.; Snurr, R. Q. Molecular simulation of adsorption sites of light gases in the metal-organic framework IRMOF-1, *Fluid Phase Equilib.* **2007**, *261*, 152-161.

(19) Chui, S. S. Y.; Lo, S. M. F.; Charmant, J. P. H.; Orpen, A. G.; Williams, I. D. A chemically functionalizable nanoporous material $[Cu_3(TMA)_2(H2O)_3]_n$, *Science* **1999**, *283*, 1148-1150.

(20) Yang, Q.; Zhong, C. Electrostatic-Field-Induced Enhancement of Gas Mixture Separation in Metal-Organic Frameworks: A Computational Study, *ChemPhysChem* **2006**, *7*, 1417-1421.

(21) Bárcia, P. S.; Zapata, F.; Silva, J. A. C.; Rodrigues, A. E.; Chen, B. Kinetic Separation of Hexane Isomers by Fixed-Bed Adsorption with a Microporous Metal-Organic Framework, *J. Phys. Chem. B* **2008**, *111*, 6101-6103.

(22) Lee, J. Y.; Olson, D. H.; Pan, L.; Emge, T. J.; Li, J. Microporous Metal–Organic Frameworks with High Gas Sorption and Separation Capacity, *Adv. Funct. Mater.* **2007**, *17*, 1255-1262.

(23) Alaerts, L.; Kirschhock, C. E. A.; Maes, M.; van der Veen, M.; Finsy, V.; Depla, A.; Martens, J. A.; Baron, G. V.; Jacobs, P. A.; Denayer, J. F. M.; De Vos, D. Selective Adsorption and Separation of Xylene Isomers and Ethylbenzene with the Microporous Vanadium(IV) Terephthalate MIL-47, *Angew. Chem. Int. Ed.* **2007**, *46*, 4293-4297.

(24) Finsy, V.; Verelst, H.; Alaerts, L.; De Vos, D.; Jacobs, P. A.; Baron, G. V.; Denayer, J. F. M. Pore-Filling-Dependent Selectivity Effects in the Vapor-Phase Separation of Xylene Isomers on the Metal-Organic Framework MIL-47, *J. Am. Chem. Soc.* **2008**, *130*, 7110-7118.

(25) Barthelet, K.; Marrot, J.; Riou, D.; Férey, G. A Breathing Hybrid Organic - Inorganic Solid with Very Large Pores and High Magnetic Characteristics, *Angew. Chem. Int. Ed.* **2007**, *41*, 281-284.

(26) Coombes, D. S.; Corà, F.; Mellot-Draznieks, C.; Bell, R. G. Sorption-Induced Breathing in the Flexible Metal Organic Framework CrMIL-53: Force-Field Simulations and Electronic Structure Analysis, *J. Phys. Chem. C* **2009**, *113*, 544-552.

(27) Britt, D.; Furukawa, H.; Wang, B.; Glover, T. G.; Yaghi, O. M. Highly efficient separation of carbon dioxide by a metal-organic framework replete with open metal sites, *Proc. Natl. Acad. Sci. U.S.A.* **2009**, *106*, 20637-20640.

(28) Rosi, N. L.; Kim, J.; Eddaoudi, M.; Chen, B.; O'Keeffe, M.; Yaghi, O. M. Rod Packings and Metal-Organic Frameworks Constructed from Rod-Shaped Secondary Building Units, *J. Am. Chem. Soc.* **2005**, *127*, 1504-1518.

(29) Dietzel, P. D. C.; Panella, B.; Hirscher, M.; Blom, R.; Fjellvåg, H. Hydrogen adsorption in a nickel based coordination polymer with open metal sites in the cylindrical cavities of the desolvated framework, *Chem. Commun.* **2006**, 959-961.

(30) Dietzel, P. D. C.; Besikiotis, V.; Blom, R. Application of metal–organic frameworks with coordinatively unsaturated metal sites in storage and separation of methane and carbon dioxide, *J. Mater. Chem.* **2009**, *19*, 7362-7370.

(31) Caskey, S. R.; Wong-Foy, A. G.; Matzger, A. J. Dramatic Tuning of Carbon Dioxide Uptake via Metal Substitution in a Coordination Polymer with Cylindrical Pores, *J. Am. Chem. Soc.* **2008**, *130*, 10870-10871.

(32) Yazaydın, A. Ö.; Snurr, R. Q.; Park, T. H.; Koh, K.; Liu, J.; LeVan, M. D.; Benin, A. I.; Jakubczak, P.; Lanuza, M.; Galloway, D. B.; Low, J. J.; Willis, R. R. Screening of Metal-Organic Frameworks for Carbon Dioxide Capture from Flue Gas using a Combined Experimental and Modeling Approach, *J. Am. Chem. Soc.* **2009**, *131*, 18198-18199.

(33) Bloch, E. D.; Murray, L.; Queen, W. L.; Chavan, S. M.; Maximoff, S. N.; Bigi, J. P.; Krishna, R.; Peterson, V. K.; Grandjean, F.; Long, G. J.; Smit, B.; Bordiga, S.; Brown, C. M.; Long, J. R. Selective Binding of O_2 over N_2 in a Redox-Active Metal-Organic Framework with Open Iron(II) Coordination Sites, *J. Am. Chem. Soc.* **2011**, *133*, 14814-14822.

(34) Herm, Z. R.; Wiers, B. M.; Van Baten, J. M.; Hudson, M. R.; Zajdel, P.; Brown, C. M.; Maschiocchi, N.; Krishna, R.; Long, J. R. Separation of Hexane Isomers in a Metal-Organic Framework with Triangular Channels *Science* **2013**, *340*, 960-964.

(35) Choi, H. J.; Dincă, M.; Long, J. R. Broadly Hysteretic H_2 Adsorption in the Microporous Metal-Organic Framework Co(1,4-benzenedipyrazolate), *J. Am. Chem. Soc.* **2008**, *130*, 7848-7850.

(36) Salles, F.; Maurin, G.; Serre, C.; Llewellyn, P. L.; Knöfel, C.; Choi, H. J.; Filinchuk, Y.; Oliviero, L.; Vimont, A.; Long, J. R.; Férey, G. Multistep N_2 Breathing in the Metal-Organic Framework Co(1,4-benzenedipyrazolate), *J. Am. Chem. Soc.* **2010**, *132*, 13782-13788.

(37) Banerjee, R.; Phan, A.; Wang, B.; Knobler, C.; Furukawa, H.; O'Keeffe, M.; Yaghi, O. M. High-Throughput Synthesis of Zeolitic Imidazolate Frameworks and Application to CO_2 Capture, *Science* **2008**, *319*, 939-943.

(38) Krishna, R. Diffusion in Porous Crystalline Materials, *Chem. Soc. Rev.* **2012**, *41*, 3099-3118.

(39) Siepmann, J. I.; Martin, M. G.; Mundy, C. J.; Klein, M. L. Intermolecular potentials for branched alkanes and the vapour-liquid phase equilibria of n-heptane, 2-methylhexane, and 3-ethylpentane, *Mol. Phys.* **1997**, *90*, 687-693.

(40) Dubbeldam, D.; Calero, S.; Vlugt, T. J. H.; Krishna, R.; Maesen, T. L. M.; Smit, B. United Atom Forcefield for Alkanes in Nanoporous Materials, *J. Phys. Chem. B* **2004**, *108*, 12301-12313.

(41) Dubbeldam, D.; Krishna, R.; Calero, S.; Yazaydın, A. Ö. Computer-Assisted Screening of Ordered Crystalline Nanoporous Adsorbents for Separation of Alkane Isomers, *Angew. Chem. Int. Ed.* **2012**, *51*, 11867-11871.

(42) Bezus, A. G.; Kiselev, A. V.; Lopatkin, A. A.; Du, P. Q. Molecular statistical calculation of the thermodynamic adsorption characteristics of zeolites using the atom-atom approximation. Part 1. Adsorption of methane by zeolite sodium-X, *J.Chem.Soc., Faraday Trans. II* **1978**, *74*, 367-379.

(43) Krishna, R.; van Baten, J. M. Hydrogen bonding effects in adsorption of water-alcohol mixtures in zeolites and the consequences for the characteristics of the Maxwell-Stefan diffusivities, *Langmuir* **2010**, *26*, 10854-10867.

(44) Krishna, R.; van Baten, J. M. In Silico Screening of Zeolite Membranes for CO_2 Capture, *J. Membr. Sci.* **2010**, *360*, 323-333.

(45) Krishna, R.; van Baten, J. M. Highlighting Pitfalls in the Maxwell-Stefan Modeling of Water-Alcohol Mixture Permeation across Pervaporation Membranes, *J. Membr. Sci.* **2010**, *360*, 476-482.

(46) Krishna, R.; van Baten, J. M. Mutual slowing-down effects in mixture diffusion in zeolites, *J. Phys. Chem. C* **2010**, *114*, 13154-13156.

(47) Torres-Knoop, A.; Krishna, R.; Dubbeldam, D. Separating Xylene Isomers by Commensurate Stacking of p-Xylene within Channels of MAF-X8, *Angew. Chem. Int. Ed.* **2014**, *53*, 7774-7778.

(48) Vlugt, T. J. H.; Krishna, R.; Smit, B. Molecular Simulations of Adsorption Isotherms for Linear and Branched Alkanes and Their Mixtures in Silicalite, *J. Phys. Chem. B* **1999**, *103*, 1102-1118.

(49) Frenkel, D.; Smit, B. Understanding Molecular Simulations: From Algorithms to Applications; 2nd Edition, Academic Press: San Diego, 2002.

(50) Krishna, R. Describing the diffusion of guest molecules inside porous structures, *J. Phys. Chem. C* **2009**, *113*, 19756-19781.

(51) Bloch, E. D.; Queen, W. L.; Krishna, R.; Zadrozny, J. M.; Brown, C. M.; Long, J. R. Hydrocarbon Separations in a Metal-Organic Framework with Open Iron(II) Coordination Sites, *Science* **2012**, *335*, 1606-1610.

(52) Gücüyener, C.; van den Bergh, J.; Gascon, J.; Kapteijn, F. Ethane/Ethene Separation Turned on Its Head: Selective Ethane Adsorption on the Metal-Organic Framework ZIF-7 through a Gate-Opening Mechanism, *J. Am. Chem. Soc.* **2010**, *132*, 17704-17706.

(53) Yang, J.; Krishna, R.; Li, J.; Li, J. Experiments and Simulations on Separating a CO_2/CH_4 Mixture using K-KFI at Low and High Pressures, *Microporous Mesoporous Mater.* **2014**, *184*, 21-27.

(54) Krishna, R.; Long, J. R. Screening metal-organic frameworks by analysis of transient breakthrough of gas mixtures in a fixed bed adsorber, *J. Phys. Chem. C* **2011**, *115*, 12941-12950.

(55) Krishna, R.; Baur, R. Modelling issues in zeolite based separation processes, *Sep. Purif. Technol.* **2003**, *33*, 213-254.

(56) Myers, A. L.; Prausnitz, J. M. Thermodynamics of mixed gas adsorption, *A.I.Ch.E.J.* **1965**, *11*, 121-130.

(57) Krishna, R.; van Baten, J. M. Entropy-based separation of linear chain molecules by exploiting differences in the saturation capacities in cage-type zeolites, *Sep. Purif. Technol.* **2011**, *76*, 325-330.

(58) Remy, T.; Saint-Remi, J. C.; Singh, R.; Webley, P. A.; Baron, G. V.; Denayer, J. F. M. Adsorption and Separation of C1-C8 Alcohols on SAPO-34, *J. Phys. Chem. C* **2011**, *115*, 8117-8125.

(59) Titze, T.; Chmelik, C.; Kärger, J.; van Baten, J. M.; Krishna, R. Uncommon Synergy Between Adsorption and Diffusion of Hexane Isomer Mixtures in MFI Zeolite Induced by Configurational Entropy Effects *J. Phys. Chem. C* **2014**, *116*, 2660-2665.

(60) Zhang, K.; Lively, R. P.; Dose, M. E.; Brown, A. J.; Zhang, C.; Chung, J.; Nair, S.; Koros, W. J.; Chance, R. R. Alcohol and water adsorption in zeolitic imidazolate frameworks, *Chem. Commun.* **2013**, *49*, 3245-3247.

(61) Sun, J.-K.; Min Ji, M.; Chen, C.; Wang, W.-G.; Wang, P.; Chen, R.-P.; Zhang, J. A charge-polarized porous metal–organic framework for gas chromatographic separation of alcohols from water, *Chem. Commun.* **2013**, *49*, 1624-1626.

(62) Van der Perre, S.; Van Assche, T.; Bozbiyik, B.; Lannoeye, J.; De Vos, D. E.; Baron, G. V.; Denayer, J. F. M. Adsorptive characterization of the ZIF-68 Metal-Organic Framework: a complex structure with amphiphilic properties., *Langmuir* **2014**, *30*, 8416-8424.

(63) Chmelik, C.; Kärger, J.; Wiebcke, M.; Caro, J.; van Baten, J. M.; Krishna, R. Adsorption and Diffusion of Alkanes in CuBTC Crystals Investigated Using Infrared Microscopy and Molecular Simulations, *Microporous Mesoporous Mater.* **2009**, *117*, 22-32.

(64) Zhao, Z.; Wang, S.; Yang, Y.; Li, X.; Li, J.; Li, Z. Competitive Adsorption and Selectivity of Benzene and Water Vapor on the Microporous Metal Organic Frameworks (HKUST-1), *Chem. Eng. J.* **2015**, *259*, 79-89.

(65) Kärger, J.; Binder, T.; Chmelik, C.; Hibbe, F.; Krautscheid, H.; Krishna, R.; Weitkamp, J. Microimaging of transient guest profiles to monitor mass transfer in nanoporous materials, *Nature Materials* **2014**, *13*, 333-343.

(66) Nalaparaju, A.; Zhao, X. S.; Jiang, J. W. Molecular Understanding for the Adsorption of Water and Alcohols in Hydrophilic and Hydrophobic Zeolitic Metal-Organic Frameworks, *J. Phys. Chem. C* **2010**, *114*, 11542-11550.

(67) Pluth, J. J.; Smith, J. V. Accurate redetermination of crystal structure of dehydrated zeolite A. Absence of near zero coordination of sodium. Refinement of silicon,aluminum-ordered superstructure, *J. Am. Chem. Soc.* **1980**, *102*, 4704-4708.

(68) García-Sánchez, A.; García-Pérez, E.; Dubbeldam, D.; Krishna, R.; Calero, S. A Simulation Study of Alkanes in Linde Type A Zeolites, *Adsorpt. Sci. Technol.* **2007**, *25*, 417-427.

(69) Hedin, N.; DeMartin, G. J.; Roth, W. J.; Strohmaier, K. G.; Reyes, S. C. PFG NMR self-diffusion of small hydrocarbons in high silica DDR, CHA and LTA structures, *Microporous Mesoporous Mater.* **2008**, *109*, 327-334.

(70) Hedin, N.; DeMartin, G. J.; Strohmaier, K. G.; Reyes, S. C. PFG NMR self-diffusion of propylene in ITQ-29, CaA and NaCaA: Window size and cation effects, *Microporous Mesoporous Mater.* **2007**, *98*, 182-188.

(71) Fritzsche, S.; Haberlandt, R.; Kärger, J.; Pfeifer, H.; Heinzinger, K.; Wolfsberg, M. Influence of Exchangeable Cations on the Diffusion of Neutral Diffusants in Zeolites of Type LTA - an MD Study, *Chem. Phys. Lett.* **1995**, *242*, 361-366.

(72) Simo, M.; Sivashanmugam, S.; Brown, C. J.; Hlavacek, V. Adsorption/Desorption of Water and Ethanol on 3A Zeolite in Near-Adiabatic Fixed Bed, *Ind Eng Chem Res* **2009**, *48*, 9257-9260.

(73) Pera-Titus, M.; Fité, C.; Sebastián, V.; Lorente, E.; Llorens, J.; Cunill, F. Modeling Pervaporation of Ethanol/Water Mixtures within 'Real' Zeolite NaA Membranes, *Ind. Eng. Chem. Res.* **2008**, *47*, 3213-3224.

(74) Plessius, R.; Kromhout, R.; Ramos, A. L. D.; Ferbinteanu, M.; Mittelmeijer-Hazeleger, M. C.; Krishna, R.; Rothenberg, G.; Tanase, S. Highly selective water adsorption in a lanthanum metal-organic framework, *Chem. Eur. J.* **2014**, *20*, 7922-7925.

(75) Uchida, S.; Mizuno, N. Zeotype Ionic Crystal of $Cs_5[Cr_3O(OOCH)_6(H_2O)_3][\alpha\text{-}CoW_{12}O_{40}]$-$7.5H_2O$ with Shape-Selective Adsorption of Water, *J. Am. Chem. Soc.* **2004**, *126*, 1602-1603.

(76) Efthymiou, C. G.; Kyprianidou, E. J.; Milios, C. J.; Manos, M. J.; Tasiopoulos, A. J. Flexible lanthanide MOFs as highly selective and reusable liquid MeOH sorbents, *J. Mater. Chem. A* **2013**, *1*, 5061-5069.

(77) Lin, Z.; Zou, R.; Liang, J.; Xia, W.; Xia, D.; Wang, Y.; Lin, J.; Hu, T.; Chen, Q.; Wang, X.; Zhao, Y.; Burrell, A. K. Pore size-controlled gases and alcohols separation within ultramicroporous homochiral lanthanide–organic frameworks, *J. Mater. Chem.* **2012**, *22*, 7813-7818.

(78) Horike, S.; Tanaka, D.; Nakagawa, K.; Kitagawa, S. Selective guest sorption in an interdigitated porous framework with hydrophobic pore surfaces{, *Chem. Commun.* **2007**, 3395-3397.

(79) Chen, B.; Ji, Y.; Xue, M.; Fronczek, F. R.; Hurtado, E. J.; Mondal, J. U.; Liang, C.; Dai, S. Metal-Organic Framework with Rationally Tuned Micropores for Selective Adsorption of Water over Methanol, *Inorg. Chem.* **2008**, *47*, 5543-5545.

(80) Zheng, X.; Zhou, L.; Huang, Y.; Wang, C.; Duan, J.; Wen, L.; Tian, Z.; Li, D. A Series of Metal-Organic Frameworks Based on 5-(4-Pyridyl)-Isophthalic Acid: Selective Sorption and Fluorescence Sensing, *J. Mater. Chem. A* **2014**, *2*, 12413-12422.

(81) Zheng, X.; Huang, Y.; Duan, J.; Wang, C.; Wen, L.; Zhao, J.; Li, D. A microporous Zn(II)–MOF with open metal sites: structure and selective adsorption properties, *Dalton Trans.* **2014**, *43*, 8311-8317.

(82) Gu, J.-Z.; Lu, W.-G.; Jiang, L.; Zhou, H. C.; Lu, T.-B. 3D Porous Metal-Organic Framework Exhibiting Selective Adsorption of Water over Organic Solvents, *Inorg. Chem.* **2007**, *46*, 5835-5837.

(83) Borjigin, T.; Sun, F.; Zhang, J.; Cai, K.; Ren, H.; Zhu, G. S. A microporous metal–organic framework with high stability for GC separation of alcohols from water, *Chem. Commun.* **2012**, *48*, 7613-7615.

(84) Minceva, M.; Rodrigues, A. E. Modeling and Simulation of a Simulated Moving Bed for the Separation of *p*-Xylene, *Ind. Eng. Chem. Res.* **2002**, *41*, 3454-3461.

(85) Peralta, D.; Barthelet, K.; Pérez-Pellitero, J.; Chizallet, C.; Chaplais, G.; Simon-Masseron, A.; Pirngruber, G. D. Adsorption and Separation of Xylene Isomers: CPO-27-Ni vs HKUST-1 vs NaY, *J. Phys. Chem. C* **2012**, *116*, 21844-21855.

(86) Kulprathipanja, S. Zeolites in Industrial Separation and Catalysis; Wiley-VCH: Weinheim, 2010.

(87) El Osta, R.; Carlin-Sinclair, A.; Guillou, N.; Walton, R. I.; Vermoortele, F.; Maes, M.; De Vos, D.; Millange, F. Liquid-Phase Adsorption and Separation of Xylene Isomers by the Flexible Porous Metal−Organic Framework MIL-53(Fe), *Chem. Mater.* **2012**, *24*, 2781-2791.

(88) Remy, T.; Baron, G. V.; Denayer, J. F. M. Modeling the Effect of Structural Changes during Dynamic Separation Processes on MOFs, *Langmuir* **2011**, *27*, 13064-13071.

(89) Niekiel, F.; Lannoeye, J.; Reinsch, H.; Munn, A. S.; Heerwig, A.; Zizak, I.; Kaskel, S.; Walton, R. I.; de Vos, D.; Llewellyn, P.; Lieb, A.; Maurin, G.; Stock, N. Conformation-Controlled Sorption Properties and Breathing of the Aliphatic Al-MOF [Al(OH)(CDC)], *Inorg. Chem.* **2012**, *53*, 4610-4620.

(90) Fang, Z. L.; Zheng, S. R.; Tan, J. B.; Cai, S. L.; Fan, J.; Yan, X.; Zhang, W. G. Tubular metal–organic framework-based capillary gas chromatography column for separation of alkanes and aromatic positional isomers, *J. Chromatogr. A* **2013**, *1285*, 132-138.

(91) Chiang, A. S. T.; Lee, C.-K.; Chang, Z.-H. Adsorption and diffusion of aromatics in $AlPO_4$-5, *Zeolites* **1991**, 380-386.

(92) Hu, E.; Derebe, A. T.; Almansoori, A.; Wang, K. Xylene Separation on Plate-Like SAPO-5 Zeolite Molecular Sieves, *Int. Journal. Materials Sci. Eng.* **2014**, *2*, 10-14.

(93) Hu, E.; Lai, Z.; Wang, K. Adsorption Properties of the SAPO-5 Molecular Sieve, *J. Chem. Eng. Data* **2010**, *55*, 3286-3289.

(94) Rosenfeld, D. D.; Barthomeuf, D. M., Separation of Ortho Aromatic Isomers by Selective Adsorption with an Aluminophosphate, Exxon Research & Engineering Co., Florham Park, N.J., *U.S. Pat.*, US 4482776, 1984.

(95) Mukherjee, S.; Joarder, B.; Manna, B.; Desai, A. V.; Chaudhari, A. K.; Ghosh, S. K. Framework-Flexibility Driven Selective Sorption of p-Xylene over Other Isomers by a Dynamic Metal-Organic Framework, *Sci. Rep.* **2014**, *4*, 5761. http://dx.doi.org/10.1038/srep05761

(96) Maes, M.; Vermoortele, F.; Alaerts, L.; Couck, S.; Kirschhock, C. E. A.; Denayer, J. F. M.; De Vos, D. E. Separation of Styrene and Ethylbenzene on Metal-Organic Frameworks: Analogous Structures with Different Adsorption Mechanisms, *J. Am. Chem. Soc.* **2010**, *132*, 15277-15285.

(97) Remy, T.; Ma, L.; Maes, M.; De Vos, D. E.; Baron, G. V.; Denayer, J. F. M. Vapor-Phase Adsorption and Separation of Ethylbenzene and Styrene on the Metal−Organic Frameworks MIL-47 and MIL-53(Al), *Ind. Eng. Chem. Res.* **2012**, *51*, 14824-14833.

(98) Krishna, R.; van Baten, J. M. In silico screening of metal-organic frameworks in separation applications, *Phys. Chem. Chem. Phys.* **2011**, *13*, 10593-10616.

(99) Maesen, T.; Harris, T., Process for producing high RON gasoline using CFI zeolite, Chevron U.S.A. Inc, San Ramon, CA, US, *U.S. Pat.*, US 70374222 B2, 2006.

(100) Maesen, T.; Harris, T., Process for producing high RON gasoline using ATS zeolite, Chevron U.S.A. Inc, San Ramon, CA, US, *U.S. Pat.*, US 7029572 B2, 2006.

(101) Krishna, R.; Smit, B.; Calero, S. Entropy effects during sorption of alkanes in zeolites, *Chem. Soc. Rev.* **2002**, *31*, 185-194.

(102) van Baten, J. M.; Krishna, R. Entropy effects in adsorption and diffusion of alkane isomers in mordenite: An investigation using CBMC and MD simulations, *Microporous Mesoporous Mater.* **2005**, *84*, 179-191.

(103) Krishna, R.; Smit, B.; Vlugt, T. J. H. Sorption-induced Diffusion-selective Separation of Hydrocarbon Isomers Using Silicalite, *J. Phys. Chem. A* **1998**, *102*, 7727-7730.

(104) Krishna, R. Exploiting Configurational Entropy Effects for Separation of Hexane Isomers Using Silicalite-1, *Chem. Eng. Res. Des.* **2001**, *79*, 182-194.

(105) Habgood, H. W. The Kinetics of Molecular Sieve Action. Sorption of Nitrogen-Methane Mixtures by Linde Molecular Sieve 4A, *Canad. J. Chem.* **1958**, *36*, 1384-1397.

(106) Niessen, W.; Karge, H. G. Diffusion of *p*-xylene in Single and Binary Systems Investigated by FTIR Spectroscopy, *Microporous Mater.* **1993**, *1*, 1-8.

(107) Karge, H. G. Infrared Spectroscopic Investigation of Diffusion, Co-diffusion and Counter-diffusion of Hydrocarbon Molecules in Zeolites, *C.R. Chim.* **2005**, *8*, 303-319.

(108) Kärger, J.; Bülow, M. Theoretical Prediction of Uptake Behaviour in Adsorption Kinetics of Binary Gas Mixtures Using Irreversible Thermodynamics, *Chem. Eng. Sci.* **1975**, *30*, 893-896.

(109) Saint-Remi, J. C.; Baron, G. V.; Denayer, J. F. M. Non-Uniform Chain Length Dependent Diffusion of Short 1-Alcohols in SAPO-34 in Liquid Phase, *J. Phys. Chem. C* **2013**, *117*, 9758-9765.

(110) Geus, E. R.; van Bekkum, H.; Bakker, W. J. W.; Moulijn, J. A. High-temperature Stainless Steel Supported Zeolite (MFI) Membranes: Preparation, Module Construction, and Permeation Experiments, *Microporous Mater.* **1993**, *1*, 131-147.

(111) Courthial, L.; Bandot, A.; Tayakout-Fayolle, M.; Jallut, C. Transient Method for Mass-Transfer Characterization Through Supported Zeolite Membranes: Extension to Two Components, *A.I.Ch.E.J.* **2013**, *59*, 959-970.

(112) Matsufuji, T.; Watanabe, K.; Nishiyama, N.; Egashira, Y.; Matsukata, M.; Ueyama, K. Permeation of Hexane Isomers Through an MFI Membrane, *Ind. Eng. Chem. Res.* **2000**, *39*, 2434-2438.

(113) Matsufuji, T.; Nishiyama, N.; Matsukata, M.; Ueyama, K. Separation of Butane and Xylene Isomers with MFI-type Zeolitic Membrane Synthesized by a Vapor-Phase Transport Method, *J. Membr. Sci.* **2000**, *178*, 25-34.

(114) Krishna, R.; van Baten, J. M. Investigating the Relative Influences of Molecular Dimensions and Binding Energies on Diffusivities of Guest Species Inside Nanoporous Crystalline Materials *J. Phys. Chem. C* **2012**, *116*, 23556-23568.

(115) Krishna, R.; van Baten, J. M. Influence of Adsorption Thermodynamics on Guest Diffusivities in Nanoporous Crystalline Materials, *Phys. Chem. Chem. Phys.* **2013**, *15*, 7994-8016.

(116) Priegnitz, J. W., Process for the Separation of 1,3-butadient by Selective Adsorption on a Zeolite Adsorbent, UOP Inc., Des Plaines, Illinois, *U.S. Pat.*, US 3992471, 1976.

(117) Takahashi, A.; Yang, R. T.; Munson, C. L.; Chinn, D. Influence of Ag Content and H_2S Exposure on 1,3-Butadiene/1-Butene Adsorption by Ag Ion-Exchanged Y-Zeolites (Ag-Y), *Ind. Eng. Chem. Res.* **2001**, *40*, 3979-3988.

(118) Granato, M. A.; Lamia, N.; Vlugt, T. J. H.; Rodrigues, A. E. Adsorption Equilibrium of Isobutane and 1-Butene in Zeolite 13X by Molecular Simulation, *Ind. Eng. Chem. Res.* **2008**, *47*, 6166-6174.

(119) Jin, M.; Kim, S. S.; Kim, Y. D.; Park, J.-N.; Kim, J. H.; Ko, C. H.; Kim, J.-N.; Kim, J. M. Redox-buffer effect of Fe^{2+} ions on the selective olefin/paraffin separation and hydrogen tolerance of a Cu^+-based mesoporous adsorbent, *J. Mater. Chem. A* **2013**, *1*, 6653-6657.

(120) Hartmann, M.; Kunz, S.; Himsl, D.; Tangermann, O.; Ernst, S.; Wagener, A. Adsorptive Separation of Isobutene and Isobutane on $Cu_3(BTC)_2$, *Langmuir* **2008**, *24*, 8634-8642.

(121) Wang, F.; Wang, W.; Huang, S.; Teng, J.; Xie, Z. Experiment and Modeling of Pure and Binary Adsorption of n-Butane and Butene-1 on ZSM-5 Zeolites with Different Si/Al Ratios, *Chin. J. Chem. Eng.* **2007**, *15*, 376-386.

(122) Kim, H.; Jung, Y. Can Metal−Organic Framework Separate 1‑ Butene from Butene Isomers?, *J. Phys. Chem. Lett.* **2014**, *5*, 440-446.

(123) Krishna, R.; Paschek, D. Separation of hydrocarbon mixtures using zeolite membranes: a modelling approach combining molecular simulations with the Maxwell-Stefan theory, *Sep. Purif. Technol.* **2000**, *21*, 111-136.

(124) Krishna, R.; Paschek, D. Molecular simulations of adsorption and siting of light alkanes in silicalite-1, *Phys. Chem. Chem. Phys.* **2001**, *3*, 453-462.

(125) Vroon, Z. A. E. P.; Keizer, K.; Gilde, M. J.; Verweij, H.; Burggraaf, A. J. Transport properties of alkanes through ceramic thin zeolife MFI membranes, *J. Membr. Sci.* **1996**, *113*, 293-300.

(126) Fernandez, M.; Kärger, J.; Freude, D.; Pampel, A.; van Baten, J. M.; Krishna, R. Mixture Diffusion in Zeolites Studied by MAS PFG NMR and Molecular Simulation, *Microporous Mesoporous Mater.* **2007**, *105*, 124-131.

(127) Chmelik, C.; Heinke, L.; van Baten, J. M.; Krishna, R. Diffusion of *n*-butane/*iso*-butane Mixtures in Silicalite-1 Investigated Using Infrared (IR) Microscopy, *Microporous Mesoporous Mater.* **2009**, *125*, 11-16.

(128) Tijsebaert, B.; Varszegi, C.; Gies, H.; Xiao, F. S.; Bao, X.; Tatsumi, T.; Müller, U.; De Vos, D. Liquid phase separation of 1-butene from 2-butenes on all-silica zeolite RUB-41, *Chem. Commun.* **2008**, 2480-2482.

(129) Peng, Y.; Zhang, Z.; Zheng, X.; Wang, H.; Xu, C.; Xiao, Q.; Zhong, Y.; Zhu, W. Comparison Study on the Adsorption of CFC-115 and HFC-125 on Activated Carbon and Silicalite-1, *Ind. Eng. Chem. Res.* **2010**, *49*, 10009-10015.

(130) Lee, C. K.; Chiang, A. S. T. Adsorption of aromatic compounds in large MFI zeolite crystals, *J. Chem. Soc. - Faraday Trans.* **1996**, *92*, 3445-3451.

(131) Hansen, N.; Krishna, R.; van Baten, J. M.; Bell, A. T.; Keil, F. J. Analysis of Diffusion Limitation in the Alkylation of Benzene over H-ZSM-5 by Combining Quantum Chemical Calculations, Molecular Simulations, and a Continuum Approach, *J. Phys. Chem. C* **2009**, *113*, 235-246.

(132) Hansen, N.; Krishna, R.; van Baten, J. M.; Bell, A. T.; Keil, F. J. Reactor simulation of benzene ethylation and ethane dehydrogenation catalyzed by ZSM-5: A multiscale approach, *Chem. Eng. Sci.* **2010**, *65*, 2472-2480.

(133) Takahashi, A.; Yang, R. T. New Adsorbents for Purification: Selective Removal of Aromatics, *A.I.Ch.E.J.* **2002**, *48*, 1457-1468.

(134) Ren, H.; Ben, T.; Wang, E.; Jing, X.; Xue, M.; Liu, B.; Cui, Y.; Qui, S.; Zhu, G. Targeted synthesis of a 3D porous aromatic framework for selective sorption of benzene, *Chem. Commun.* **2010**, *46*, 291-293.

(135) Lin, J.-B.; Zhang, J.-P.; Zhang, W.-X.; Wei Xue, W.; Xue, D.-X.; Chen, X.-M. Porous Manganese(II) 3-(2-Pyridyl)-5-(4-Pyridyl)-1,2,4-Triazolate Frameworks: Rational Self-Assembly, Supramolecular Isomerism, Solid-State Transformation, and Sorption Properties, *Inorg. Chem.* **2009**, *46*, 6852-6660.

(136) Foster, M. D.; Rivin, I.; Treacy, M. M. J.; Friedrichs, O. D. A geometric solution to the largest-free-sphere problem in zeolite frameworks, *Microporous Mesoporous Mater.* **2006**, *90*, 32-38.

(137) He, Y.; Krishna, R.; Chen, B. Metal-Organic Frameworks with Potential for Energy-Efficient Adsorptive Separation of Light Hydrocarbons, *Energy Environ. Sci.* **2012**, *5*, 9107-9120.

(138) Xiang, S. C.; He, Y.; Zhang, Z.; Wu, H.; Zhou, W.; Krishna, R.; Chen, B. Microporous Metal-Organic Framework with Potential for Carbon Dioxide Capture at Ambient Conditions, *Nat. Commun.* **2012**, *3*, 954. http://dx.doi.org/doi:10.1038/ncomms1956.

(139) Zhu, W.; Kapteijn, F.; van der Linden, B.; Moulijn, J. A. Equilibrium adsorption of linear and branched C_6 alkanes on silicalite-1 studied by the tapered element oscillating microbalance, *Phys. Chem. Chem. Phys.* **2001**, *3*, 1755-1761.

31. Caption for Figures

Figure 1. (a, b, c, d) The variation of the fractional pore occupancy, θ_t, as a function of the bulk fluid phase pressure, p_t, for adsorption of (a) 20/80 CO_2/H_2 mixtures in Cu-TDPAT, 50/50 CO_2/CH_4 mixtures in NiMOF-74, and 15/85 CO_2/N_2 mixtures in MgMOF-74, (b) O_2/N_2, and Kr/Xe, (c) C_2H_4/C_2H_6, and (d) nC6/2MP/3MP/22DMB/23DMB mixtures in a variety of materials. The data plotted in (a, b, c, d) are IAST calculations with the isotherm fit parameters culled from the literature.[3, 12, 137, 138] (e) The data θ_t vs p_t for adsorption of equimolar water/ethanol, and methanol/ethanol/1-propanol/1-butanol mixtures in ZIF-8 at 308 K. The IAST calculations of adsorption equilibrium in (e) are based on the pure component isotherm fits reported in Table 12. (f) The data θ_t vs c_t for adsorption of o-xylene/m-xylene/p-xylene/ethylbenzene mixtures in BaX zeolite at 393 K, and 453 K; these IAST calculations are based on the pure component isotherm data of Minceva and Rodrigues.[13, 14]

Figure 2. Schematic of a packed bed adsorber.

Figure 3. (a) CBMC simulations[57] of pure component adsorption isotherms for water, and 1-alcohols in CHA at 300 K. (b) Saturation capacities for adsorption of 1-alcohols in CHA at 300 K. (c) Snapshots showing the conformations of 1-alcohols in CHA at saturation conditions.

Figure 4. CBMC mixture simulations for (a) ethanol - 1-propanol, (b) ethanol -1-hexanol in CHA at 300 K. The partial fugacities in the bulk fluid phase are taken to be equal, i.e. $f_1=f_2$. The continuous solid lines represent calculations of the Ideal Adsorbed Solution Theory (IAST) [56] using dual-Langmuir-Freundlich fits of pure component isotherms. Table 11 provides the pure component isotherm fit parameters. The range of liquid phase operation is indicated by the shaded region; the transition between vapor and liquid bulk phase is determined using the Peng-Robinson equation of state.

Figure 5. Transient breakthrough experimental data of Remy et al.[58] for separation of (a) ethanol/1-propanol and (b) ethanol-1-hexanol mixtures in a fixed bed adsorber packed with SAPO-34.

Figure 6. (a) Experimental data of Zhang et al.[60] for pure component adsorption isotherms for 1-alcohols in ZIF-8 at 308 K. The continuous solid lines are the dual-Langmuir-Freundlich fits of the isotherms using the parameter values listed in Table 12. (b) Comparison of the saturation capacities of CHA zeolite with that of ZIF-8.

Figure 7. IAST calculations of the component loading in ZIF-8 in equilibrium with bulk fluid phase containing an equimolar methanol/1-ethanol/1-propanol/1-butanol mixture at 308 K. Table 12 provides the dual-Langmuir-Freundlich fit parameters for the pure component isotherms. The range of liquid phase operation is indicated by the shaded region; the transition between vapor and liquid bulk phase is determined using the Peng-Robinson equation of state.

Figure 8. Transient breakthrough simulations for mixtures of 1-alcohols using ZIF-8. In (a) the inlet consists of an equimolar methanol/1-ethanol/1-propanol/1-butanol mixture at 308 K at a total pressure p_t = 10 kPa. In (c) the inlet consists of an equimolar methanol/1-ethanol/1-propanol mixture at 308 K at a

total pressure p_t = 300 kPa. Intra-crystalline diffusion effects are accounted for by taking $Đ_{methanol}/r_c^2$ = 1×10^{-2} s^{-1}; $Đ_{ethanol}/r_c^2 = 5\times10^{-3}$ s^{-1}; $Đ_{1-propanol}/r_c^2 = 1\times10^{-3}$ s^{-1}; $Đ_{1-butanol}/r_c^2 = 1\times10^{-3}$ s^{-1}.

Figure 9. Transient breakthrough simulations for 1-alcohols/water mixture using ZIF-8. The inlet consists of 25/25/25/25/900 methanol/1-ethanol/1-propanol/1-butanol/water mixture at 308 K at a total pressure of 10^5 Pa. Intra-crystalline diffusion effects are accounted for by taking $Đ_{methanol}/r_c^2 = 1\times10^{-2}$ s^{-1}; $Đ_{ethanol}/r_c^2 = 5\times10^{-3}$ s^{-1}; $Đ_{1-propanol}/r_c^2 = 1\times10^{-3}$ s^{-1}; $Đ_{1-butanol}/r_c^2 = 1\times10^{-3}$ s^{-1}; $Đ_{water}/r_c^2 = 1\times10^{-3}$ s^{-1}.

Figure 10. Experimental data of Van der Perre et al.[62] for pure component adsorption isotherms of 1-alcohols in ZIF-68 at 323 K. The continuous solid lines are the dual Langmuir-Freundlich fits of the isotherms using the parameters specified in Table 13. In (a) the pressures are plotted on a linear scale, whereas in (b) the pressures are plotted on a logarithmic scale.

Figure 11. IAST calculations of the component loadings for equimolar (a) 6-component methanol/ethanol/1-propanol/1-butanol/1-pentanol/1-hexanol mixture, and (b) equimolar binary equimolar ethanol/1-butanol mixture in ZIF-68 at 323 K.

Figure 12. Transient uptake within ZIF-68 crystal exposed to a bulk gas phase pressure of (a) 400 kPa, and (b) 4 MPa. Intra-crystalline diffusion effects are accounted for by taking $Đ_{ethanol}/r_c^2 = 5\times10^{-7}$ s^{-1}; $Đ_{1-butanol}/r_c^2 = 2\times10^{-8}$ s^{-1}.

Figure 13. Pure component isotherms for (a) water, and (b) benzene in CuBTC. The experimental data are from Zhao et al.,[64] measured at temperatures of 288 K, 298 K, 308 K, and 318 K.The continuous solid lines are dual-site Langmuir parameters are provided in Table 14.

Figure 14. IAST calculations of water/benzene adsorption selectivities for equimolar water/benzene mixtures in CuBTC at temperatures of 288 K, 298 K, 308 K, and 318 K. These calculations are based on the pure isotherm fits in Table 14.

Figure 15. Transient breakthrough simulations for (a) 13/87 water/benzene, and (b) 34/66 water/benzene mixtures in a fixed bed adsorber packed with CuBTC at 308 K. The inlet concentration of benzene is 2.1 mol m^{-3} in both cases. In both simulations intra-crystalline diffusion effects are considered to be negligible. (c) Pulse chromatographic simulations with pulse injection of 34/66 water/benzene mixture at 8.15 kPa.

Figure 16. CBMC simulations of pure component adsorption isotherms for water, methanol, and ethanol in all-silica FAU zeolite at 300 K. The CBMC data are from Krishna and van Baten.[43] The continuous solid lines are the Dual-Langmuir-Freundlich fits using the parameters specified in Table 15.

Figure 17. (a, b) CBMC simulations for adsorption of equimolar ($f_1=f_2$) (a) water/methanol, and (b) water/ethanol in FAU zeolite at 300 K. The continuous solid lines are the IAST calculations using the pure component fits in Table 15. (c, d) Comparison of (c) water/methanol and (d) water/ethanol adsorption selectivities in FAU determined from CBMC mixture simulations with IAST calculations.

Figure 18. MD simulations of Krishna and van Baten[43] for (a) self-diffusivities of water, and methanol in water/methanol mixtures, and (b) self-diffusivities in water/ethanol mixtures, in FAU zeolite at 300 K.

Figure 19. CBMC simulations of pure component adsorption isotherms for water, methanol, and ethanol in all-silica DDR zeolite at 300 K. The CBMC data are from Krishna and van Baten.[43] The continuous solid lines are the Dual-Langmuir-Freundlich fits using the parameters specified in Table 16.

Figure 20. (a, b) CBMC simulations for adsorption of equimolar (f_1=f_2) (a) water/methanol, and (b) water/ethanol in DDR zeolite at 300 K. The continuous solid lines are the IAST calculations using the pure component fits in Table 15. (c, d) Comparison of (c) water/methanol and (d) water/ethanol adsorption selectivities in DDR determined from CBMC mixture simulations with IAST calculations.

Figure 21. MD simulations of Krishna and van Baten[43] for self-diffusivities in water/methanol mixtures in DDR zeolite at 360 K.

Figure 22. CBMC simulations of pure component adsorption isotherms for water, methanol, and ethanol in all-silica MFI zeolite at 300 K. The CBMC data are from Krishna and van Baten.[43] The continuous solid lines are the Dual-Langmuir-Freundlich fits using the parameters specified in Table 17.

Figure 23.(a, b) CBMC simulations for adsorption of equimolar (f_1=f_2) (a) water/methanol, and (b) water/ethanol in MFI zeolite at 300 K. The continuous solid lines are the IAST calculations using the pure component fits in Table 17.

Figure 24. MD simulations of Krishna and van Baten[43] for self-diffusivities in water/methanol mixtures in MFI zeolite at 300 K.

Figure 25. CBMC simulations of pure component adsorption isotherms for water, methanol, and ethanol in all-silica FER zeolite at 300 K. The CBMC data are from unpublished work of Krishna. The continuous solid lines are the Dual-Langmuir-Freundlich fits using the parameters specified in Table 18.

Figure 26. (a, b) IAST calculations for adsorption of equimolar (f_1=f_2) (a) water/methanol, and (b) water/ethanol in FER zeolite at 300 K. (c) IAST calculations of water/methanol and water/ethanol adsorption selectivities in FER.

Figure 27. MD simulations (unpublished work of Krishna) for self-diffusivities in water/ethanol mixtures in FER zeolite at 300 K.

Figure 28. (a) CBMC simulation data of Nalaparaju et al.[66] for pure component adsorption isotherms of water (only the "adsorption" branch of the isotherms are shown here), methanol and ethanol in ZIF-71 at 298 K. (b, c) CBMC simulations of the component loadings for equimolar (b) water/methanol, (c) water/ethanol mixtures in ZIF-71. (d) CBMC simulations for the water/methanol and water/ethanol adsorption selectivities.

Figure 29. Snapshots showing the location of cations in LTA-5A, and LTA-4A.

Figure 30. (a,b) Experimental data of Pera-Titus et al. [73] for pure component isotherms of (a) water, and (b) ethanol in LTA-4A zeolite at various temperatures. The continuous solid lines are the dual-Langmuir-Freundlich fits of the isotherms using the parameters reported in Table 19.

Figure 31. (a) Comparison of the experimental data of Pera-Titus et al. [73] for component loadings in water/ethanol mixtures in LTA-4A zeolite at 333 K as a function of the vapor phase mole fraction of water. The total pressure in the experiments is 2.1 kPa. The continuous solids lines are IAST calculations using the parameters reported in Table 19. (b) IAST calculations of the water/ethanol adsorption selectivities.

Figure 32. Water permeates preferentially across LTA-4A zeolite membrane used in hybrid scheme for production of 99.5% pure ethanol.

Figure 33. Experimental data of Efthymiou et al.[76] for transient uptake of (a) 1:1 methanol/ethanol, and (b) 1:2 methanol/ethanol mixtures in UCY-5. The data in Figure 9a, and 9b of Efthymiou et al.[76] are re-plotted here using the square root of time (in minutes) on the *x*-axis.

Figure 34. (a) Pure component isotherms for methanol, and ethanol in Ce(BTB).[77] The continuous solid lines are the dual-Langmuir-Freundlich isotherm fits using the parameter values reported in Table 20. (b) IAST calculations of component loadings for equimolar methanol/ethanol mixtures in Ce(BTB) at 298 K. (c) Simulations of transient uptake within Ce(BTB) crystals, using the methodology described in

detail in earlier works.[12, 59] The bulk fluid phase is at 100 kPa, and is an methanol/ethanol equimolar mixture. Intra-crystalline diffusion effects are accounted for by taking $Đ_{methanol}/r_c^2 = 1\times10^{-3}$ s^{-1}; $Đ_{ethanol}/r_c^2 = 1\times10^{-4}$ s^{-1};

Figure 35. (a) Experimental data of Horike et al.[78] for pure component adsorption isotherms of water, methanol and ethanol in CID-1 at 298 K. The continuous solid lines are the dual-Langmuir-Freundlich fits of the isotherms using the parameter values listed in Table 21. (b, c, d) IAST calculations of the component loadings for equimolar (b) water/methanol, (c) water/ethanol, and (d) methanol/ethanol mixtures.

Figure 36. Transient breakthrough simulations for (a) 20/80 water/methanol, and (b) 11/89 water/ethanol, and (c) 50/50 methanol/ethanol mixtures in a fixed bed adsorber packed with CID-1 at 298 K. For water/alcohol mixtures the total pressure is 100 kPa; for methanol/ethanol mixture the total pressure is 1 MPa. Intra-crystalline diffusion effects are accounted for by taking $Đ_{water}/r_c^2 = 1\times10^{-2}$ s^{-1}; $Đ_{methanol}/r_c^2 = 2\times10^{-3}$ s^{-1}; $Đ_{ethanol}/r_c^2 = 1\times10^{-3}$ s^{-1}.

Figure 37. (a) Experimental data of Chen et al.[79] of pure component adsorption isotherms for water and methanol in Cu-GLA at 298 K. The continuous solid lines are the dual-Langmuir-Freundlich fits of the isotherms using the parameter values listed in Table 22. (b) IAST calculations of component loadings for equimolar water/methanol mixtures.

Figure 38. (a) Pure component isotherms for water, methanol, ethanol, 1-propanol, and 2-propanol at 298 K in Co(pbdc).[80] The continuous solids lines are the dual-Langmuir-Freundlich isotherm fits using the parameter values reported in Table 23. (b, c) IAST calculations of component loadings for equimolar (b) water/alcohol, and (c) ethanol/1-propanol, and 1-propanol/2-propanol mixtures in Co(pbdc) at 298 K.

Figure 39. Transient breakthrough simulations for (a) 11/89 water/ethanol, (b) 57/43 water/1-propanol, and (c) 31/69 water/2-propanol mixture in a fixed bed adsorber packed with Co(pbdc) at 298 K. The total pressure is 100 kPa. Intra-crystalline diffusion effects are accounted for by taking $Đ_{water}/r_c^2$ = 1×10^{-2} s^{-1}; $Đ_{ethanol}/r_c^2$ = 1×10^{-3} s^{-1}; $Đ_{1-proanol}/r_c^2$ = 1×10^{-4} s^{-1}; $Đ_{2-propanol}/r_c^2$ = 1×10^{-4} s^{-1}.

Figure 40. (a) Pure component isotherms for water, methanol, ethanol, 1-propanol, and 2-propanol at 298 K in Zn(II)-MOF.[81] The continuous solids lines are the dual-Langmuir-Freundlich isotherm fits using the parameter values reported in Table 24. (b) IAST calculations of component loadings for equimolar water/methanol/ethanol/1-propanol/2-propanol mixtures in Zn(II)-MOF at 298 K.

Figure 41. Transient breakthrough simulations for (a) 11/89 water/ethanol, (b) 57/43 water/1-propanol, and (c) 31/69 water/2-propanol mixture in a fixed bed adsorber packed with Zn(II) MOF at 298 K. The total pressure is 100 kPa. Intra-crystalline diffusion effects are accounted for by taking $Đ_{water}/r_c^2$ = 1×10^{-2} s^{-1}; $Đ_{ethanol}/r_c^2$ = 1×10^{-3} s^{-1}; $Đ_{1-proanol}/r_c^2$ = 1×10^{-4} s^{-1}; $Đ_{2-propanol}/r_c^2$ = 1×10^{-4} s^{-1}.

Figure 42. (a) Experimental data of Borjigin et al.[83] for pure component adsorption isotherms for water, methanol and ethanol in JUC-110 at 298 K. The continuous solid lines are the dual-Langmuir-Freundlich fits of the isotherms using the parameter values listed in Table 25. (b, c, d) IAST calculations of the component loadings for equimolar (b) water/methanol, (c) water/ethanol, and (d) methanol/ethanol mixtures.

Figure 43. Transient breakthrough simulations for (a) 20/80 water/methanol, and (b) 11/89 water/ethanol, and (c) 50/50 methanol/ethanol mixtures in a fixed bed adsorber packed with JUC-110 at 298 K. For water/alcohol mixtures the total pressure is 100 kPa; for methanol/ethanol mixture the total pressure is 200 kPa. Intra-crystalline diffusion effects are accounted for by taking $Đ_{water}/r_c^2 = 1\times10^{-2}$ s^{-1}; $Đ_{methanol}/r_c^2 = 2\times10^{-3}$ s^{-1}; $Đ_{ethanol}/r_c^2 = 1\times10^{-3}$ s^{-1}.

Figure 44. Schematic showing the separations of the products from a catalytic reforming unit.

Figure 45. Boiling points, and freezing points of C8 hydrocarbons.

Figure 46. Moving bed adsorption technology for separation of feed mixture containing o-xylene/m-xylene/p-xylene/ethylbenzene. The simulated moving bed technology, used in industrial practice, is depicted here in its (mathematically) equivalent form of true moving bed with counter-current contacting between the downflowing adsorbent material and upflowing desorbent (eluent) liquid.

Figure 47. (a) Pure component isotherms for hydrocarbons in BaX zeolite at 453 K, plotted using the Langmuir parameters reported by Minceva and Rodrigues.[13, 14] (b, c, d) Calculations using the Ideal Adsorbed Solution Theory (IAST) of Myers and Prausnitz,[56] for adsorption equilibrium for 4-component o-xylene/m-xylene/p-xylene/ethylbenzene mixture. (b) Fractional occupancies, θ_t, as a function of the bulk phase fluid concentrations, c_t. (c, d) Component loadings as a function of the fractional occupancies θ_t. for mixture adsorption at (c) 393 K, and (d) 453 K.

Figure 48. Qualitative representation of the liquid phase concentrations of a mixture of o-xylene/m-xylene/p-xylene/ethylbenzene in a SMB adorption unit with zeolite selective to p-xylene. The data shown are plotted using the information presented by Minceva and Rodrigues.[84]

Figure 49. An alternative separation scheme in which o-xylene is recovered at the bottom of the reformate splitter.

Figure 50. The molecular dimensions of xylene isomers, culled from Torres-Knoop et al.[47]

Figure 51. Departures from planarity of ethylbenzene, styrene, and p-xylene.

Figure 52. Cartoons showing stacking of (a) o-xylene and (b) p-xylene within the 1D 8.5 Å channels.

Figure 53. Snapshots, obtained from Configurational-bias Monte Carlo simulations,[47] showing the stacking of o-xylene within 8.5 Å channels of MIL-47. Also shown are the CBMC simulation data of Torres-Knoop et al.[47] for pure component isotherms of C8 hydrocarbons at 433 K.

Figure 54. Experimental data of Chiang et al.[91] for pure component isotherms for xylene isomers in $AlPO_4$-5 at 303 K. The continuous solid lines are dual-site Langmuir Freundlich fits of the isotherms; the isotherm fit parameters are provided in Table 26.

Figure 55. Isosteric heats of adsorption of xylene isomers in $AlPO_4$-5. These values are calculated using the Clausius-Clapeyron equations along with the T-dependent isotherm fit parameters specified in Table 26.

Figure 56. Calculations using the Ideal Adsorbed Solution Theory (IAST) of Myers and Prausnitz[56] for adsorption equilibrium in a 3-component o-xylene/m-xylene/p-xylene in $AlPO_4$-5 at 303 K. (a, c) component loadings in mixture, and (b, d) o-xylene/p-xylene and o-xylene/m-xylene selectivities.

Figure 57. (a) Transient breakthrough simulations for step-input of 3-component o-xylene/m-xylene/p-xylene in $AlPO_4$-5 at 303 K and a total pressure of 30 kPa. (b) Pulse chromatographic simulations for pulse-input of 3-component o-xylene/m-xylene/p-xylene in $AlPO_4$-5 at 303 K and a total pressure of 30 kPa. The duration of the pulse is 10 s. Video animations of these transient breakthroughs are also uploaded as ESI.

Figure 58. (a) Snapshots, obtained from Configurational-bias Monte Carlo simulations,[47] showing the stacking of p-xylene within 10 Å channels of MAF-X8. (b) Snapshots showing the stacking of p-xylene within 10 Å channels of Co(BDP).

Figure 59. CBMC simulations[47] for the component loadings for 4-component o-xylene/ m-xylene/ p-xylene/ethylbenzene in MAF-X8 at 433 K. The continuous lines are IAST predictions of mixture adsorption equilibrium using the pure component isotherm fits. The dual-Langmuir-Freundlich isotherm fit parameters are provided in Table 29.

Figure 60. Transient breakthroughs for ethylbenzene/styrene mixtures in fixed beds packed with (a) MIL-47(V), and (b) MIL-53(Al) at 298 K. The operations are in the liquid phase, with step inputs of feed concentrations c_{i0} = 0.47 mol L^{-1} in both cases.The large symbols are the experimental breakthrough data, scanned from Figures 2a and 2b of the paper by Maes et al.[96]

Figure 61. (a) CBMC simulations for adsorption equilibrium in nC6/3MP/22DMB mixtures in AFI zeolite.[98] (b) Snapshots showing the molecular configurations of nC6, 3MP, and 22DMB within 1D channels of AFI zeolite.[98]

Figure 62. CBMC simulations for adsorption equilibrium in nC6/2MP/3MP/22DMB/23DMB mixtures in (a) ATS, and (b) CFI zeolites.[34, 41] The continuous solid lines are IAST calculations using the pure component isotherm fit parameters provided in Table 30, and Table 31.

Figure 63. The isotherm data for nC6 at 298 K determined from Infra-Red Microscopy (IRM)[59] are compared with the corresponding CBMC simulations for nC6; the CBMC data are fitted with the dual-

Langmuir-Freundlich parameters specified in Table 32. Also shown are snapshots showing the location of nC6 molecules within the straight and zig-zag channels of MFI.

Figure 64. CBMC simulations of pure component isotherm for 2-methylpentane (= 2MP) compared with the experimental data obtained from IRM,[59] and from experimental data of Zhu et al.[139] at 303 K. The CBMC simulations for 2MP are fitted with the dual-Langmuir-Freundlich parameters specified in Table 32. Also shown are snapshots of 2MP molecules located within MFI.

Figure 65. (a) CBMC simulations of loadings in the adsorbed phase in equilibrium with binary nC6/2MP mixture with partial pressures $p_1 = p_2$ in the bulk gas phase at 298 K. Also shown (using open symbols) are IRM experimental data.[59] The continuous solid lines are IAST calculations using the pure component isotherm fits in Table 32. (b) Calculations of the adsorption selectivity, S_{ads}, using Equation (13). Also shown are snapshots showing the location of nC6 (Θ_1 = 2/uc) and 2MP (Θ_2 = 2/uc) molecules at a total loading Θ_t = 4/uc.

Figure 66. Comparison of IRM experimental data, reported by Titze et al.[59] for transient uptake of nC6/2MP mixtures with the Maxwell-Stefan model simulation results (indicated by continuous solid lines) in Runs 1, 2, 3, and 4 presented sequentially. Details of the M-S model are provided in Titze et al.[59]

Figure 67. Plot of the fitted diffusivity values, reported by Titze et al.[59], $Đ_1/r_c^2$, and $Đ_2/r_c^2$ as a function of the 2MP loading at the end of the equilibration of each of the four experimental runs for transient uptake of nC6/2MP mixtures.

Figure 68. (a) CBMC simulations of the component loadings for nC6/2MP/3MP/22DMB/23DMB mixture adsorption in MFI as a function of the total mixture loading.[98] (b) Snapshots showing the location of nC6, 3MP and 22DMB within the MFI zeolite.[98] (c) Transient breakthrough simulations in fixed bed adsorber with MFI reported in earlier work.[12]

Figure 69. Conventional distillation processing scheme for separation of a mixture of C4 hydrocarbons that is devoid of both 1,3 butadiene and iso-butene.

Figure 70. Processing scheme for separation of C4 hydrocarbons with selective adsorption.

Figure 71. (a) Breakthrough experiments of Hartmann et al. [120] for 50/50 isobutene/isobutane mixture in adsorber packed with CuBTC and maintained at isothermal conditions at 303 K.

Figure 72. (a, b) Snapshots showing the location of (a) n-butane and (b) iso-butane within the intersecting channels of MFI zeolite. (c) Component loadings of n-butane and iso-butane for mixture adsorption in MFI; comparison of CBMC simulations and IRM experimental data (shown by open symbols) reported by Titze et al.[59]. (d) nC4/iC4 adsorption selectivity.

Figure 73. (a) Pure component isotherms of Tijsebaert et al.[128] for trans-2-butene, cis-2-butene, and 1-butene in RUB-41 zeolite at 298 K. Experimental data on the breakthrough characteristics of (a) cis-2-butene/1-butene, and (b) trans-2-butene/1-butene mixtures using RUB-41 zeolite.

Figure 74. (a) Pure component isotherm data of Peng et al.[129] for CFC-115, and HFC-125 in MFI zeolite at 298 K. The continuous solid lines are the isotherm fits using the parameters that are provided in Table 34. (b) IAST calculations of the component loadings for equimolar CFC-115/HFC-125 mixtures in MFI zeolite at 298 K.

Figure 75. Transient breakthrough simulations for equimolar CFC-115/HFC-125 mixture with MFI zeolite at 298 K and total pressures of (a) 1 kPa, and (b) 100 kPa. These simulations include the influence of thermodynamic coupling, as described in detail in our earlier work.[12] Intra-crystalline diffusion effects are accounted for by taking $Đ_i/r_c^2$ = 1×10^{-3} s^{-1} for both components.

Figure 76. (a) Pure component isotherm data of Peng et al.[129] for CFC-115, and HFC-125 in Varuf Activated Carbon at 298 K. The continuous solid lines are the isotherm fits using the parameters that are provided in Table 34. (b) IAST calculations of the component loadings for equimolar CFC-115/HFC-125 mixtures in Varuf Activated Carbon at 298 K.

Figure 77. Pure component isotherms for benzene, toluene, p-xylene, and ethylbenzene in MFI zeolite at 283 K. Experimental data from Lee.[130] The continuous solid lines are isotherm fits with dual-site Langmuir-Freundlich parameters provided in Table 35. Also shown are snapshots of guest molecules within the channels of MFI.

Figure 78. (a,b) IAST calculations of the component loadings for adsorption of equimolar mixtures benzene, and ethylbenzene in MFI zeolite at 283 K. (c, d) Transient breakthrough simulations for equimolar feed mxture of benzene, and ethylbenzene in MFI zeolite at 283 K at total pressures of (b) 4 kPa, and (c) 20 kPa.

Figure 79. Molecular structures of benzene and cyclohexane. Also indicated are the boiling points and freezing points.

Fractional occupancies

ESI Figure 1

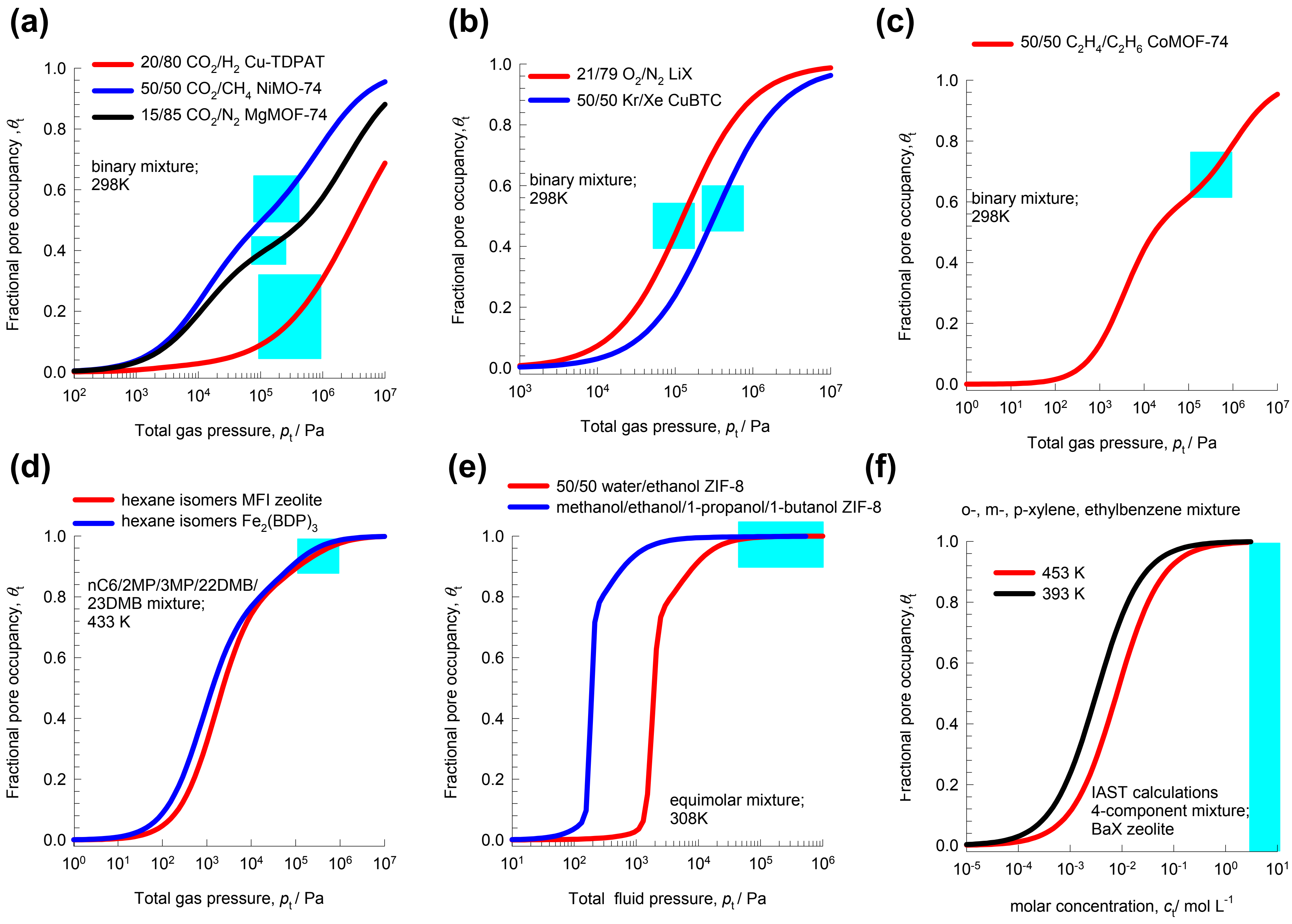

ESI Figure 2

Fixed bed adsorber

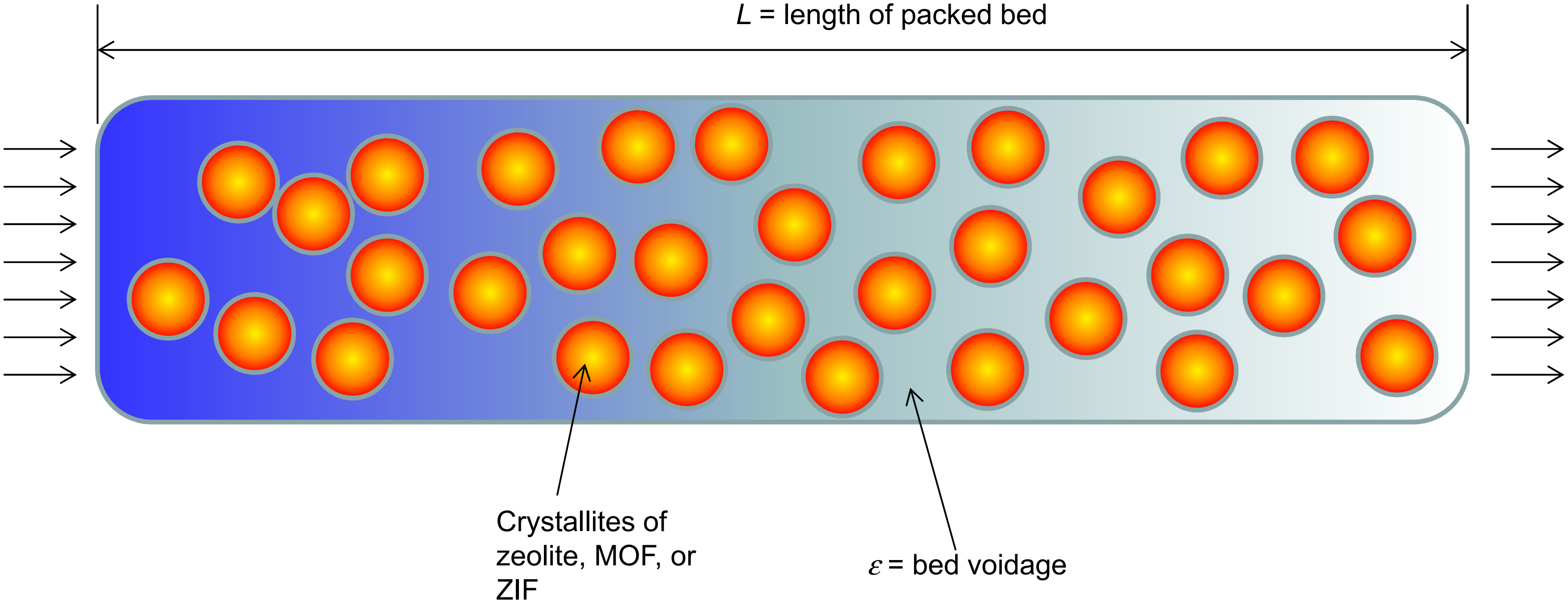

1-alcohols adsorption in CHA zeolite

ESI Figure 3

(a)

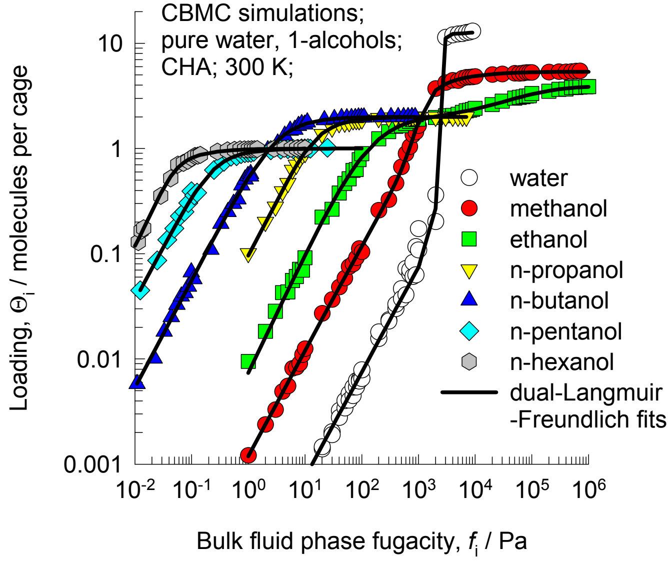

(b)

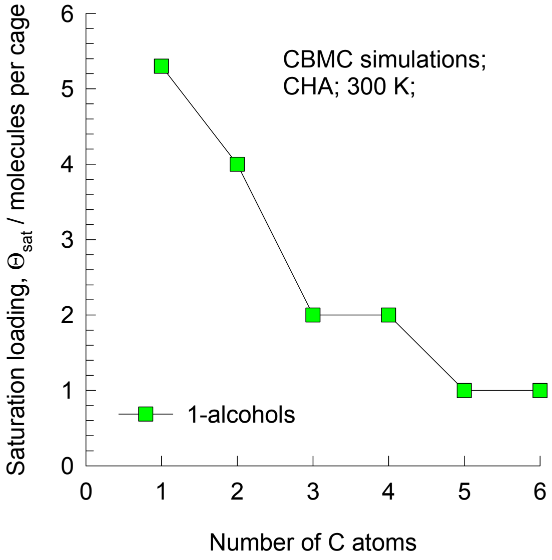

There are 6 cages per unit cell.
The volume of one CHA cage is 316.4 Å^3, slightly larger than that of a single cage of DDR (278 Å^3), but significantly lower than FAU (786 Å^3).

(c)

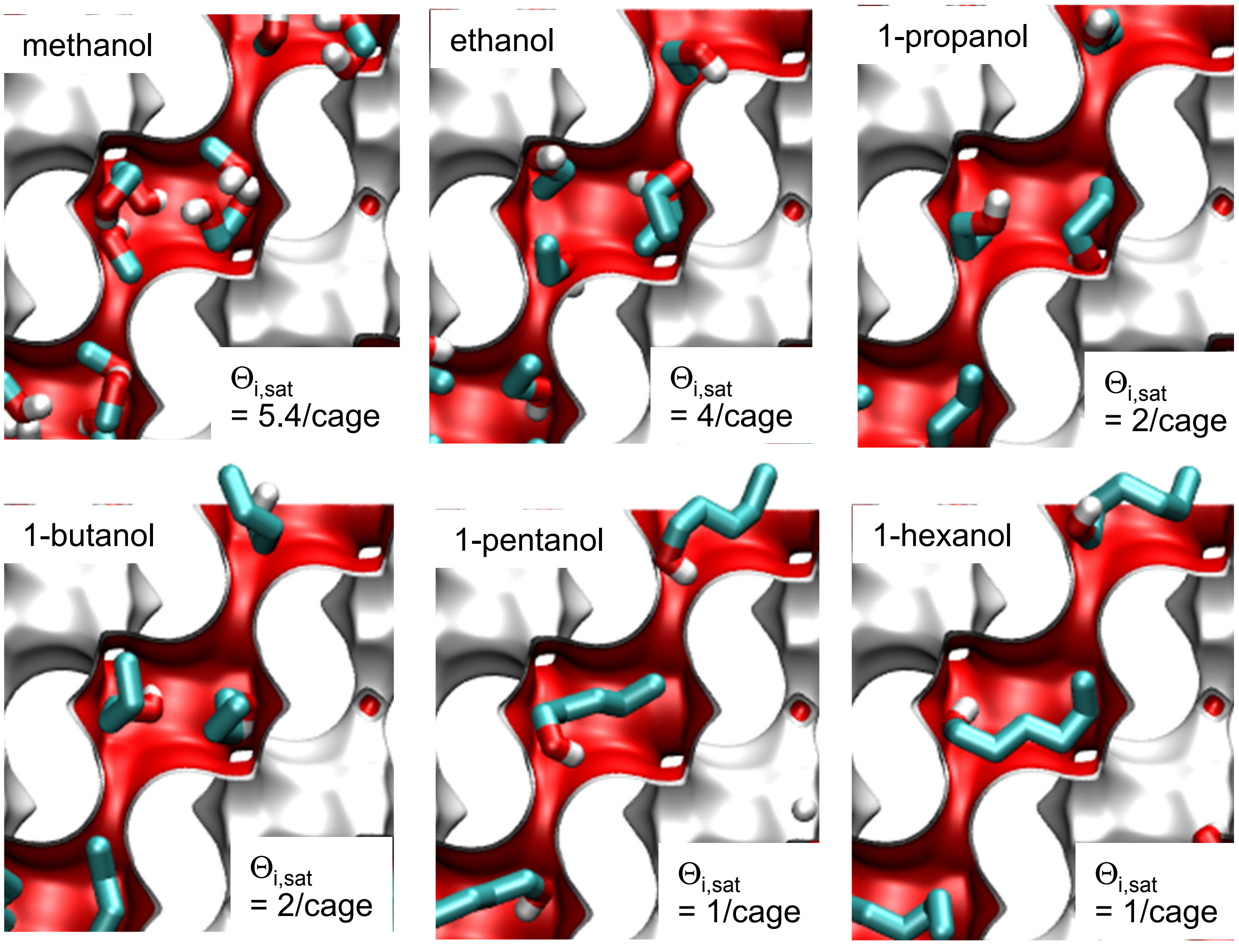

1-alcohols mixture adsorption in CHA zeolite

ESI Figure 4

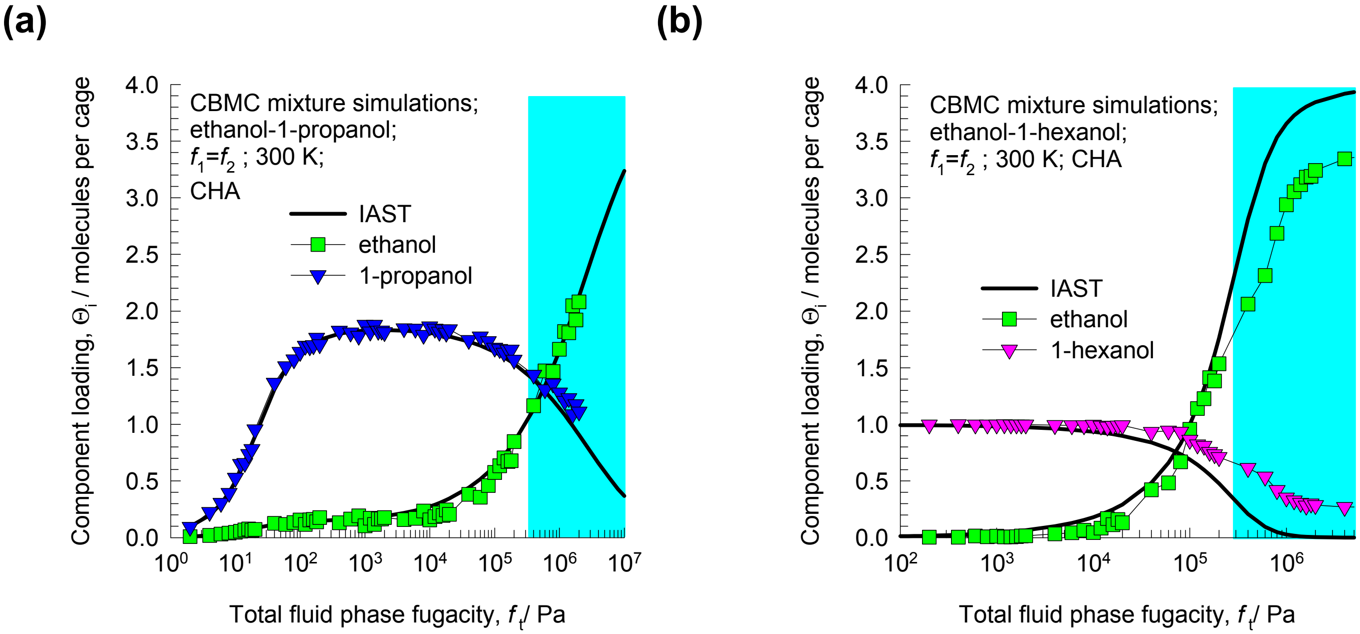

1-alcohols mixture breakthroughs in SAPO-34

ESI Figure 5

SAPO-34

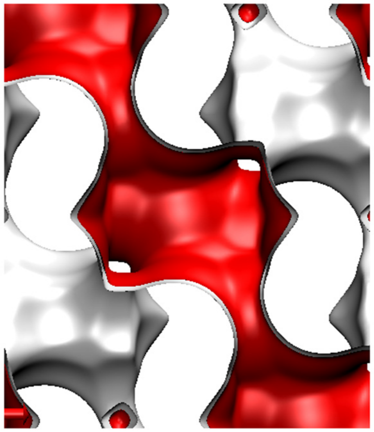

SAPO-34 is the structural analog of CHA zeolite

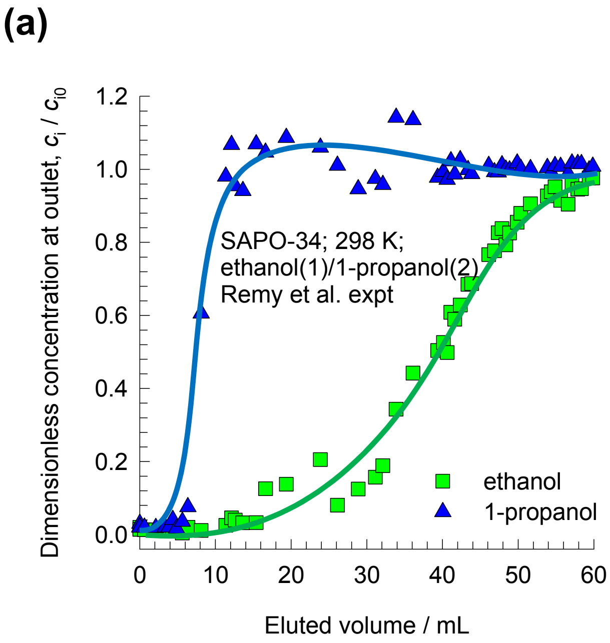

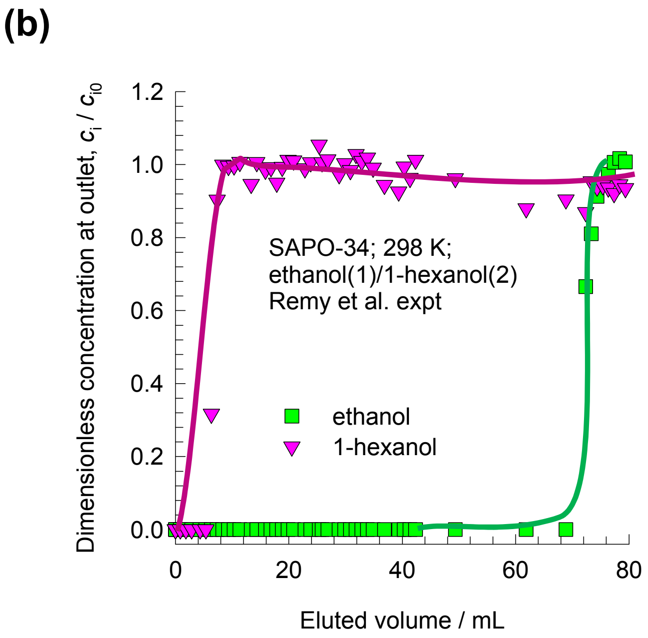

Water and 1-alcohols adsorption in ZIF-8

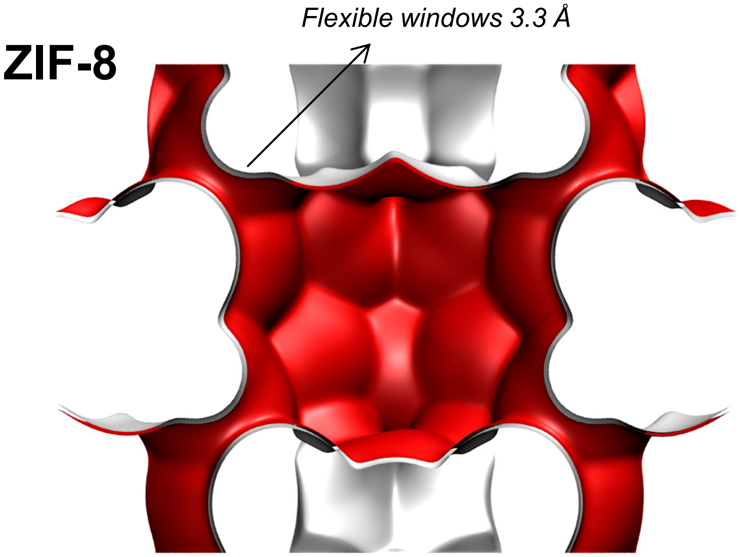

There are 2 cages per unit cell. The volume of one ZIF-8 cage is 1168 Å^3, significantly larger than that of a single cage of DDR (278 Å^3), or FAU (786 Å^3).

(a)

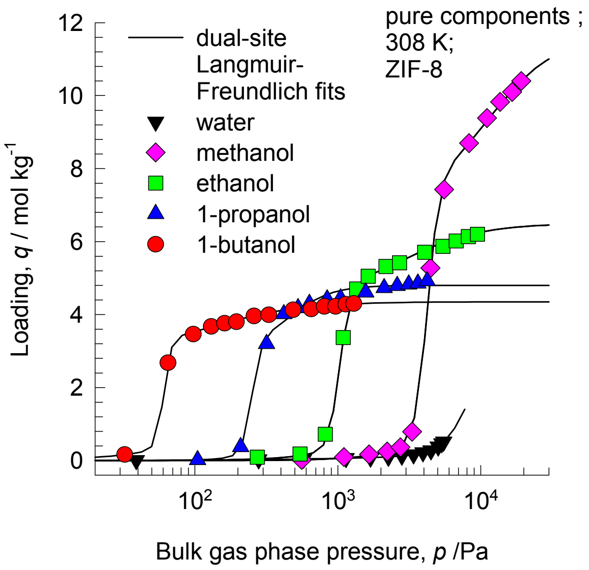

(b)

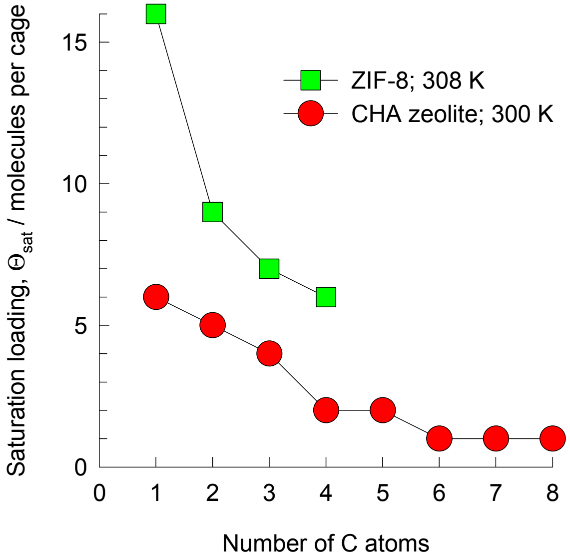

1-alcohols mixture adsorption in ZIF-8

ESI Figure 7

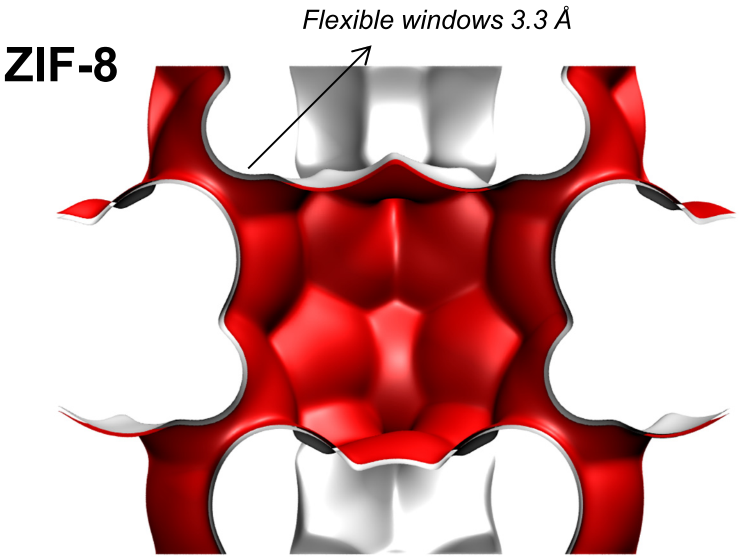

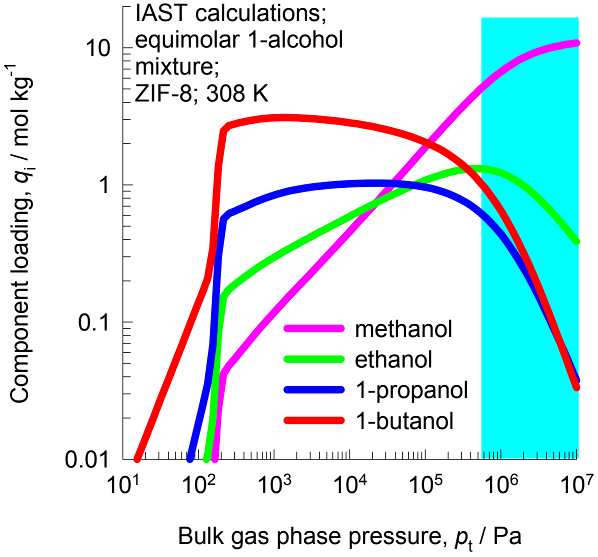

ESI Figure 8

1-alcohols mixture separation with ZIF-8

ZIF-8

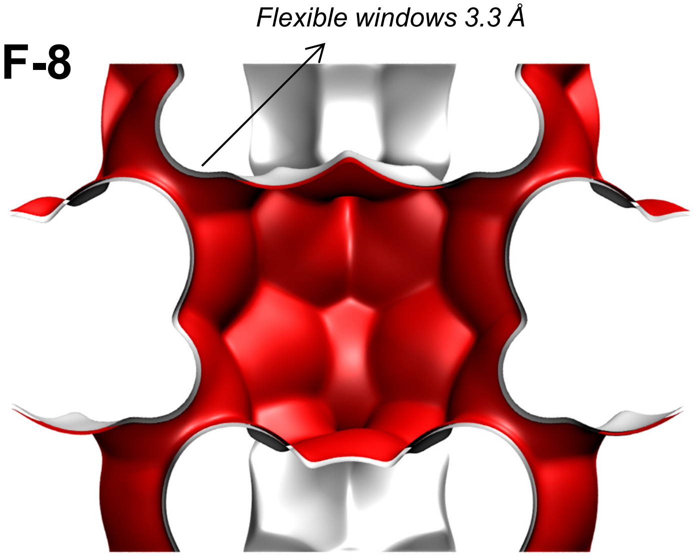

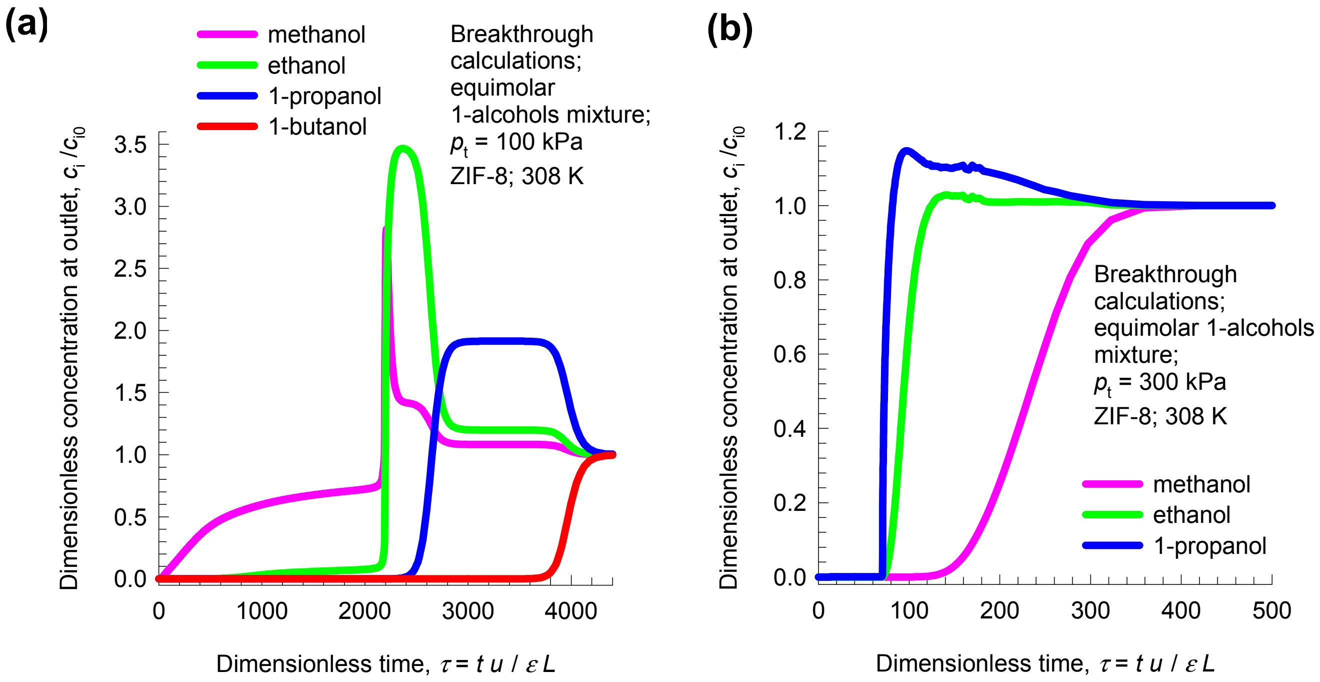

Bioalcohols separation with ZIF-8

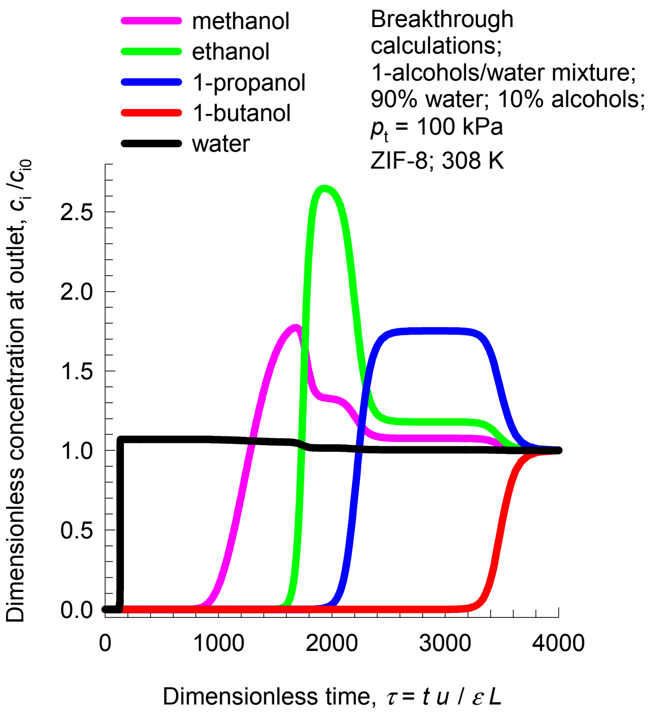

1-alcohols adsorption in ZIF-68

ESI Figure 10

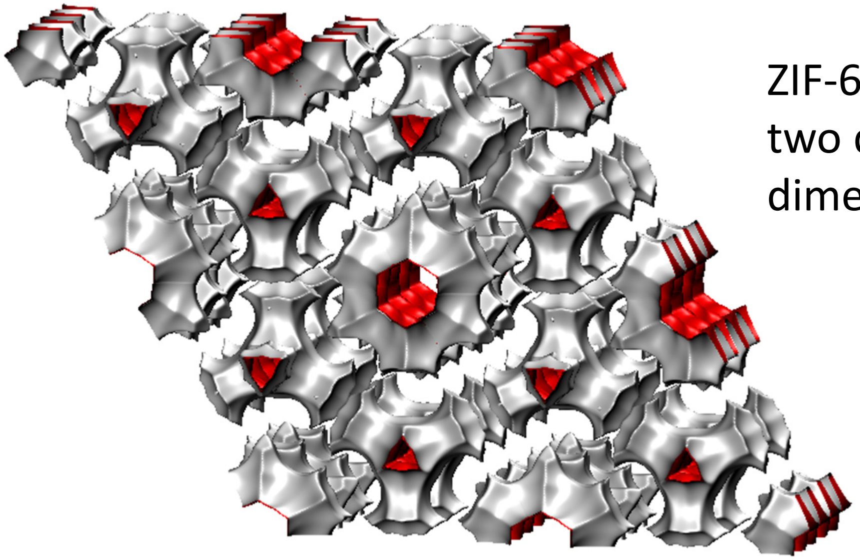

ZIF-68 landscape showing two different channel dimensions

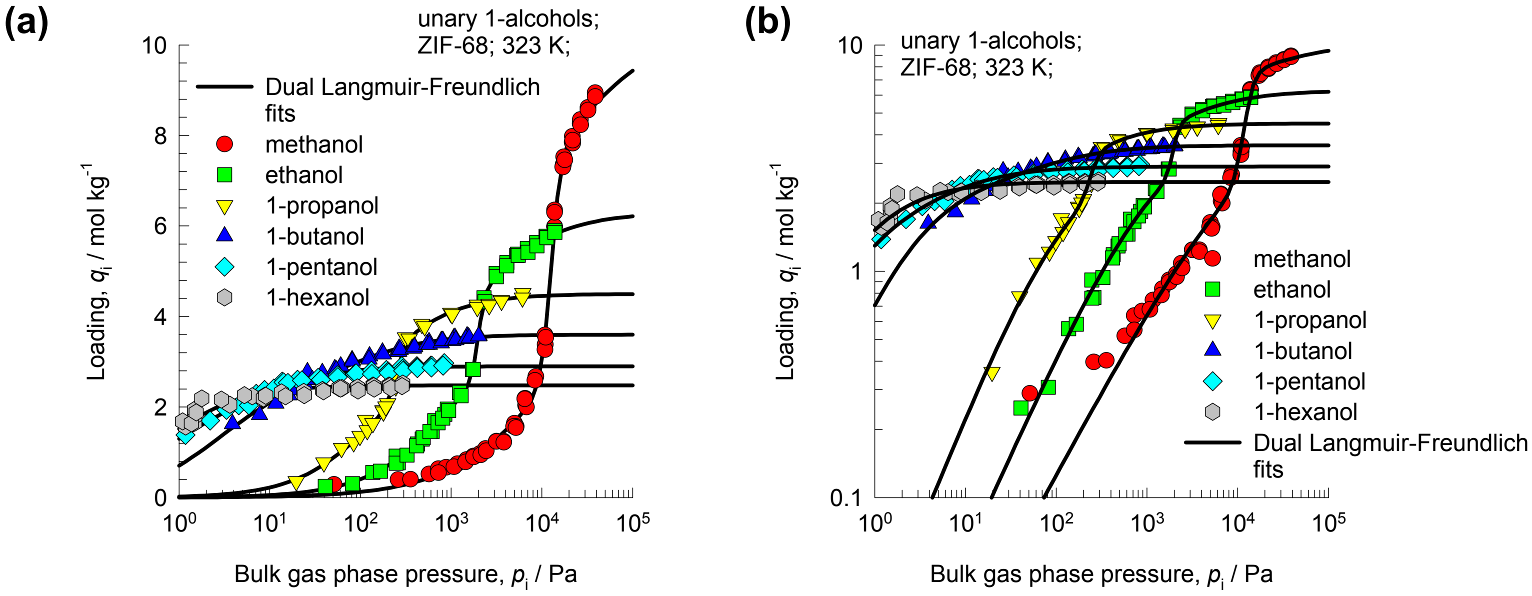

1-alcohols mixture adsorption in ZIF-68

ESI Figure 11

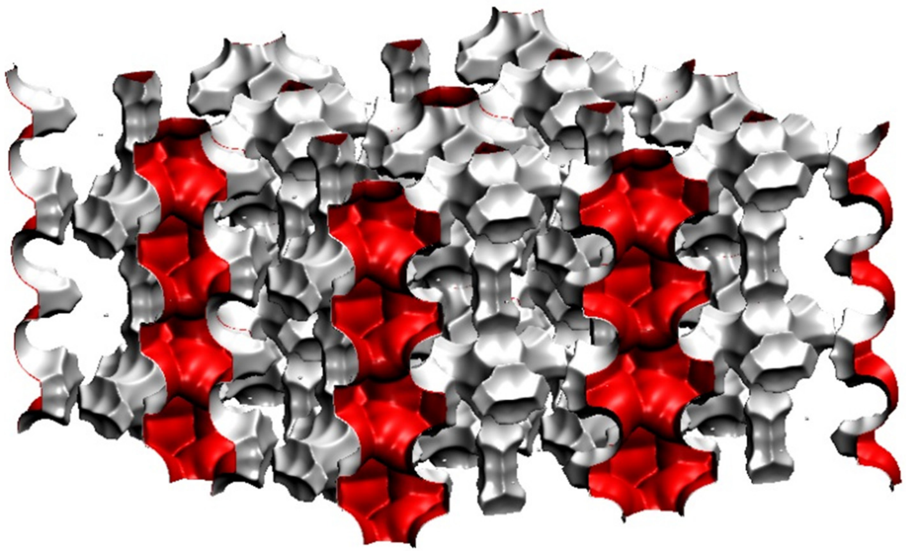

ZIF-68 landscape with intersecting channels

(a)

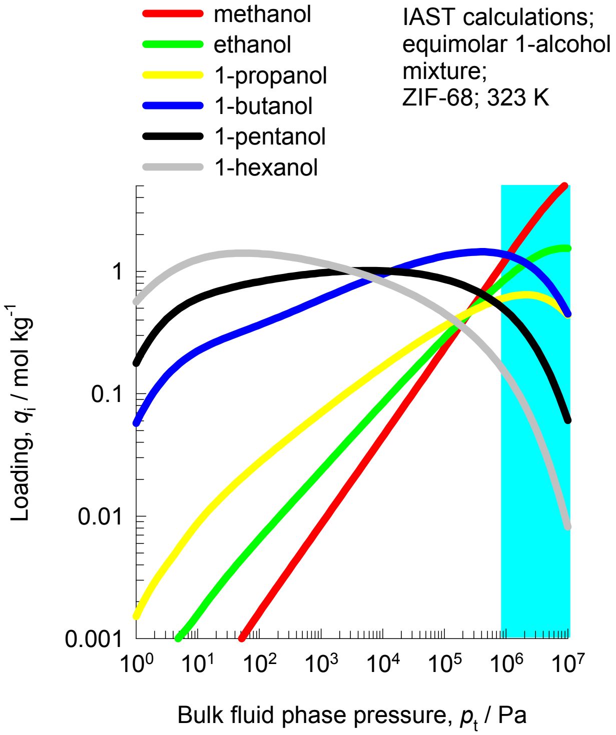

(b)

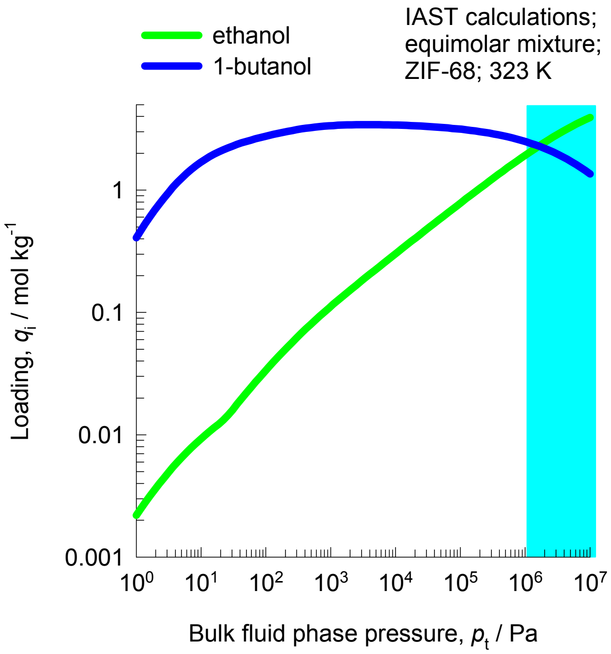

1-alcohols mixture uptake n ZIF-68

ESI Figure 12

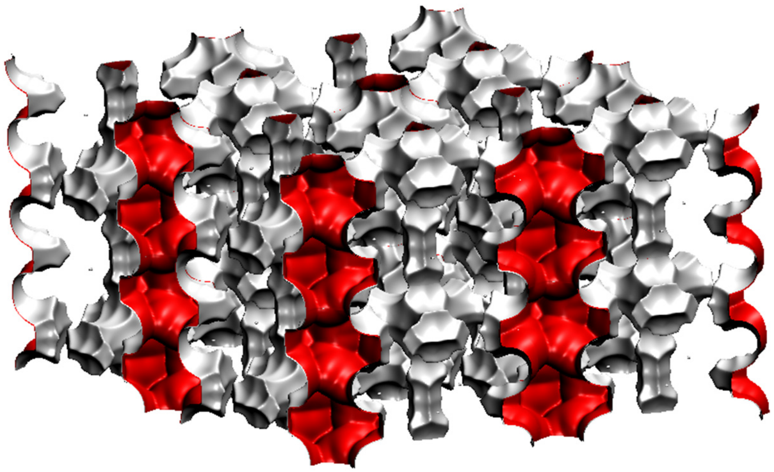

ZIF-68 landscape with intersecting channels

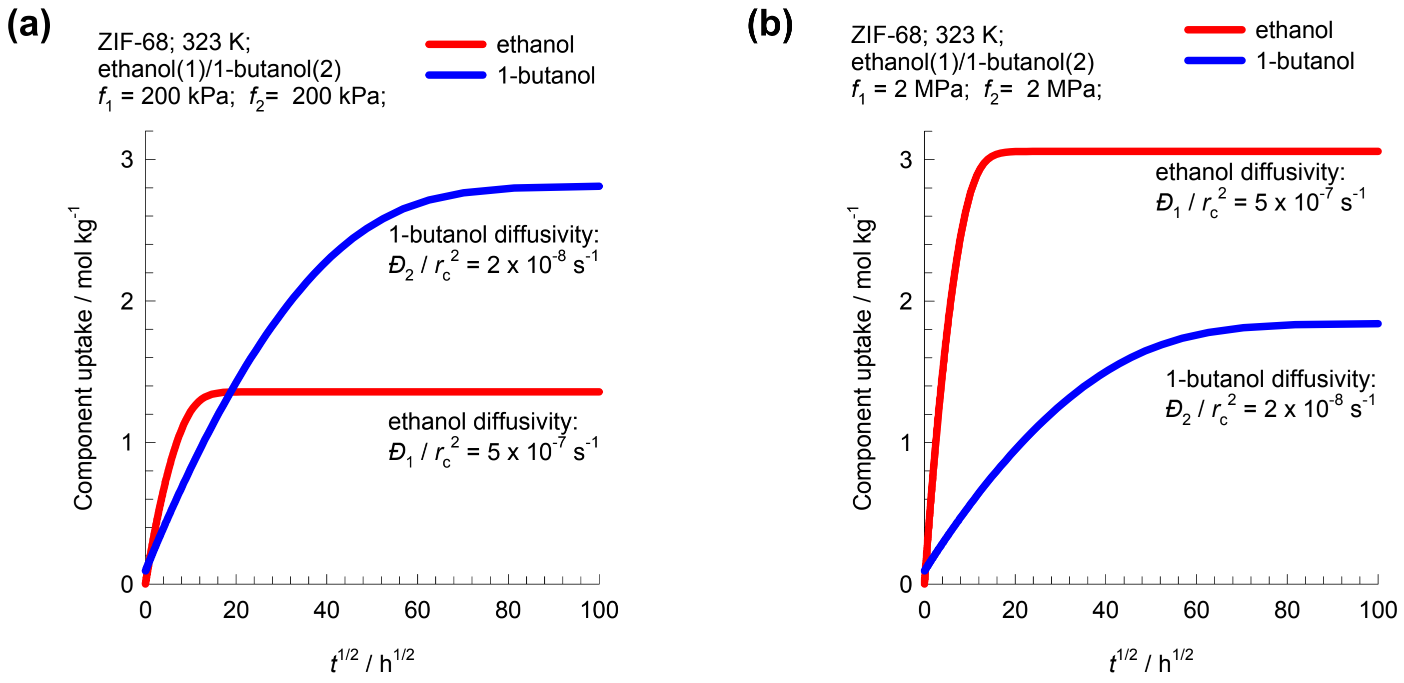

Water and benzene isotherms in CuBTC

ESI Figure 13

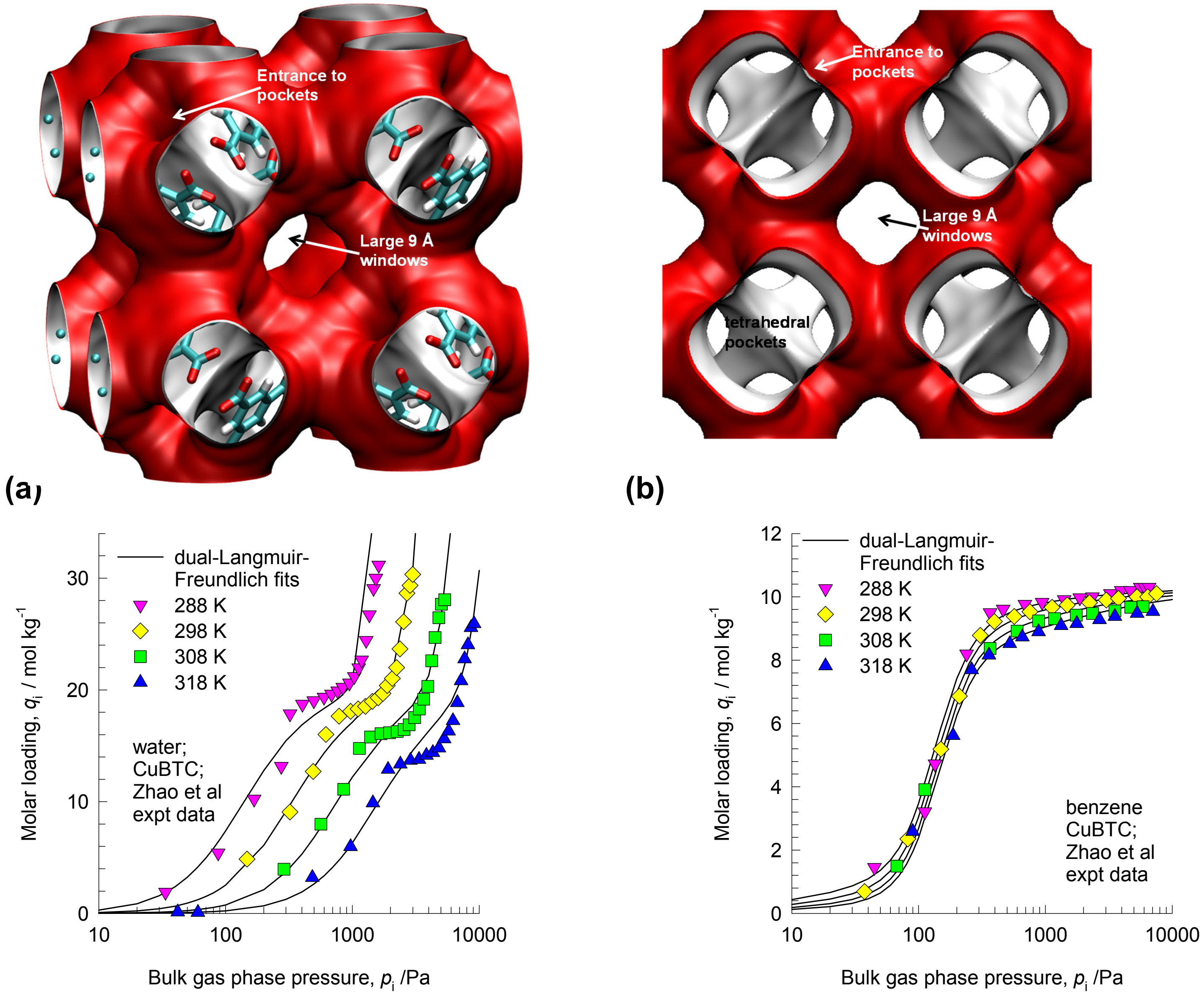

Water/benzene selectivities in CuBTC

ESI Figure 14

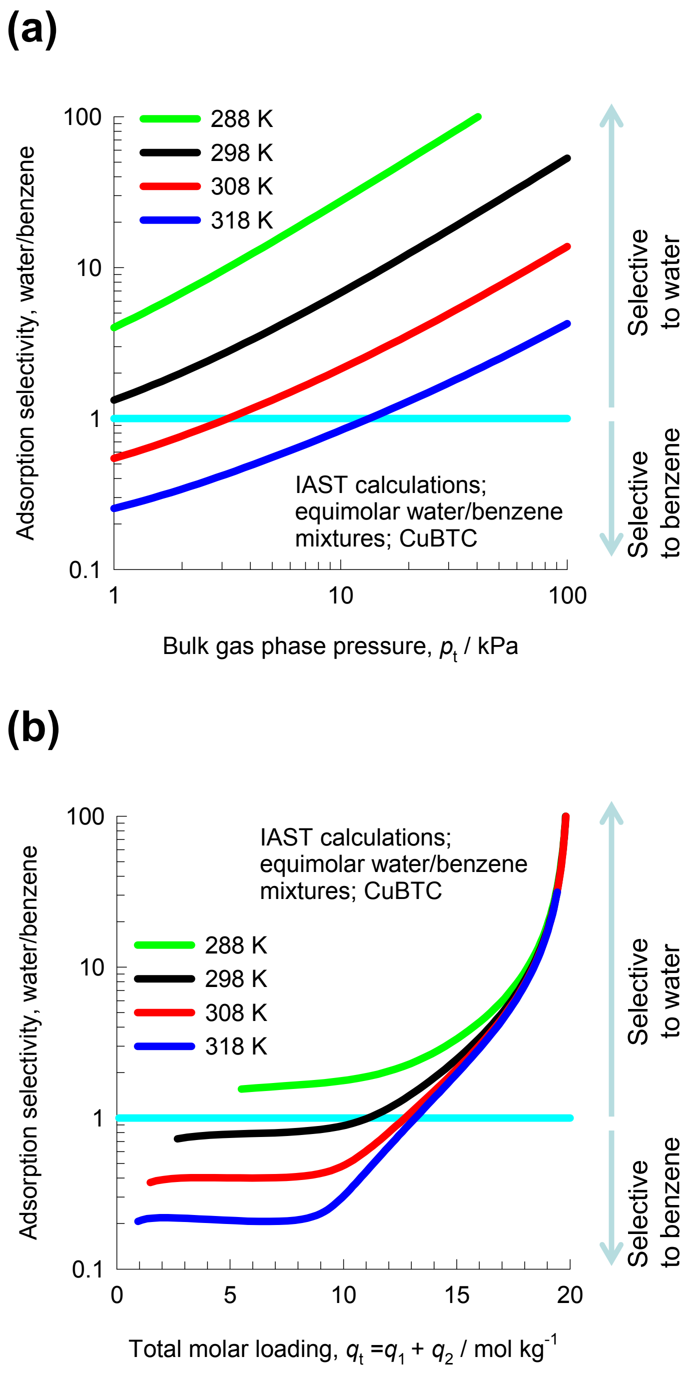

Water/benzene breakthroughs in CuBTC

ESI Figure 15

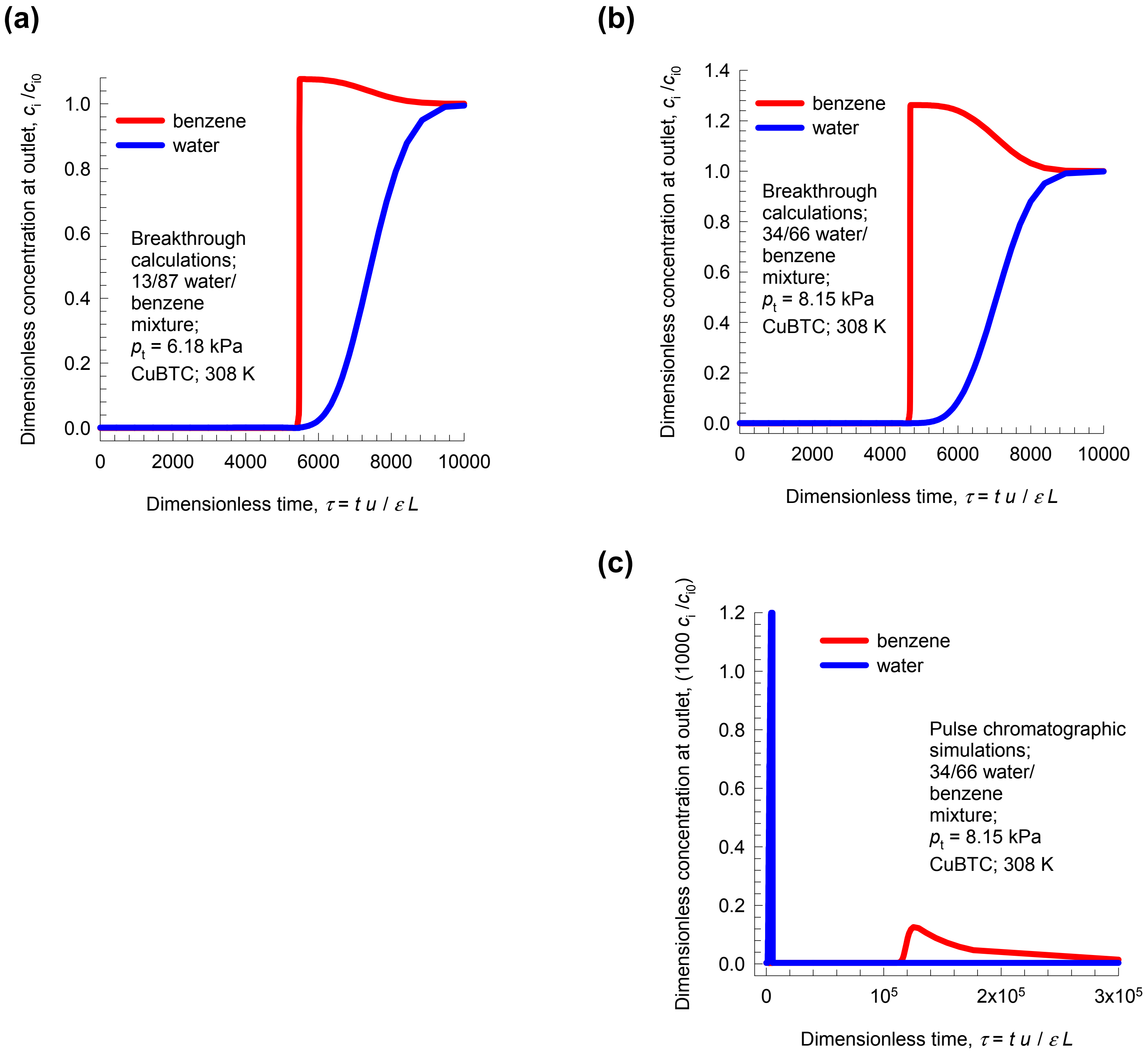

Water, alcohols isotherms in FAU

ESI Figure 16

12-ring
window of FAU

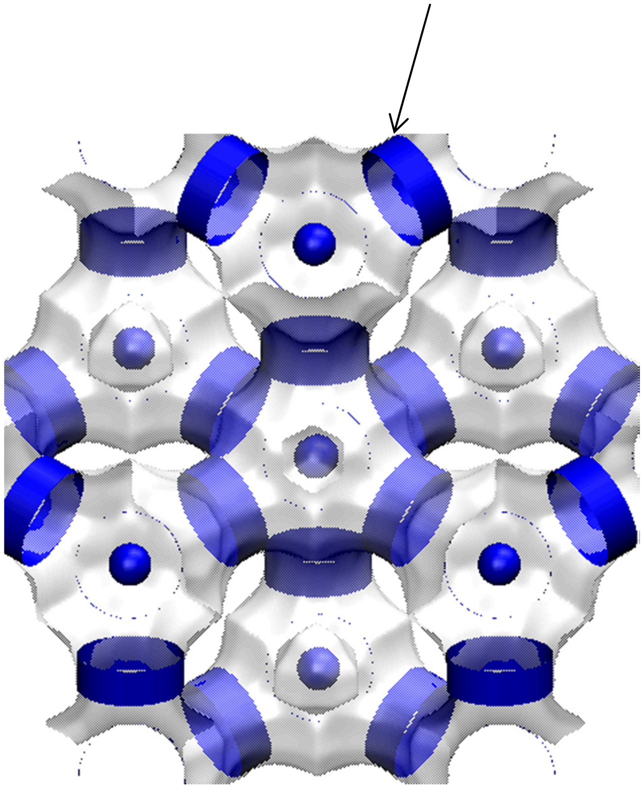

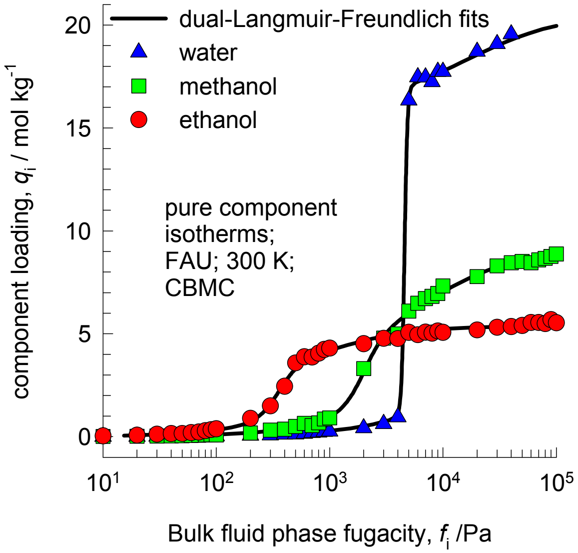

There are 8 cages per unit cell. The volume of one FAU cage is 786 Å^3, larger in size than that of CHA (316.4 Å^3) and DDR (278 Å^3).

Water/alcohols separations in FAU

ESI Figure 17

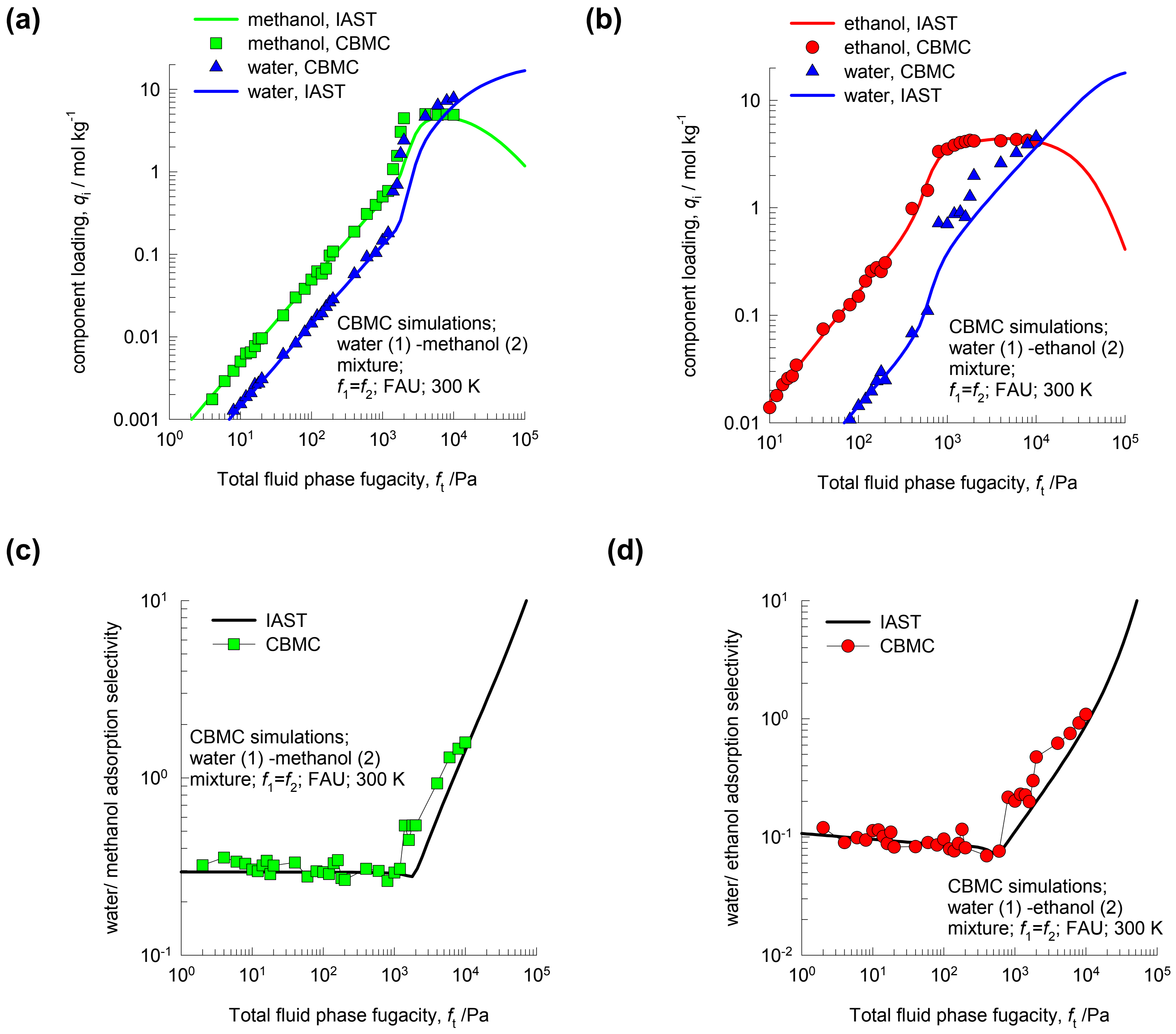

Water/alcohols intra-crystalline diffusivities in FAU

(a)

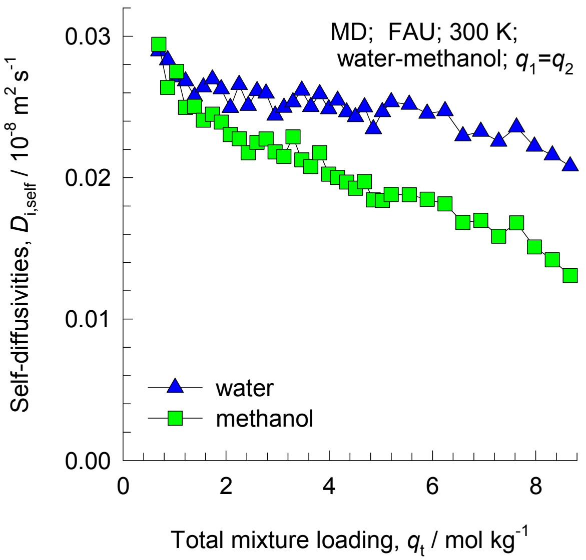

(b)

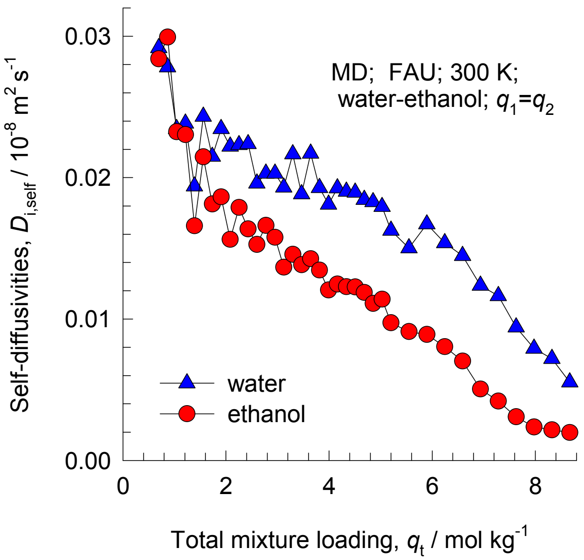

Water, methanol, ethanol isotherms in DDR

ESI Figure 19

There are 12 cages per unit cell. The volume of one DDR cage is 278 Å^3, significantly smaller than that of a single cage of FAU (786 Å^3), or ZIF-8 (1168 Å^3).

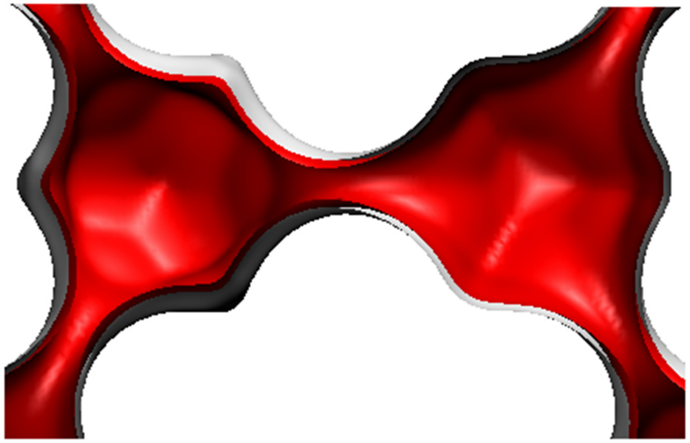

The volume of one DDR cage is 278 Å^3, significantly smaller than that of a single cage of FAU (786 Å^3), or ZIF-8 (1168 Å^3).

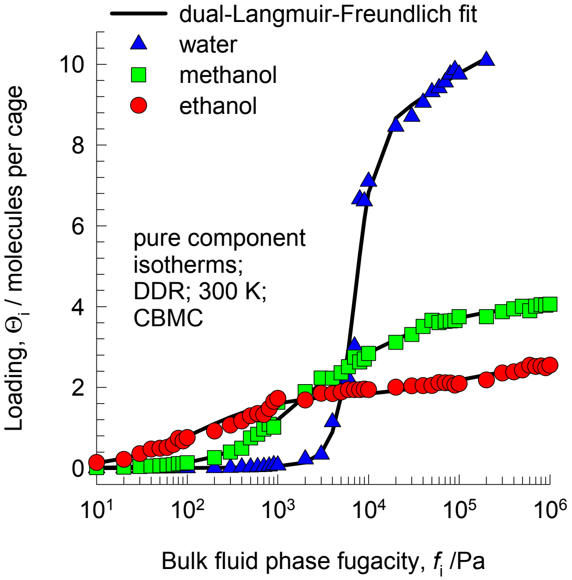

Water/alcohols separations in DDR

ESI Figure 20

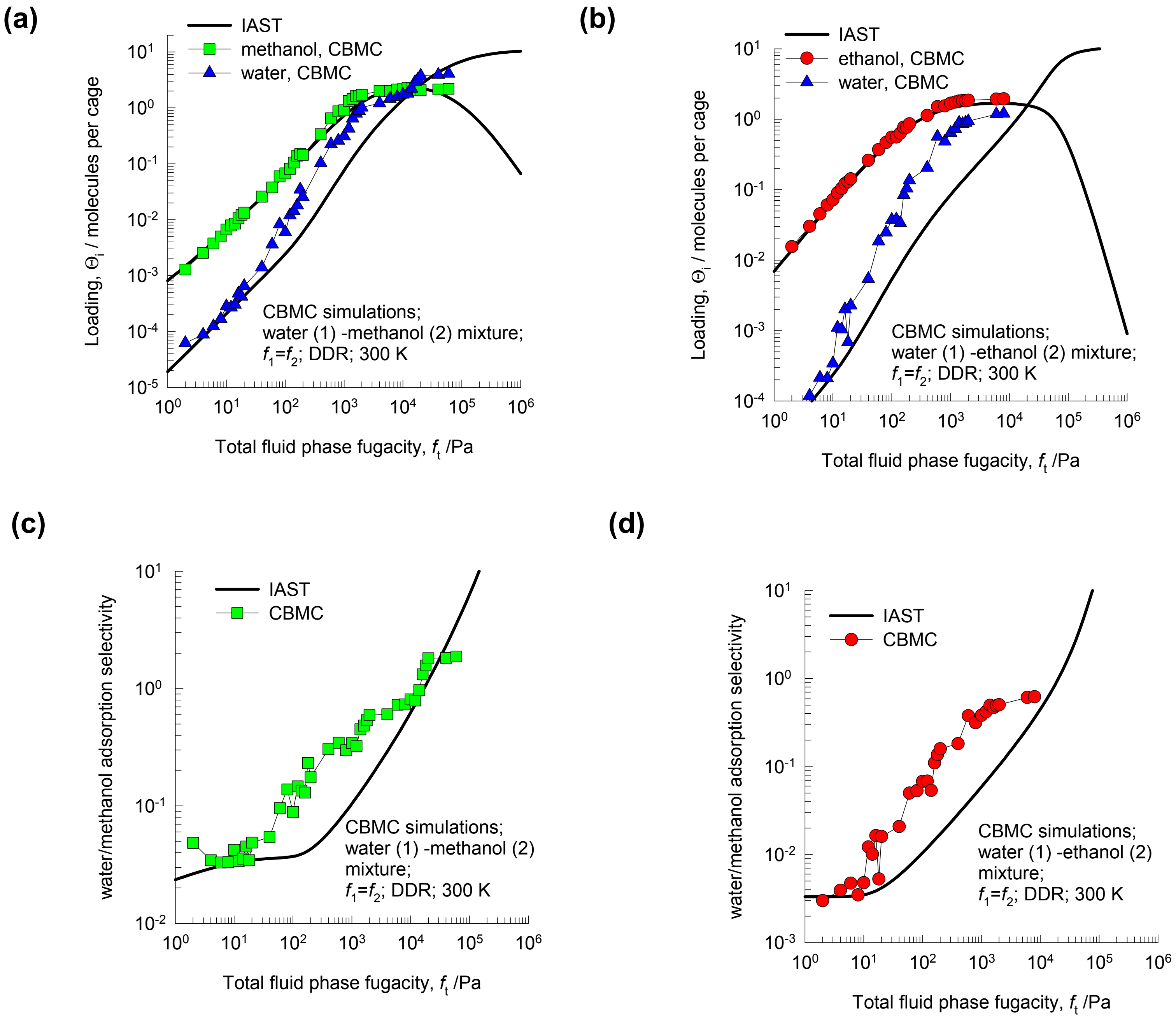

Water/alcohol diffusivities in DDR

ESI Figure 21

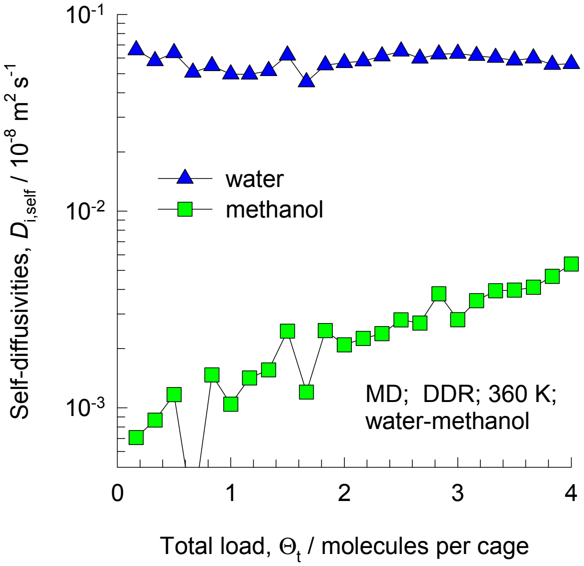

Water, methanol, ethanol isotherms in MFI

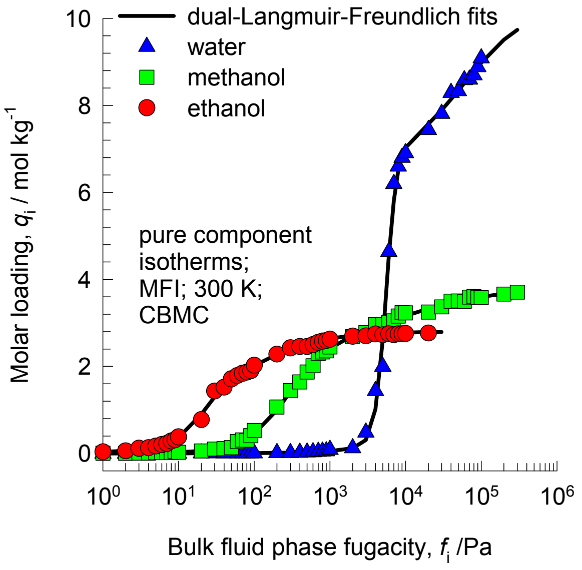

water

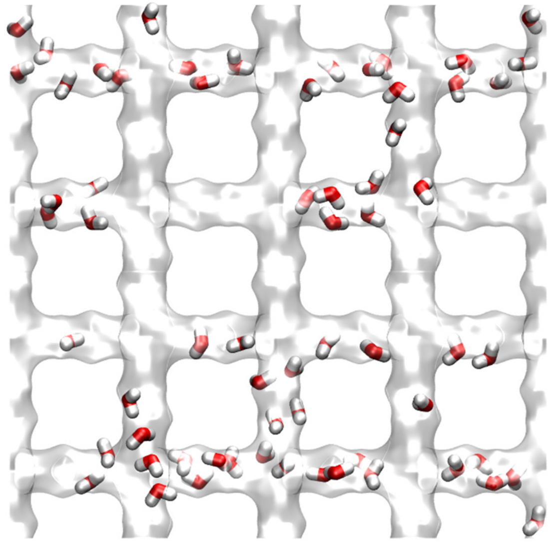

methanol

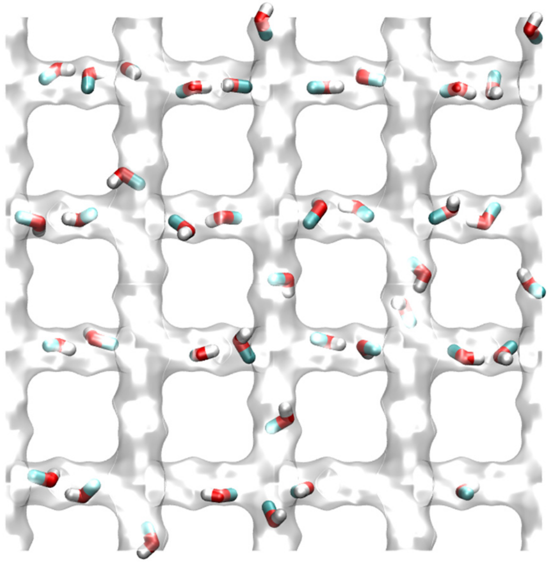

ethanol

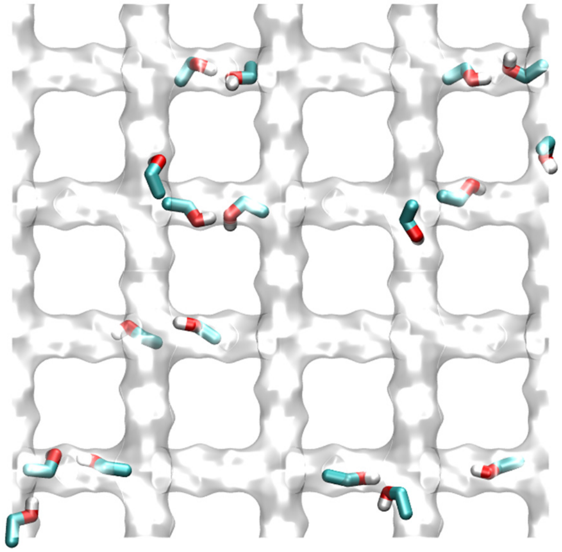

Water/alcohols separations in MFI

ESI Figure 23

(a)

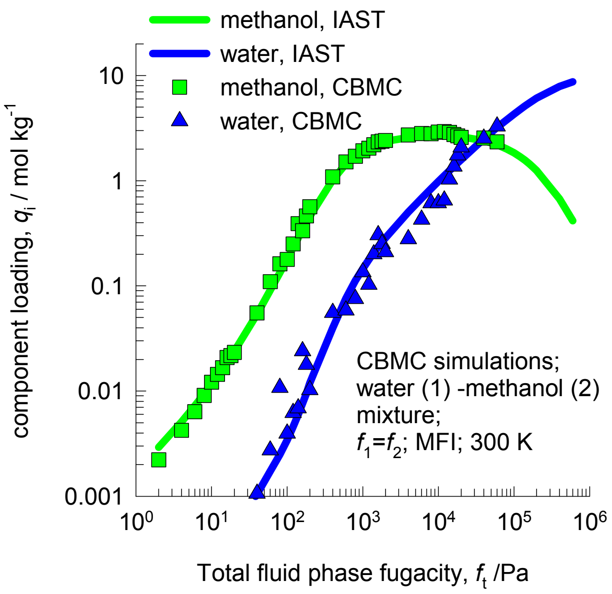

(b)

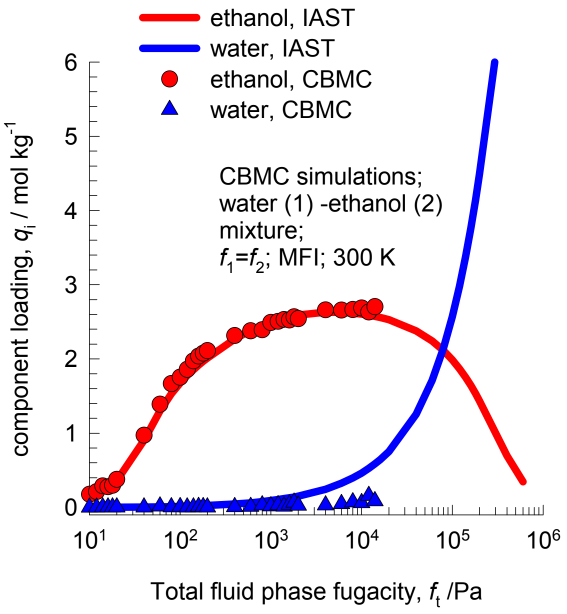

water/methanol

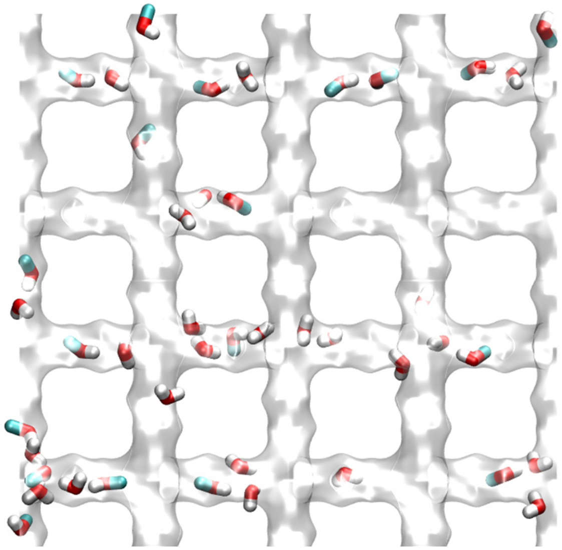

water/ethanol

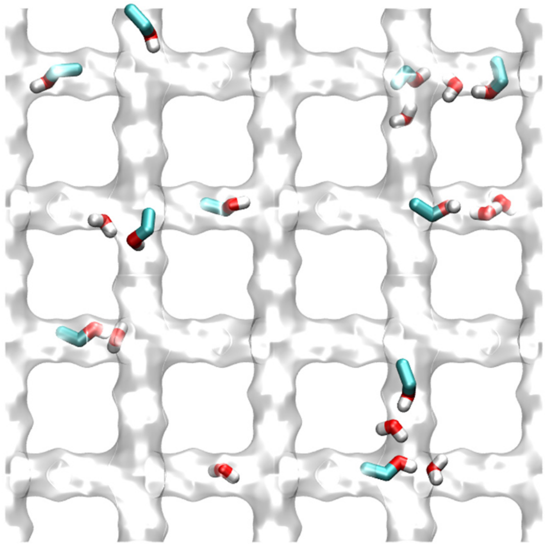

Water/alcohol diffusivities in MFI

ESI Figure 24

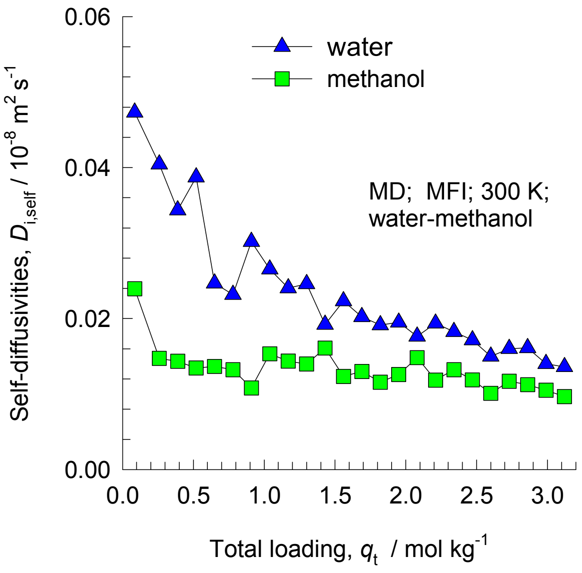

Water, alcohols isotherms in FER

ESI Figure 25

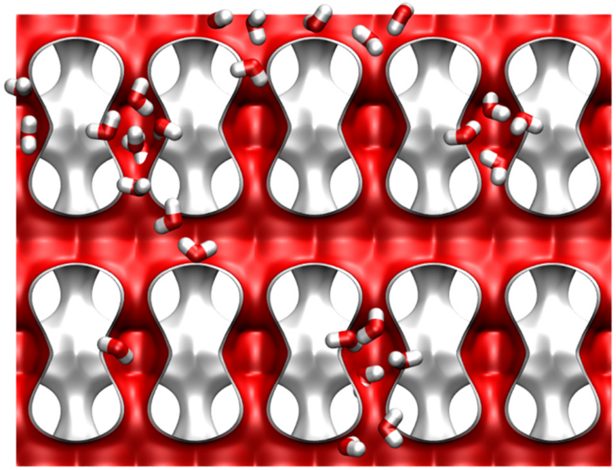

water

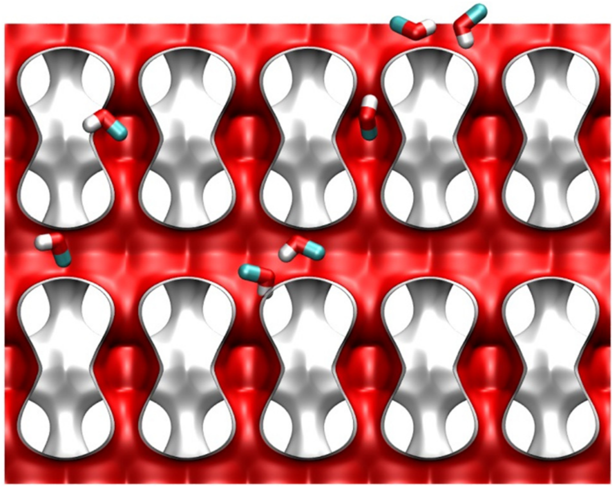

methanol

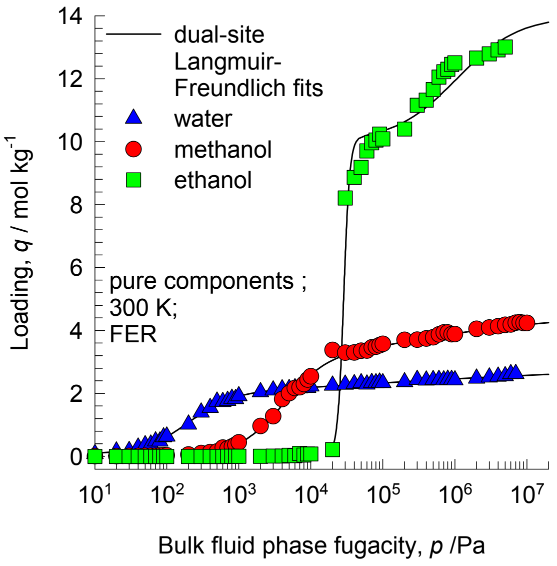

ethanol

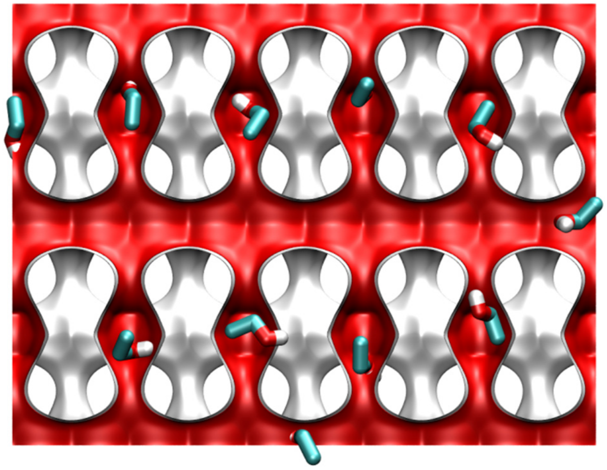

Water/alcohols separations in FER

ESI Figure 26

(a)

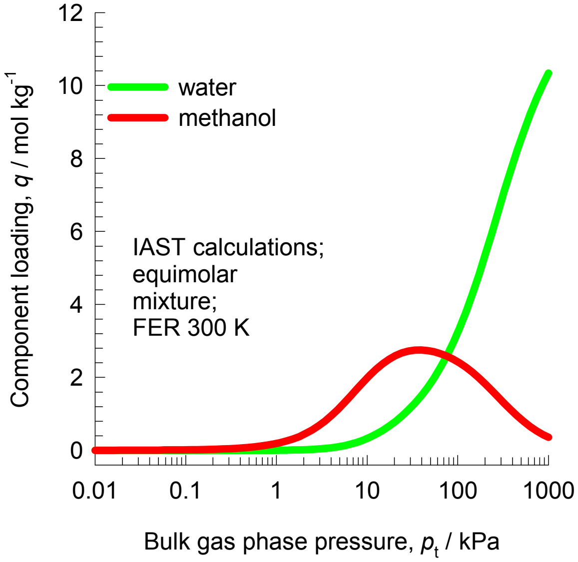

(b)

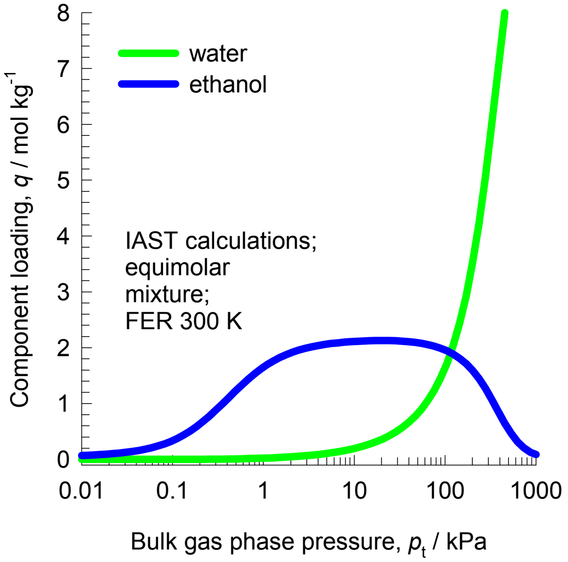

(c)

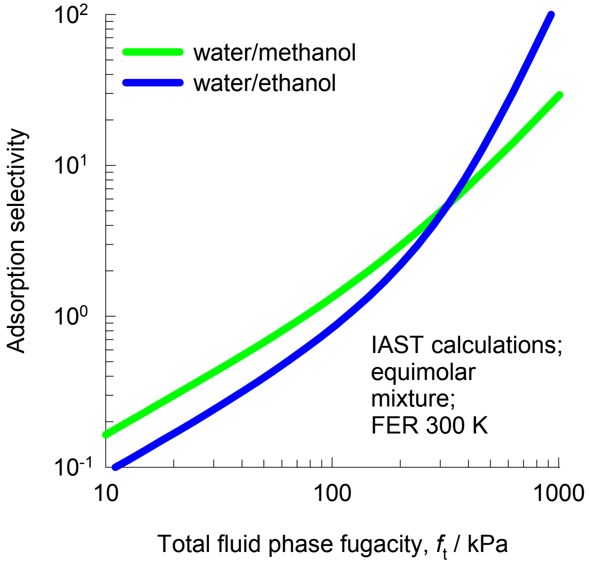

Water, alcohols diffusivities in FER

ESI Figure 27

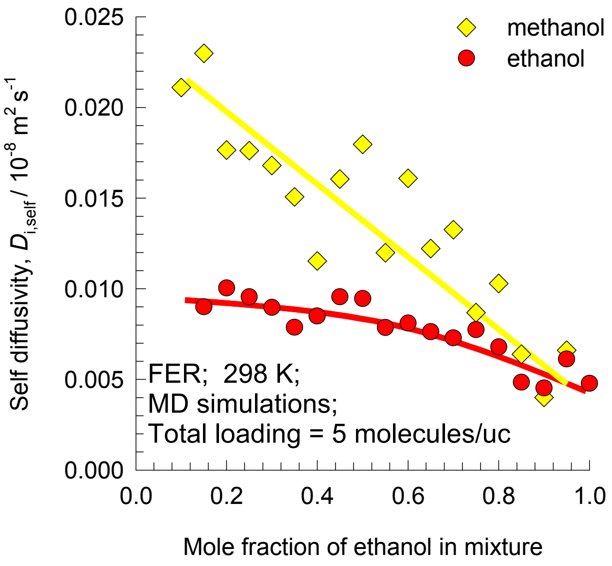

Water/alcohols separations in ZIF-71

(a)

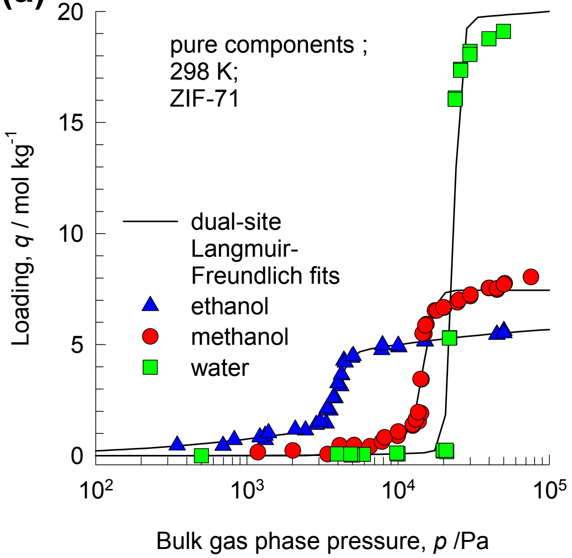

pure components ;
298 K;
ZIF-71

(b)

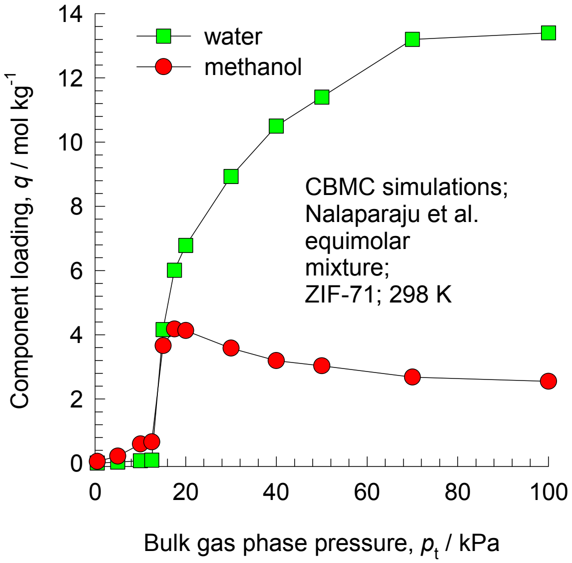

CBMC simulations;
Nalaparaju et al.
equimolar
mixture;
ZIF-71; 298 K

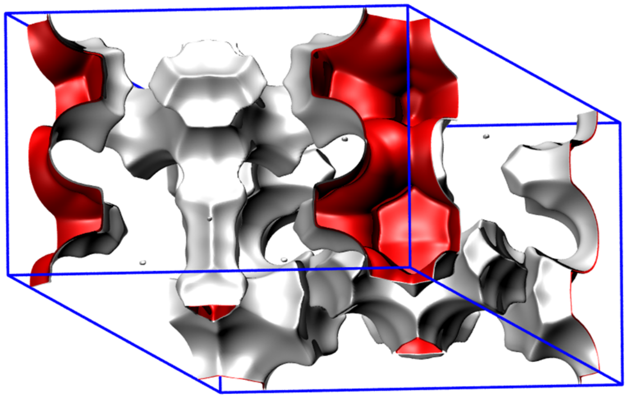

ZIF-71 landscape

(c)

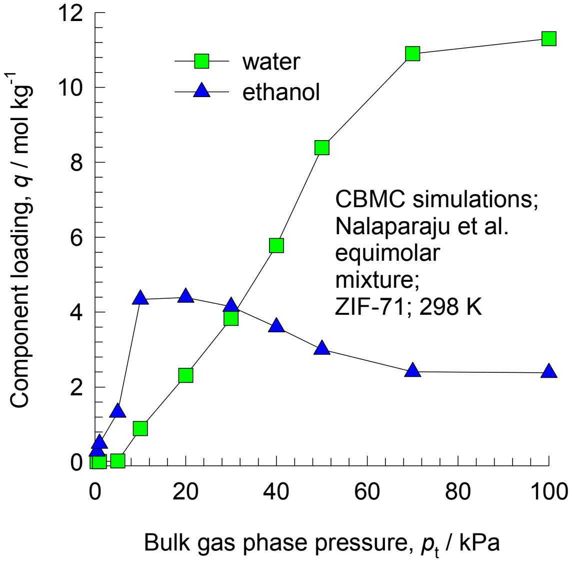

CBMC simulations;
Nalaparaju et al.
equimolar
mixture;
ZIF-71; 298 K

(d)

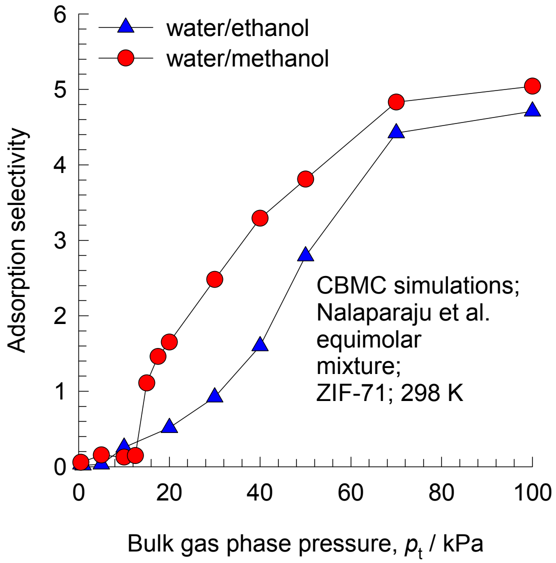

CBMC simulations;
Nalaparaju et al.
equimolar
mixture;
ZIF-71; 298 K

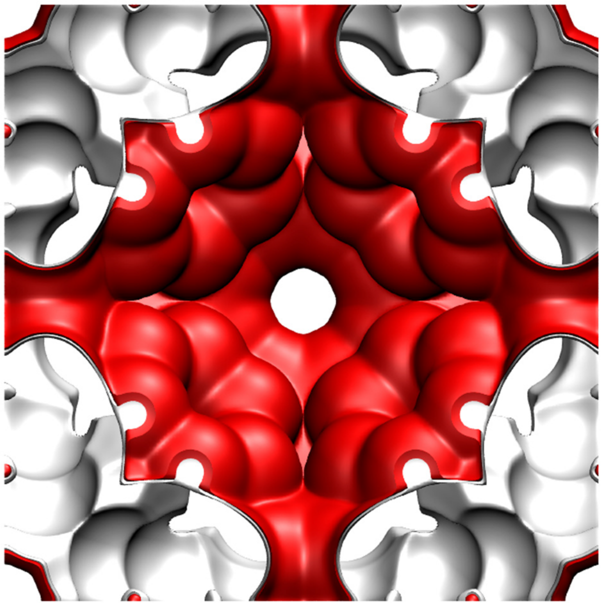

LTA landscape; cation positions

There are 8 cages per unit cell.
The volume of one LTA cage is 743 Å^3, intermediate in size between a single cage of ZIF-8 (1168 Å^3) and of DDR (278 Å^3).

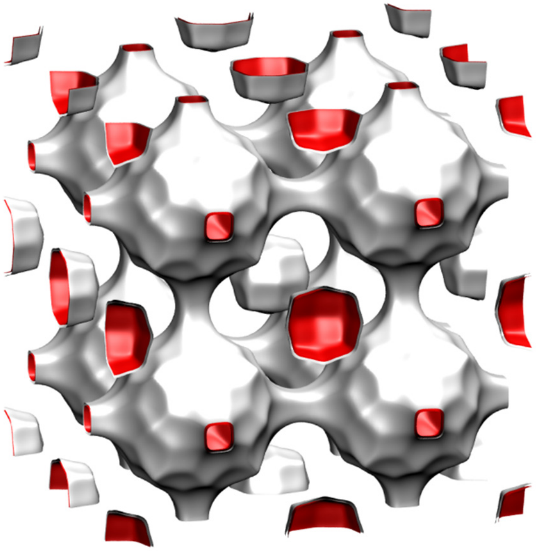

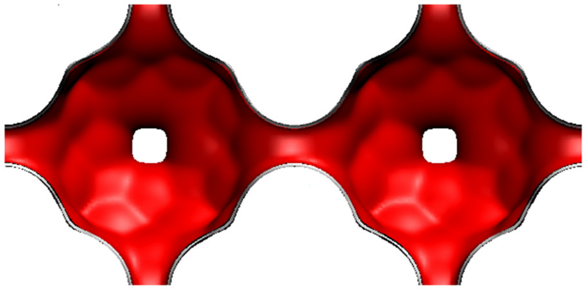

LTA-5A (32 Na$^+$, 32 Ca^{++})

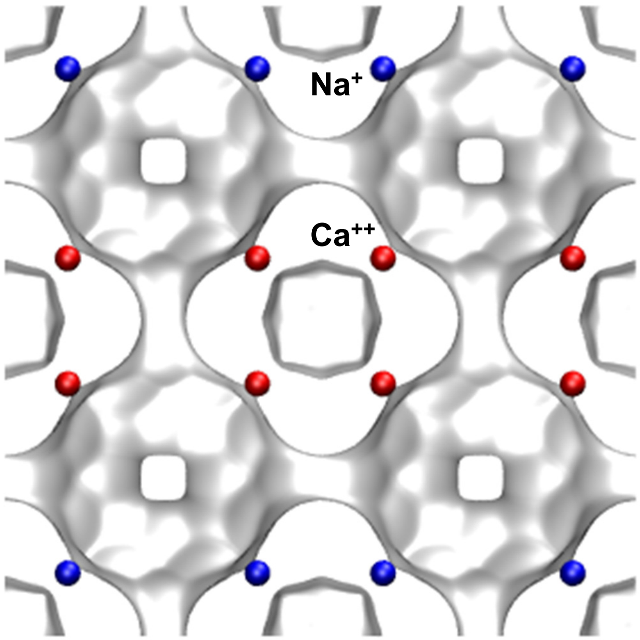

LTA-4A (96 Na$^+$)

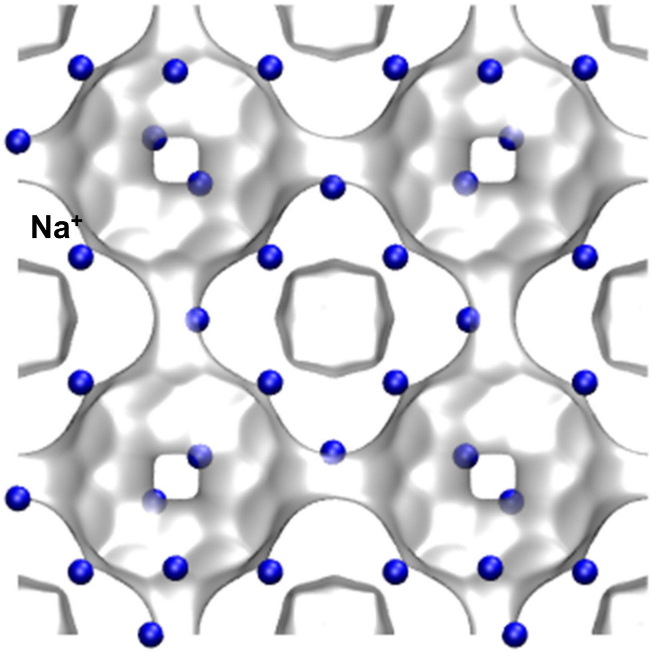

Water, ethanol isotherms in LTA-4A

ESI Figure 30

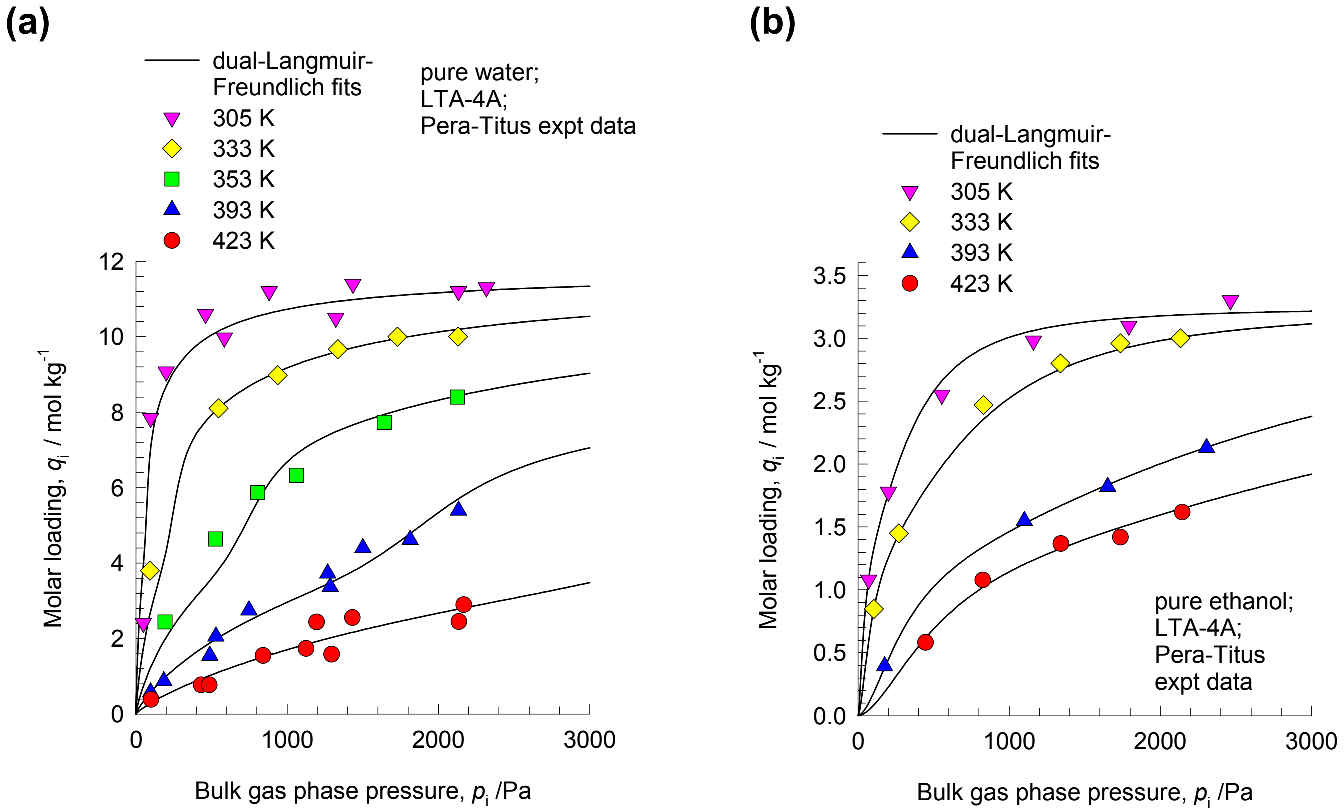

Water/ethanol mixture adsorption in LTA-4A

ESI Figure 31

(a)

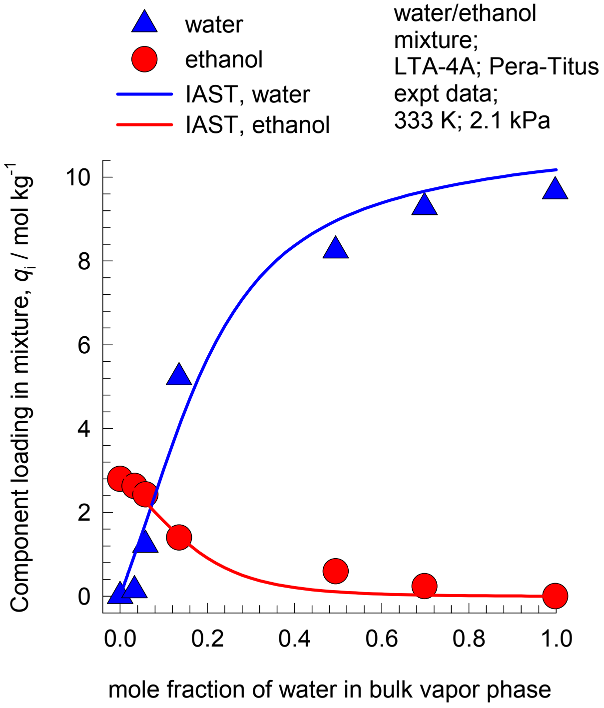

(b)

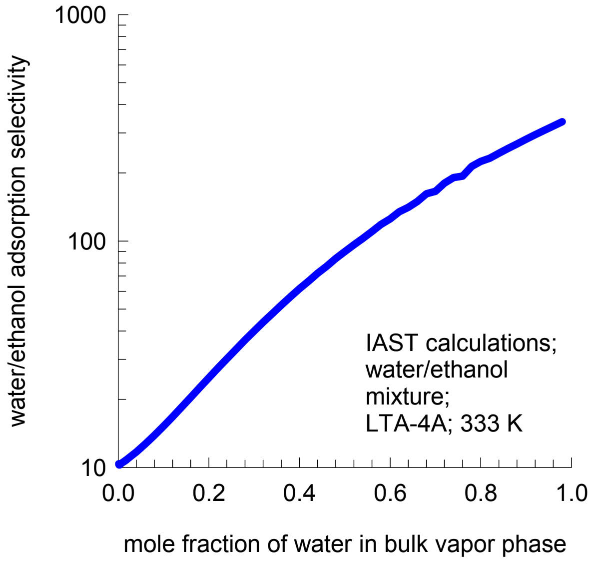

Water/ethanol pervaporation in LTA-4A; hybrid processing

ESI Figure 32

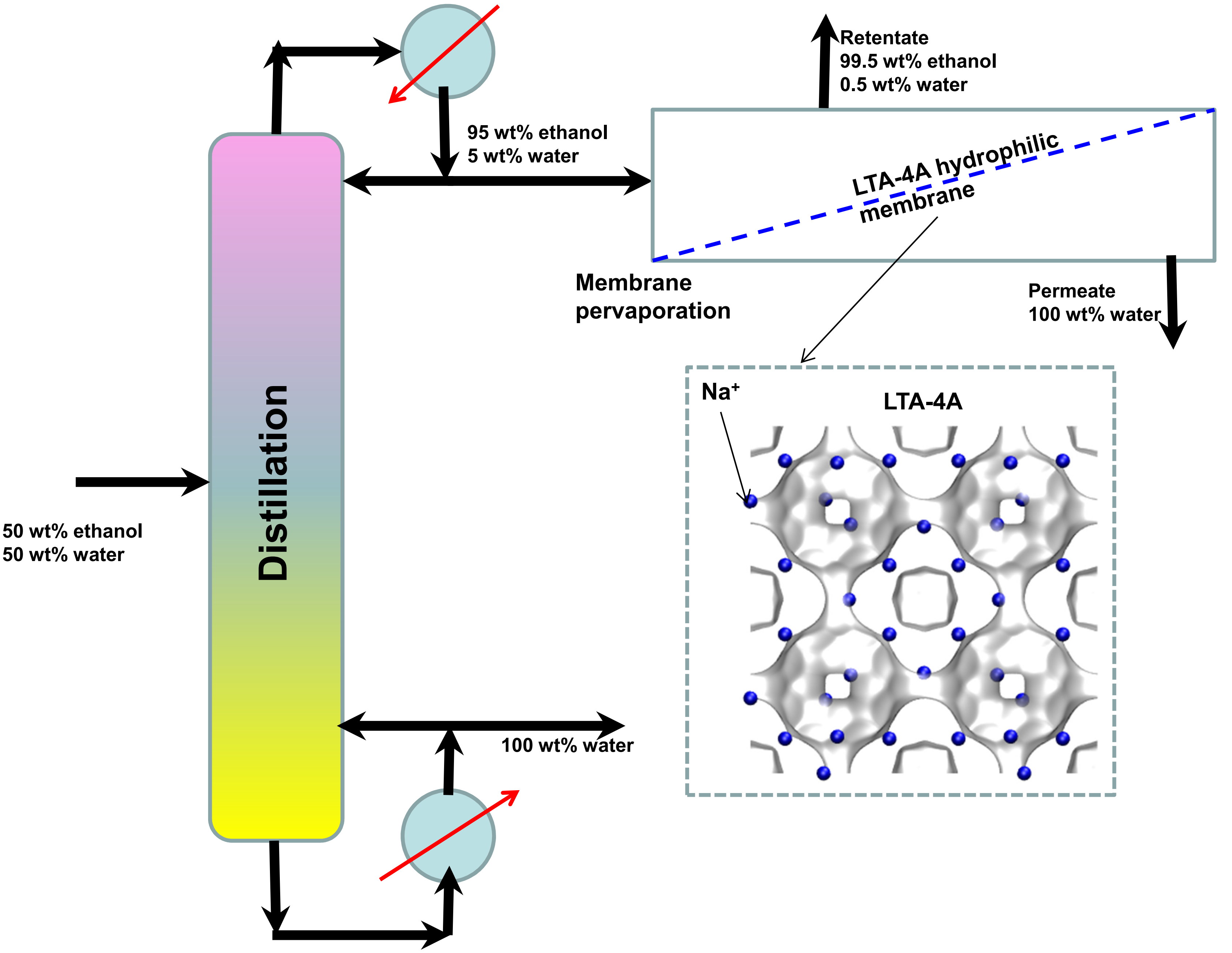

Retentate
99.5 wt% ethanol
0.5 wt% water

95 wt% ethanol
5 wt% water

LTA-4A hydrophilic membrane

Membrane
pervaporation

Permeate
100 wt% water

Distillation

50 wt% ethanol
50 wt% water

100 wt% water

Na$^+$

LTA-4A

Methanol/ethanol uptake in UCY-5

ESI Figure 33

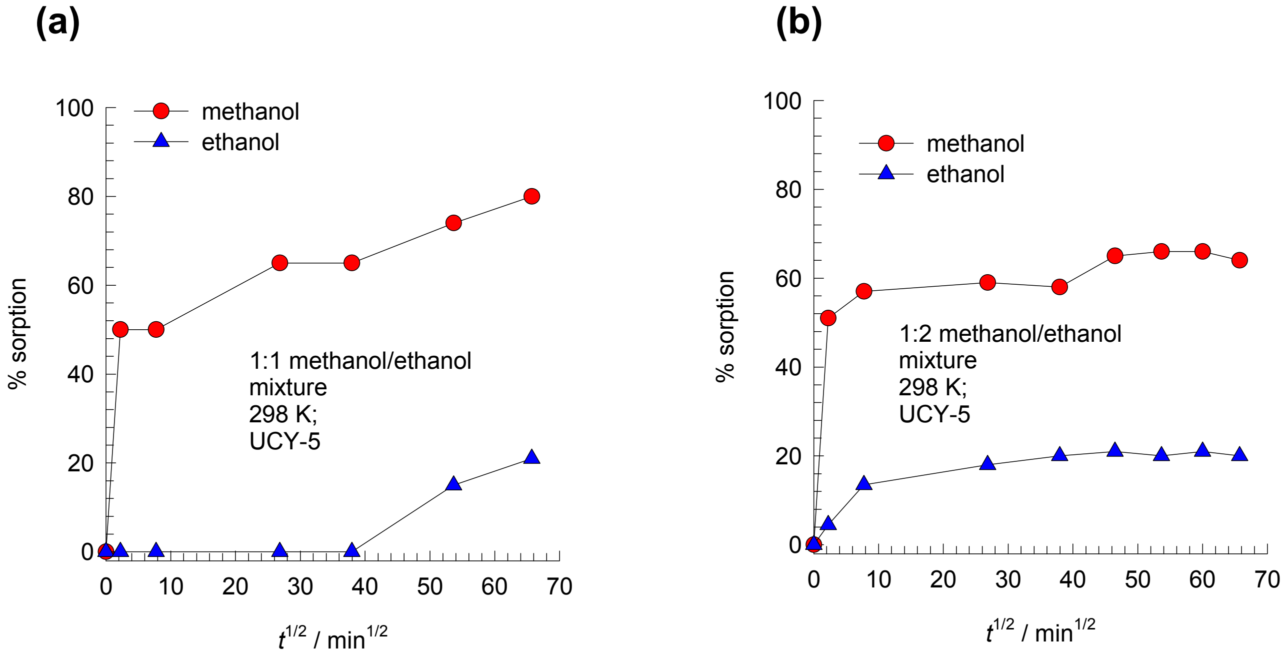

Methanol/ethanol separation in Ce(BTB)

ESI Figure 34

(a)

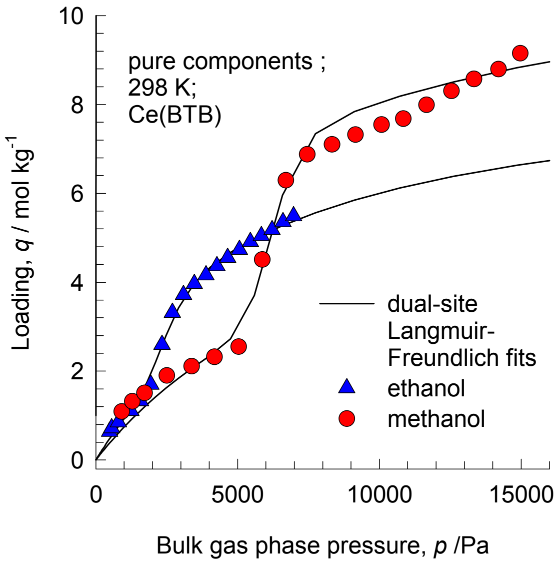

(b)

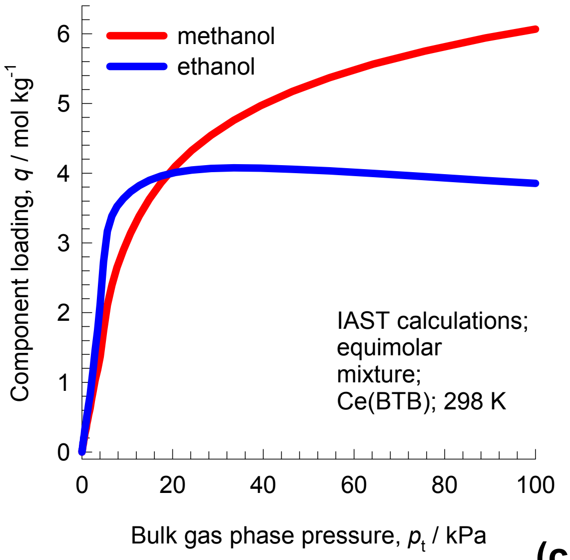

(c)

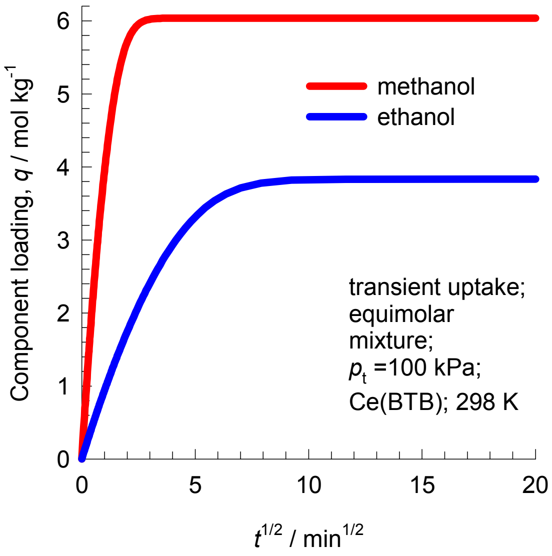

Water/alcohols separation in CID-1

ESI Figure 35

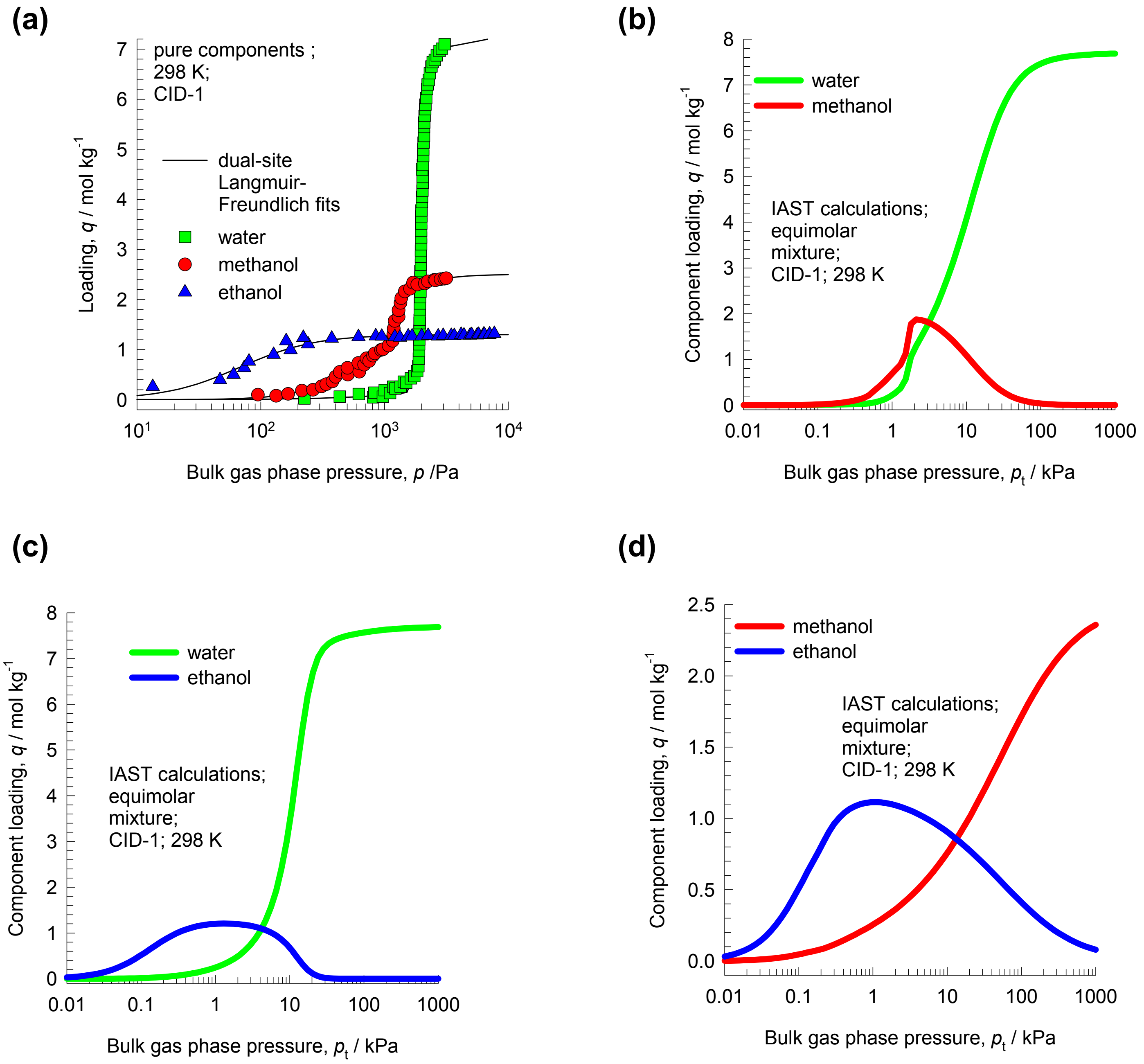

Water/alcohols separation in CID-1

ESI Figure 36

(a)

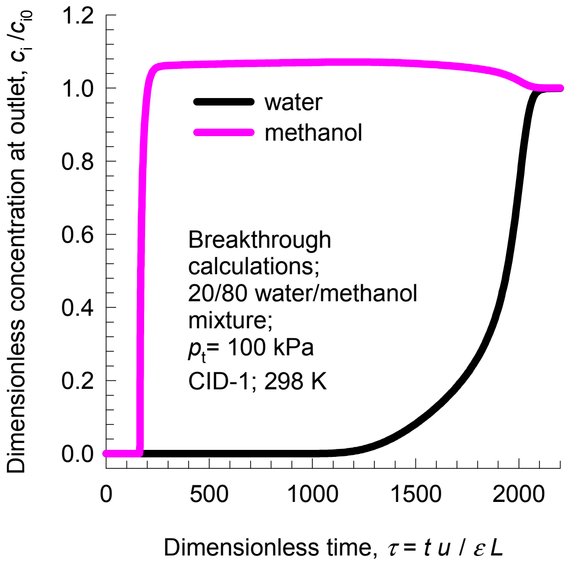

Breakthrough calculations; 20/80 water/methanol mixture; p_t= 100 kPa
CID-1; 298 K

(b)

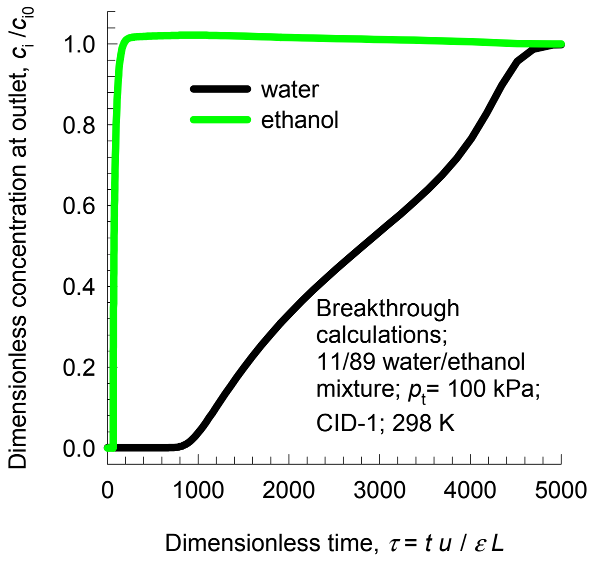

Breakthrough calculations; 11/89 water/ethanol mixture; p_t= 100 kPa;
CID-1; 298 K

(c)

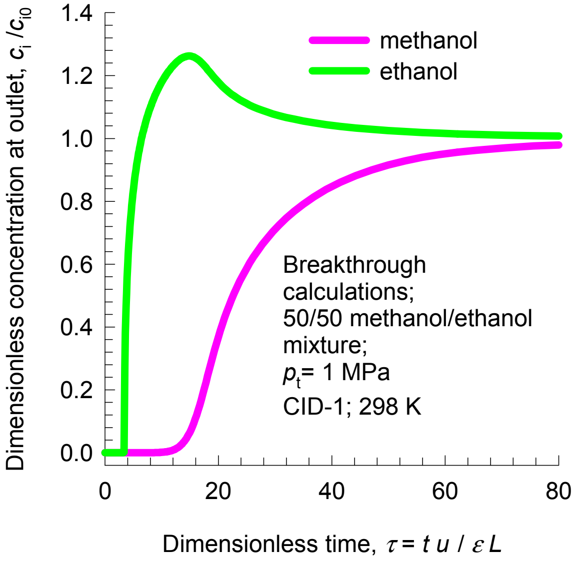

Breakthrough calculations; 50/50 methanol/ethanol mixture; p_t= 1 MPa
CID-1; 298 K

Water/methanol separation in Cu-GLA

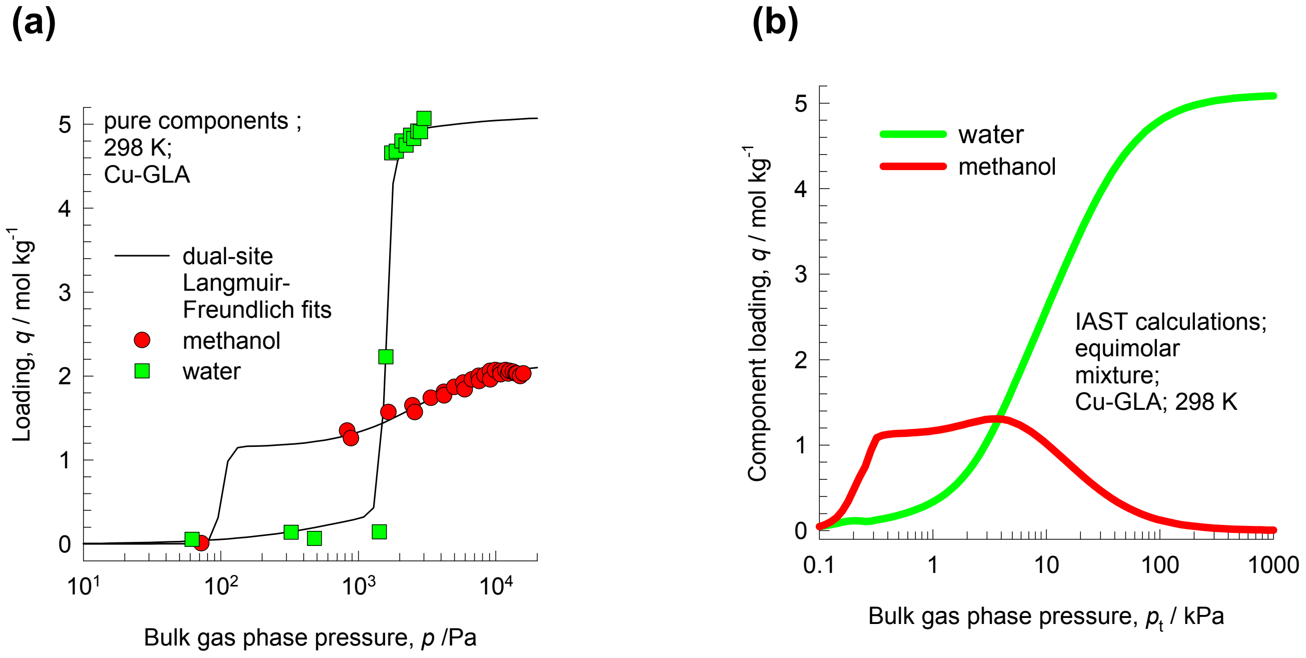

Water/alcohols, alcohol/alcohol separation in Co(pbdc)

ESI Figure 38

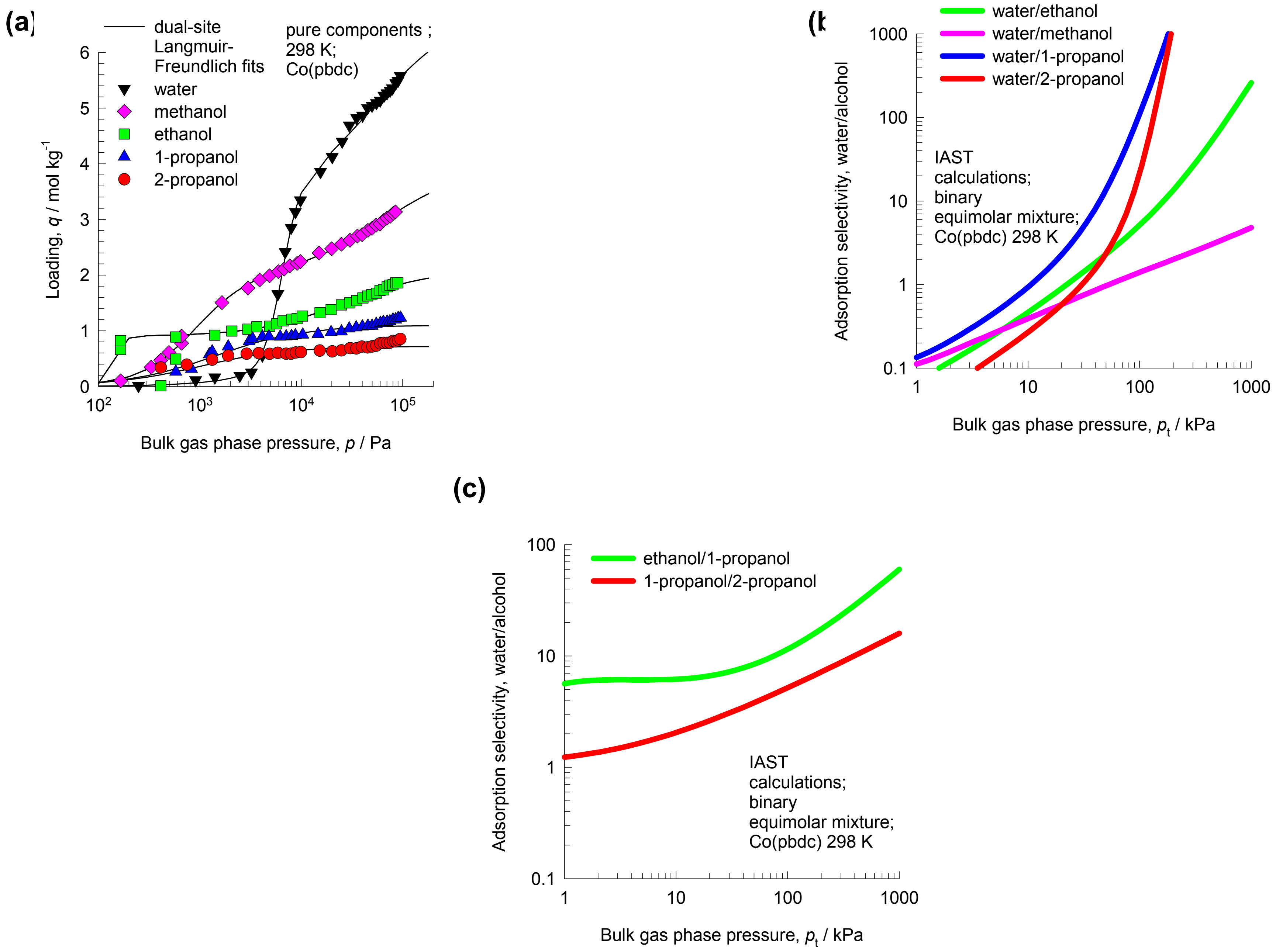

Water/alcohols, alcohol/alcohol separation in Co(pbdc)

ESI Figure 39

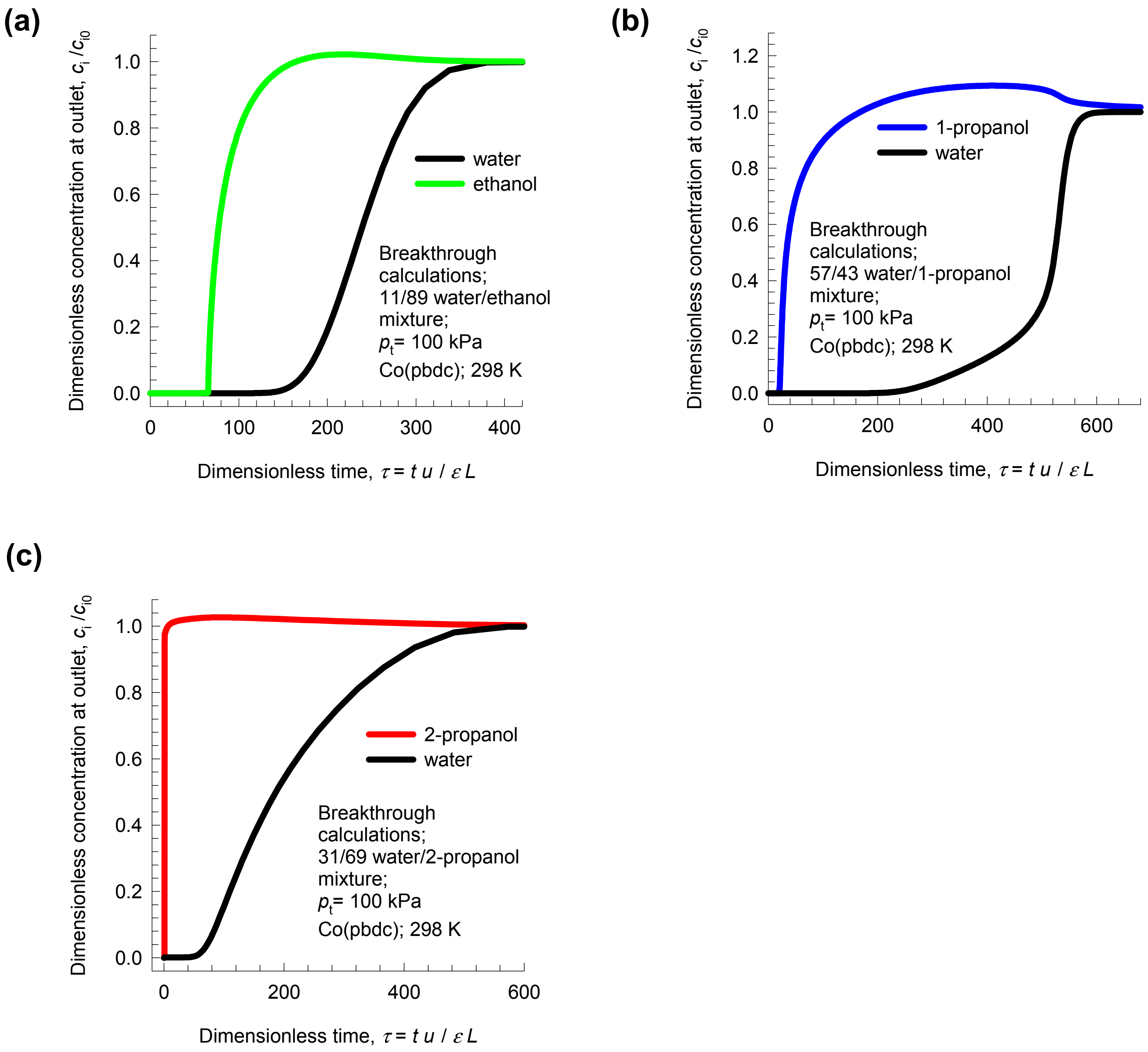

Water, alcohols isotherms in Zn(II)MOF

ESI Figure 40

(a)

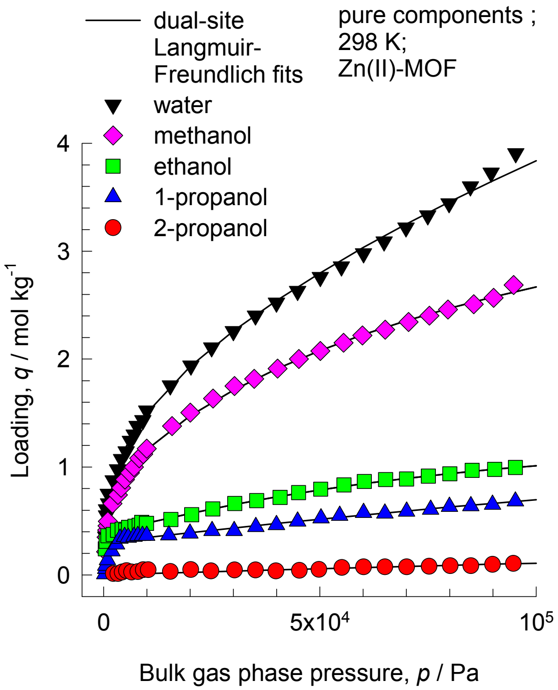

(b)

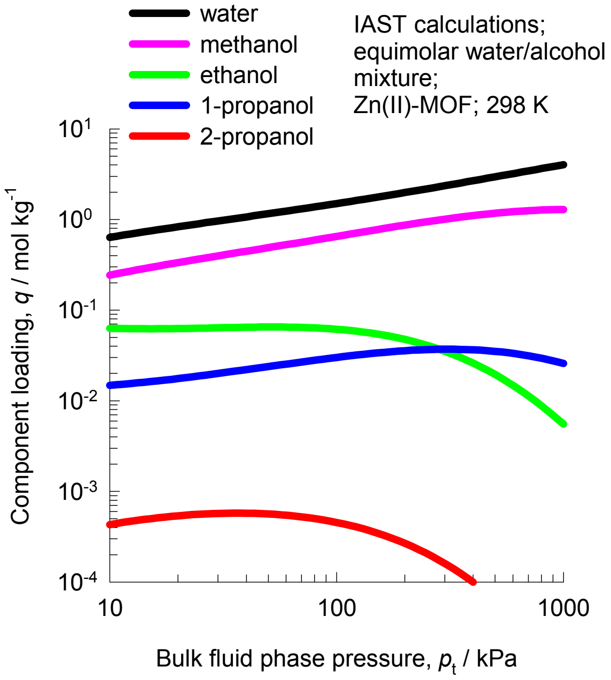

Water/alcohols separation in Zn(II)MOF

ESI Figure 41

(a)

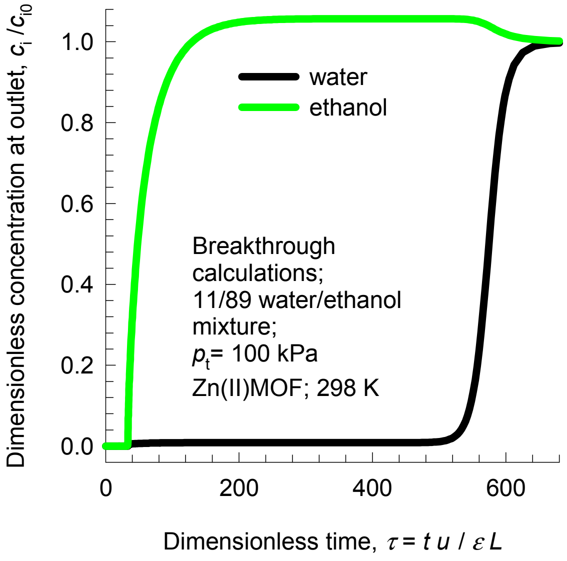

(b)

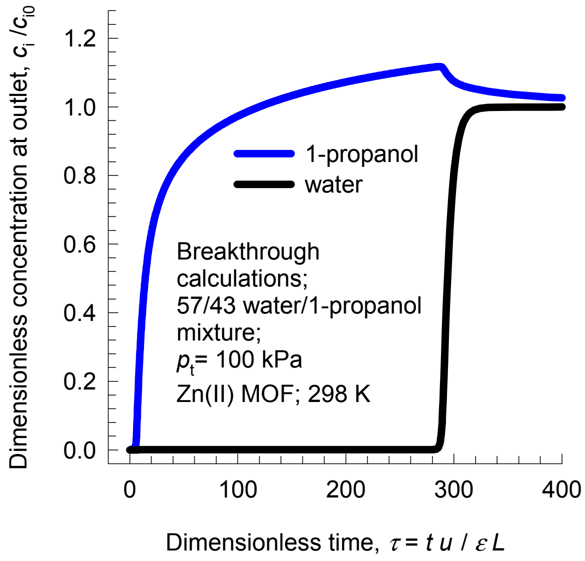

(c)

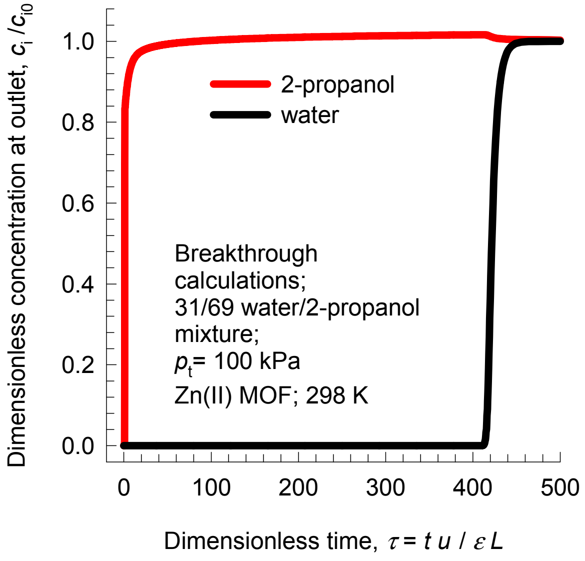

Water/alcohols, alcohol/alcohol separation in JUC-110

ESI Figure 42

(a)

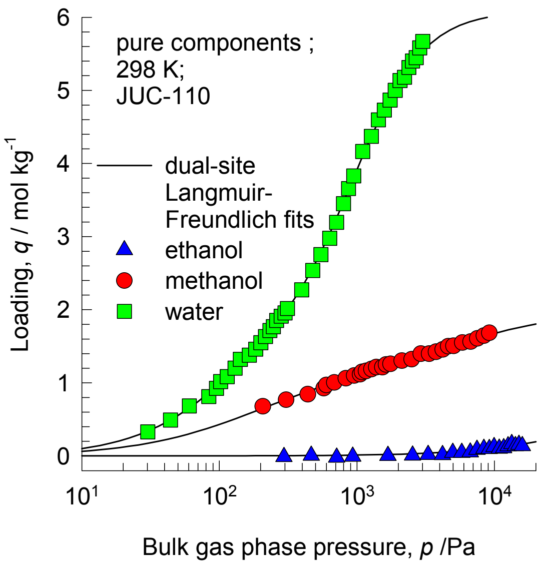

(b)

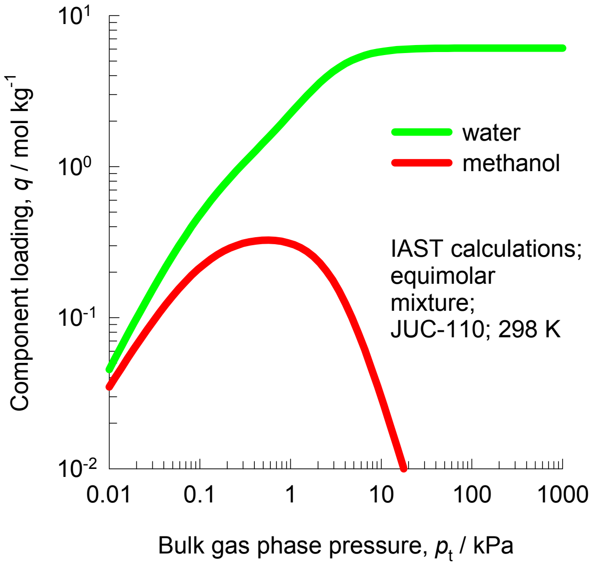

(c)

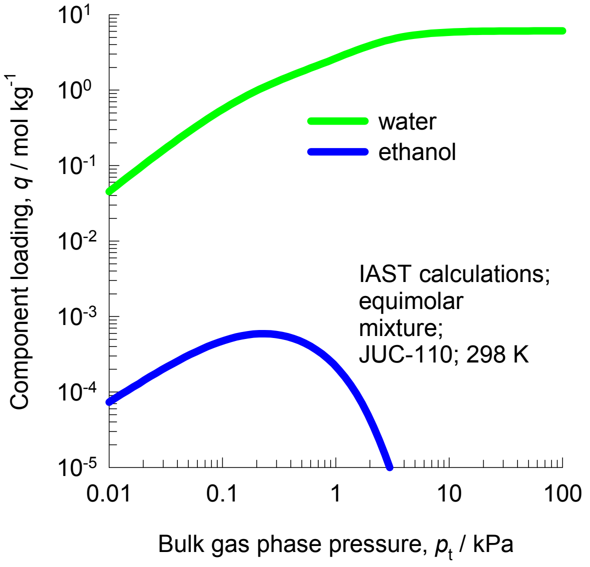

(d)

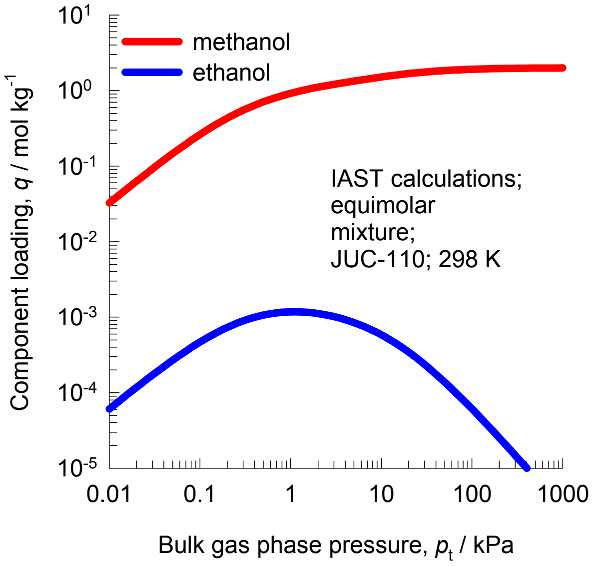

Water/alcohols, alcohol/alcohol separation in JUC-110

ESI Figure 43

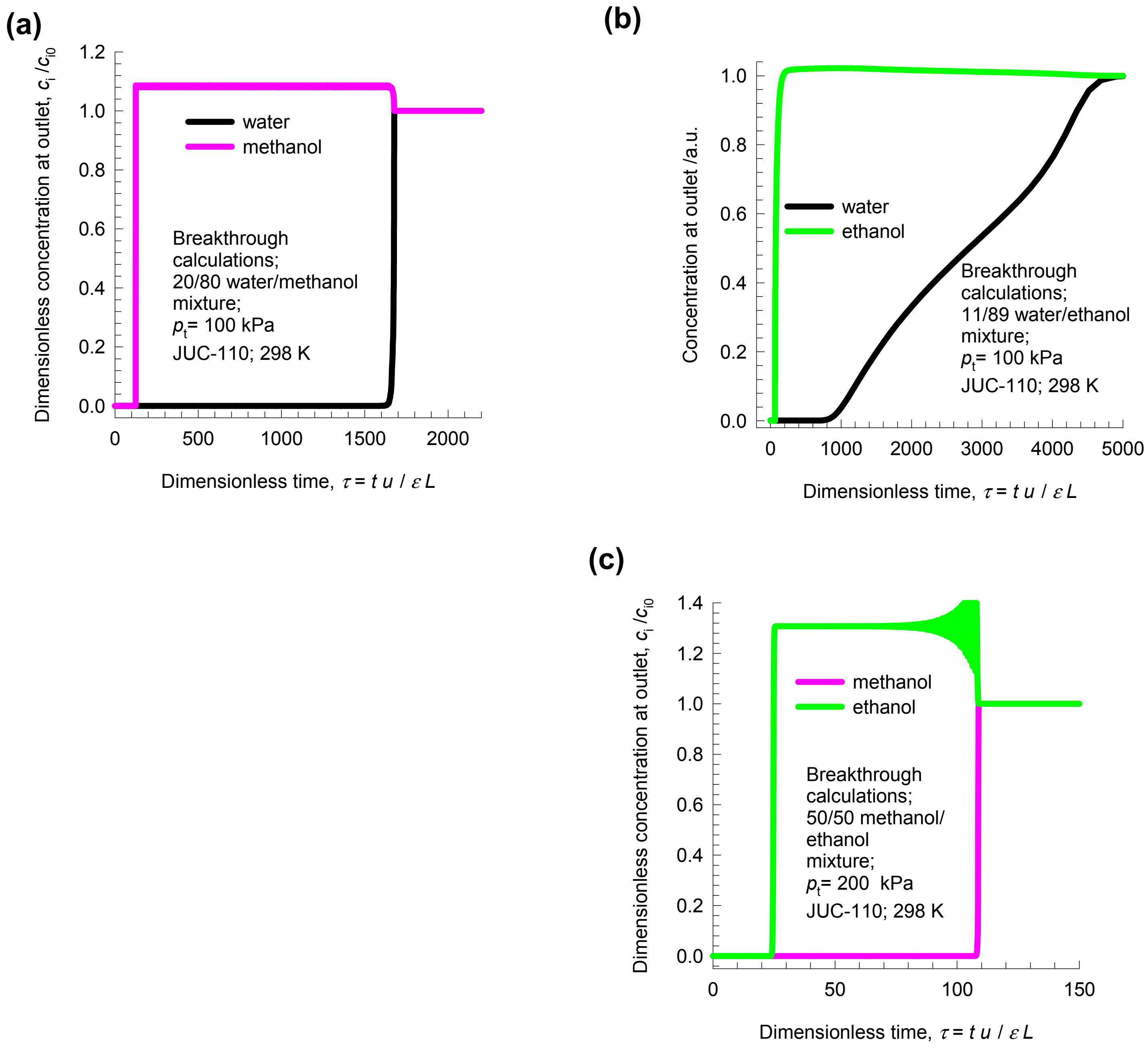

(a) Breakthrough calculations; 20/80 water/methanol mixture; p_t= 100 kPa JUC-110; 298 K

(b) Breakthrough calculations; 11/89 water/ethanol mixture; p_t= 100 kPa JUC-110; 298 K

(c) Breakthrough calculations; 50/50 methanol/ ethanol mixture; p_t= 200 kPa JUC-110; 298 K

Separation processes in aromatics processing

ESI Figure 44

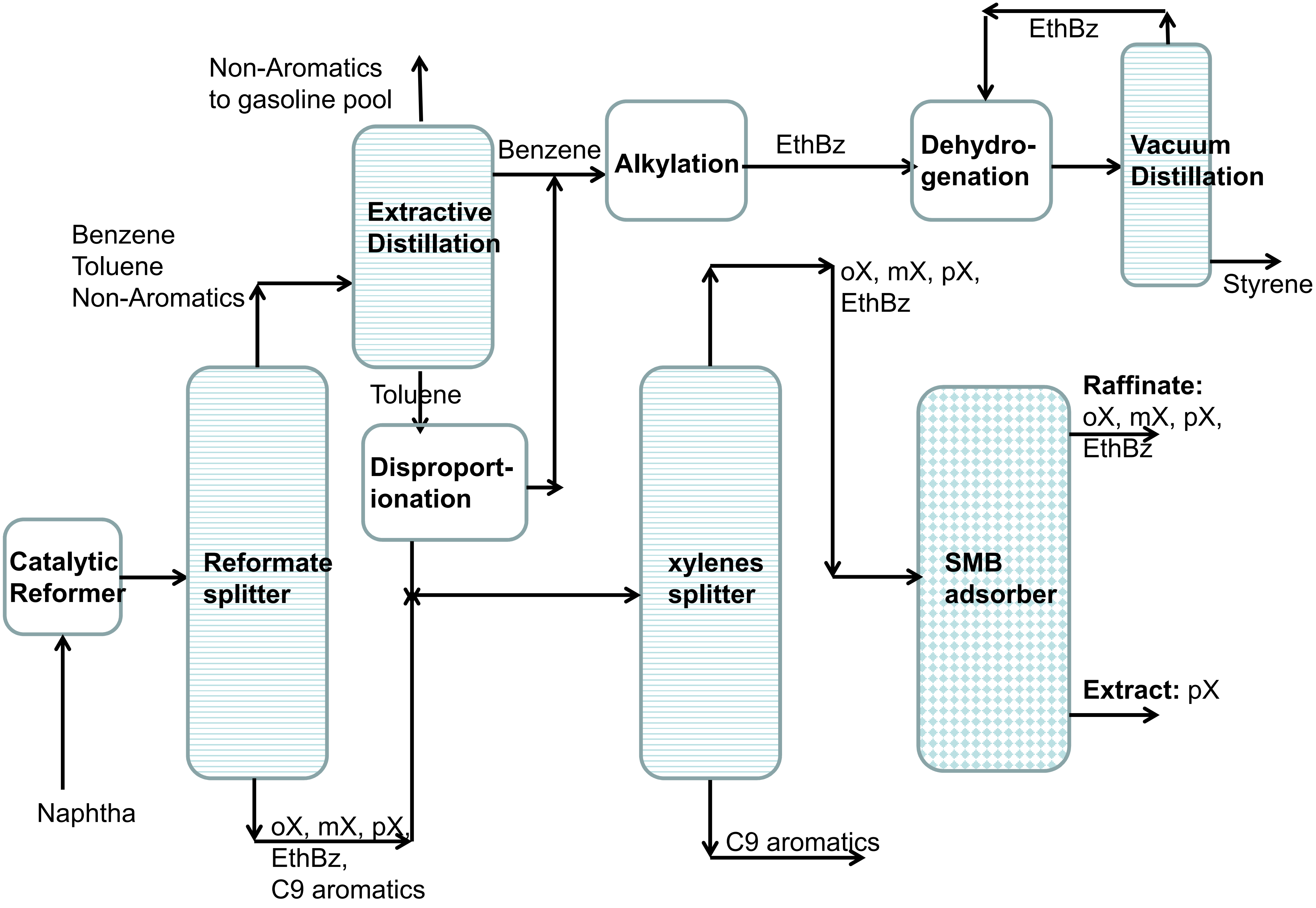

Boiling point and freezing points of aromatics

ESI Figure 45

	Boiling point / K	**Freezing point / K**
benzene	353.3	278.7
toluene	384	178
o-xylene (oX)	417.6	248
m-xylene (mX)	412.3	222.5
p-xylene (pX)	411.5	286.4
n-octane (nC8)	398.8	216.4
Ethylbenzene (EtBz)	409.3	178.2
Styrene (St)	418.3	242.5

SMB with BaX zeolite

ESI Figure 46

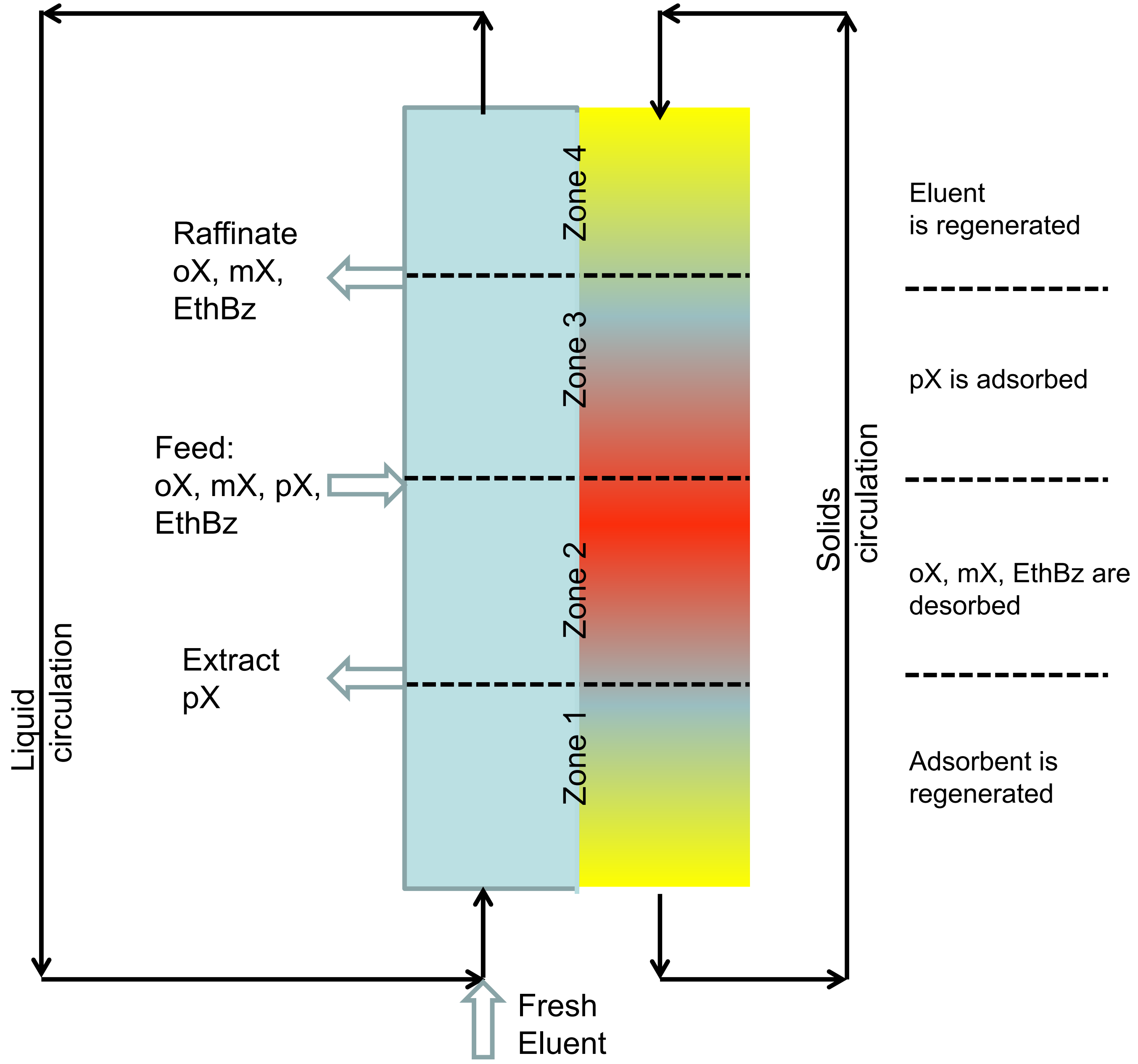

Raffinate
oX, mX,
EthBz

Feed:
oX, mX, pX,
EthBz

Extract
pX

Fresh
Eluent

Eluent
is regenerated

pX is adsorbed

oX, mX, EthBz are
desorbed

Adsorbent is
regenerated

ESI Figure 47

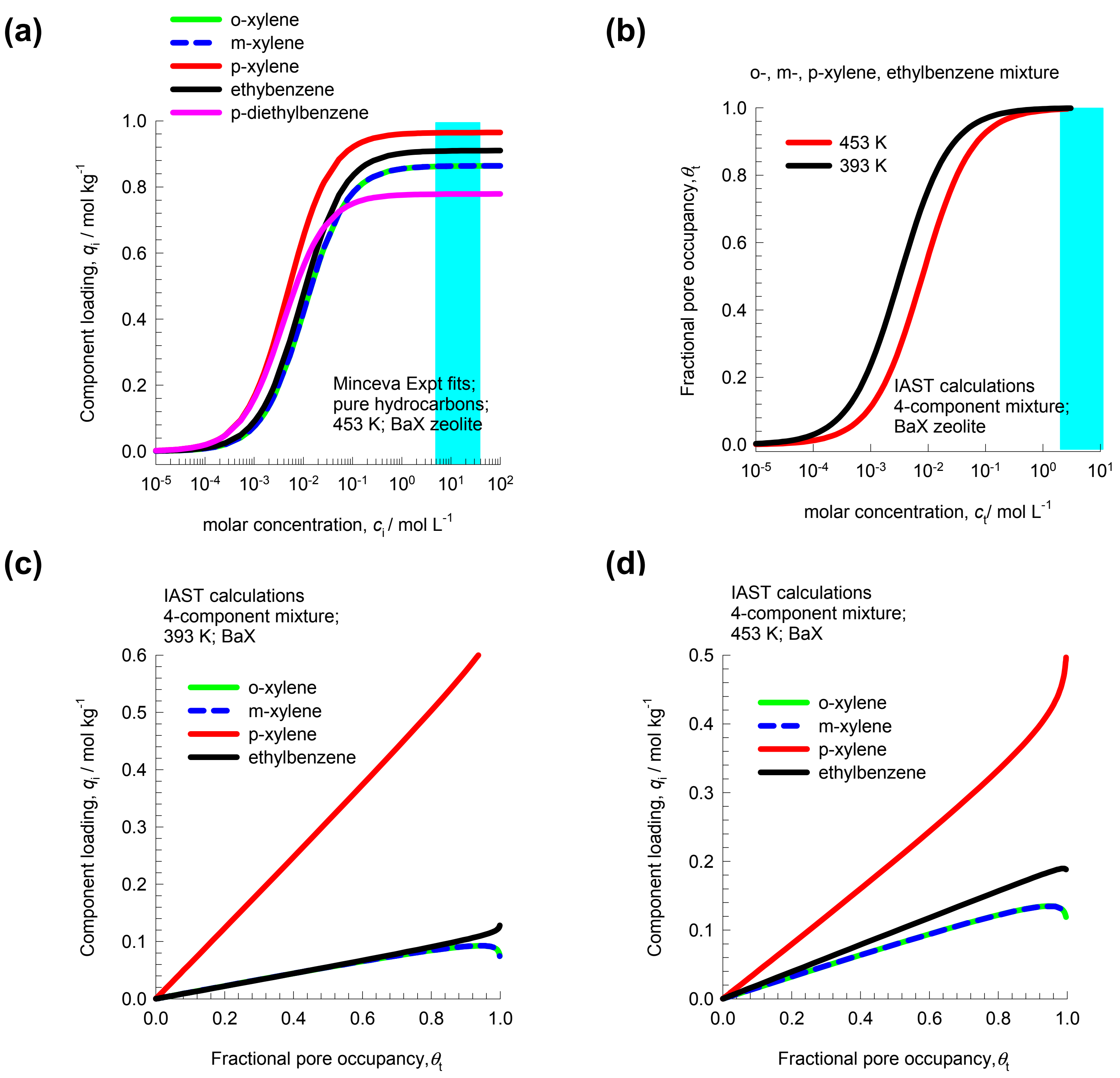

SMB with BaX zeolite

ESI Figure 48

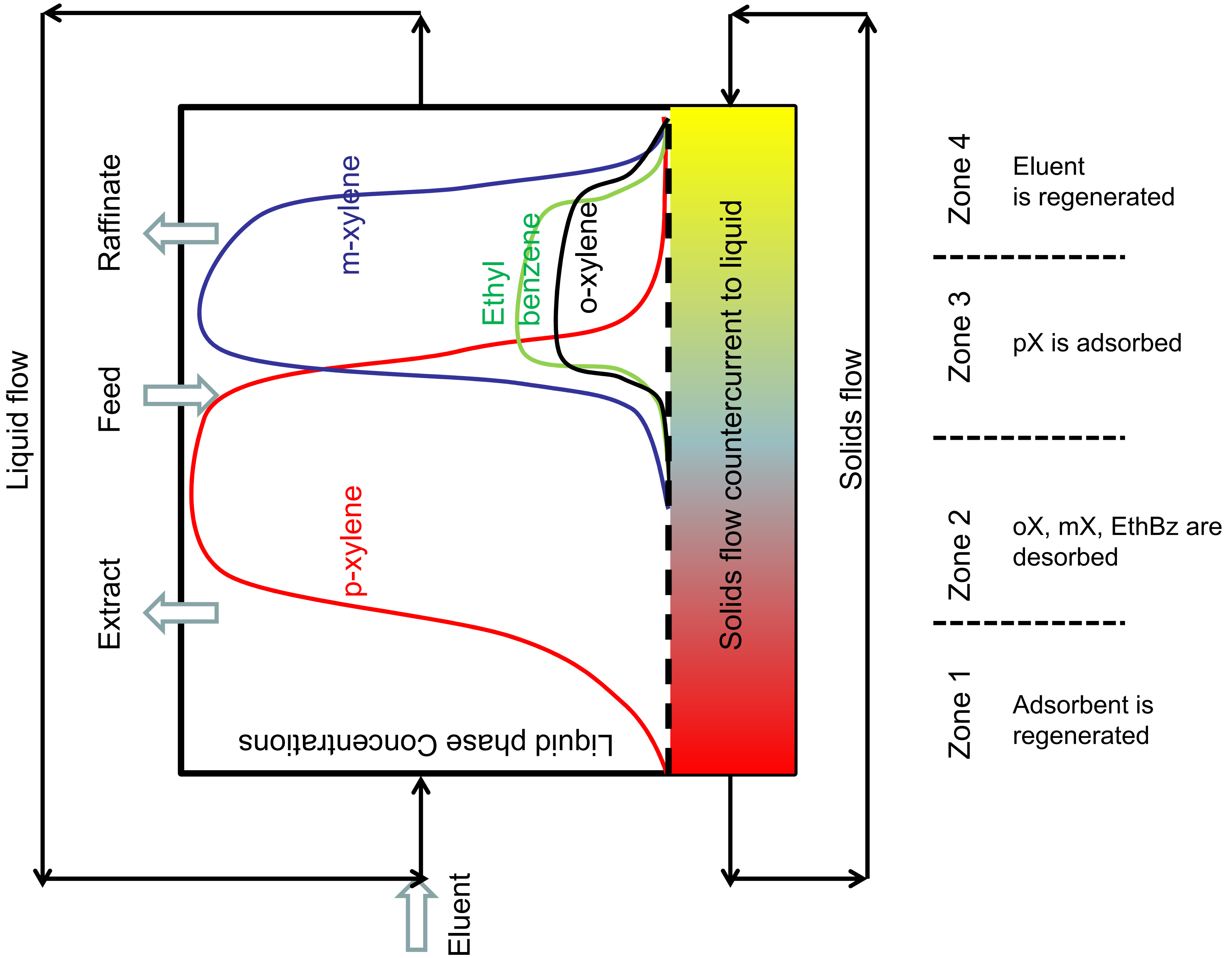

Alternative separation scheme

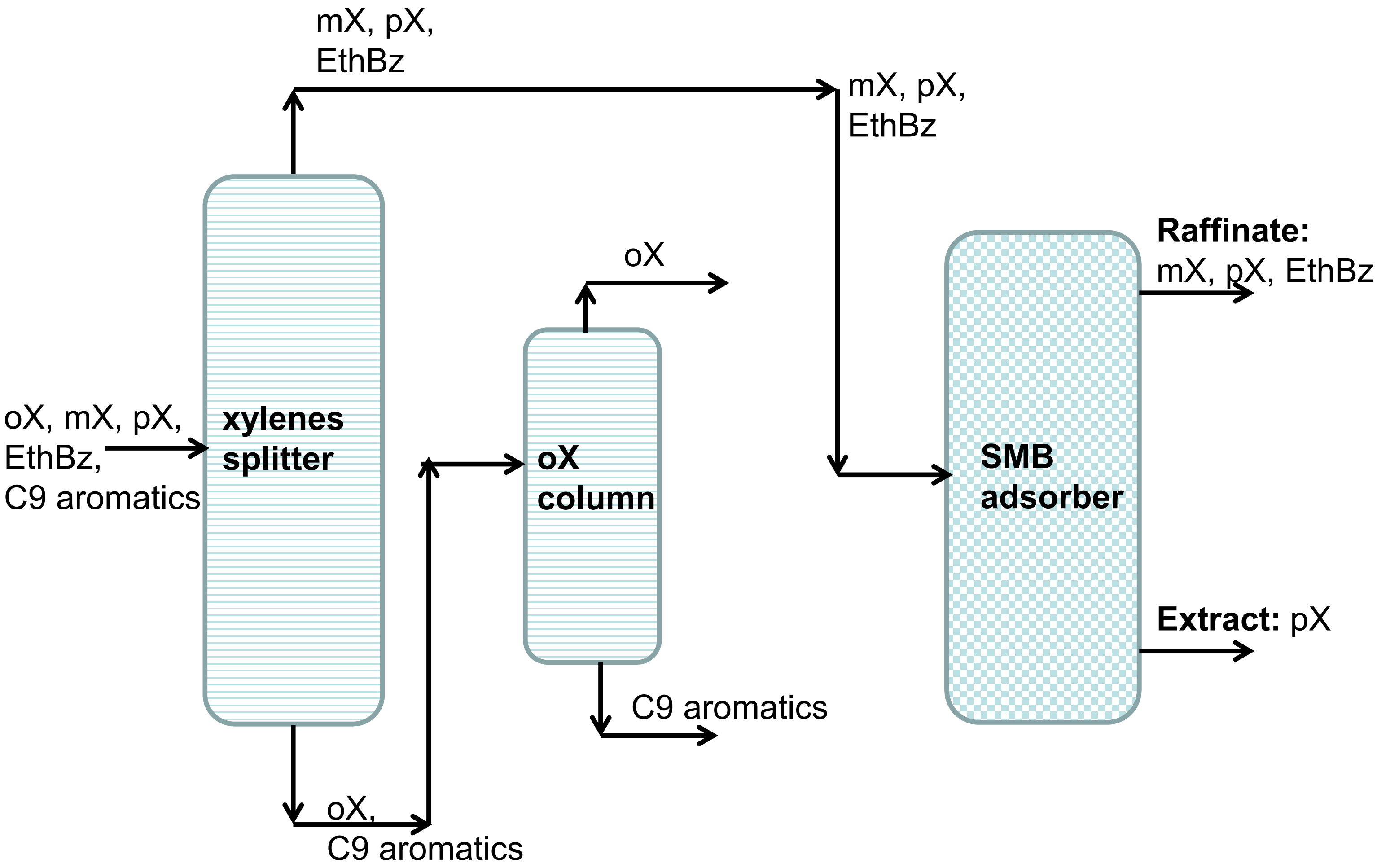

Molecular dimensions of aromatic molecules

ESI Figure 50

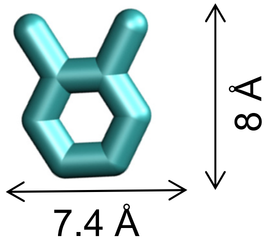

o-xylene (oX)

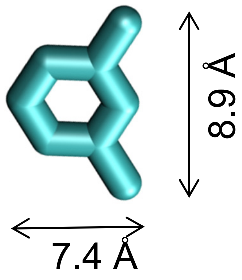

m-xylene (mX)

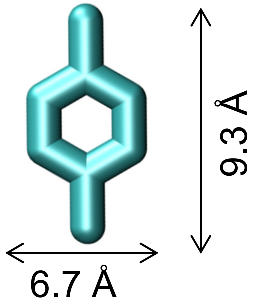

p-xylene (pX)

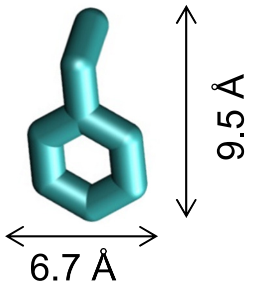

Ethylbenzene (EtBz)

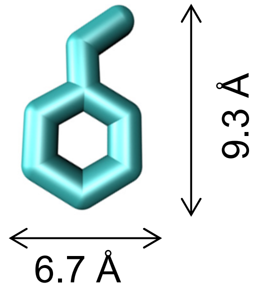

Styrene (St)

Planarity of aromatic molecules

ESI Figure 51

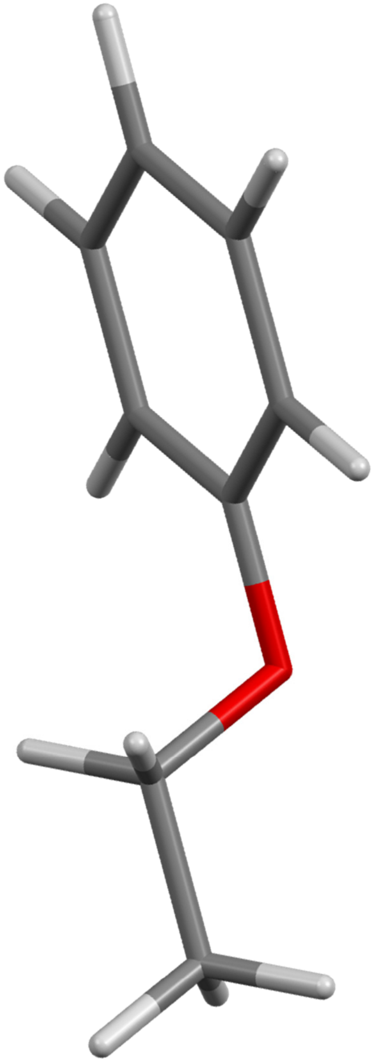

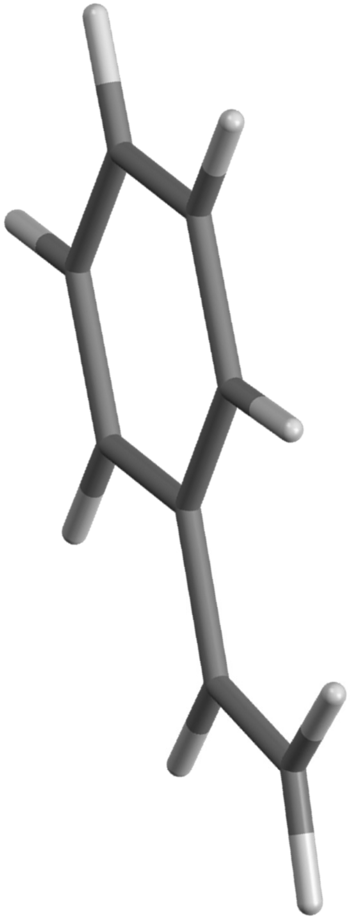

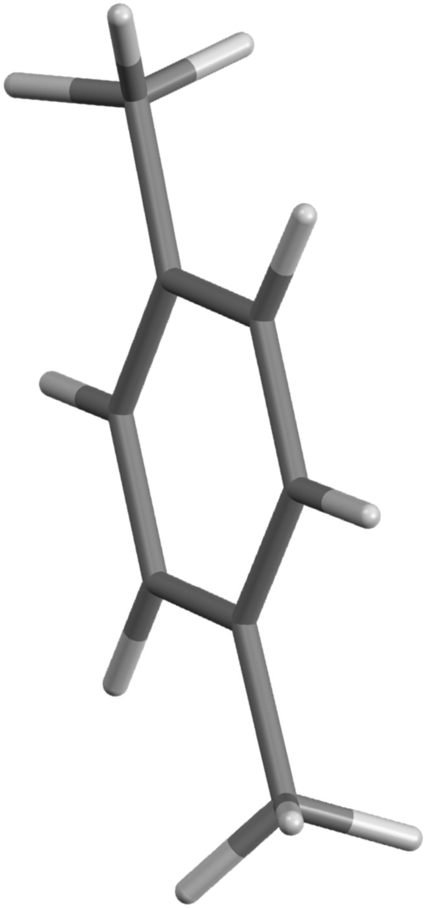

	Ethylbenzene (EtBz)	Styrene (St)	p-xylene (pX)
Boiling point / K	409.3	418.3	411.5
Freezing point / K	178.2	242.5	286.4

Stacking of o-xylene, and p-xylene in 8.5 Å channel

ESI Figure 52

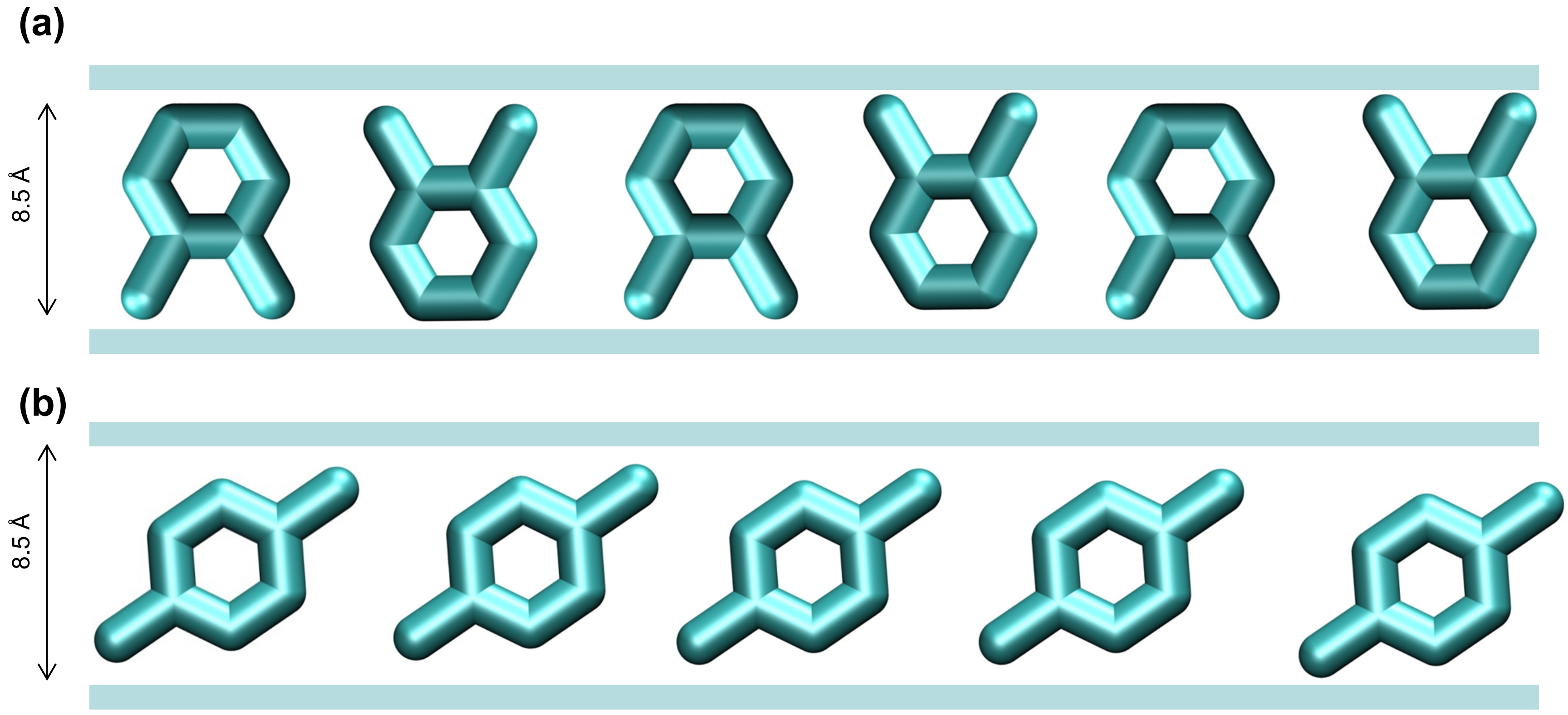

ESI Figure 53

Commensurate stacking of o-xylene within the 1D channels of MIL-47

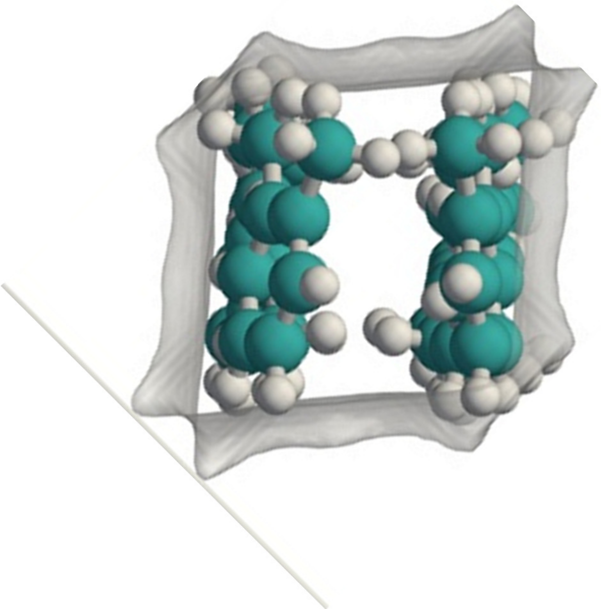

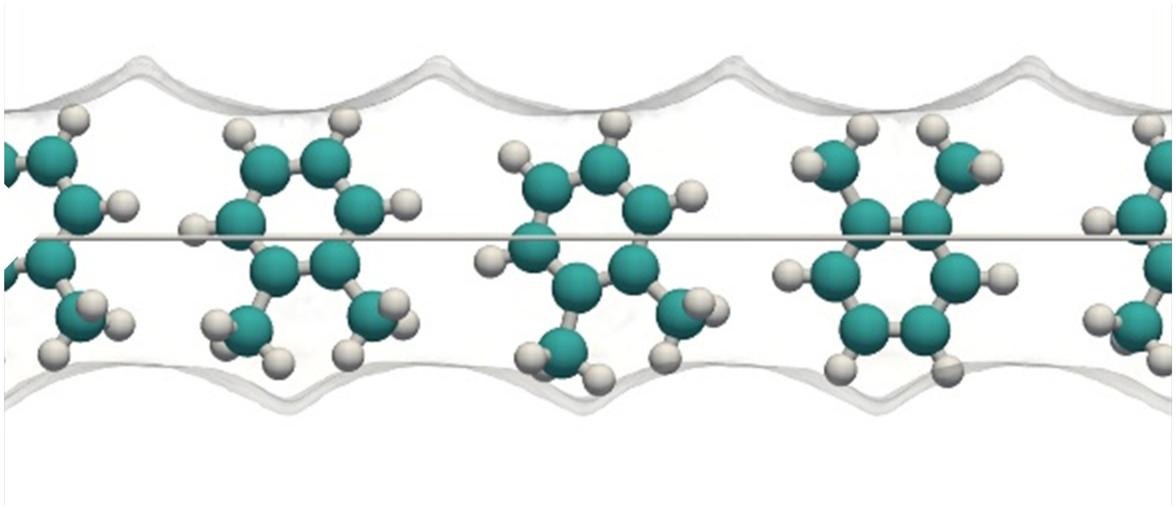

Pure component isotherms for C8 aromatics in MIL-47

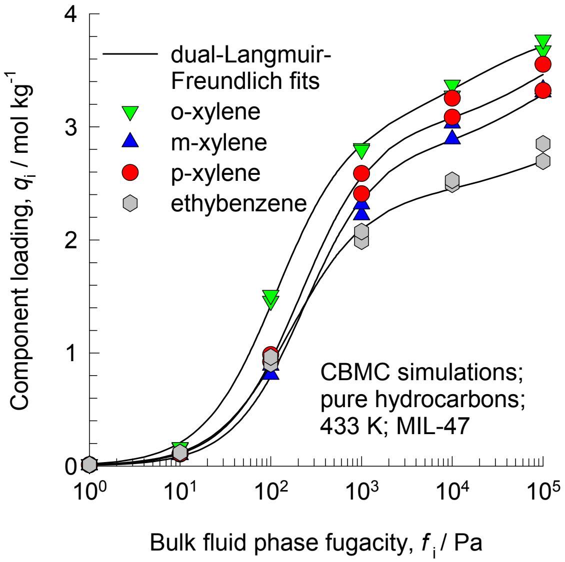

Pure component isotherms for xylenes in AlPO$_4$-5

ESI Figure 54

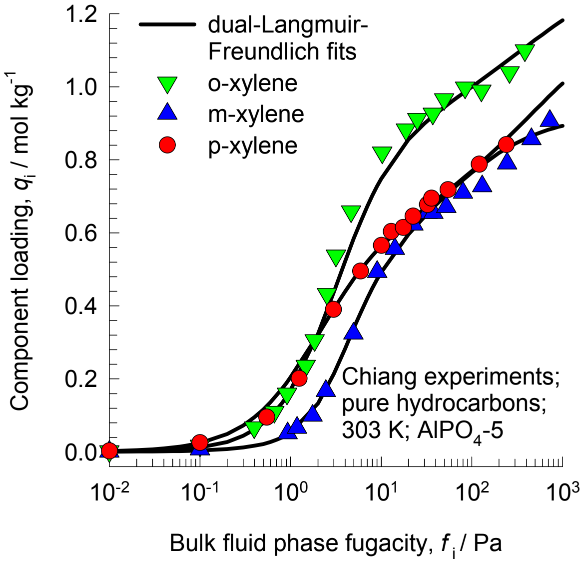

Isosteric heats of adsorption for xylenes in AlPO$_4$-5

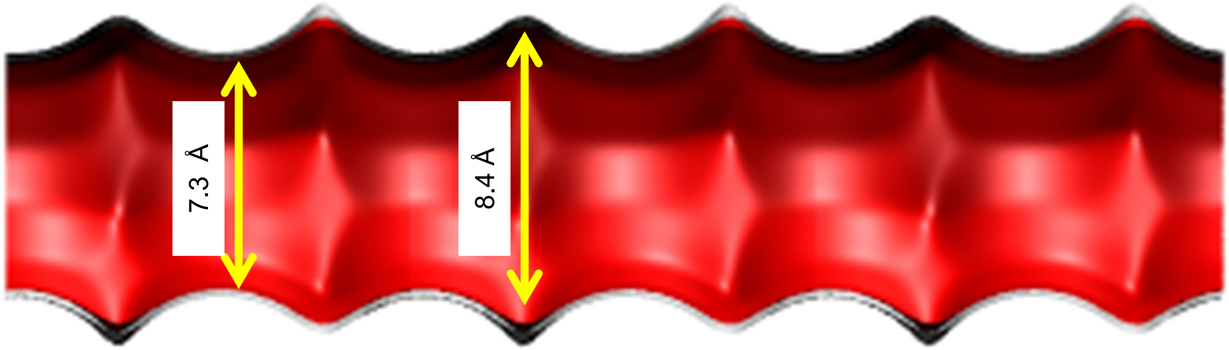

Only o-xylene can locate within the 8.4 Å grooves

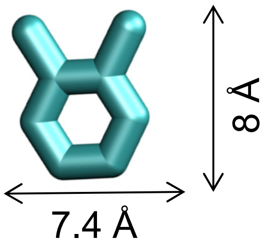

o-xylene (oX)

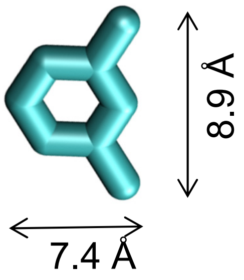

m-xylene (mX)

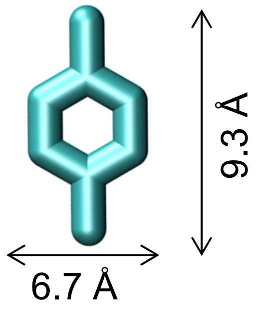

p-xylene (pX)

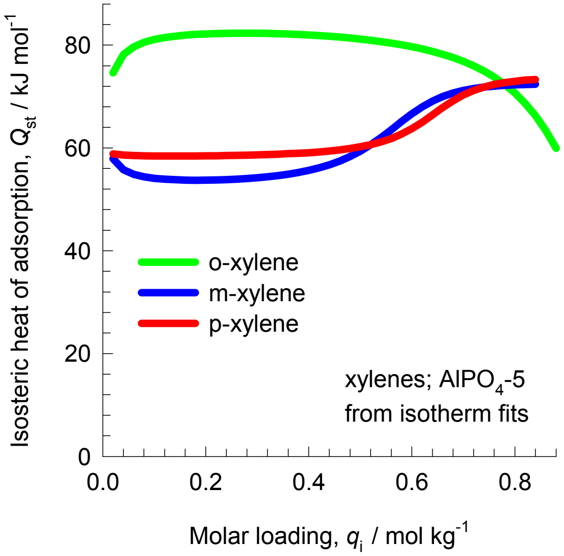

ESI Figure 56

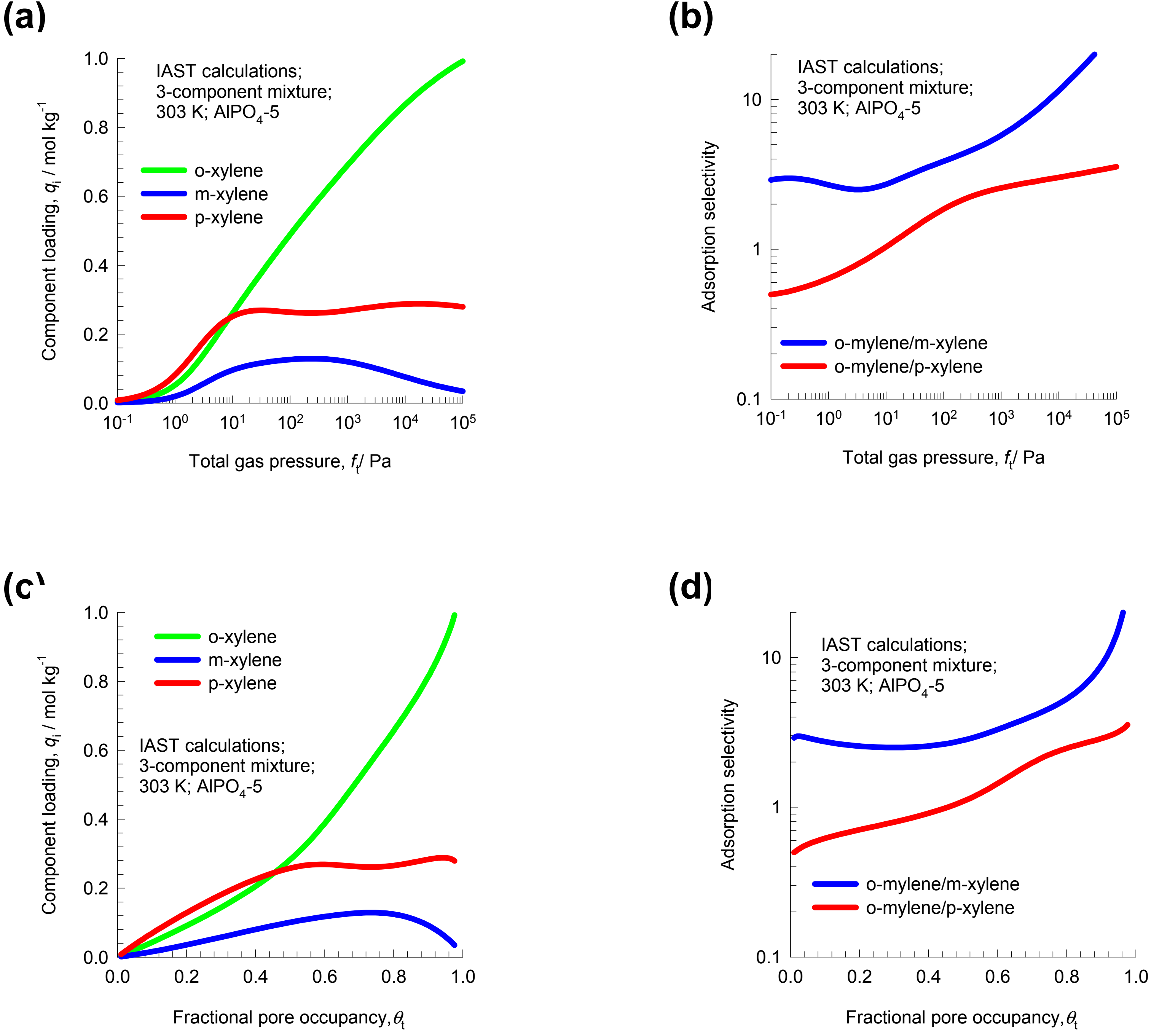

Breakthroughs for xylenes mixture with $AlPO_4$-5

ESI Figure 57

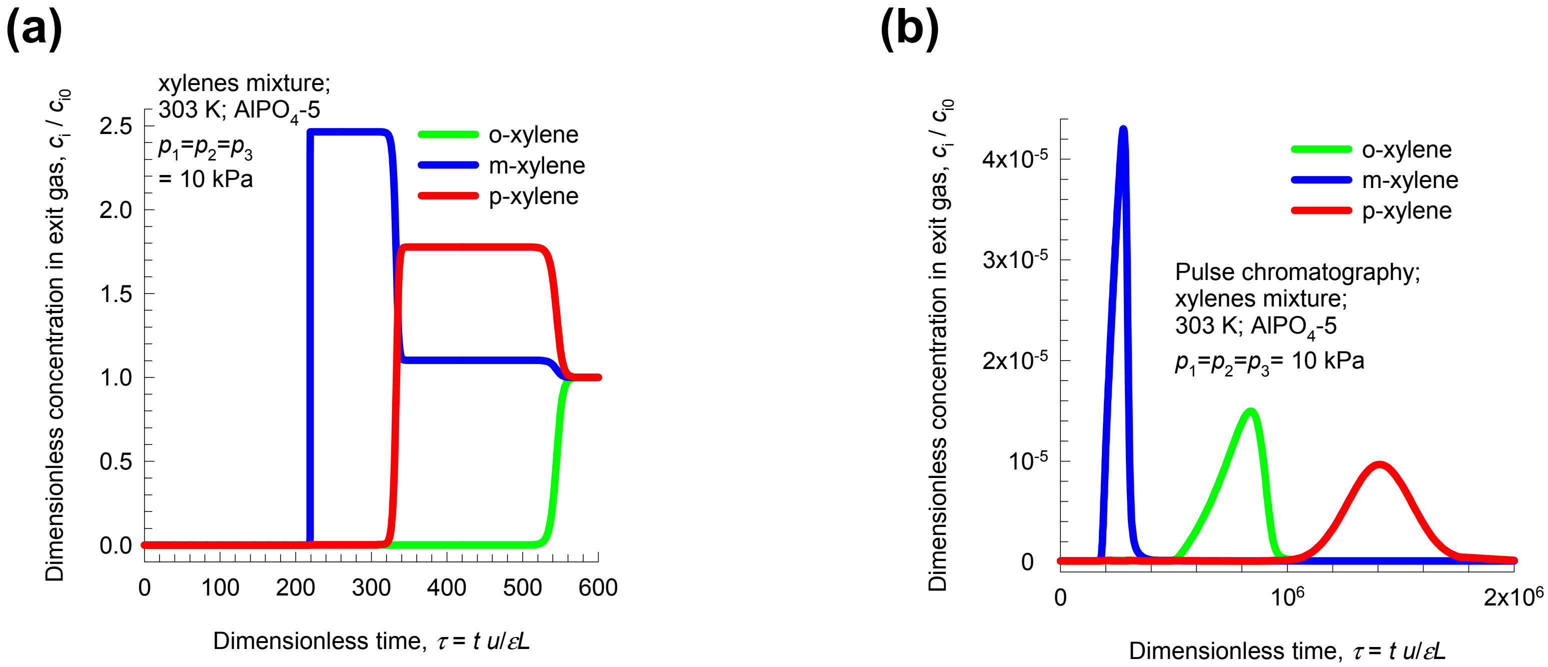

ESI Figure 58

(a) Commensurate stacking of p-xylene within the 1D channels of MAF-X8

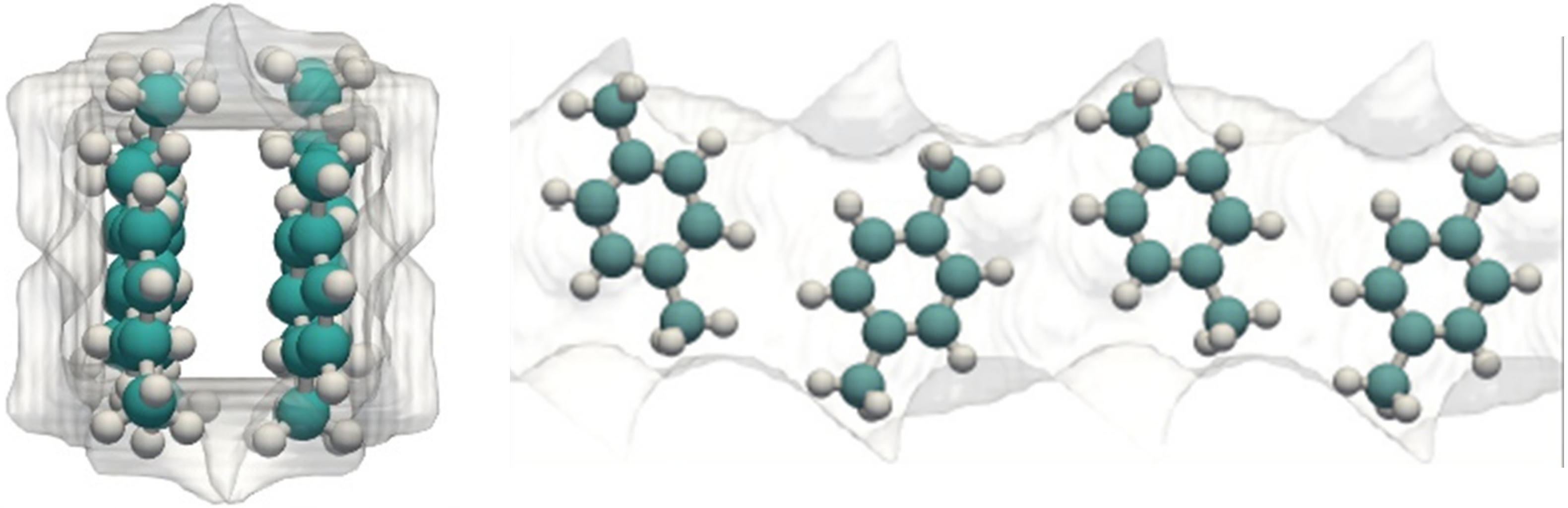

(b) Stacking of p-xylene within the 1D channels of Co(BDP)

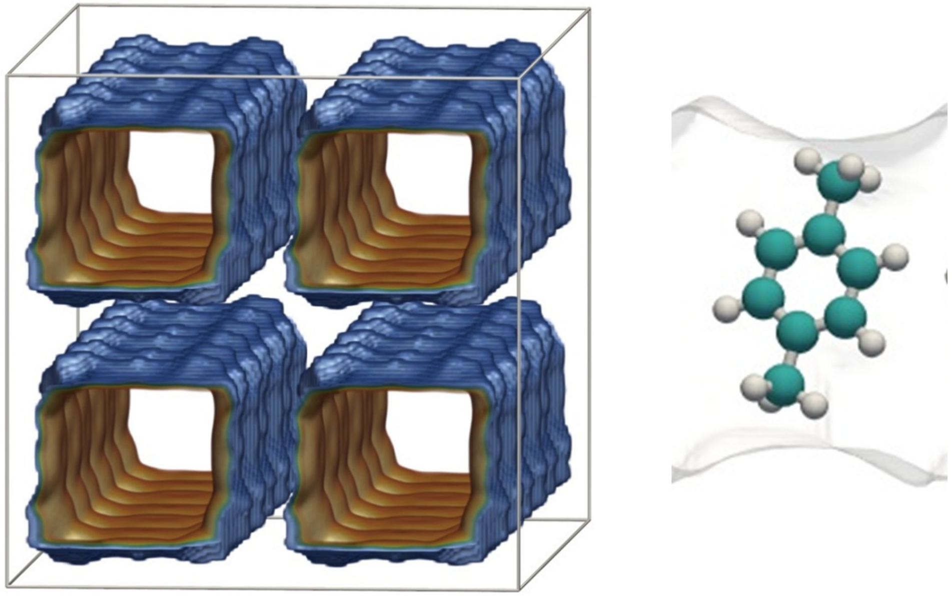

Adsorption of C8 aromatics mixture in MAF-8

ESI Figure 59

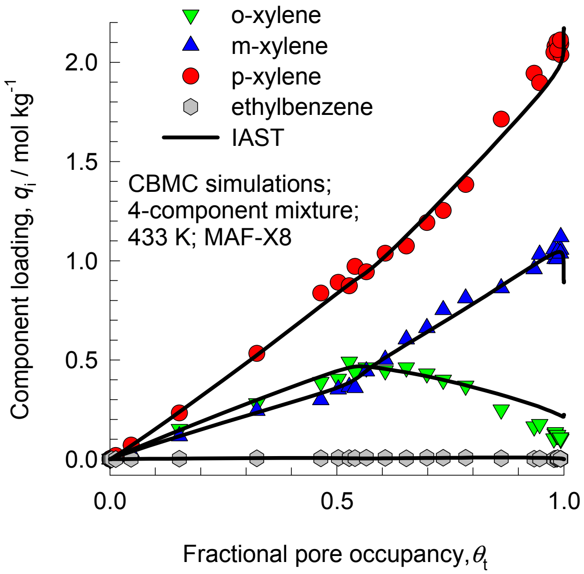

ESI Figure 60

Breakthroughs for Ethylbenzene/Styrene using MIL-47(V) and MIL-53(Al)

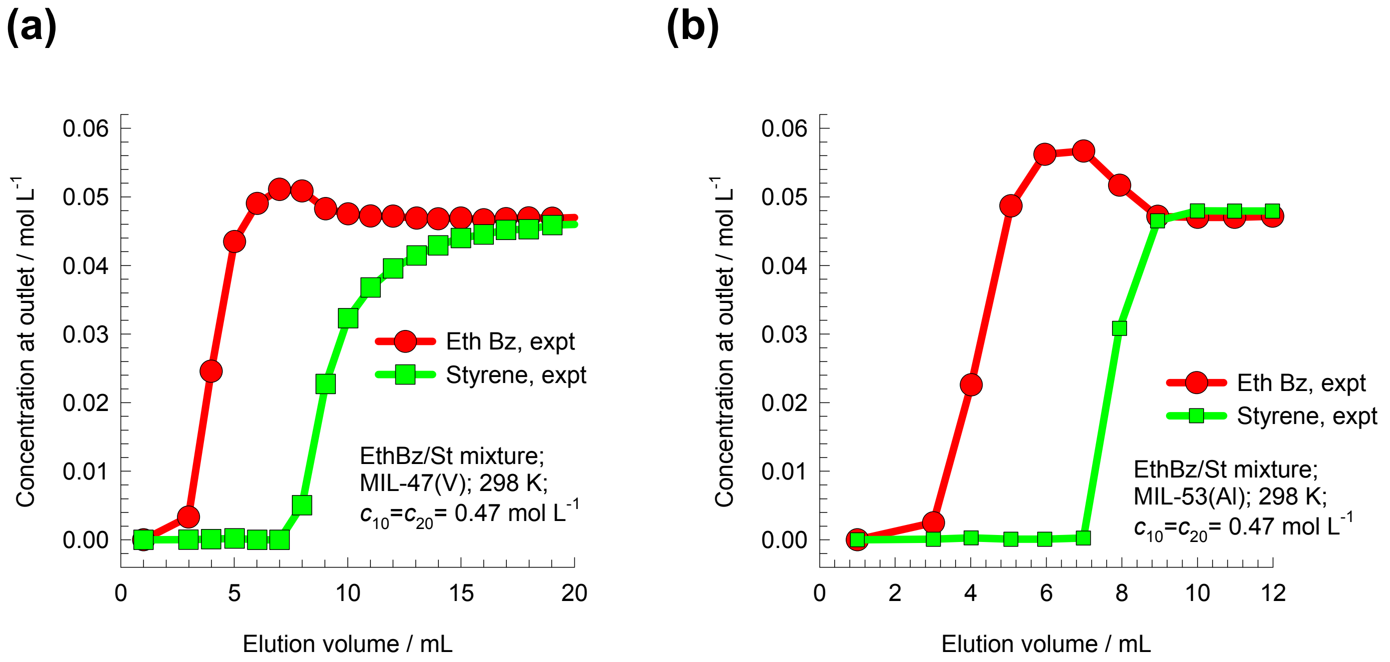

Adsorption of hexane isomers mixture in AFI zeolite

ESI Figure 61

(a)

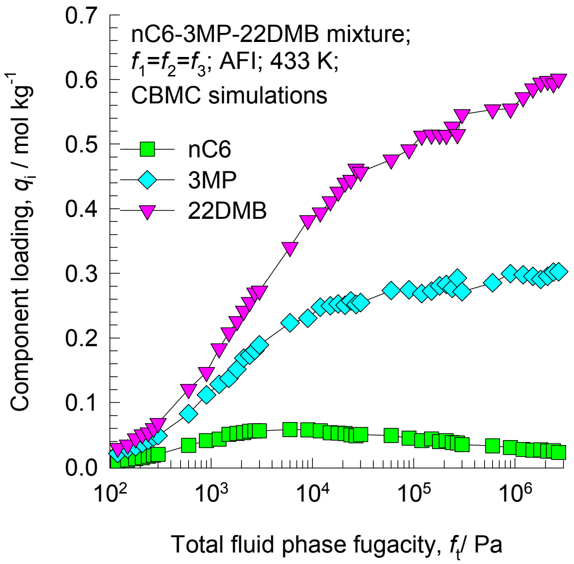

(b)

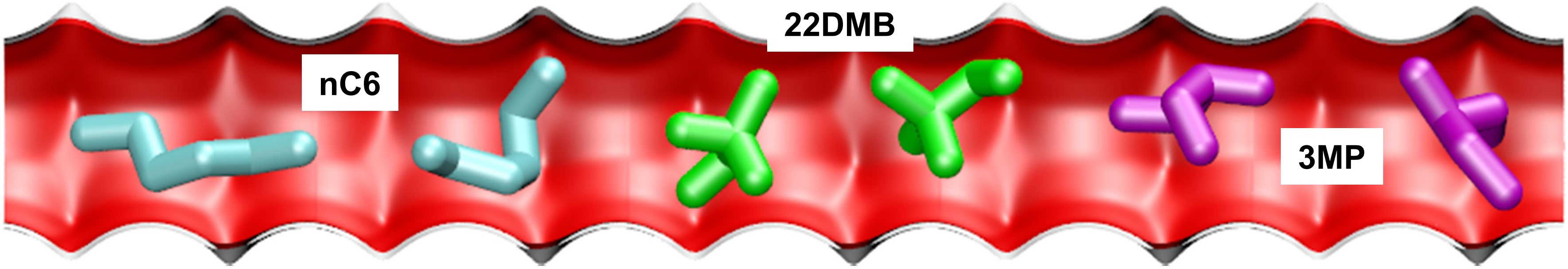

Adsorption of hexane isomers mixture in ATS and CFI zeolites

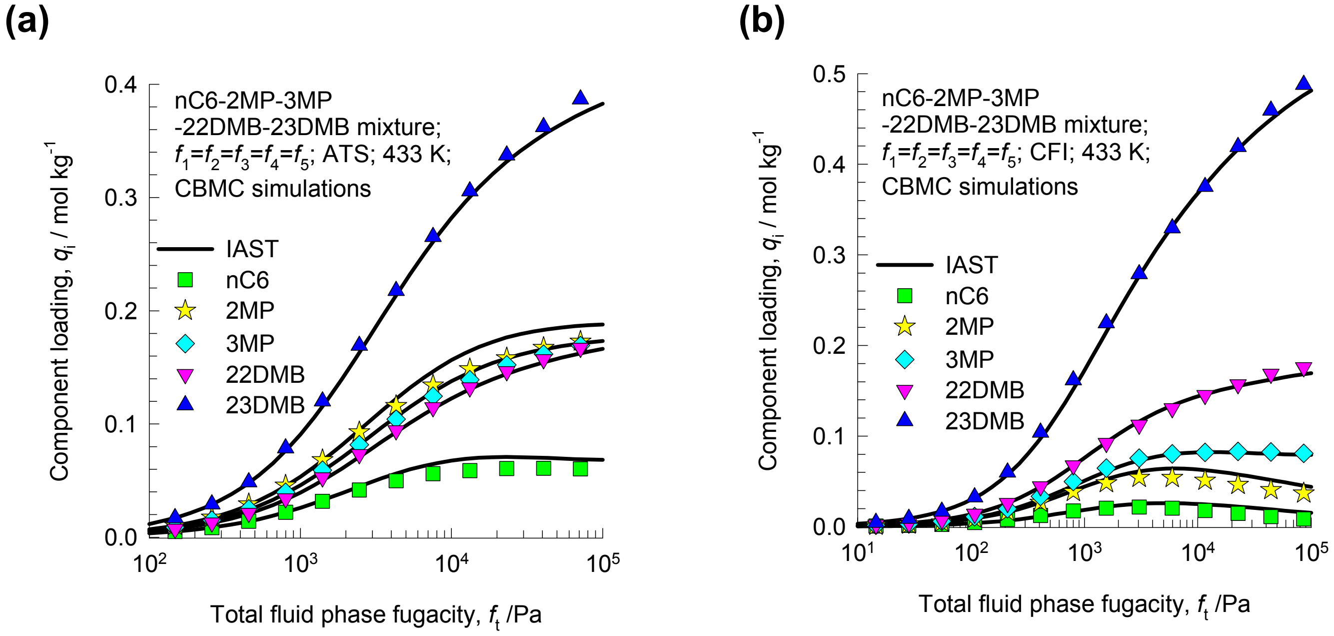

Adsorption of nC6 in MFI zeolite

ESI Figure 63

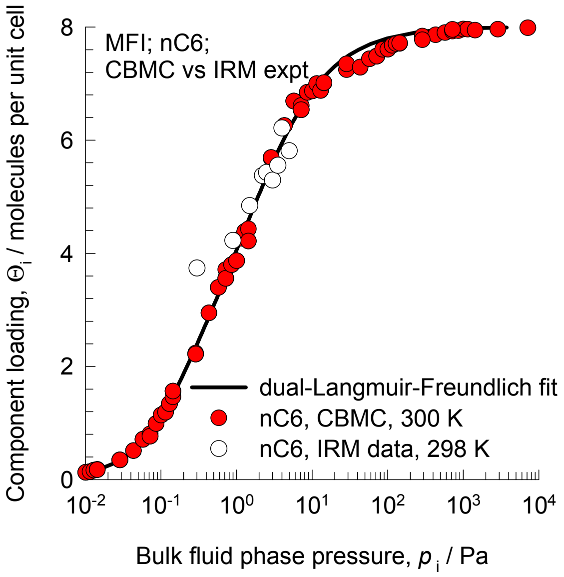

10 ring channel
of MFI viewed
along [100]

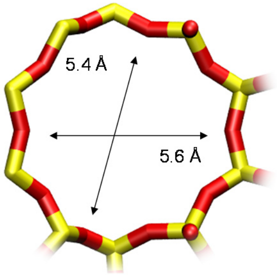

10 ring channel
of MFI viewed
along [010]

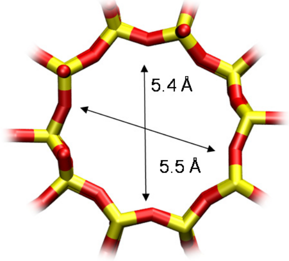

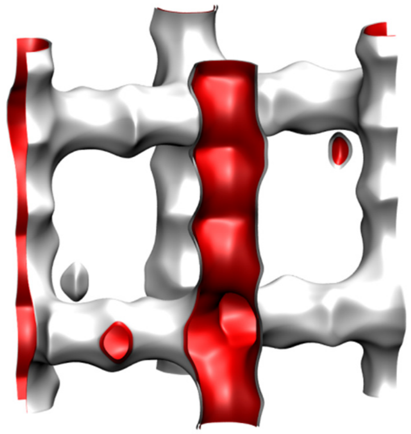

nC6 at loading of 4 molecules/uc
x-y view

nC6 x-z view

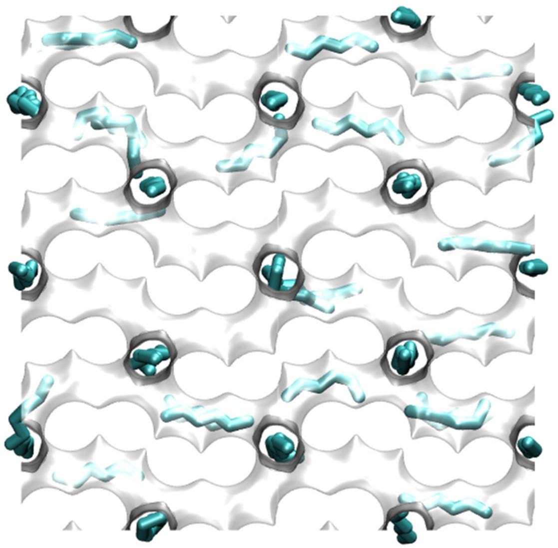

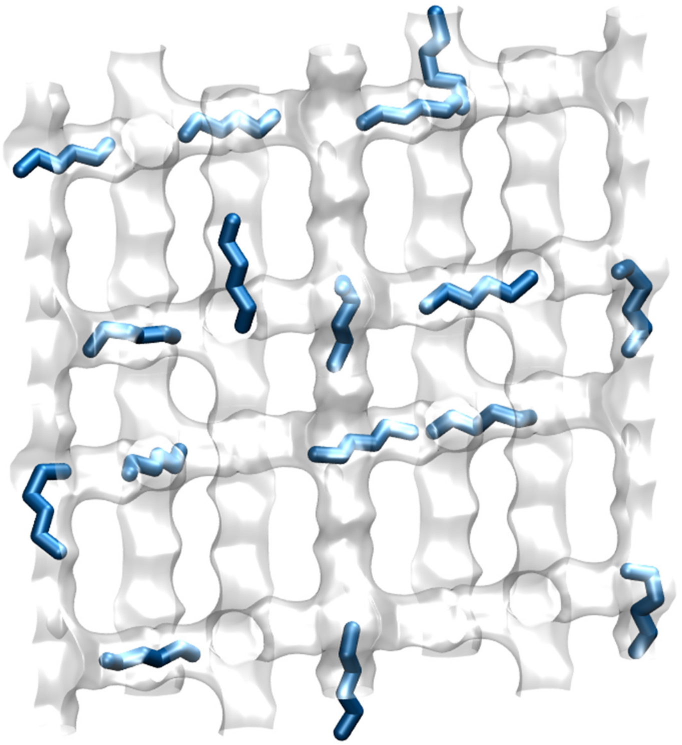

Adsorption of 2MP in MFI zeolite

ESI Figure 64

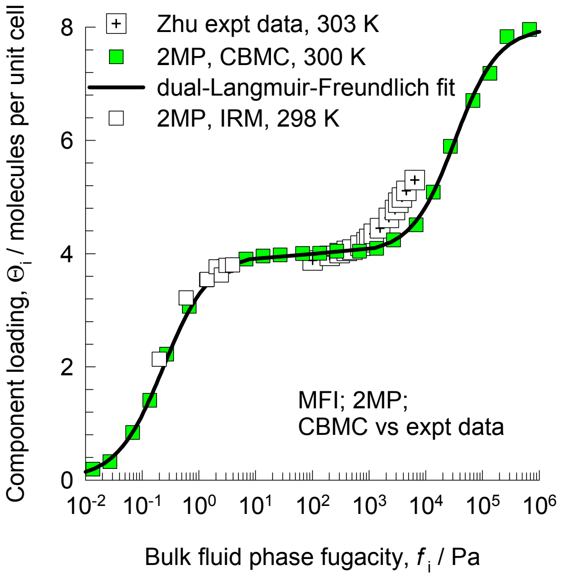

x-z view of 2MP molecules

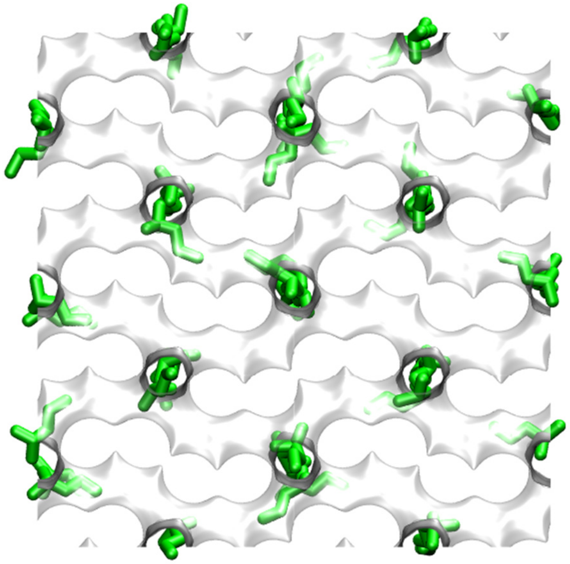

x-y view of 2MP molecules

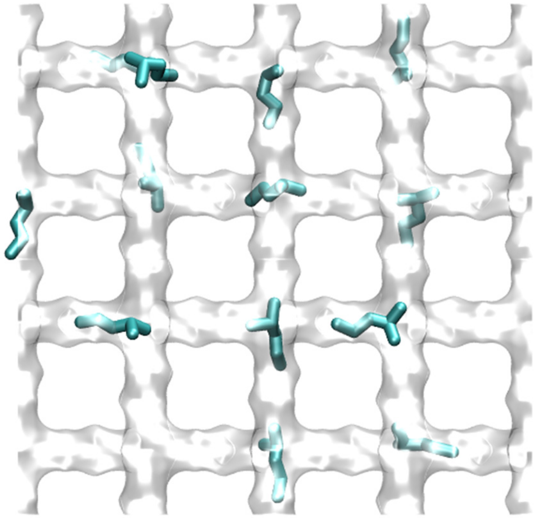

Adsorption of nC6/2MP mixture in MFI zeolite

ESI Figure 65

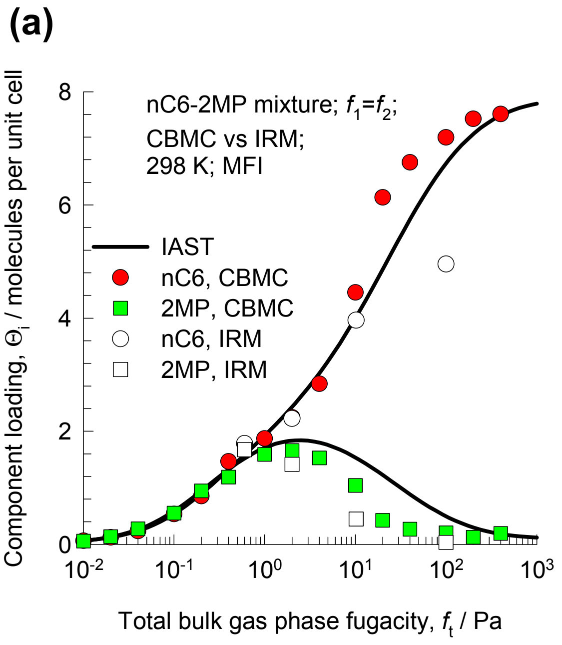

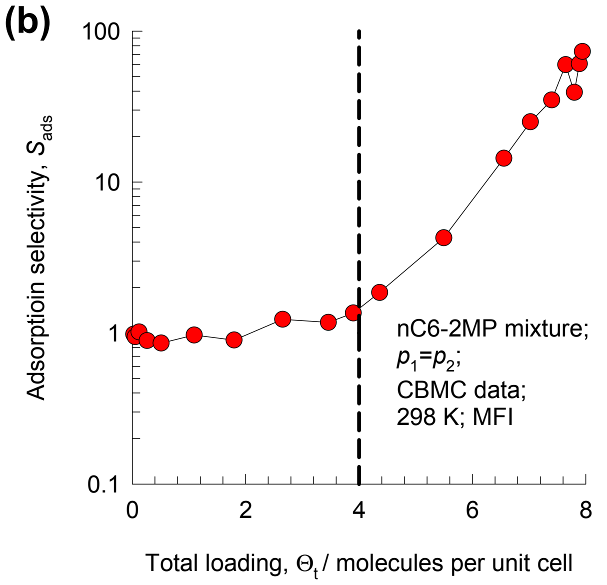

x-z view

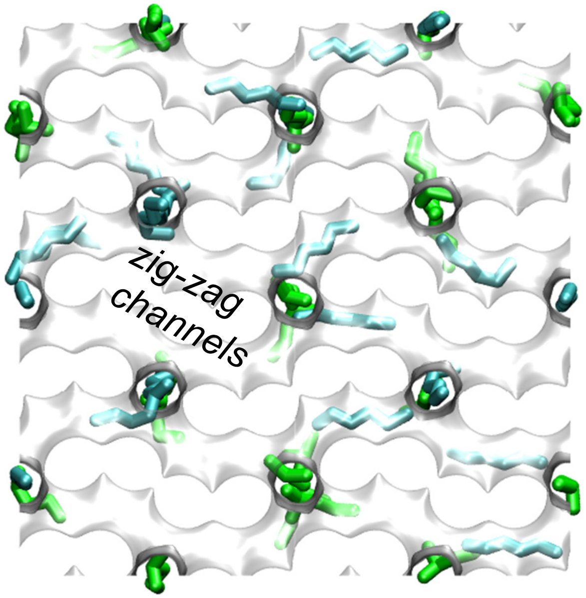

x-y- view

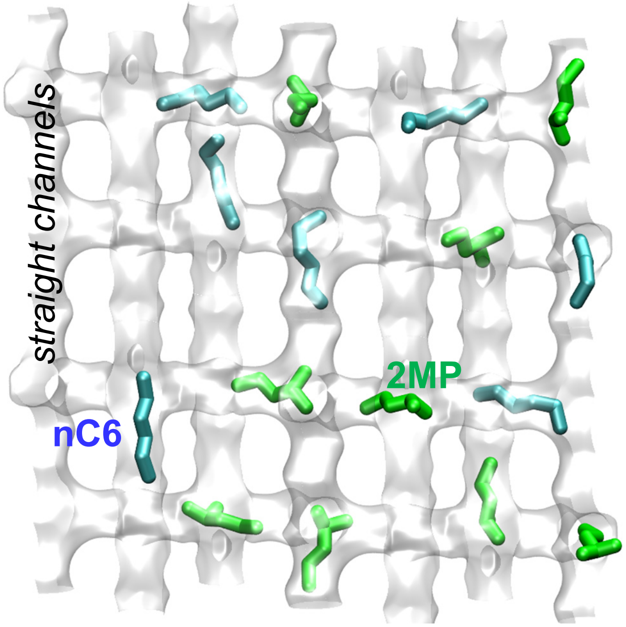

Transient uptake of nC6/2MP mixture in MFI zeolite

ESI Figure 66

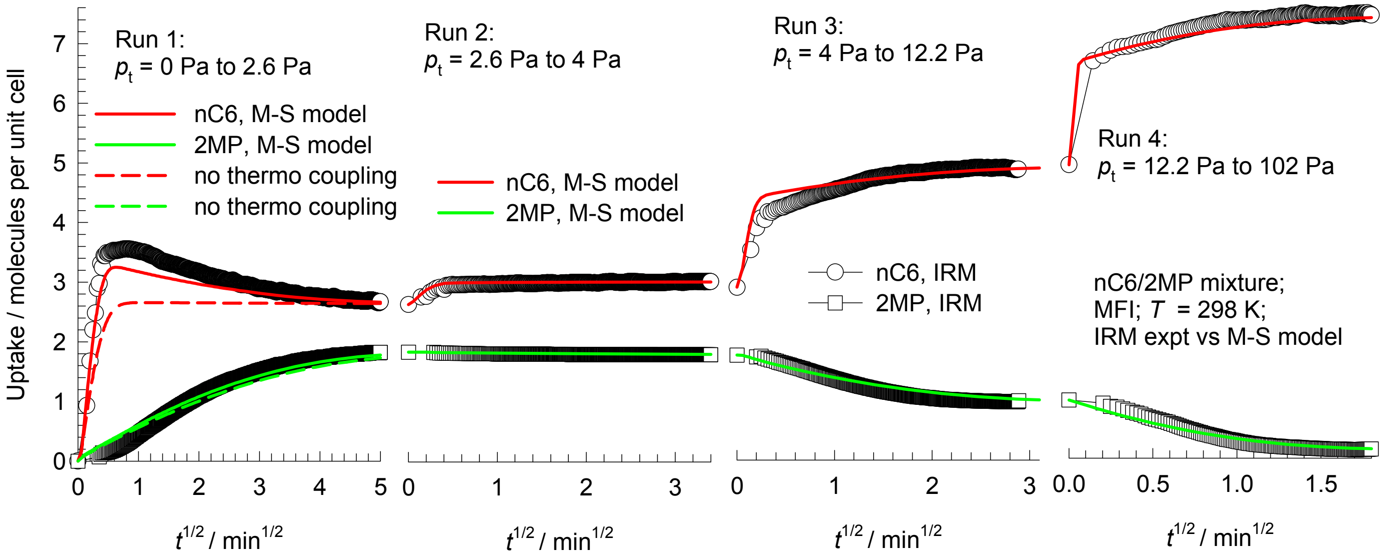

Intra-crystalline diffusivities for nC6/2MP mixture in MFI zeolite

ESI Figure 67

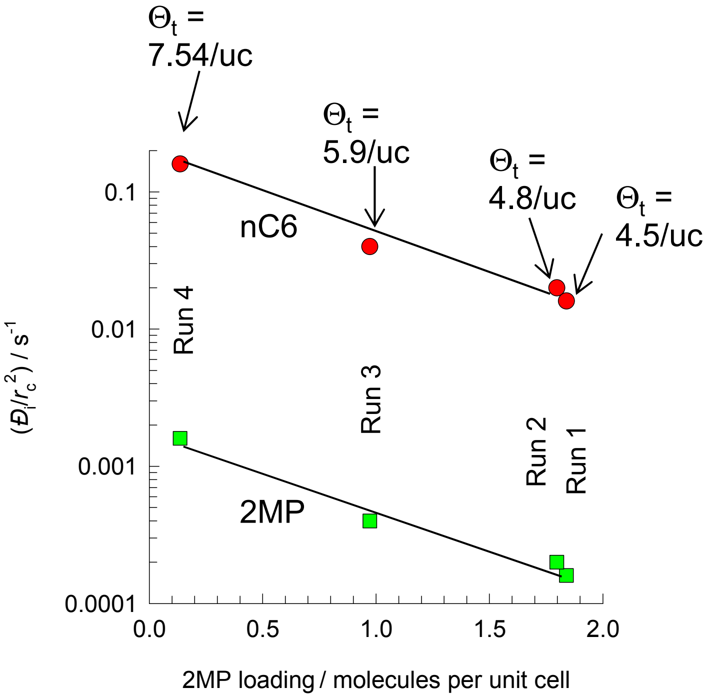

ESI Figure 68

(a)

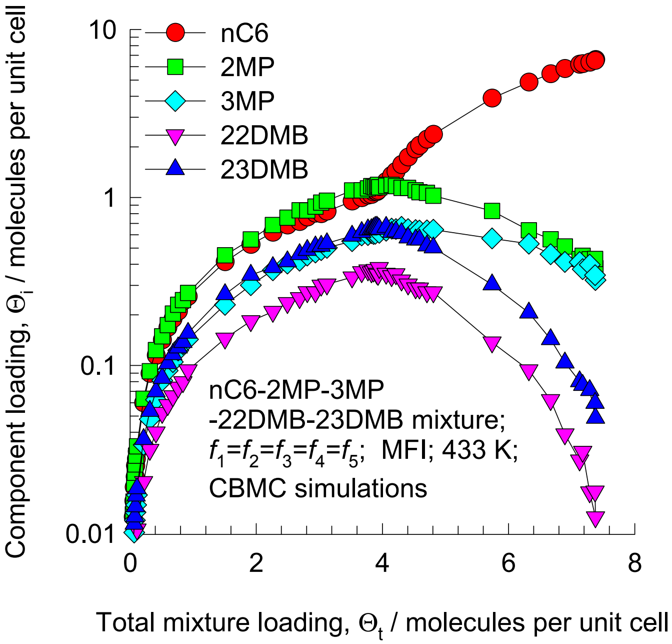

nC6-2MP-3MP
-22DMB-23DMB mixture;
$f_1=f_2=f_3=f_4=f_5$; MFI; 433 K;
CBMC simulations

(b) Snapshot of hexane isomers

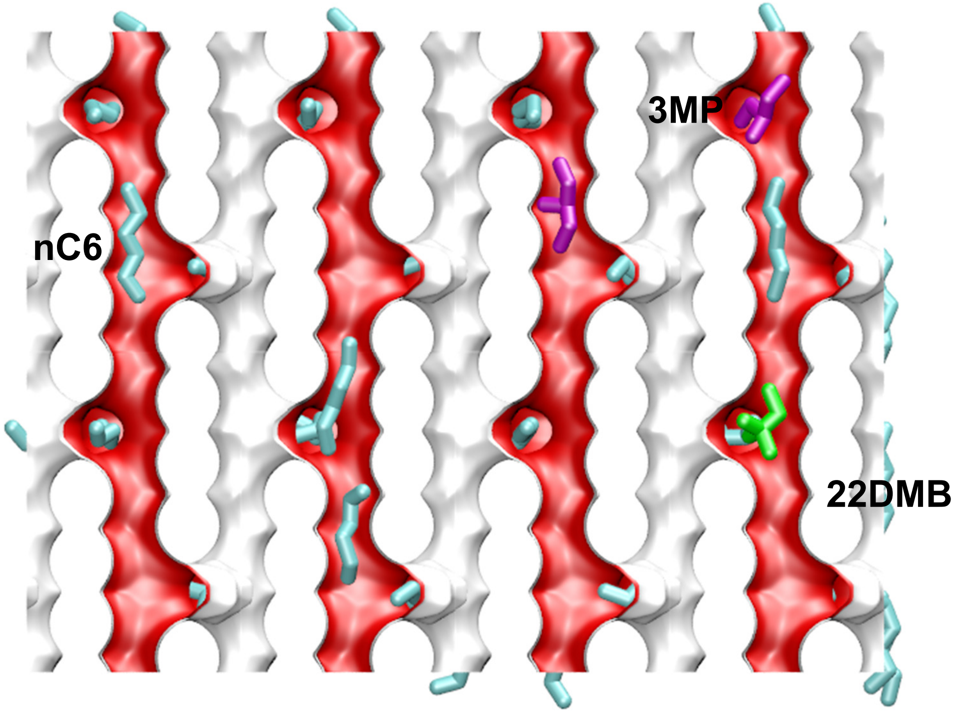

(c)

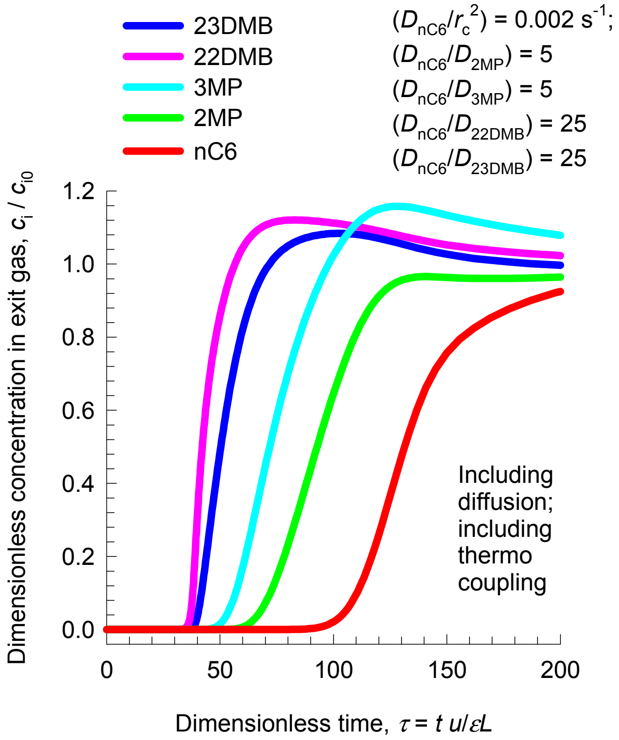

$(D_{nC6}/r_c^2) = 0.002\ s^{-1}$;
$(D_{nC6}/D_{2MP}) = 5$
$(D_{nC6}/D_{3MP}) = 5$
$(D_{nC6}/D_{22DMB}) = 25$
$(D_{nC6}/D_{23DMB}) = 25$

Including
diffusion;
including
thermo
coupling

ESI Figure 69

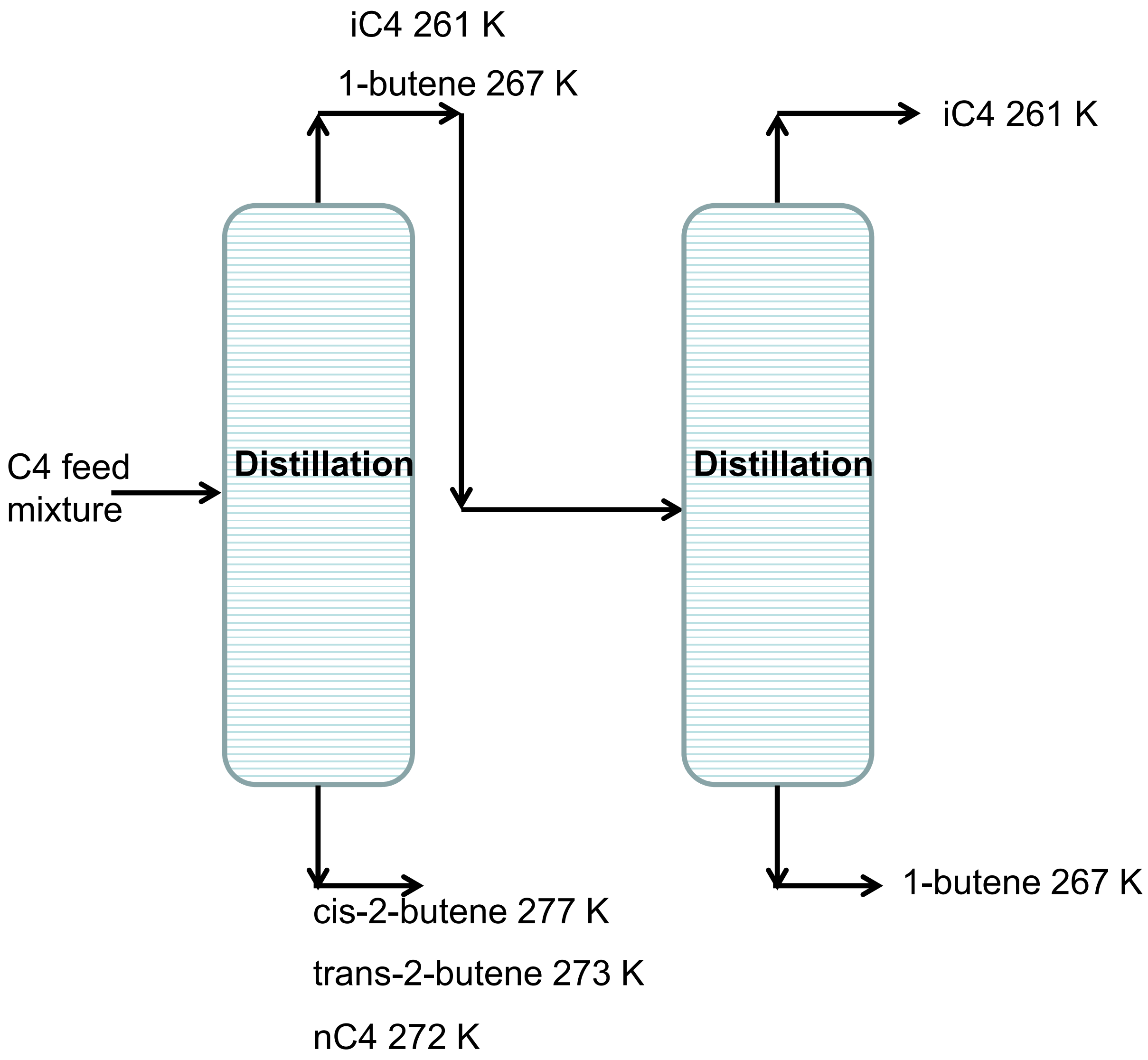

ESI Figure 70

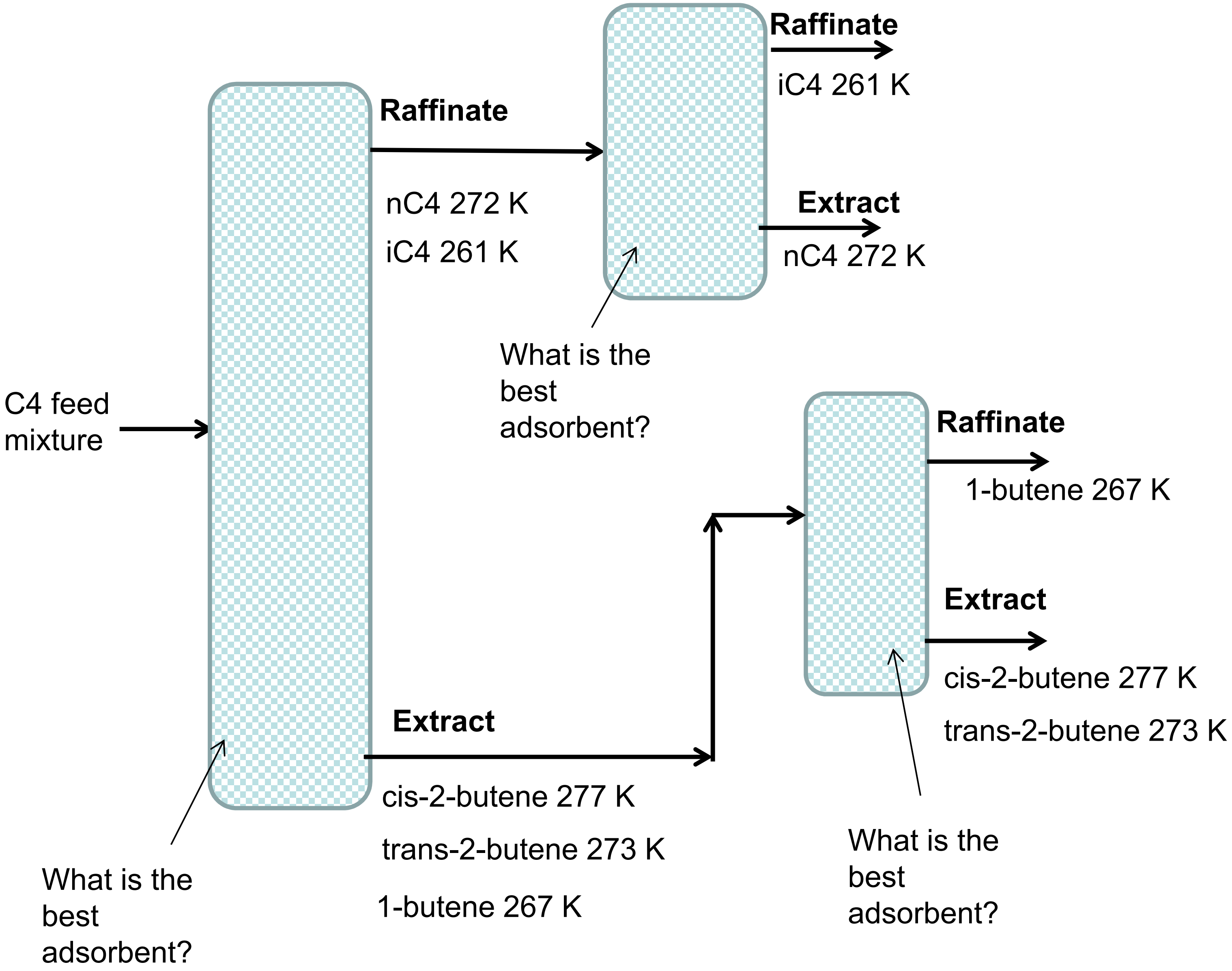

C4 feed mixture

Raffinate

nC4 272 K

iC4 261 K

Raffinate

iC4 261 K

Extract

nC4 272 K

What is the best adsorbent?

Extract

cis-2-butene 277 K

trans-2-butene 273 K

1-butene 267 K

Raffinate

1-butene 267 K

Extract

cis-2-butene 277 K

trans-2-butene 273 K

What is the best adsorbent?

What is the best adsorbent?

Separation of isobutene/isobutane

CuBTC

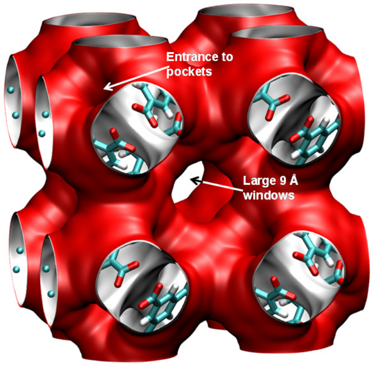

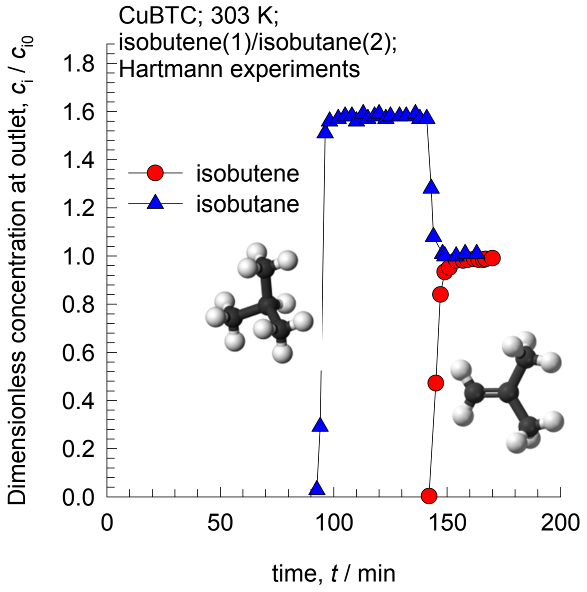

ESI Figure 72

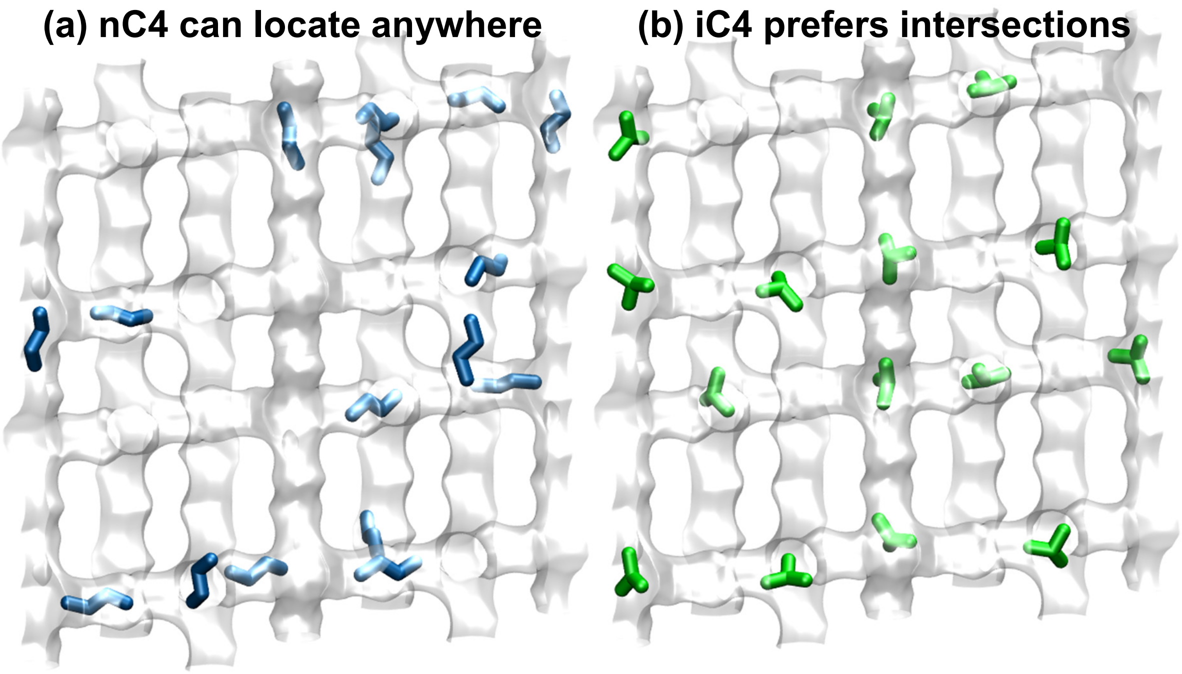

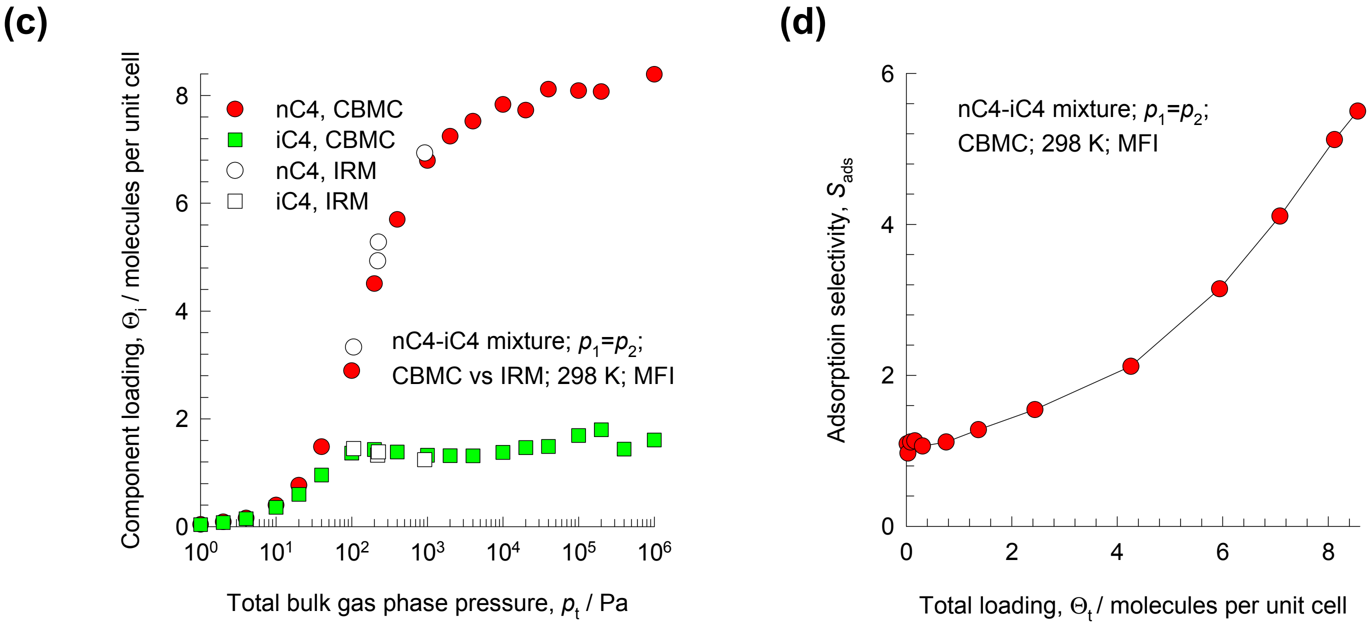

ESI Figure 73

Separation of 2-butenes from 1-butene

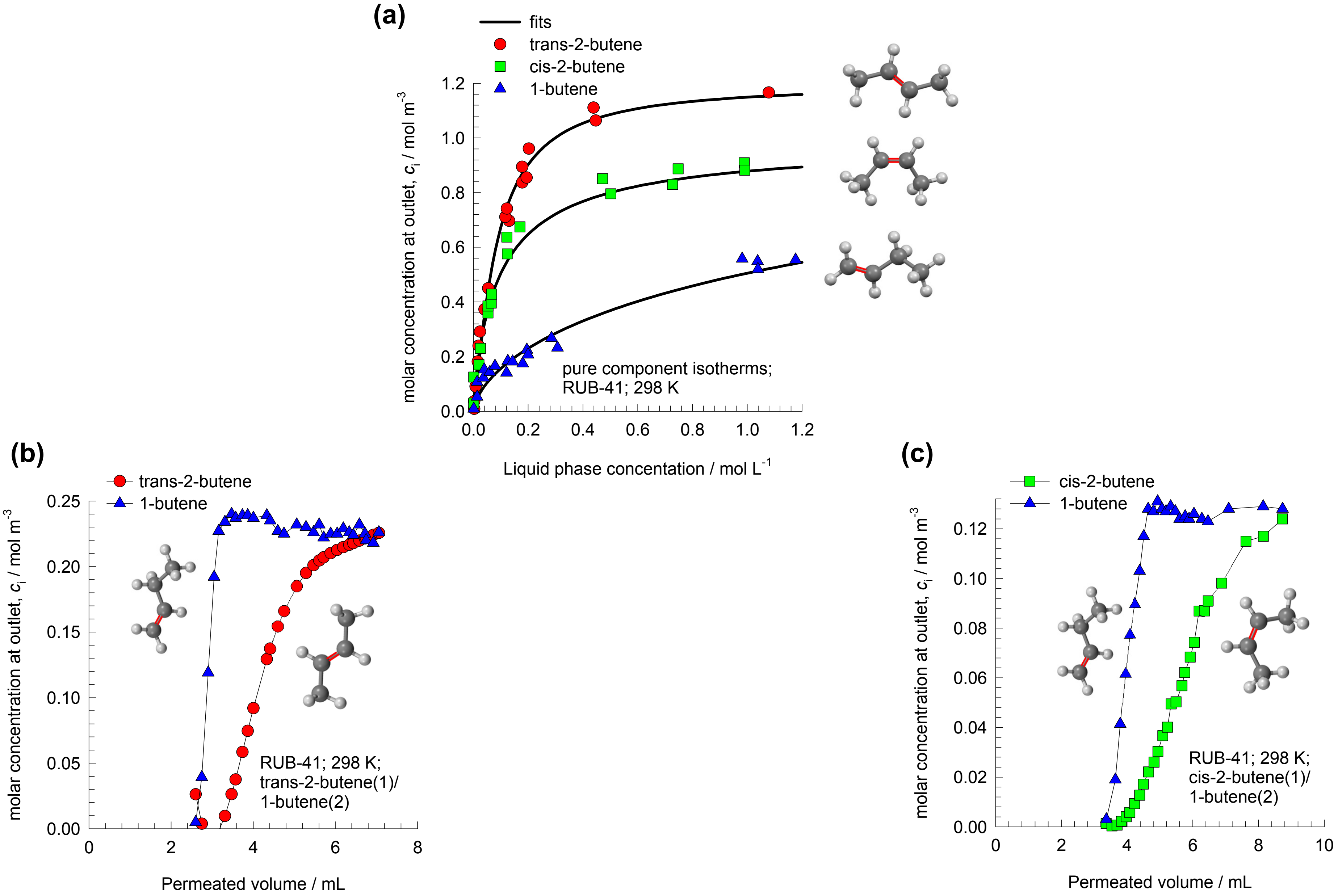

ESI Figure 74

CFC-115 and HFC-125 adsorption in MFI

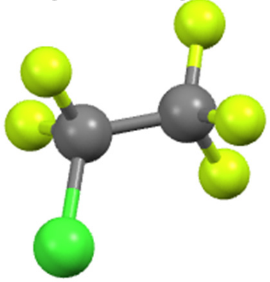

CFC-115
(1-chloro-1,1,2,2,2-pentafluoroethane)
MW = 154.47 g mol^{-1}
Boiling point = 234.1 K
Critical temperature = 353.2 K
Critical pressure = 3.229 MPa
Enthalpy of vaporization = 14.62 kJ mol^{-1}

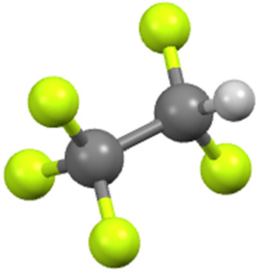

HFC-125
(1,1,1,2,2-pentafluoroethane)
MW = 120.02 g mol^{-1}
Boiling point = 224.7 K
Critical temperature = 339.2 K
Critical pressure = 3.617 MPa
Enthalpy of vaporization = 13.19 kJ mol^{-1}

4 molecules/uc =
0.69346 mol kg^{-1}

(a)

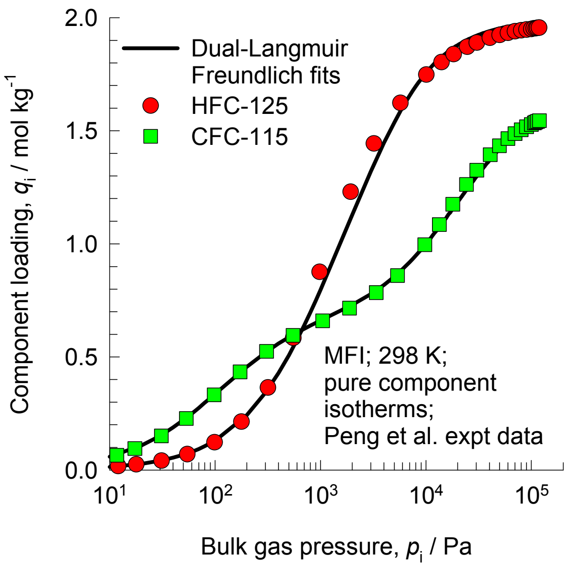

(b)

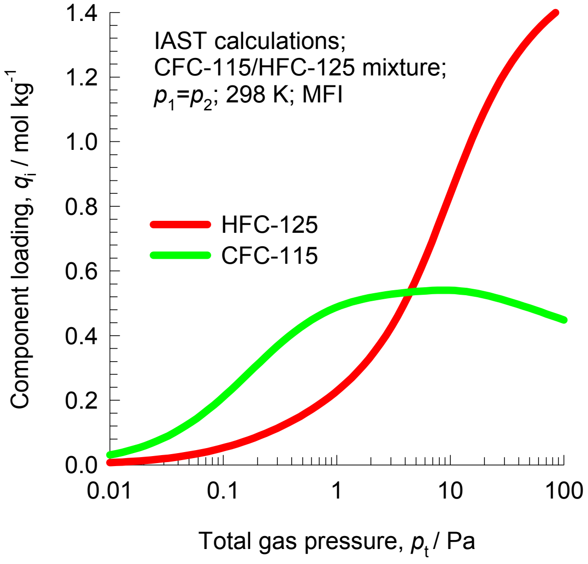

ESI Figure 75

Separation of chlorofluorocarbons

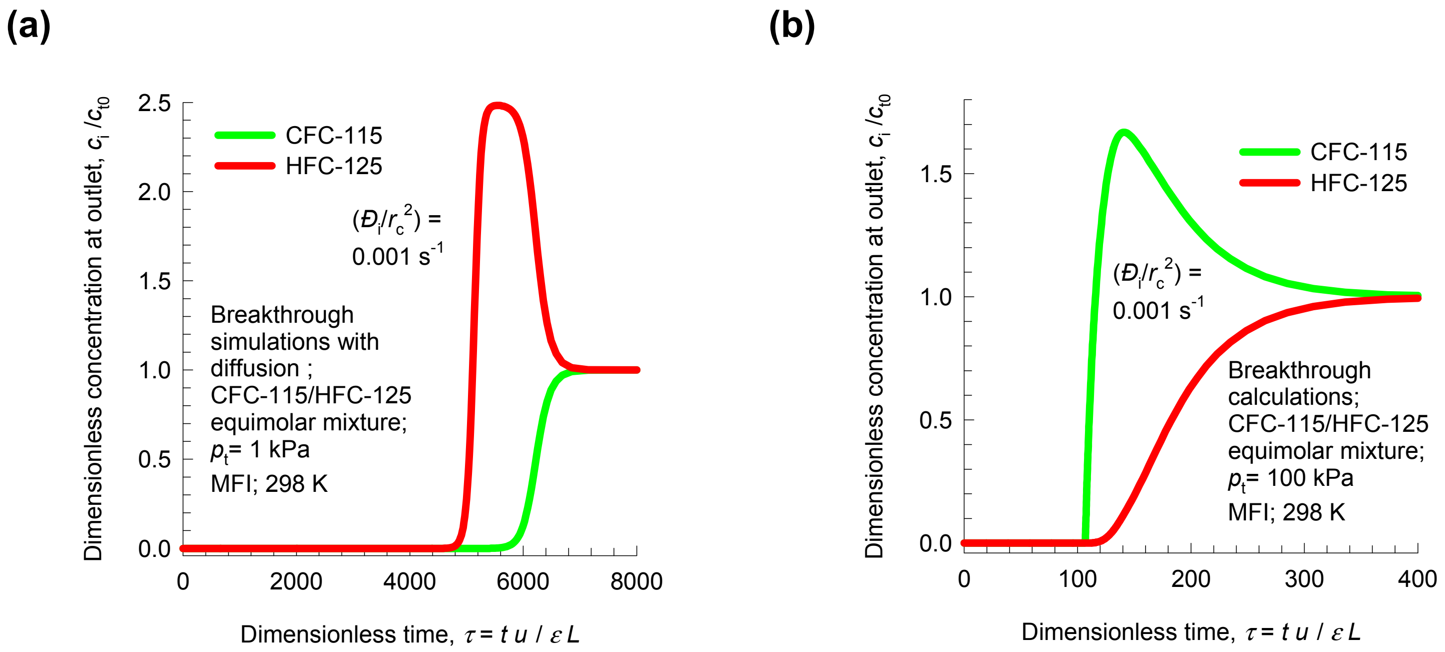

(a) $(Đ_i/r_c^2)$ = 0.001 s^{-1}

Breakthrough simulations with diffusion ; CFC-115/HFC-125 equimolar mixture; p_t= 1 kPa
MFI; 298 K

(b) $(Đ_i/r_c^2)$ = 0.001 s^{-1}

Breakthrough calculations; CFC-115/HFC-125 equimolar mixture; p_t= 100 kPa
MFI; 298 K

ESI Figure 76

Separation of chlorofluorocarbons

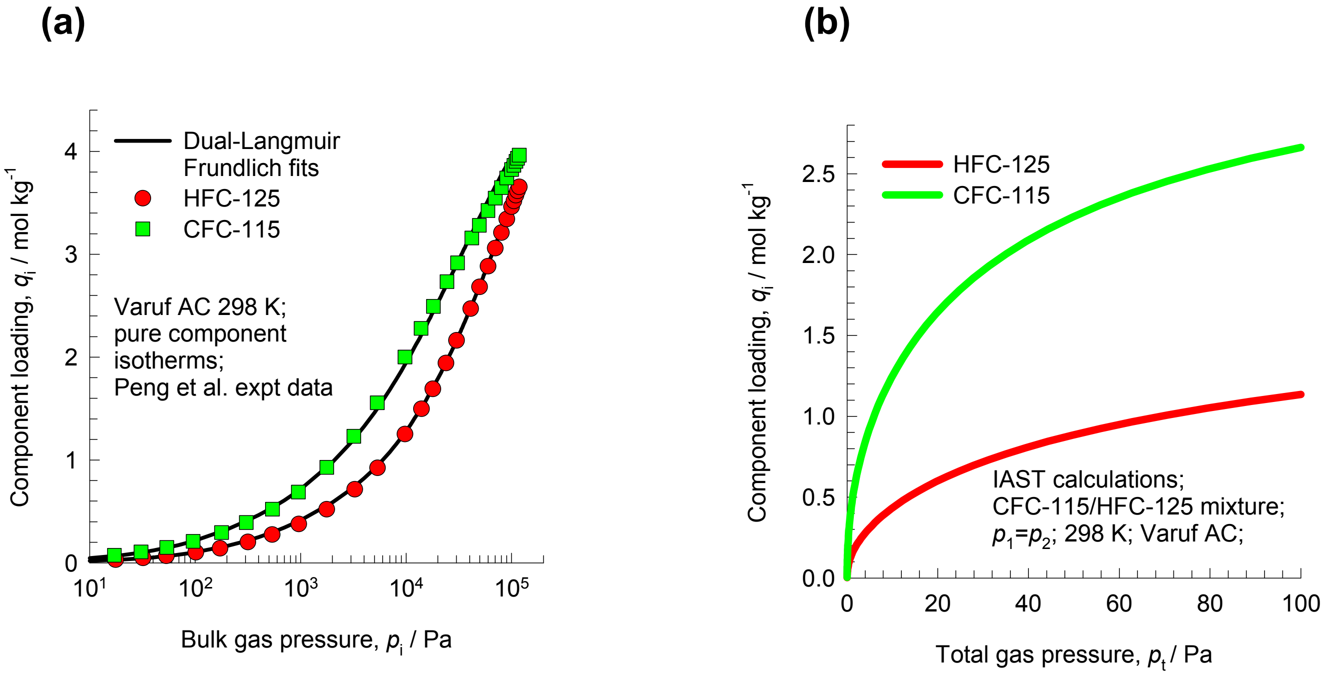

ESI Figure 77

Aromatics in MFI: Lee & Chiang Experiments

(a)

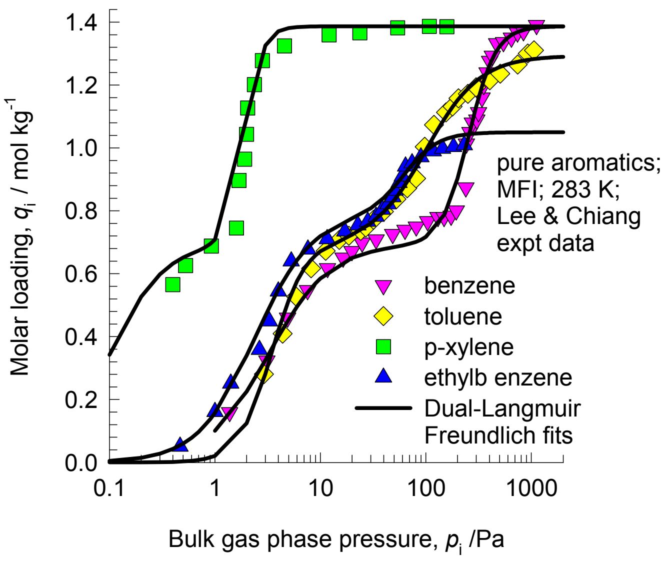

p-xylene

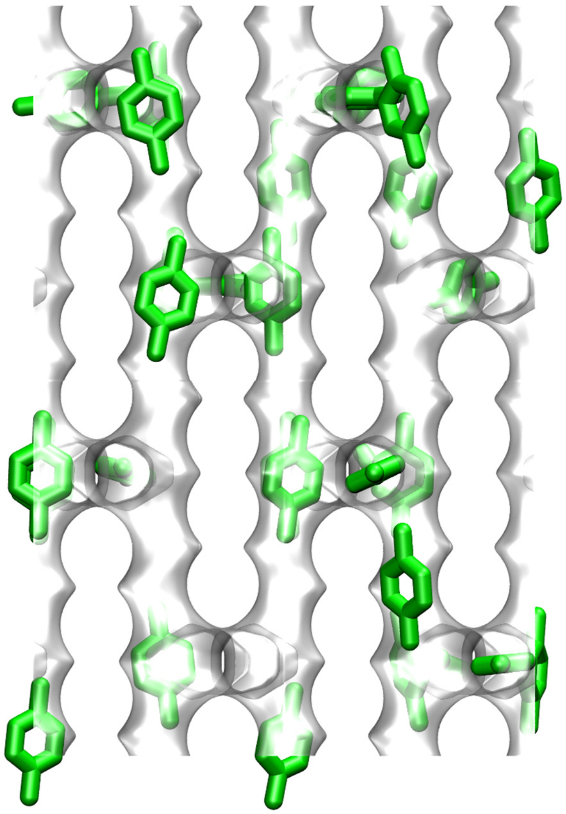

Benzene

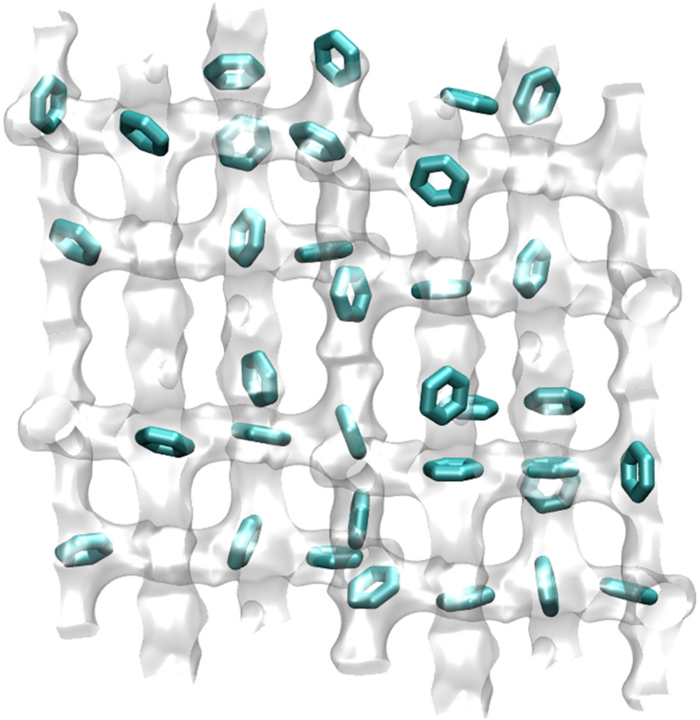

Ethylbenzene

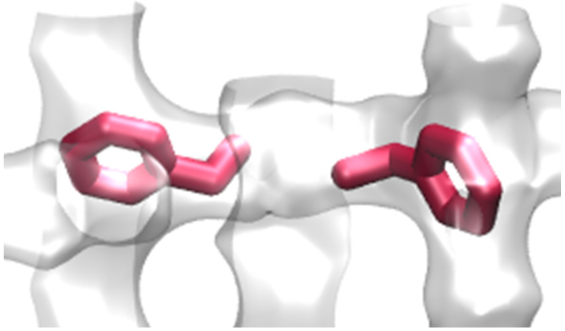

ESI Figure 78

Separation of Benzene/Ethylbenzene in MFI

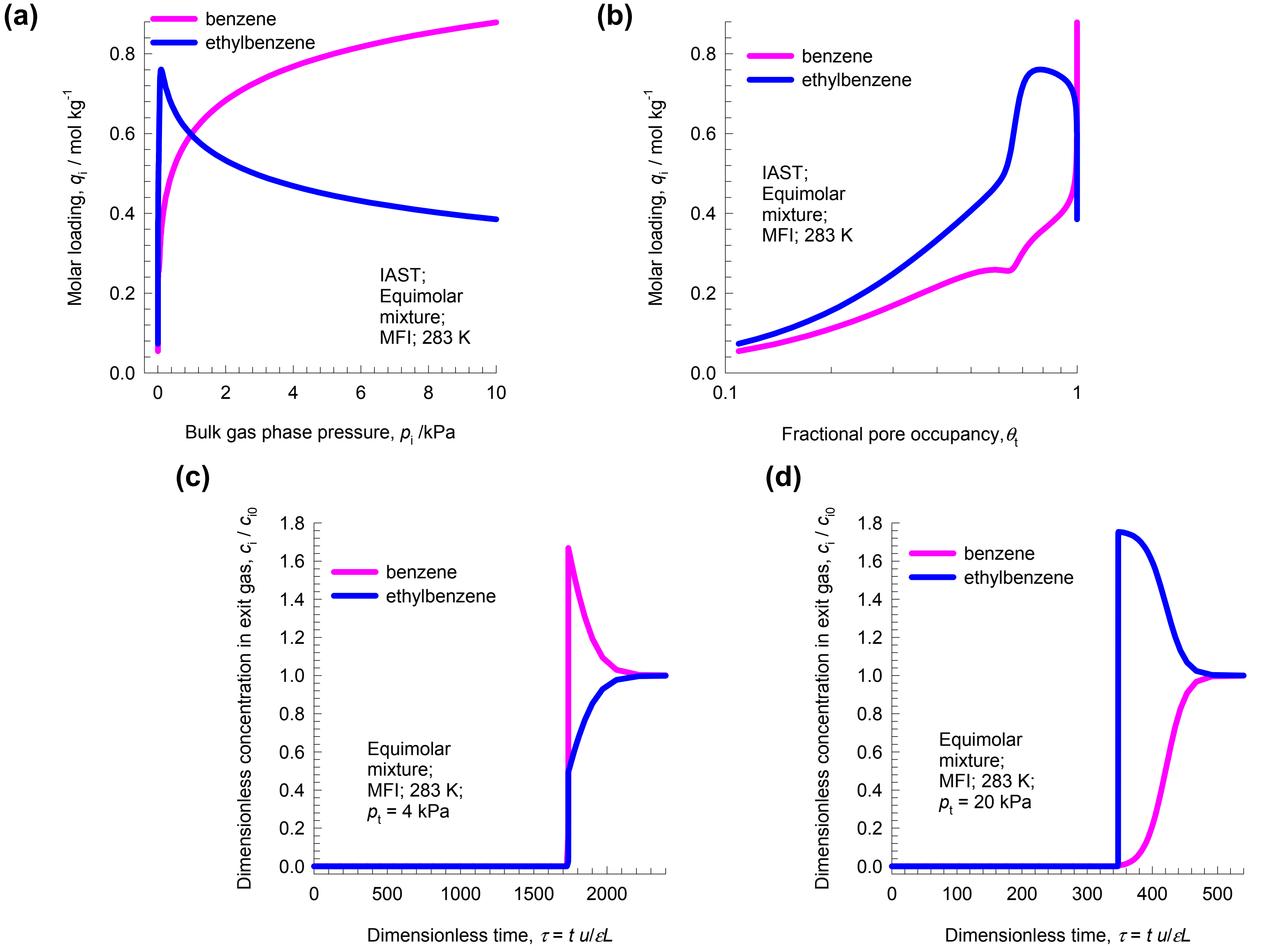

ESI Figure 79

Benzene, Cylcohexane structures

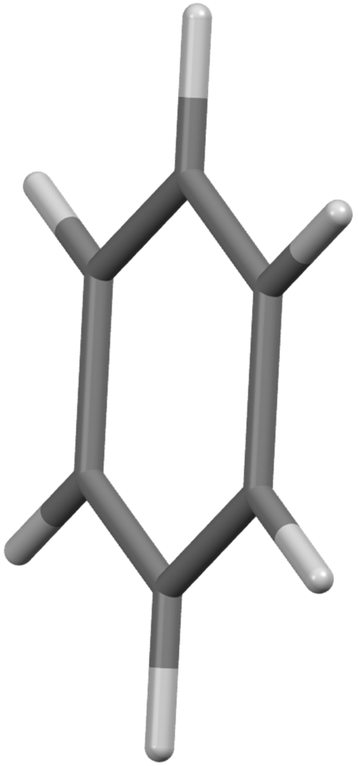

benzene

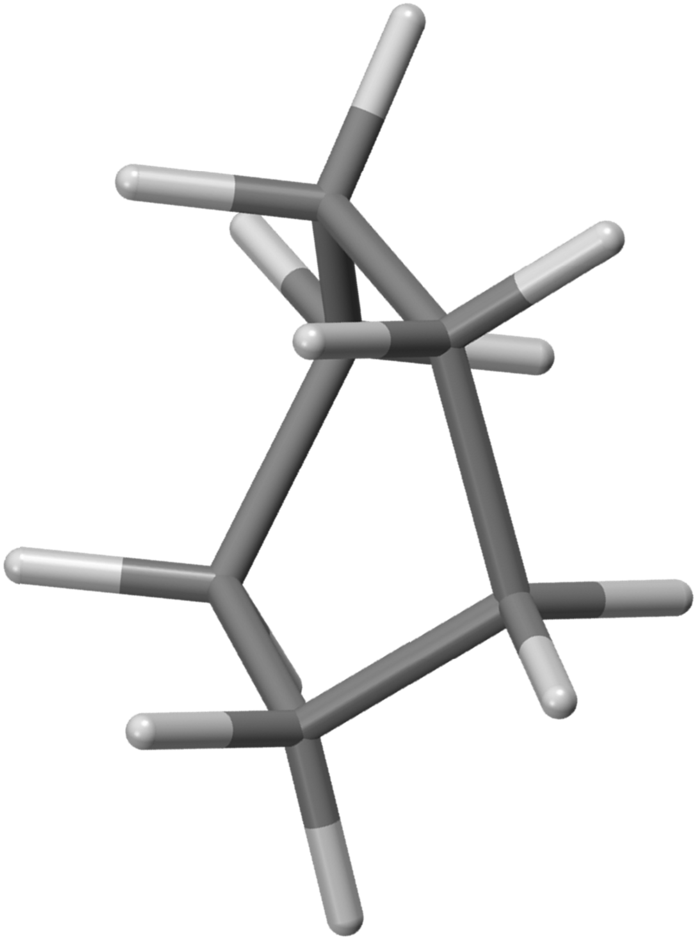

Cyclohexane boat

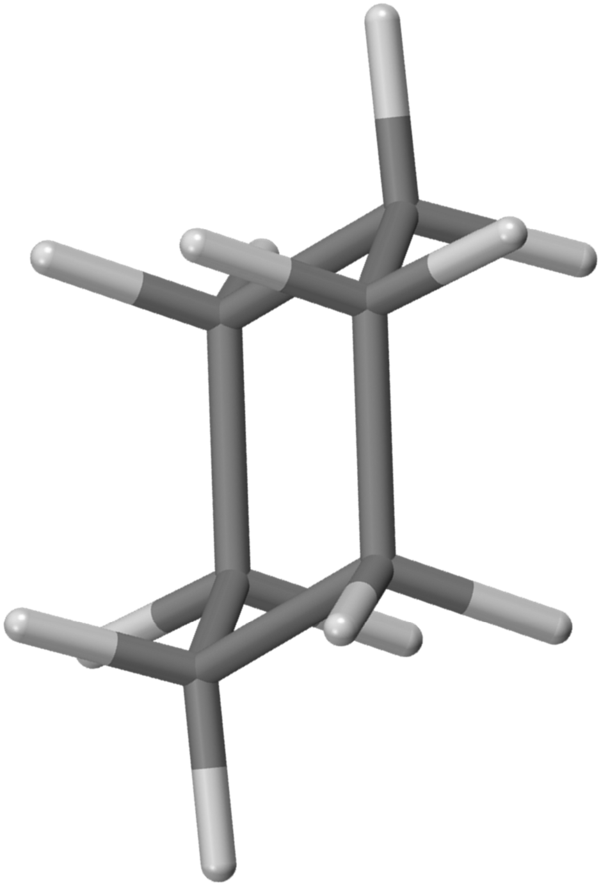

Cyclohexane chair

b.p.= 353.3 K

f.p. = 278.7 K

b.p.= 353.9 K

f.p. = 279.6 K